Summer 2013

Isocyanate-derived organic aerogels: polyurethanes, polyureas, polyamides and polyimides

Chakkaravarthy Chidambareswarapattar

Department: Chemistry

ISOCYANATE-DERIVED ORGANIC AEROGELS: POLYURETHANES, POLYUREAS, POLYAMIDES AND POLYIMIDES

by

CHAKKARAVARTHY CHIDAMBARESWARAPATTAR

A DISSERTATION

Presented to the Faculty of the Graduate School of the

MISSOURI UNIVERSITY OF SCIENCE AND TECHNOLOGY

In Partial Fulfillment of the Requirements for the Degree

DOCTOR OF PHILOSOPHY

in

CHEMISTRY

2013

Approved

Dr. Nicholas Leventis, Advisor
Dr. Chariklia Sotiriou-Leventis, Co-Advisor
Dr. Jeffrey G. Winiarz
Dr. Manashi Nath
Dr. Lokeswarappa R. Dharani

DEDICATED TO

MY BELOVED PARENTS

Smt. INDRA CHIDAMBARESWARAN

&

Shri. R. CHIDAMBARESWARAPATTAR

PUBLICATION DISSERTATION OPTION

This dissertation has been prepared in the format used by *Chemistry of Materials*, *Journal of American Chemical Society*, *Journal of Materials Chemistry* and *Advanced Materials*. This dissertation consists of two articles that have been published, three articles which have been submitted for publication. Paper I found on pages 72-180 has been submitted to *Chemistry of Materials*. Paper II has been submitted to *Journal of American Chemical Society* (*J. Am. Chem. Soc.*) (Pages 181-214). Paper III (Pages 215-238) and Paper IV (Pages 239-284) are published in *Journal of Materials Chemistry*. Paper V found on pages 285-333 has been submitted to *Advanced Materials*.

ABSTRACT

Aerogels are 3D assemblies of nanoparticles with high open porosity and high surface area, and are pursued for their low density, low thermal conductivity, low dielectric constant and high acoustic attenuation. The foundation for those exceptional properties is their complex hierarchical solid framework (agglomerates of porous, fractal secondary nanoparticles). On the down side, however, aerogels are also fragile materials. The mechanical strength of silica aerogels has been improved by crosslinking the framework with organic polymers. The crosslinking polymer has been assumed to form a conformal coating on the surface of the skeletal framework bridging covalently the elementary building blocks. However, the drawback of this method is the lengthy post-gelation crosslinking process. Since the exceptional mechanical properties of polymer crosslinked aerogels are dominated by the crosslinking polymer, it was reasoned that purely organic aerogels with the same nanostructure and interparticle connectivity should behave similarly. That was explored and confirmed by organic aerogels derived from multifunctional isocyanates through reaction with (a) alcohols (polyurethanes); (b) water (polyureas); (c) carboxylic acids (polyamides); and, (d) acid anhydrides (polyimides). All processes are invariably single-step, one-pot and take place at room temperature or slightly elevated temperatures. The resulting materials are robust, they have very wide range of densities and their nanomorphologies vary from fibrous to particulate or both. By relating the molecular functional group density with the functional group density on the nanoparticle surfaces, this study established that in order for three-dimensional (3D) assemblies of nanoparticles to form rigid nanoporous frameworks, they have first and foremost to be able to develop strong *covalent bonding* with one another. Thus, all macroscopic properties of an aerogel depend on the surface functionality of the 'growing colloidal particle'. Those findings are relevant to the rational design of 3D nanostructured matter, not limited to organic aerogels. The materials synthesized in this study should have a broad range of applications from flexible thermal and acoustic insulations to ballistic protection.

ACKNOWLEDGEMENTS

I would like to express my deepest gratitude to my advisor, Professor Nicholas Leventis and co-advisor Professor Chariklia Sotiriou-Leventis for their continuous guidance, encouragement, support and constructive criticism throughout my graduate studies. Over the years, my personality has been highly influenced by some of their qualities the thorough and systematic approach of Prof. Sotiriou-Leventis, and the dynamic, in genius and willing to go the extra intellectual mile of Prof. Leventis. I am very fortunate to have had them as my advisors.

I would like to thank my committee members, Dr. Jeffrey Winiarz, Dr. Manashi Nath and Dr. L. R. Dharani for investing their valuable time reading my thesis and their valuable suggestions. I thank the Department of Chemistry of Missouri S&T for providing teaching assistantships and its resources. Special thanks are reserved for Mr. Joe Counsil for his timely help with all instrumentations. I would also like to extend my thanks to Dr. Hongbing Lu (UT-Dallas), Dr. Mandakini Kanungo (Xerox Corporation) and Dr. Stephan Steiner (MIT) for their encouragement and support.

I would like to thank all past and fellow group members Shruti, Abhishek, Suraj, Tyler for their help, guidance and more importantly their friendship. I also want to thank Dr. Lai and all the undergraduates for their help and support in completing my projects.

I would also extend my thanks to all my friends and to name a few – Subramanian, Raja, Priya, George, Hari, Abhijit, Prashant, Sasmit, Sukanya who always stood by me during good and tough times.

Most importantly, I would like to thank my father, Mr. R. Chidambareswarapattar, who lives in my heart forever and my beloved mother, Mrs. Indra C, who supported me in every decision I have made so far. Words alone cannot express my feelings for how much I owe them. I would also like to thank my brothers Ramaswamy and Visu, sister-in-law Ramya and my lovely nephew Ishaan, my periamma, periappa and their family for their incomparable love, motivation and support.

TABLE OF CONTENTS

Page

LIST OF ILLUSTRATIONS

PAPER III

PAPER IV

LIST OF SCHEMES

PAPER I

PAPER II

PAPER IV

PAPER V

LIST OF TABLES

PAPER V

1. INTRODUCTION

1.1 AEROGELS – BRIEF HISTORY

Aerogels, nicknamed frozen smoke, are one of the world's lowest-density solids.[1] Typically, they consist of more than 90% v/v of empty space. Owing to their finely structured porous skeletal framework, aerogels show high surface areas, low thermal conductivities and dielectric constants, and high acoustic attenuation.[2] Aerogels were once synonymous with silica aerogels, and were first synthesized by S. S. Kistler in the 1930s. By converting the liquid into a supercritical fluid (SCF) he replaced the pore-filling solvent of wet-gels with air without destroying the gel structure.[3] Besides silica, he successfully prepared other metal oxide aerogels along with some organic aerogels.[4] Kistler realized the potential economic significance of aerogels and commercialized the first silica aerogels through Monsanto Chemical Company. The main drawback of Kistler's method for the preparation of silica aerogels was the time-consuming gelation and solvent exchange process. In 1966 Peri introduced a new process for synthesizing aerogels using alkoxides as precursors.[5] Subsequent research efforts have extended this class of materials to non-silica inorganic oxides, natural and synthetic organic polymers, carbons, metals and ceramic materials.[6]

1.2 THE SOL-GEL PROCESS LEADING TO HIERARCHICAL NETWORK FORMATION – SILICA AEROGELS

Preparation of aerogels involves formation of three dimensional (3D) porous assemblies of nanoparticles. As with any porous materials, the size and shape of the pores influences the bulk physical properties. In particular, aerogel structures are characterized by open, accessible, mesopores (2–50 nm). Figure 1.1 shows the typical solid network structure of silica aerogels. The solid network consists of a complex

hierarchical structure comprising aggregation of smaller primary particles to fractal porous secondary particles, which eventually agglomerate to a pearl-necklace like structure.

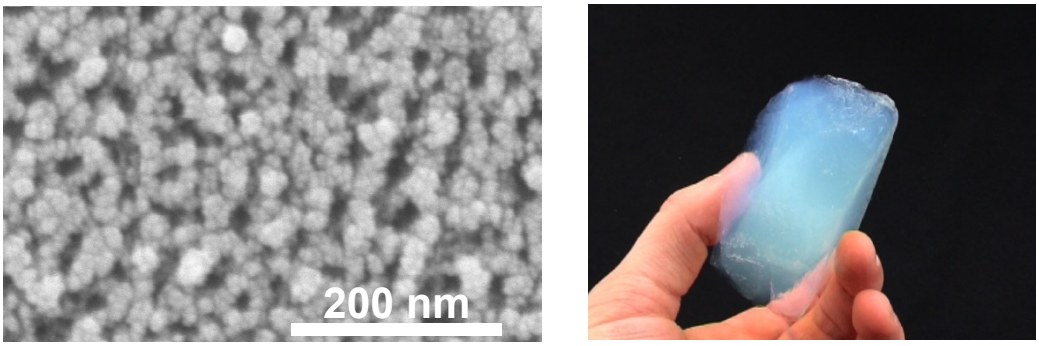

Figure 1.1 The typical nanostructure of a silica aerogel (left) and its macroscopic appearance (right).[7]

Typical alkoxy silane precursors used for the synthesis of silica aerogels include tetramethylorthosilicate ($Si(OCH_3)_4$, abbreviated as TMOS) or tetraethylorthosilicate ($Si(OC_2H_5)_4$, abbreviated as TEOS). Those precursors are dissolved in their respective alcohol, which acts as a co-solvent for the silane and water needed for hydrolysis. The first step of the process is either an acid- or a base-catalyzed hydrolysis of the alkoxy silane to form silanols, which undergo a condensation reaction *in situ* to form Si-O-Si linkages as shown in Scheme 1. The linkages grow in 3D to form a silica network that in turn yields sequentially primary particles, secondary particles and higher aggregates.[8]

Scheme 1. Formation of silica network from the hydrolysis and condensation of TMOS

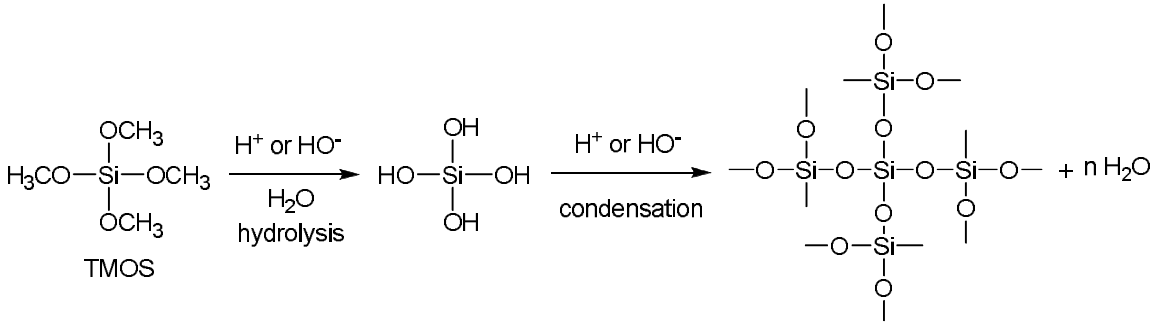

The generation and agglomeration of particles is controlled by the sol-gel process. The physical properties of aerogels are effectively derived from the shape and size of pores in the solid network.[9] Consequently, a significant effort has been directed towards understanding and controlling the nanoporous structure. Figure 1.2 shows the preparation of silica aerogels via sol-gel process, which involves mixing of precursors to form nanoparticles through polymerization and phase separation of colloidal primary nanoparticles. When enough primary nanoparticles are formed, they are connected to one another to form fractal secondary particles. These secondary particles agglomerate, forming a network that grows in three dimensions to yield a wet-gel. The resulting solvent-filled wet-gels are solvent-exchanged with alcohol to remove water from the network before drying.

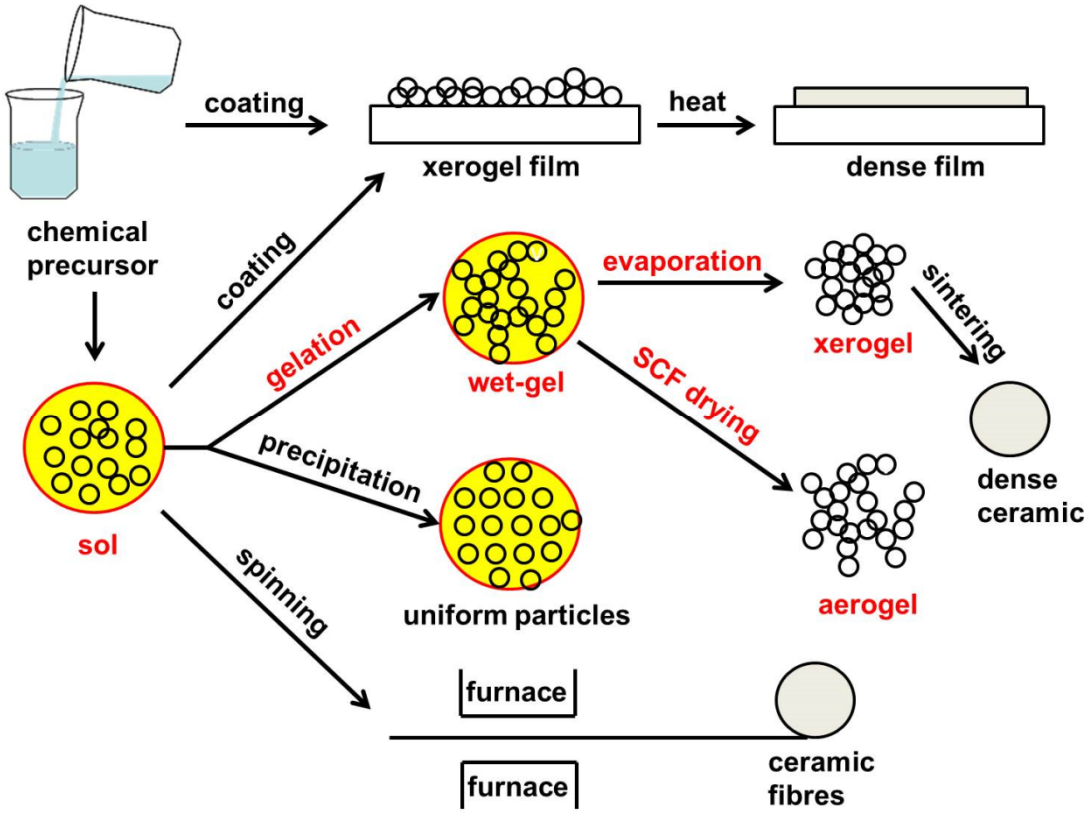

Figure 1.2 Preparation of aerogel via the sol-gel process.

Silica wet-gels can be dried in two different ways: (a) by allowing entrapped solvent to evaporate at atmospheric pressure to form a collapsed porous structure with extensive shrinkage; the resulting materials are referred to as xerogels; or, (b) by using a SCF such as CO_2 to form an aerogel whereas the volume and the porous structure of the original wet-gel are retained. In practice, supercritical drying involves use of an autoclave to replace the gelation solvent with liquid CO_2, which is then converted to SCF and vented off isothermally (critical point of CO_2: 31.1 ^{o}C at 1072 psi).[10]

1.3 CROSSLINKED SILICA AEROGELS (X-AEROGELS)

Silica aerogels have been considered for many applications including thermal and acoustic insulation,[11] dielectrics,[12] catalyst supports[13] and as hosts for functional guests in chemical, electronic and optical applications.[14] However, silica aerogels have been actually used only in specialized environments, like as Cerenkov radiation detectors in certain nuclear reactors, aboard spacecraft as collectors for cosmic particles (NASA's Stardust program),[15] and for thermal insulation in planetary vehicles on Mars. The main reason for the slow commercialization of silica aerogels is their fragility and poor mechanical properties. The poor mechanical properties of silica aerogels are generally attributed to the well-defined narrow interparticle necks.[16] The fragility issue of silica aerogels has been resolved by crosslinking aerogels with organic polymers.[17]

Briefly, it was realized that skeletal silica nanoparticles possess surface silanol groups, which can react with polyisocyanates to form polyurethane tethers that bridge the nanoparticles chemically, reinforcing the interparticle necks. Thus, the entire skeletal framework is coated conformally with a polymer, while the open porosity is preserved (Figure 1.3). The resulting materials have been referred to as polymer-crosslinked aerogels (X-aerogels). While all the other bulk properties of X-aerogels are not compromised significantly by crosslinking, an increase in the bulk density by a factor of 3 leads to a 300 × increase in the flexural strength of typical X-aerogel monoliths. X-aerogels are exceptionally strong in comparison not only with their non-crosslinked counterparts (native aerogels), but also with other materials that are usually considered strong, such as steel, Kevlar, and silicon carbide.[18]

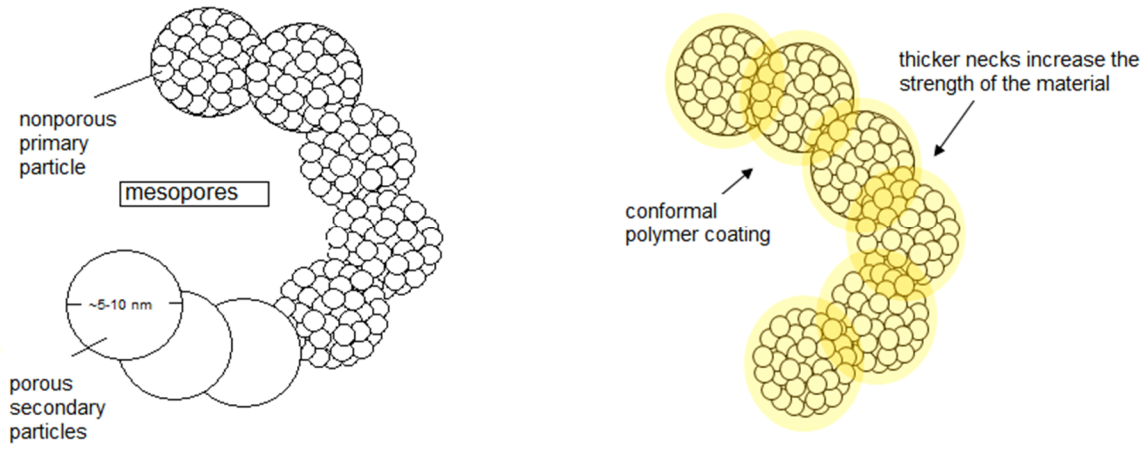

Figure 1.3 A thin polymer layer is formed conformally on the skeletal silica nanoparticles.

In X-linked aerogels, the silica nanoparticle framework serves as a template for the accumulation of polymer, which covalently connects the skeletal particles. However, since the exceptional mechanical properties of X-aerogels are traced to the polymer coating, it was reasoned that aerogels made out of the crosslinkers themselves, i.e., purely polymeric aerogels with the same nanomorphology and interparticle connectivity of X-aerogels, should have similar mechanical properties and a much simpler synthetic protocol.

Our most widely used crosslinkers, isocyanates, are industrial precursors for the synthesis of polyurethanes and polyureas.[19] These isocyanate-derived polymers are very robust and their mechanical properties can be easily tuned. Therefore, we explored isocyanates and their chemistry in order to synthesize new porous materials for specific applications especially for ballistics.

1.4 THE CHEMISTRY OF ISOCYANATES

The isocyanate, -N=C=O, is one of the most reactive organic groups. Owing to the electron withdrawing ability of both the oxygen and nitrogen atoms, the electron density at the carbon is much smaller than in a typical carbonyl group (Scheme 2).

Scheme 2. Possible resonance structures of the isocyanate group

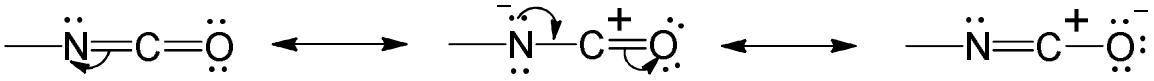

Therefore, the isocyanate group is susceptible to nucleophilic attack (Scheme 3).

Scheme 3. Addition of nucleophile to the isocyanates

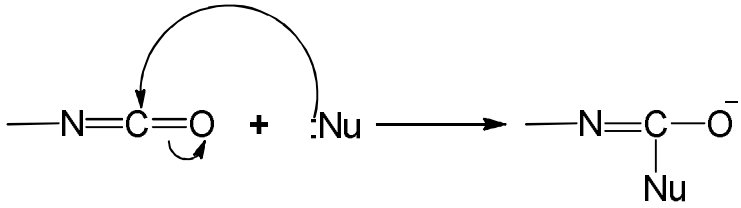

Typical nucleophiles and their relative reactivity are summarized in Table 1.1.

Table 1.1 Active hydrogen compounds ordered by decreasing isocyanate reactivity[20]

active hydrogen compound	relative reaction rate (uncatalyzed at 25 °C)
primary aliphatic amine	100,000
secondary aliphatic amine	20,000 - 50,000
primary aromatic amine	200-300
primary hydroxyl	100
water	100
carboxylic acid	40
secondary hydroxyl	30
ureas	15
tertiary hydroxyl	0.5
urethane	0.3
amide	0.1

The reactivity of the isocyanate group (N=C=O) is further modulated by electron withdrawing or electron donating groups attached on N. The aromatic isocyanates are generally more reactive than their aliphatic counterparts.[21] In addition, electron-withdrawing substitution on aromatic isocyanates will increase the positive charge on the carbon atom, thereby will increase the reactivity of the isocyanate towards nucleophilic attack when steric factors are neglected.[22] Conversely, electron donating group (EDG) will reduce the reactivity of the NCO group, as illustrated in Scheme 4.[21]

Scheme 4. Decreasing order of isocyanate reactivity in the presence of EDG

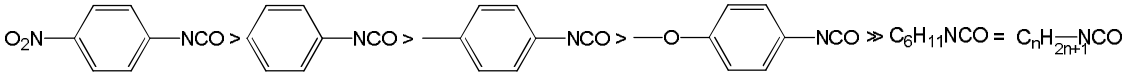

Isocyanates can react with various functional groups and can undergo self-addition reactions.[23] In particular, below we review the reaction of isocyanates with specific nucleophiles relative to the synthesis of aerogels.

1.4.1 Reaction of Isocyanates with Amines. Nucleophilic addition of the amine group to the isocyanate electrophilic carbonyl yields urea (Scheme 5).

Scheme 5. Formation of urea from isocyanates and amines

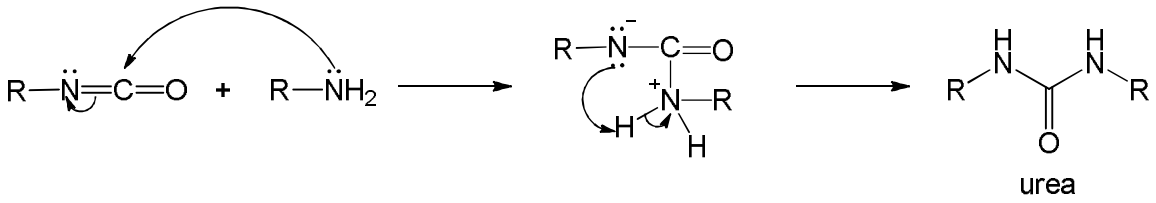

It is a very fast and exothermic reaction, and does not require any catalyst. Aromatic amines react slower than their aliphatic counterparts because of the delocalization of the amine electron pair in the aromatic ring through resonance.[24]

1.4.2 Further Reaction of Isocyanates with Ureas. Urea, acting as a nucleophile itself, is capable of attacking excess of isocyanate under more rigorous reaction conditions to yield biurets. (Scheme 6)[21,25] Due to the low reactivity of urea, biurets are normally formed at temperature between 100-150 ^{o}C.

Scheme 6. Formation of biurets from isocyanates and ureas

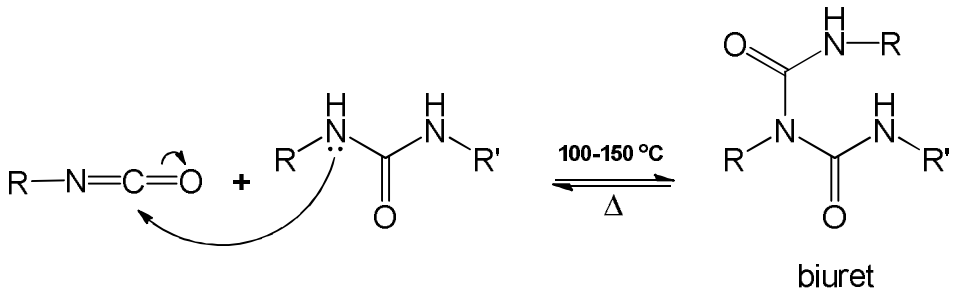

1.4.3 Reaction of Isocyanates with Water. If the nucleophile is water, it attacks the isocyanate carbonyl to yield an unstable carbamic acid, which decomposes to amine and carbon dioxide as a by-product (Scheme 7). The *in-situ* generated amine reacts rapidly with yet unreacted isocyanate to form urea as illustrated in scheme 5.[26]

Scheme 7. *In-situ* formation of amine from isocyanates and water

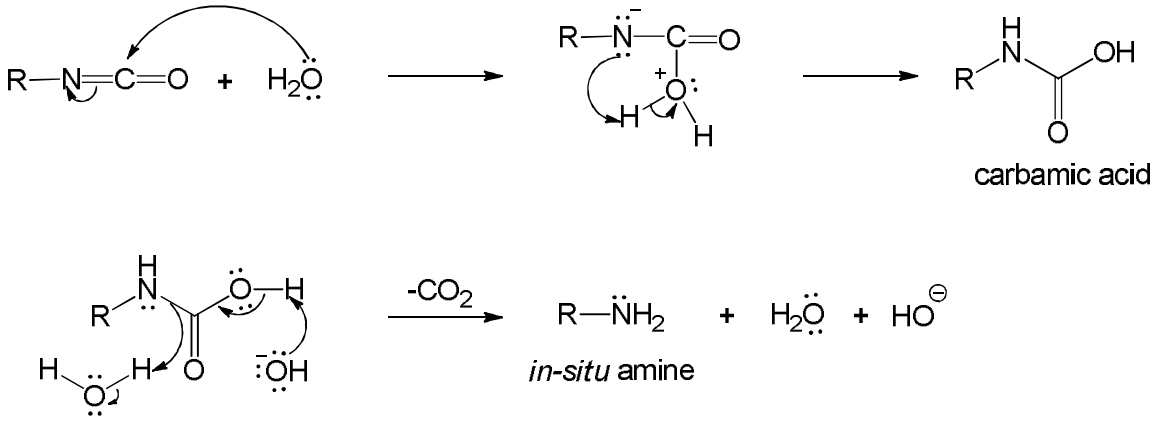

1.4.4 Reaction of Isocyanates with Alcohols. The addition reaction between an isocyanate and an alcohol yields urethane. The stoichiometry of the reaction is illustrated in Scheme 8.[26]

Scheme 8. Formation of urethanes from isocyanates and alcohols

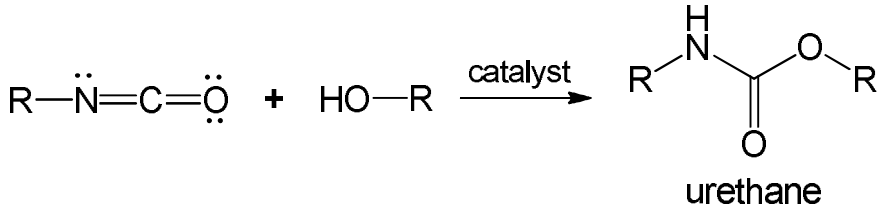

For steric reasons, the reactivity of the alcohol decreases in the order of primary to secondary. Phenols are even less reactive due to resonance delocalization of the electron pair on oxygen to the aromatic ring. Owing to the relatively low reactivity of alcohols with isocyanates, urethane formation is typically catalyzed with Lewis acids or bases.

1.4.4.1 Urethanes by base-catalysis. Baker et. al. elucidated the formation of polyurethanes via tertiary amine (B) catalysis in dibutyl ether as solvent. For this, he assumed nucleophilic catalysis involving activation of the isocyanates by addition of B (Scheme 9).[27,28]

Scheme 9. Formation of urethanes according to Baker et. al.

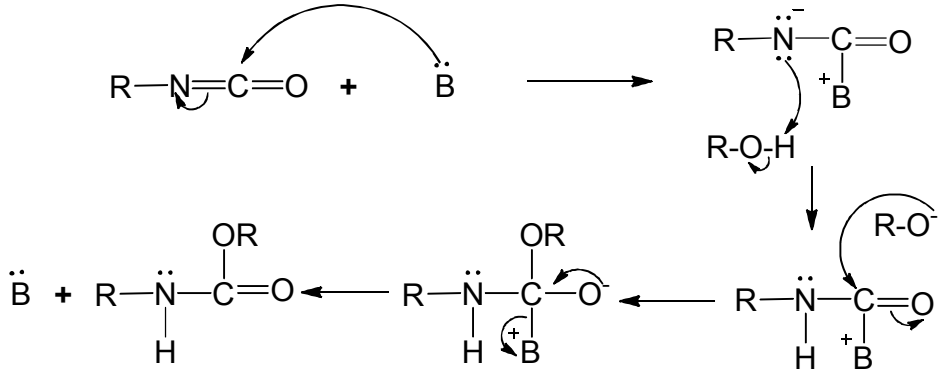

It was realized that the mechanism shown in Scheme 9, leads to many contradictions and cannot be valid in general. However, for the acidic alcohol such as phenols, are transformed by the base catalyst into the anionic O^- which is then added to isocyanate (Scheme 10).[29]

Scheme 10. Formation of urethanes from isocyanates and alcohols by base catalysis

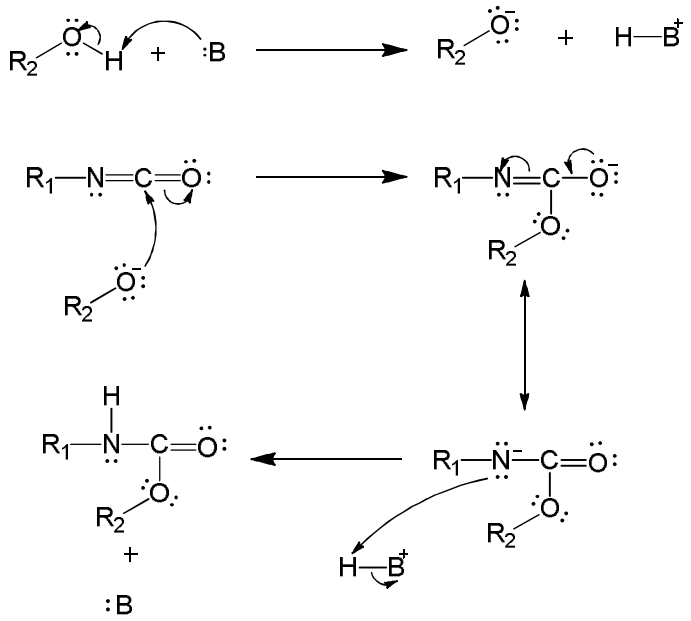

1.4.4.2 Urethanes by acid-catalysis. For the commercial foam processes, organotin compounds are widely used. Borkent et al. showed that the formation of urethane in polar solvents such as DMF is proportional to the square root of dibutyltin dilaurate concentration.[30] Britain and Gemeinhardt studied gelation at 70 ^oC in polyether solvent with a NCO/OH ratio of 1.0 showing that many metallic compounds were effective catalysts for the isocyanate-hydroxyl reaction. A roughly descending order of catalytic activity including bases, is as follows: Bi, Pb, Sn, DABCO, strong bases, Ti, Fe, Sb, U, Cd, Co, Th, Al, Hg Zn, Ni, trialkylamines, Ce, Mo, Va, Cu, Mn, Zr and trialkyl

phosphines.[31] Among those, lead-2-ethylhexoate, lead benzoate, lead oleate, sodium trichlorophenate, sodium propionate, lithium acetate, potassium oleate can be used as trimerization catalysts as well.[31] Tin catalyst such as dibutyltin dioctoate, dibutyltin dilaurate, stannous oleate and stannuous octoate are many times more powerful for the isocyanate-hydroxyl reaction than tertiary amines, but they are not strong catalysts for the isocyanate-water reaction to yield urea (foam system).[31] H. A. Smith's work on catalysis of the formation of urethane suggested that metal salts catalyze the reaction by activating both reactants by means of ternary complex. The activity of the metal salts depends on their ability to form a complex in which the two reacting groups are held in their optimum position for reaction.[32] However, the mechanism involves the N-coordination of the isocyanates with a tin alkoxide that is formed by the alcoholysis of the starting tin compound (Scheme 11).[33]

Scheme 11. Formation of urethanes from isocyanates and alcohols by acid catalysis

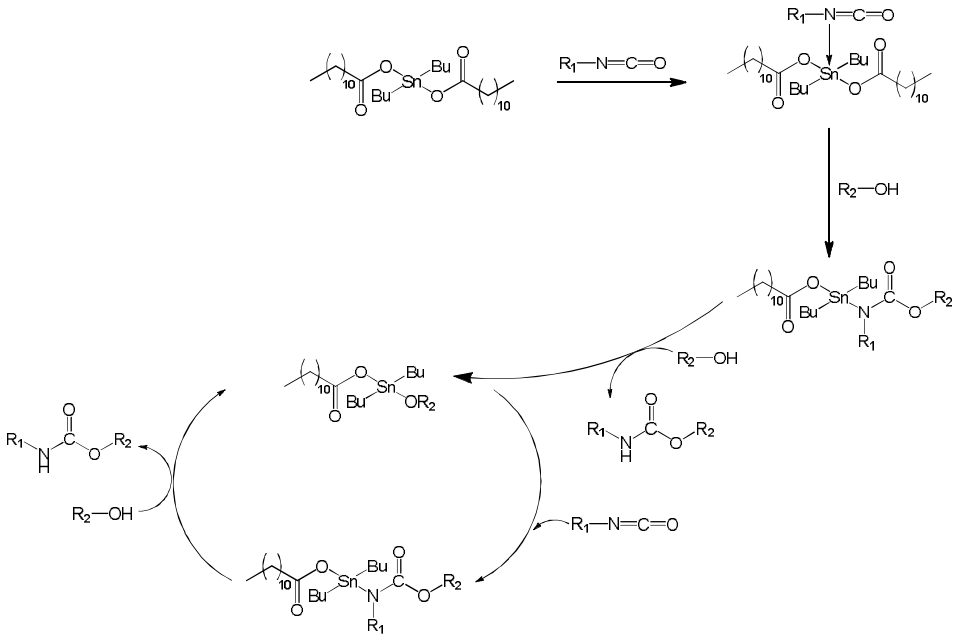

1.4.5 Further Reaction of Isocyanates with Urethanes. Similar to urea, urethanes are capable of reacting with isocyanates to yield allophanates (Scheme 12).[21,25] This reaction is also reversible and occurs at temperatures between 120 ^{o}C – 150 ^{o}C.

Scheme 12. Formation of allophanates from isocyanates and urethanes

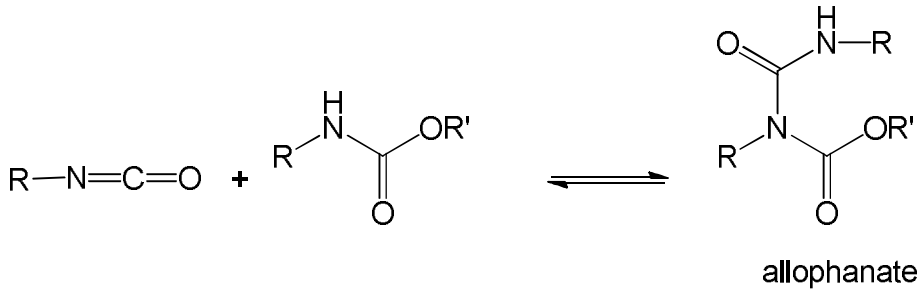

The formation of allophanates and biurets leads to the crosslinking of polyurethanes.

1.4.6 Reaction of Isocyanates with Carboxylic Acids. Polyamides are widely synthesized using carboxylic acids or corresponding acid chlorides and amines (see polyamide aerogels). The idea of preparing polyamides directly from dicarboxylic acid and diisocyanates has also been explored to a great extent.[34] The reaction can take place without catalyst at temperatures as low as the room temperature (23 ^{o}C) or at elevated temperatures such as 90 ^{o}C or 135 ^{o}C. Using suitable catalysts, the reactions will be much faster.[35] For example, Onder and Toyoda et al. reported that polyamides can be obtained from aryl diisocyanates and dicarboxylic acids in the presence of catalyst comprising alkoxy metal salts, alkali metal lactamates, and mono alkali metal salts of dicarboxylic acid. However, the polymerization process still required elevated temperatures (>100 ^{o}C) in order to achieve high molecular weight polymers. There are reports of fast synthesis of high molecular weight polyamides via the polymerization of

dicarboxylic acids with aromatic diisocyanates using Lewis acids as catalysts at relatively low temperatures (<100 ^{o}C) with a short reaction time (e.g. 3-4 h).[36] Kinetic studies of the reaction between isocyanates and acids have shown that high polarity reaction media increase the rate of reaction and aromatic isocyanates are more reactive than aliphatic counterparts.[37] The reaction of an isocyanate with a carboxylic acid in equimolar amount yields carbamic-carboxylic anhydride (Scheme 13).

Scheme 13. Synthesis of polyamide from isocyanates and carboxylic acids

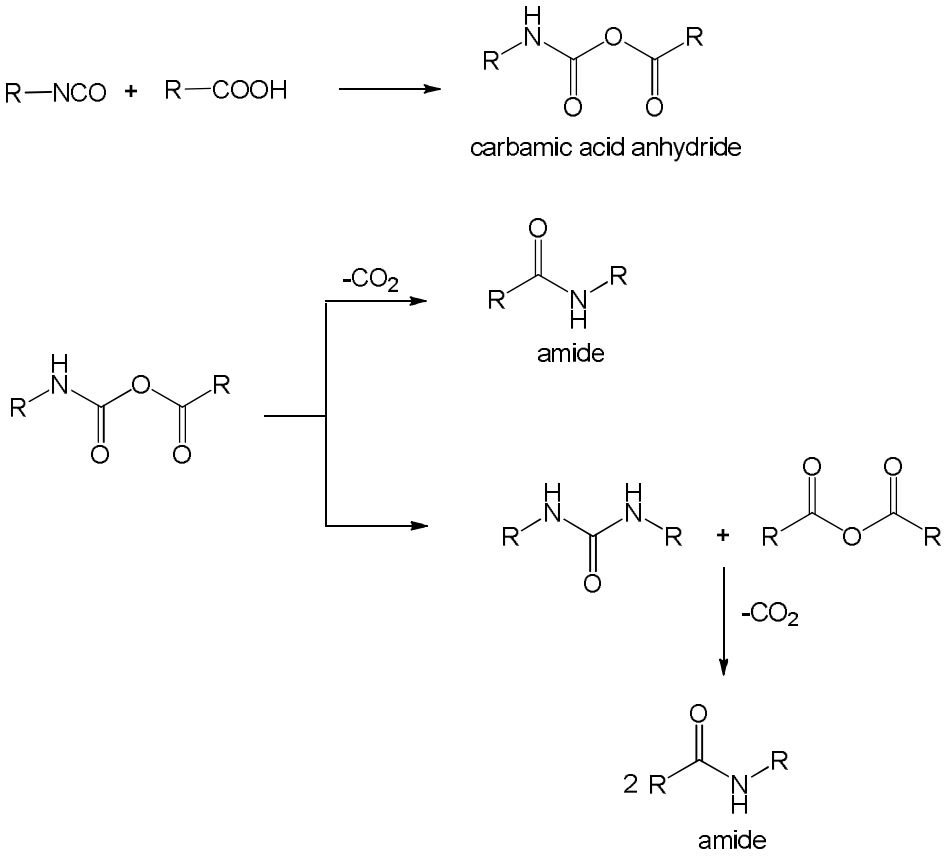

Carbamic acid anhydride is not stable in most cases although it can be isolated in some cases. The decomposition of carbamic acid anhydride proceeds by two paths (Scheme 13). The mechanism of yielding amide is shown in Scheme 14.

Scheme 14. Mechanism yielding polyamide from isocyanates and carboxylic acids

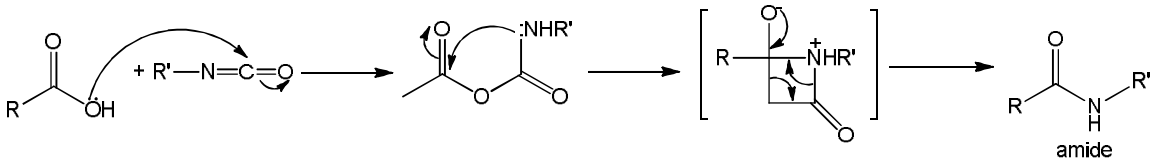

Otherwise, the carbamic-acid anhydride may decompose into symmetrical urea and the acid anhydride which can also react to yield amide with parallel evolution of carbon dioxide (Scheme 13). The *in-situ* anhydride and urea react to form amide at temperatures ≥ 135 ^{o}C.[38] Therefore, amides can be synthesized from isocyanates and carboxylic acids in good yields.[39]

1.4.7 Reaction of Isocyanates with Anhydrides. Bulk polyimides are synthesized via either the DuPont route, or polymerization of monomeric reactants (the PMR route - see polyimide aerogels), or the isocyanate route. Polyimides from isocyanates were first reported in 1854 by Wurtz,[40] who synthesized *N*-ethyldiacetimide from acetic anhydride and ethyl isocyanate. Later, Hurd et. al. and Marton et. al. indicated that imides can be prepared using isocyanates and acyclic anhydrides in fair yields (71%).[41] The reaction of aromatic isocyanates (e.g., 4,4'-diphenylmethanediisocyanate (**MDI**)) with aromatic anhydrides (e.g., pyromellitic

dianhydride (**PMDA**) was first reported by Meyers.[42] The reaction was carried out in dimethyl formamide by stepwise heating the reaction mixture from 40 to 130 °C. The final product was obtained in good (78%) yields. Meyers was the first to report that the reaction proceeds through a seven-member ring intermediate (Scheme 15).

Scheme 15. Synthesis of polyimide from isocyanates and anhydrides

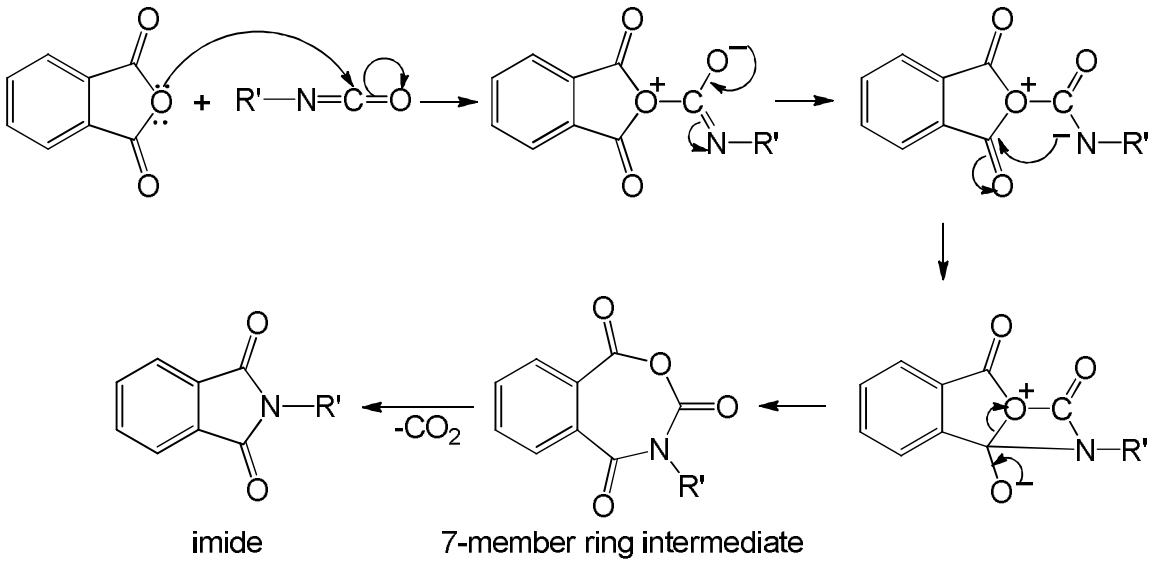

The final polymer was characterized with FTIR. The polyimides synthesized from the isocyanate route are chemically identical to the polyimides obtained from the classic dianhydride and diamine route.

1.4.8 Self-reaction of Isocyanates. In addition to the above reactions, isocyanates can also react with themselves to form dimers[43], trimers[43], polymers carbodiimides[44] and uretoneimines[45] at high temperatures in the presence of base catalysts. When two molecules of isocyanate react with each other they form a dimer, a four member heterocyclic ring, which is unstable, since the strain of the four member ring

is very high (Scheme 16). Nevertheless, there is an isocyanate in its dimerized form available commercially, e.g., Desmodur N3200 (Figure 1.4). Figure 1.4 also illustrates the chemical characterization of N3200 by liquid ^{13}C and ^{15}N NMR which confirm the four member ring. Dimerization is limited to aromatic isocyanates and it is inhibited by ortho substituents. For example, 2,4- and 2,6-toluene diisocyanates (**TDI**) do not dimerize, while methylene diisocyanates (**MDI**) dimerize slowly at room temperature. Dimerization is an equilibrium reaction catalyzed by trialkylphosphine, substituted pyridines or trialkylamines. Phosphines and especially trialkylphosphine are much more efficient than pyridine in catalyzing dimer formation (Scheme 17).

Scheme 16. Formation of uretdiones

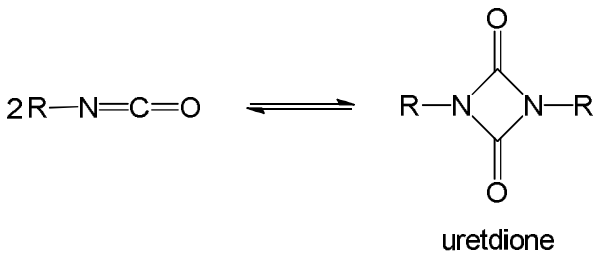

Scheme 17. Dimerization mechanism of aryl isocyanates catalyzed by phosphine[43]

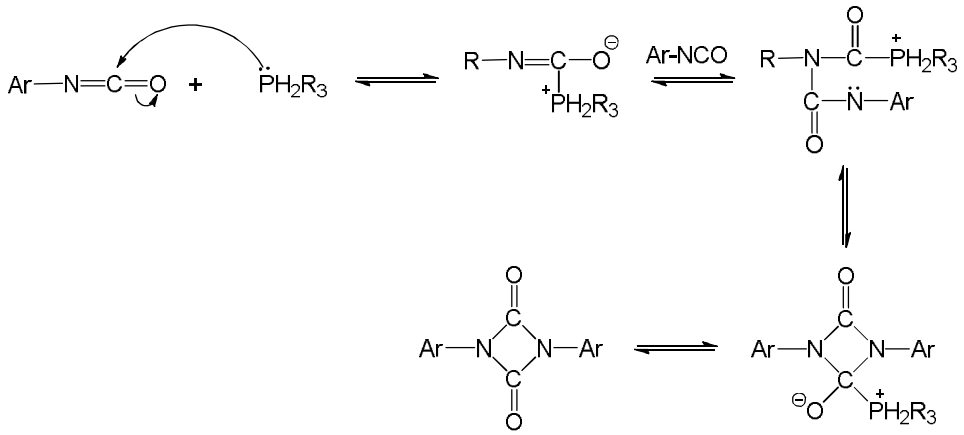

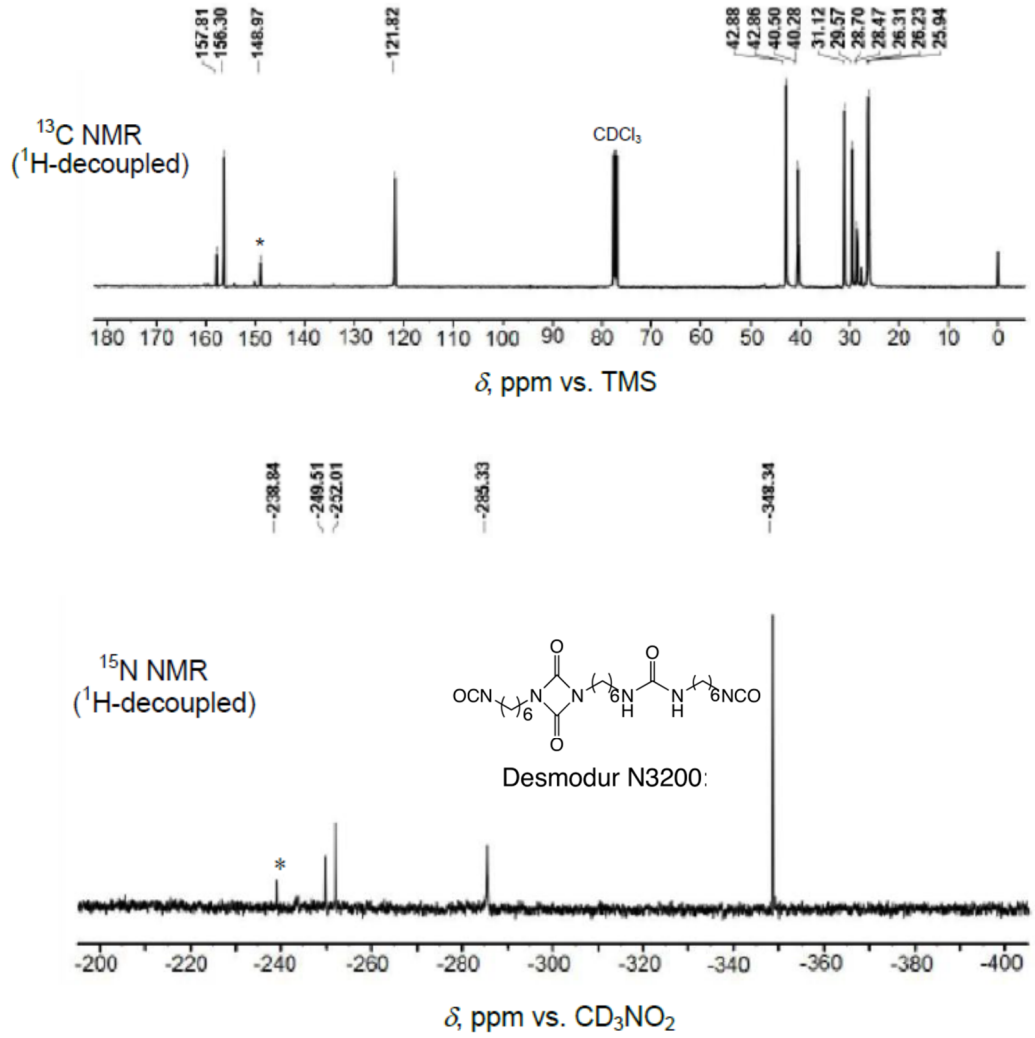

Figure 1.4 Chemical characterization of Desmodur N3200 showing the four membered ring Top: ^{13}C NMR and Bottom: ^{15}N NMR (* - solvent).[46]

Aliphatic and aromatic isocyanates trimerize to form very stable six member isocyanurate rings upon heating and the reaction can not be easily reversed (Scheme 18). Figure 1.5 shows the ^{13}C and ^{15}N liquid NMR of commercially available Desmodur N3300A (N3300A, an aliphatic isocyanate in trimerized form) from Bayer corporation, U.S.A. Some of the study described here uses N3300A.

Scheme 18. Formation of isocyanurates

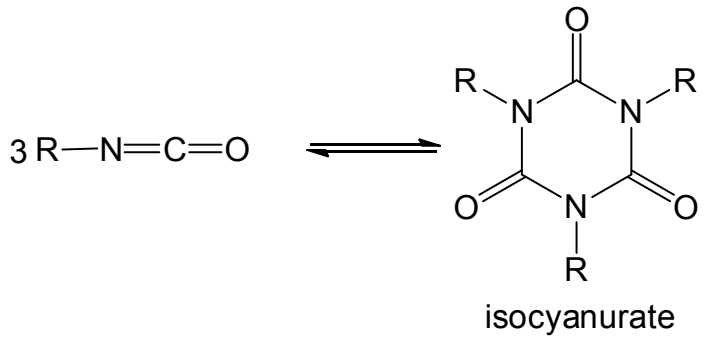

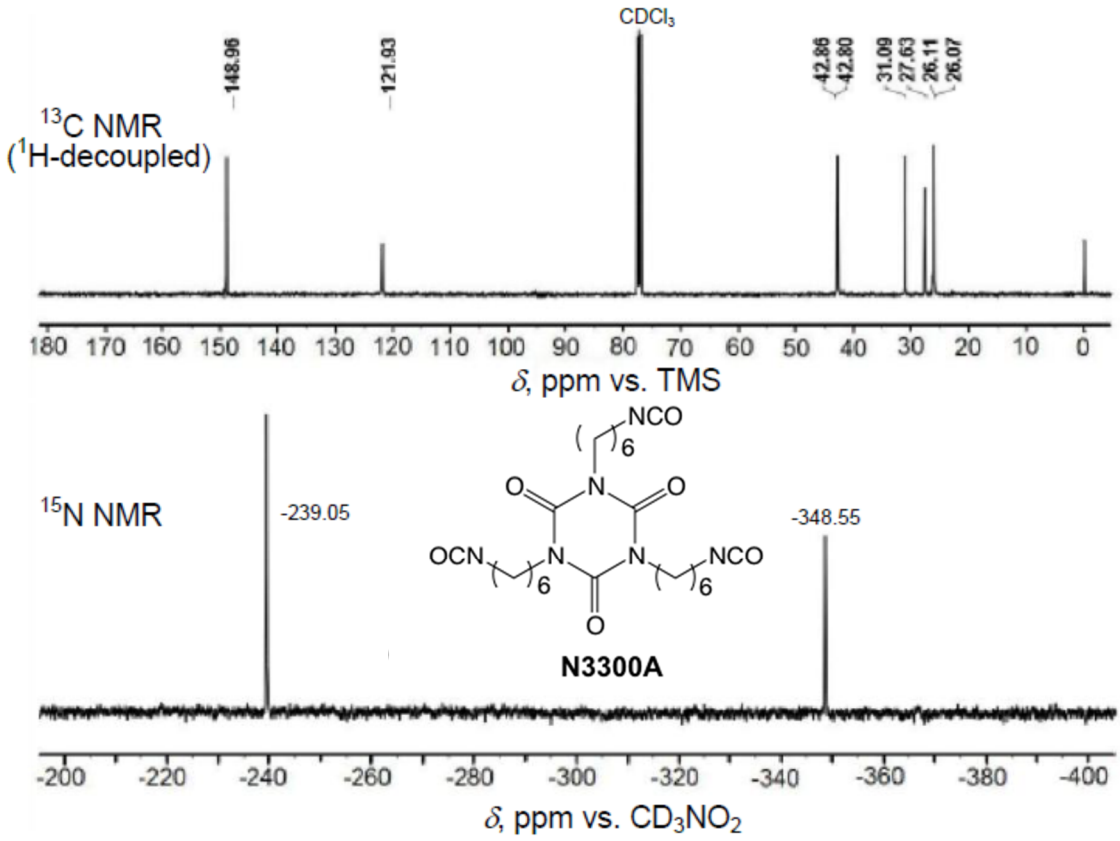

Figure 1.5 Chemical characterization of N3300A showing the six membered ring Top: ^{13}C NMR and Bottom: ^{15}N NMR.[46]

Another important self reaction of isocyanate is the formation of carbodiimides (Scheme 19), via condensation reaction that takes place at high temperatures. It can also occur at room temperature in the presence of a suitable catalyst. Polycarbodiimides are also produced if the functionality of isocyanates is more than unity. The formed carbodiimides can further react reversibly with an isocyanate group to form uretonimine (Scheme 20)

Scheme 19. Formation of carbodiimides

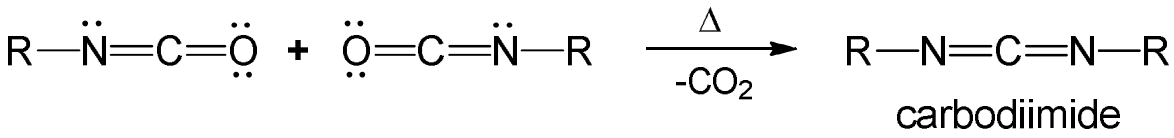

Scheme 20. Formation of uretonimine

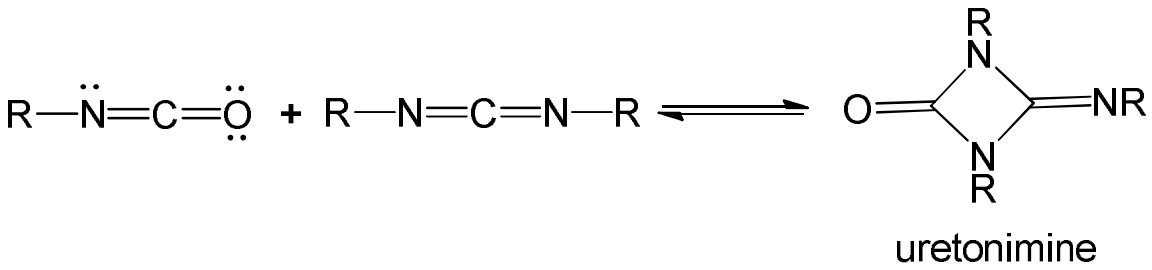

Various chemistries are possible with isocyanates. Below are the strategies and issues specific to polymeric aerogels.

1.5 POLYMERIC GELS & AEROGELS

Functionality is the criterion for a low molecular weight compound to be a suitable monomer for polymerization. A polymerizable monomer is a compound, which

has the ability to react with a minimum of two other molecules. The number of molecules with which a monomer can react is known as its functionality.[47] For any polymer, the functionality of its monomer plays an important role in building structures, molecular weight and ultimately properties and applications. In order to synthesize polymeric gels (i.e., for controlled branching), one of the reactants should have functionality > 2.[47]

There are three theories of gelation as briefly described below.[48] A gel can be classified into four categories as discussed by Flory.[49] They are 1. well-ordered lamellar structures; 2. covalent polymeric networks, completely disordered; 3. polymer networks formed through physical aggregation, predominantly disordered; 4. particular disorder structures. If the gel can withstand the supercritical drying, then it gives hierarchical fractal assemblies of nanoparticles referred to as aerogels. In the overall sol-gel process, the important parameters are the gelation point or time and the evolution of gel structure. The gelation point or time (t_{gel}) of any system can be defined as when the flow behavior of liquid stops. The sol particles grow, and their collision leads to the formation of higher sized particles.

1.5.1 Classical Theory of Gelation. The theory developed by Flory[49] indicates that the polymer forms a connected, gel-forming cluster without forming rings. Since the cluster is continuously connected from one side to the other then there must be at least two connections per node for the cluster to form gel. The critical probability, P_c, for gel formation is:

$$P_c = \frac{number\ of\ bonds}{total\ number\ of\ node\ bonds} = ½ \qquad (1)$$

or in terms of the functionality of the polymer:

$P_c = 1/(n-1)$ where n is the functionality of the polymer and it defines the degree of reaction at the gel point. Hence this model supports a nearly linear growth. The number of nodes increases as the cluster size increases. It was shown that the mass of this type of cluster increases as the fourth power of the radius, however, in reality the mass must increase linearly with volume as the third power of the radius. This model represents the minimum degree of reaction before gelation can occur.[48,49]

1.5.2. Percolation Theory. Zallen[50] and Stauffer et. al.[51] reviewed the percolation theory and its relationship to the gelation process. Percolation theory accounts for rings and closed loop to form, and thus the mass of cluster increases with the cube of the radius. When two particles are adjacent, then bonding will occur. As the structure expands, loops of various sizes may form and the probability, P, that a site may be filled is defined as

$P = \frac{z}{Z}$, where z = number of filled sites and Z = total number of sites. (2)

1.5.3. Fractal Theory. Mandelbrot designated fractal model of structures and gave order to the many seemingly random patterns.[48,52] There are two requirements for a specie to be considered as fractal: (a) self-repeating pattern, and (b) density decrease with size which distinguishes this theory from the classical theories of gelation. Using fractal concepts, sol-gel particle growth can be modeled.[53] The growth of polymers from monomeric units in sol to form fractal species can be classified into reaction-limited growth and diffusion-limited growth.[54]

In reaction limited growth, the diffusion rate of the monomers is fast compared to the polymerization (reaction) rate. That process leads to low 'sticking coefficient yielding particles of relatively even density with fractally rough surface. These particles are called surface fractals. On the other hand, in diffusion-limited growth, diffusion is slow compared to the reaction rate which leads to the morphology in which the center of the fractal has the highest density with a sharp decrease in density with increasing radius. These are termed as mass fractals.[54] Fractal objects are quantified by their fractal dimension, d_f. For linear-like structures: $1<d_f<2$. Fractally rough structures have a mass fractal dimension: $2<d_f<3$.[54] The growth in mass (M) or molecular weight of fractal object is related to the fractal dimension (d_f) and its size or radius, R, by

$$M \propto R^{d}_{f} \tag{3}$$

For a material of uniform density, the fractal dimension is 3. Then density however, decreases with increasing radius.[54]

Using the widely accepted Flory's[55] and Carother's[56] theory of gelation, it is possible to polymerize a monomer to gel.

The extent of reaction 'P' is defined as,

$$P = \frac{2\,(No-N)}{No*Favg} \tag{4}$$

where, No is the number of molecules initially present and N is the number of molecules present at a particular time and *Favg* is defined below,

$$Favg = \frac{Total\ number\ of\ reactable\ equivalent\ present}{Total\ number\ of\ mole\ present} \tag{5}$$

As per Carother's definition, gel point corresponds to an infinite number of average molecular weights. Therefore, at gelation No>>N, equation 4 simplifies to equation 6.

$$Pgel = \frac{2}{Favg} \quad (6)$$

If Favg > 2, i.e., Pgel < 1, the component will gel before reaction has reached completion.[47,56] However, all polymeric gels can not be dried in to polymeric aerogels. In order to form an aerogel, it is necessary to develop chemical (covalent) bonding between the particles. Solutions of polymers with continuously increasing molecular weights either build sufficiently high viscosity and appear as gels, or undergo phase separation due to insolubility and form colloidal particles. If phase-separated colloidal particles are stabilized by interparticle covalent bonds, they form 3D networks, which can retain their form even in the dry state after solvent removal. The formation of a covalently stabilized 3D network of colloidal particles is more often possible in hyperbranched polymers. Linear polymers on the other hand, form polymeric gels due to high viscosity. Upon drying, polymer chains try to achieve their lowest energy[57] by maximizing their Van Der Waals interactions. This causes structural collapse and extensive shrinkage. Therefore, phase separation and 3D bonding are essential, and can be induced by choosing monomers with crosslinking capability.

1.6 ISOCYANATE DERIVED POLYMERIC AEROGELS

Most of the work in organic aerogels has been concentrated on resorcinol-formaldehyde (RF) aerogels which yield carbon aerogels upon pyrolysis.[58] Subsequently, several other types of organic aerogels were reported based on similar phenolic-type resins, polyurethane, polyurea, polybenzoxazine, ROMP derived, polyacrylates and more recently polyimides. The targeted practical applications have always been in the area of thermal insulation. In that regard, high temperature thermal insulation is especially desirable.

Thus drawing from our experience with multifunctional isocyanates as crosslinkers for metal oxide aerogels, in this work isocyanates were used as precursors to synthesize polyimide, polyamide (aramid), polyurethane and polyurea aerogels utilizing reactions that have not been widely used commercially except for the synthesis of polyurethanes.

1.7 POLYURETHANES

In the last 70 years polyurethanes (**PU**), the reaction product of multifunctional isocyanate and polyols[19], have become well-established in foams, elastomers, fibers, sealants, adhesives, and coatings.[21] Their properties can be tailored by varying the chemical identity of the reagents with chain extenders and/or crosslinkers.[21] Polyurethane foams in particular are extremely successful in thermal insulation.[59] Because aerogels are also highly desirable for thermal insulation, polyurethane (**PU)** aerogels are a natural area of interest.

1.7.1 Polyurethane Aerogels. PU aerogels were first reported without chemical identification in 1998 by Biesmans, who used Suprasec DNR (an aromatic oligomeric isocyanate) and 1,4-diazabicyclo[2.2.2]octane (DABCO) as catalyst.[60] Curiously, no alcohol was reported and the materials were referred to as polyurethanes and polyisocyanurates almost interchangeably. Figure 1.6 shows the thermal conductivity of polyisocyanurate aerogels as a function of pressure, at 0.21 g cm^{-3}, those materials possessed exceptionally low thermal conductivity values (0.0085 W m^{-1} K^{-1} for evacuated and 0.015 W m^{-1} K^{-1} for air filled samples), and they were carbonizable with 40% w/w yield upon pyrolysis under inert atmosphere.[60]

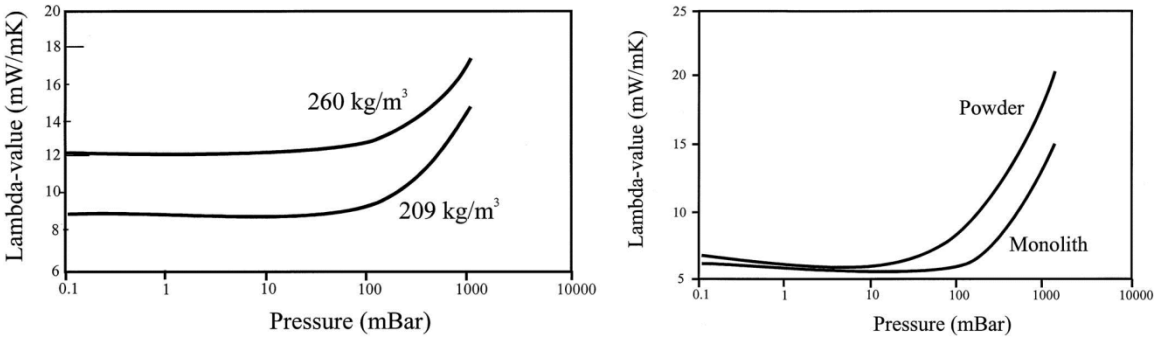

Figure 1.6 Thermal performance of polyisocyanurates aerogels as a function of pressure for different densities on left and different physical forms on right.[60]

Figure 1.6 also illustrates the effect of changing the physical form of aerogel. The monolith (ρ_b = 0.1 g cm^{-3}) has been measured and pulverized to particles with a size below 50 μm. Thermal conductivity of the pulverized aerogel has been measured again and the trend is showed in Figure 1.6 as a function of pressure. In 2001, Tan *et. al.* reported cellulose aerogels crosslinked with toluene diisocyanate (TDI) with an impact strength ten times higher than that of resorcinol-formaldehyde (RF) aerogels.[61] In 2002, silica-polyurethane hybrid aerogels reported by Yim *et. al.* aimed to improve the mechanical properties of silica aerogels and showed thermal conductivity of 0.0184 W m^{-1} K^{-1} at 1 torr for aerogels with bulk density of 0.07 g cm^{-3}. Yim's report did not include mechanical characterization data, hence the improvement over silica aerogels could not be assessed.[62] In 2004, Rigacci *et. al.* revisited **PU** aerogels with emphasis on thermal superinsulation, and synthesized materials from Lupranat M20S [4,4´-methylenebis(phenylisocyanate)] and two aliphatic polyols, saccharose and pentaerythritol, using DABCO as catalyst in DMSO/ethyl acetate mixtures.[63] Both supercritical and subcritical drying routes were used and the resultant materials were compared in terms of bulk density, pore volume, and thermal conductivity. The latter was less than that of standard polyurethane foam (0.022 versus 0.030 W m^{-1} K^{-1} at room

temperature and atmospheric pressure). Importantly, it was further shown that the aerogel morphology depends on the solubility of the precursors as well as the solubility parameter (δ_m) of the reaction medium. When δ_m was lower than the solubility parameter of the polyurethane (δ_{PU}), the aerogel consisted of aggregates of micrometer sized particles (Figure 1.7); if $\delta_m > \delta_{PU,}$ smaller-sized particles and mesoporous structures were reported (Figure 1.8).[63]

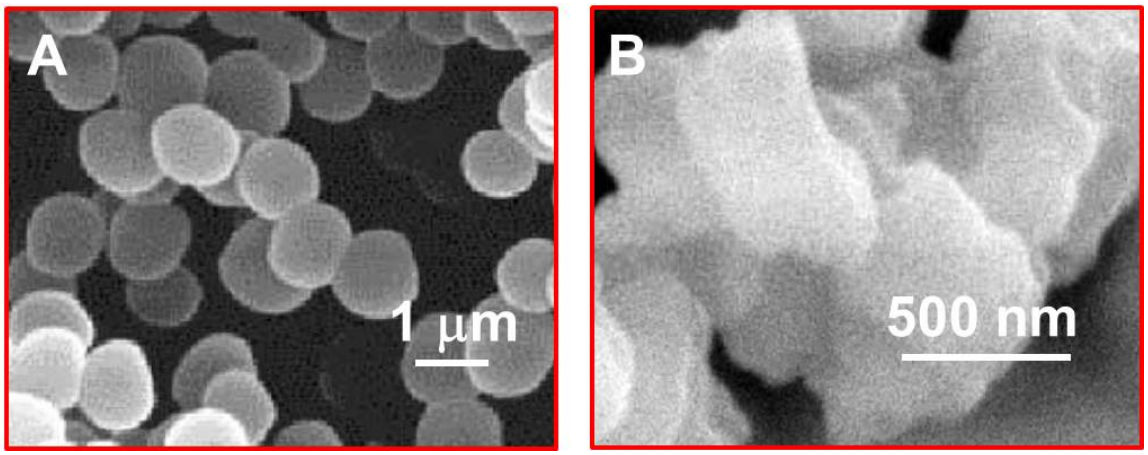

Figure 1.7 SEM of **PU** aerogels synthesized in low-solubility reaction media, i.e., $\delta_{PU}>\delta m$, using A: saccharose and polyMDI and B: pentaerythritol and polyMDI.[63]

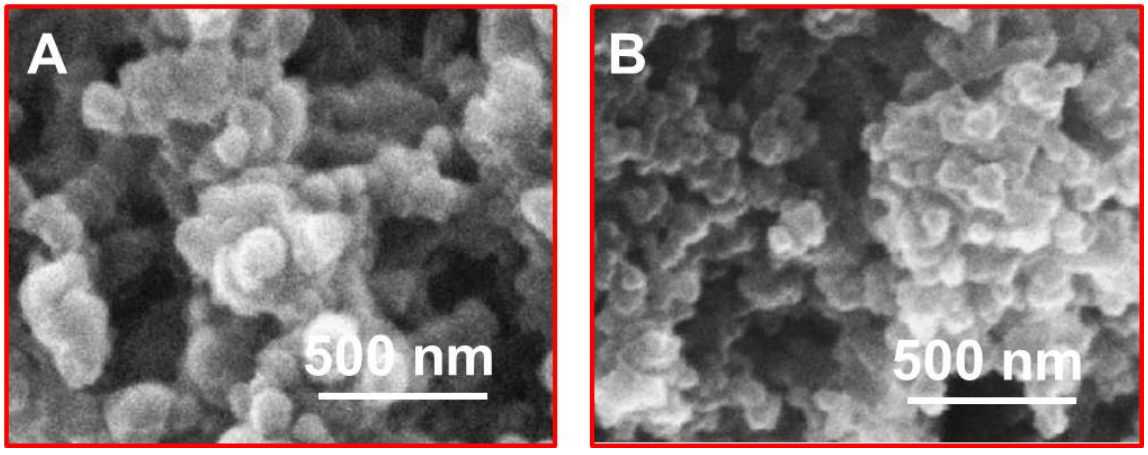

Figure 1.8 SEM of **PU** aerogels synthesized in high-solubility reaction media, i.e., $\delta_{PU} <\delta m$, using A: saccharose and polyMDI and B: pentaerythritol and polyMDI.[63]

More recently (2009), Lee *et al.* reported **PU** aerogels from 4,4´-diphenylmethyldiisocyanate (MDI) and a polyether polyol (Multranol 9185, Bayer) catalyzed with triethylamine (TEA). The properties of these aerogels were compared with silica aerogels, as well as with polyurea aerogels synthesized from MDI or polyMDI with polyamines such as Jeffamines T3000 and T5000 (see polyurea aerogels section); at 0.128 g cm^{-3} those **PU** aerogels had a surface area of 47 m^2 g^{-1}, an average pore diameter of 13 nm and a thermal conductivity of 0.027 W m^{-1} K^{-1} (Figure 1.9).[64]

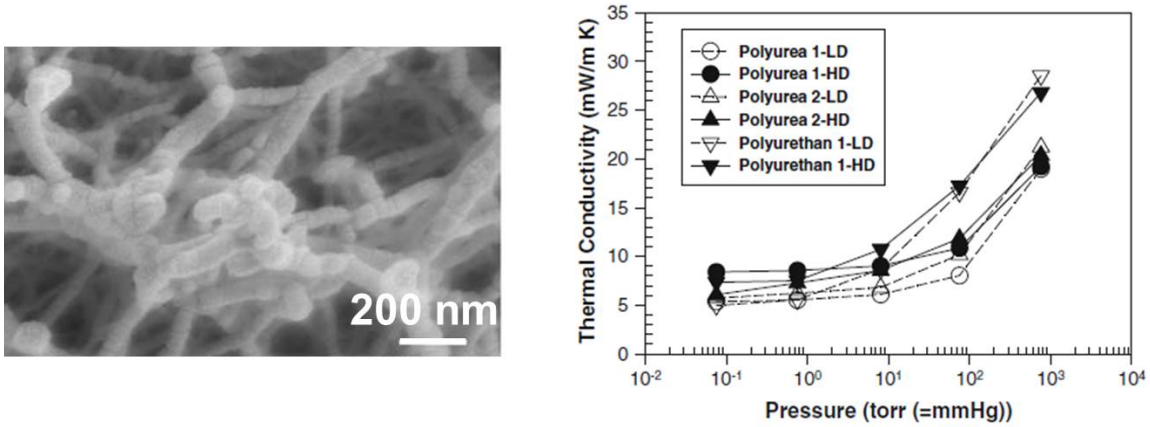

Figure 1.9 SEM of polyurethane (**PU**) aerogels for the density 0.128 g cm^{-3} on left. Thermal conductivity comparisons for two different densities (LD: 0.07 g cm^{-3} and HD: 0.1 g cm^{-3}) of polyurethanes and polyurea aerogels as a function of pressure on right.[64]

Most of the **PU** aerogels above adopted "monomers" used in bulk polyurethane polymer synthesis, i.e., oligomeric isocyanates and/or high molecular weight (M_w) polyols. Although there are advantages working with industrial materials, however, there will be some disadvantages as well: (a) given the importance of relative solubilities through Rigacci's work,[63] oligomeric reagents yield more soluble products, which delay phase-separation, yielding larger particles; consequently, (b) surface to volume ratios in those materials are relatively low, resulting in lower surface area aerogels; and, (c) oligomeric starting materials in general yield low functional group densities on the

surface of the phase-separated nanoparticles, thus interparticle crosslinking could be also compromised, and the resulting aerogels might in general be weaker mechanically.

Based on the above, in this study **PU** aerogels are synthesized from multifunctional small-molecule yet inexpensive monomers, allowing control of the onset of the phase separation, which is translated into control of the particle size, morphology, pore structure and ultimately the mechanical properties. Molecular parameters of interest include the molecular rigidity vs. flexibility of the isocyanate. Thus, as such we employ trifunctional aromatic **TIPM** (Desmodur RE) and aliphatic **N3300A** (Desmodur N3300A) both courtesy of Bayer Corp. U.S.A (Scheme 21).

Scheme 21. Triisocyanates used in this study

triisocyanates

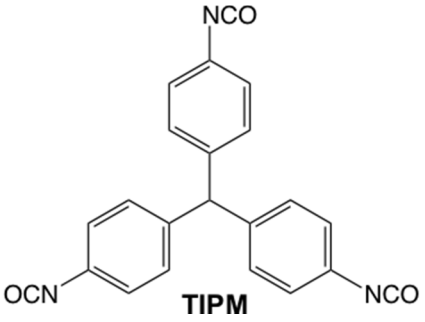

TIPM

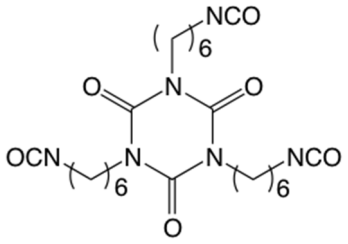

N3300A

Second, we varied the functionality as well as the molecular size and shape of the alcohols as shown in Figure 1.10.

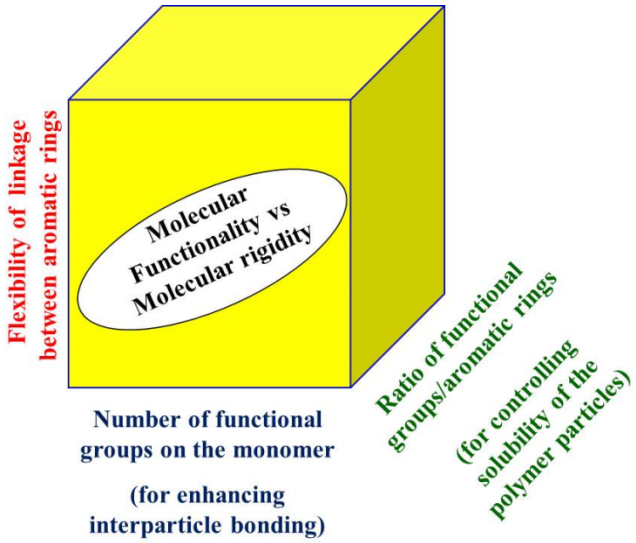

Figure 1.10 Degrees of freedom in selecting the polyols for polyurethane aerogels.

Aromatic triols include phloroglucinol (**POL**) and hydroxyl phenyl ethane (**HPE**). Diols include resorcinol (**RES**) as well as sulfonyl diphenol (**SDP**), bisphenol A (**BPA**), and dihydroxy benzophenone (**DHB**). The basis for our selection was the intent to induce very early phase separation by adjusting the aromatic-to-functional group content of the monomer. Aromatic triols included phloroglucinol (**POL**) and 1,1,1-tris(hydroxyphenyl)ethane (**HPE**). Diols included resorcinol (**RES**), sulfonyl diphenol (**SDP**), bisphenol A (**BPA**), and dihydroxy benzophenone (**DHB**). With those alcohols we varied: (a) the absolute number of -OH groups, *n*, per monomer; (b) the ratio of -OH groups per aromatic ring, *r*; and (c) the "crowding" at the bridge between aromatic rings. Our basic hypothesis was that all three factors should be related to the solubility of the developing polymer, hence to the primary particle size. In addition, parameters *n* and *r* should be expressed to the nanoparticle OH-group surface density, hence they should be related to the interparticle connectivity and mechanical strength. Samples based on aRomatic **TIPM** or aLiphatic **N3300A** are referred to as **aR-** or **aL-**, respectively.

Overall, wet-gels and aerogels are abbreviated as **aR-ALC-xx** and **aL-ALC-xx**. **ALC** refers to the alcohol according to Scheme 22, and extension **–xx** refers to the weight percent of monomers in the sol.

Scheme 22. Multifunctional small-molecule alcohols used in this study

triols

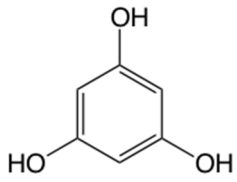

POL (n=3, r=3)

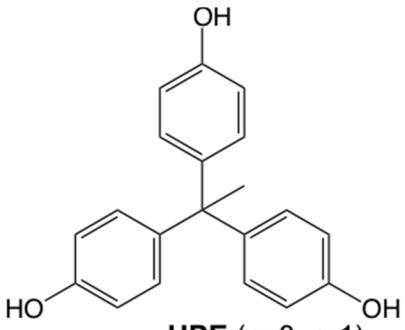

HPE (n=3, r=1)

diols

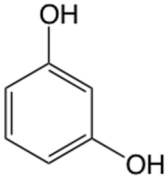

RES (n=2, r=2)

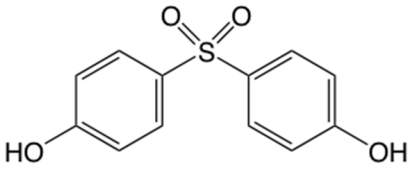

SDP (n=2, r=1)

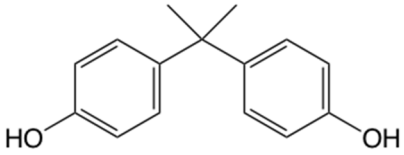

BPA (n=2, r=1)

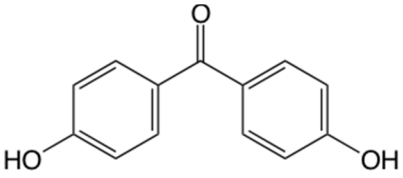

DHB (n=2, r=1)

As exemplified in Scheme 23 with **TIPM** and **RES**, polyurethane wet-gels were synthesized from small-molecule triisocyanates and alcohols according to standard reactions in industrial use.[21]

Scheme 23. Typical synthesis of polyurethane aerogels from small-molecule monomers

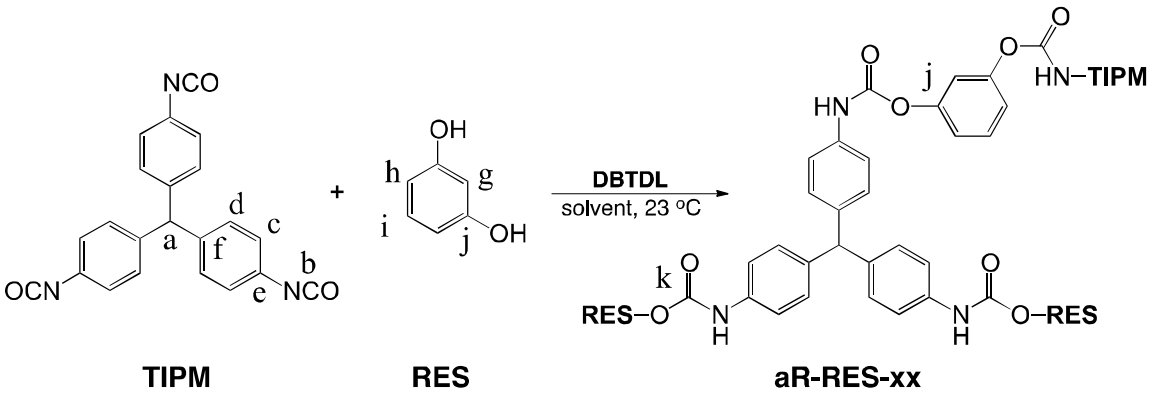

1.7.2 Characterization. Materials were characterized at the gel state, at the molecular level in terms of their chemical composition, at the nanoscopic level in terms of particle size, morphology of the hierarchical network and pore structure, and at the macroscopic level in terms of mechanical properties and thermal conductivity. Those bulk properties serve as proxies for investigating interparticle contact and bonding, which again are related to the monomer structure. The sol-gel transition of **PU** aerogels was monitored using rheology. The actual (formal) gelation point is located at the inflection point of the tanδ (=*G"*/*G'*) versus time plot (Figure 1.11).

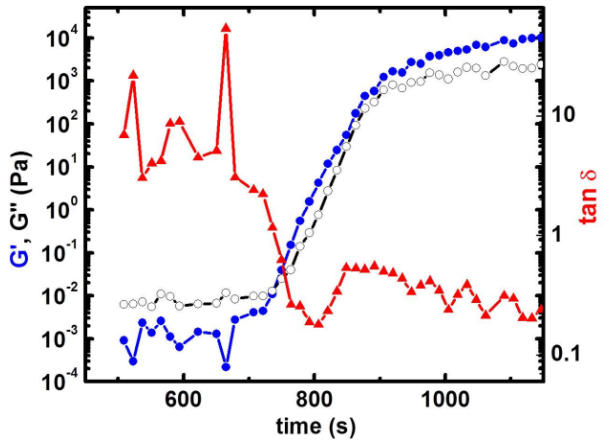

Figure 1.11 Rheology during gelation of **aR-POL-10** in acetone at 20 °C. Evolution of the storage (G´) and loss (G´´) modulii versus time from adding the catalyst in the **TIPM**/**POL** mixture. (Oscillation frequency ω=1 rad s^{-1}).

At the gel point, tanδ is related to the gel relaxation exponent 'z' via Eq. 7.[65] In turn,

$$\tan\delta = \tan(z\pi/2) \tag{7}$$

considering the excluded volume of the (primary) particles forming the clusters, 'z' is related via Eq. 8 to the mass fractal dimension, D_f, of the clusters forming the gel.[66] (Note, for three-dimensional non-fractal clusters, D_f=D=3.[66])

$$z = \frac{D(D+2-2D_f)}{2(D+2-D_f)} \tag{8}$$

The D_f values of the selected **PU** formulations are in the 2.2-2.5 range, suggesting that the gel network is formed by mass-fractal particles via either reaction-limited or diffusion-limited cluster-cluster aggregation.[67]

By IR (Figure 1.12), the band at 1740 cm^{-1} is attributed to urethane carbonyl stretch, the N-H stretch is visible at 3312 cm^{-1}, the C-N stretch near 1204 cm^{-1}, N-H bending and C-H stretching near 1510 cm^{-1}, while the band at 1590 cm^{-1} is due to aromatic C-C stretching, and the absorbance at 1127 cm^{-1} is attributed to C-O stretching [10]. Neither unreacted isocyanate at 2273-2000 cm^{-1} (N=C=O stretch), nor urea carbonyl at 1600-1640 cm^{-1} are detectable.

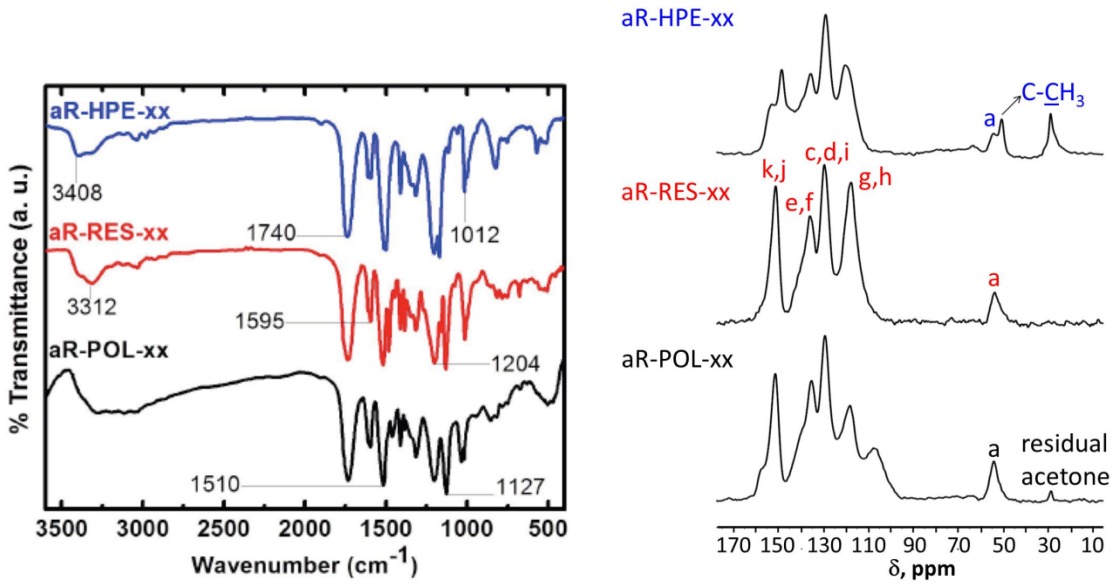

Figure 1.12 Chemical characterization of selected polyurethane (**PU**) aerogels, IR-spectra (KBr) on left and solid CPMAS ^{13}C NMR spectra on right (labeled according to Scheme 23).

By CPMAS solids ^{13}C NMR (Figure 1.12, right), resonances at 129 ppm, 118 ppm and 135 ppm are assigned to the aromatic carbons, and the peak at ~154 ppm to the urethane carbonyl. In the case of **aR-HPE-xx**, the urethane carbonyl shows up at 152 ppm and the peak at 148 ppm is assigned to the phenolic aromatic carbon. The peak at 54 ppm is assigned to the CH of **TIPM** and the peak at 51 ppm to the quaternary C of

HPE. The resonance at 29 ppm in **aR-HPE-xx** is assigned to C-$\underline{C}H_3$ and in the case of **aR-POL-xx** it may be due to residual acetone.

Figure 1.13 compares the N_2 sorption isotherms of selected **aR-ALC-xx** aerogels at similar solid percent formulations. (xx indicates 15% w/w.) The **aR-POL-xx** isotherm reaches saturation with the characteristic Type IV loop of mesoporous materials. On the other hand, the isotherms of **aR-HPE-xx** and **aR-RES-xx** rise above P/P_o=0.9 and do not reach saturation, which in combination with narrow hysteresis loops suggests both meso and macroporosity.

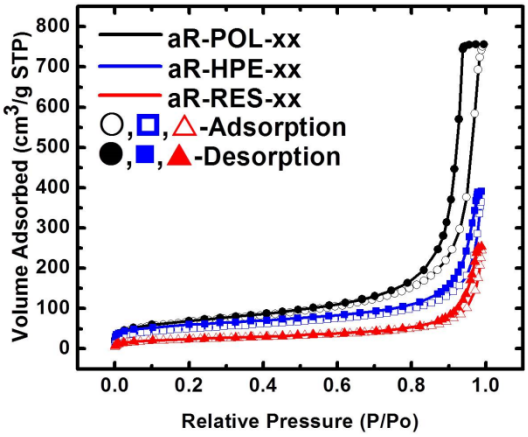

Figure 1.13 N_2 sorption porosimetry of **PU** aerogels synthesized with 15% w/w solids.

By SEM (Figure 1.14) **PU** aerogels are open-pore structures consisting of 3D networks of interconnected nanoparticles. In all cases smaller particles aggregate to form larger agglomerates. Figure 1.14 also captures the morphology of selected **PU** aerogels at two density extremes (low solids and high solids).

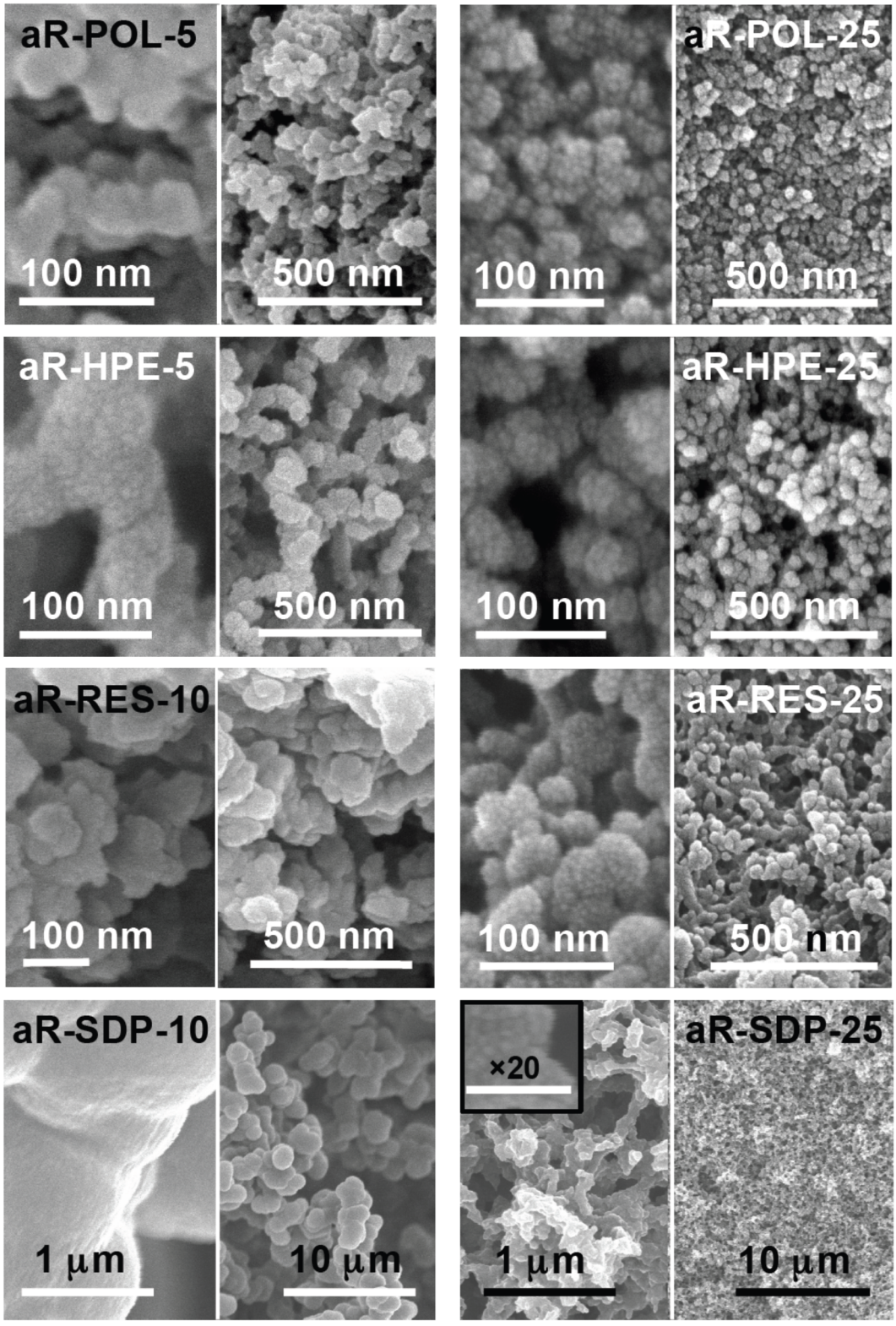

Figure 1.14 Selected scanning electron microscopy (SEM) data for **aR-ALC-xx** aerogels at two density extremes, at low and high magnification. Length scales have been selected to capture the relative sizes of the building blocks and the morphology of the networks.

Small-angle X-ray scattering (SAXS) is used to study the size and aggregation of particles. From SAXS, it is shown that with high *n* and *r* (cases of ALC = **POL**, **HPE**, and **RES**, $n+r \geq 4$), a fast reaction consumes all monomer long before the sol gels, yielding polymer of decreasing solubility with increasing $n+r$. The gelation process continues through primary particle aggregation into closely-packed secondary particles, followed by diffusion-limited aggregation of the larger secondary particles into larger mass-fractal aggomerates that meet the percolation threshold and the sol gels as shown in Figure 1.15.

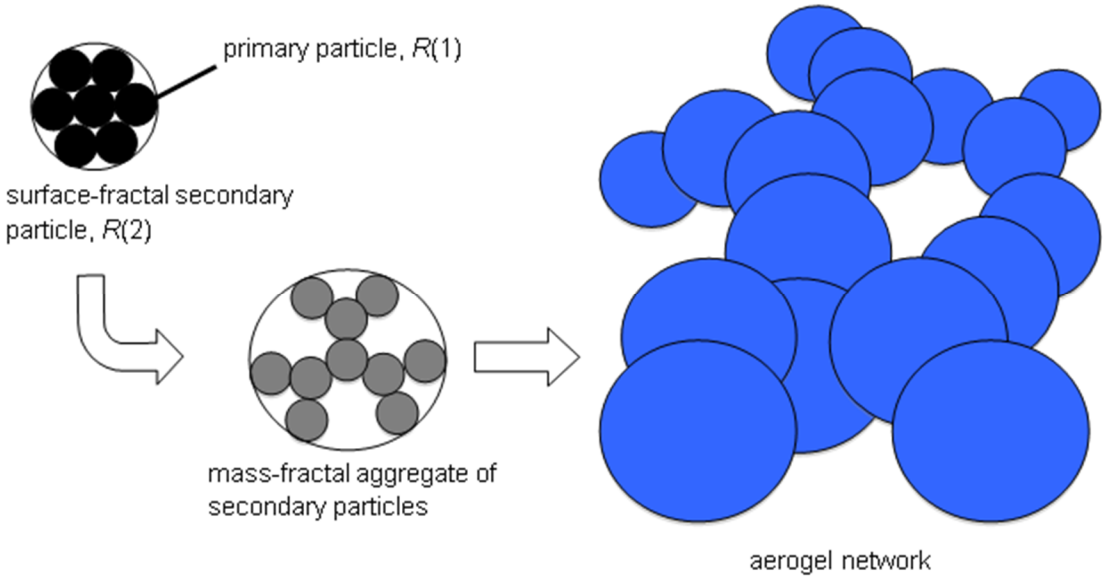

Figure 1.15 Network formation in **PU** aerogels

With lower *n* and *r*, (cases of ALC = **SDP**, **BPA** and **DHB**, $n+r=3$) the situation is markedly different: at lower densities (e.g., **aR-SPD-10**) skeletal building blocks are large and featureless (~1 μm in diameter - Figure 1.14), however SAXS shows that they still consist of smaller particles (~200 nm in diameter – Table 2). At higher densities (e.g., **aR-SDP-25**) particle sizes by SEM, N_2-sorption and SAXS converge. These data

are consistent with small primary particles embedded in a medium of different density. This is supported by the increase in skeletal densities as ρ_b increases which in turn, that suggests that when $n+r$ is low, oligomers are more soluble, phase separation is delayed, particles are generally larger and start aggregating while a significant amount of monomer (or small oligomers) remain in solution. Unreacted monomer binds to surface functional groups of aggregated particles, and new polymer (of somewhat higher density) accumulates and closes the interparticle pores; consequently, mesoporosity is lost, skeletal particles appear larger and smoother by SEM (Figure 1.14).

Thermal conductivity in conjunction with elastic modulus in monolithic aerogels are used in order to probe the interparticle connectivity. The heat transfer modes in monolithic aerogels, λ can be considered as the sum of three contributors (Eq. 9):

$$\lambda = \lambda_g + \lambda_s + \lambda_{irr} \tag{9}$$

whereas λ_g is the non-convective thermal conductivity through the pore-filling gas, λ_s is the thermal conductivity through the solid framework and λ_{irr} is the radiative heat transfer. The variation of λ_s with ρ_b has been modeled via an exponential expression, Eq. 10.[68]

$$\lambda_s = C(\rho_b)^a \tag{10}$$

Exponent α depends on how matter fills space. The pre-exponential factor C depends on the particle chemical composition and the interparticle coupling (interconnectivity and interparticle bonding). On the other hand, the macroscopic elastic (Young's) modulus (E) of the material depends on similar microscopic parameters such as the network

structure and the skeletal-interparticle connectivity.[68] Typically E varies also exponentially with ρ_b according to Eq. 11,

$$E = A(\rho_b)^x \tag{11}$$

Exponent x also depends on how matter fills space, and therefore further analysis focuses on those materials that participate in the linear correlation between α and x (Figure 1.16), as that indicates a structural similarity (or more accurately, a similar structural evolution with density).

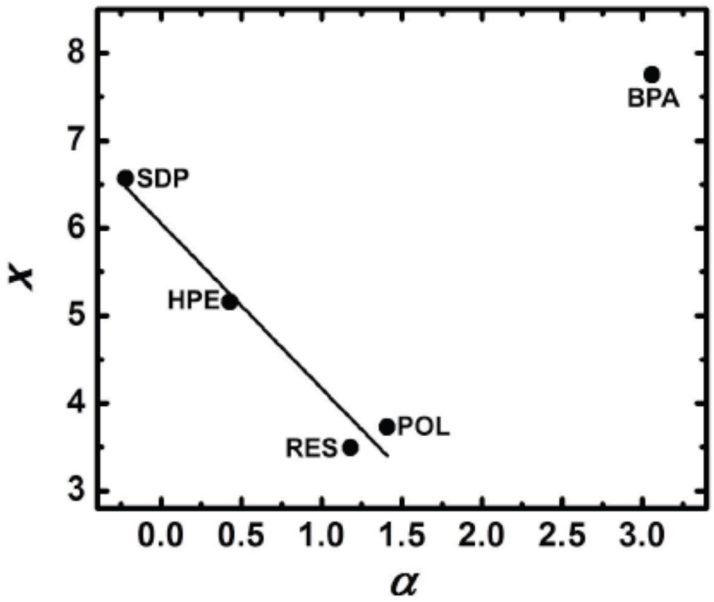

Figure 1.16 Exponent α for the dependence of solid thermal conduction on the bulk density (ρ_b), versus exponent x for the dependence of the Young's modulus (E) on the ρ_b. Data shown concern the **aR-ALC-xx** aerogels.

Such linear relationship is valid for **SDP, HPE, RES** and **POL** based polyurethane aerogels with TIPM. In that context, Figure 1.17 shows how E varies with C for three different **–xx** formulations (i.e., percent solids in the sol), as indicated.

Interestingly, it appears that the most important molecular parameter for improving interparticle connectivity (and increase stiffness) is the monomer functional group density (r). Thus, despite that **HPE** has n=3 (just like **POL**), interconnectivity and stiffness of **aR-HPE-xx** are lower than those of both **aR-RES-xx** and **aR-POL-xx** at all densities. In turn, considering the fact that the particle sizes in **aR-POL-xx** and **aR-HPE-xx** are not very different, and certainly smaller than those in all other cases, leads to the conclusion that r is important in terms of interconnectivity and stiffness, because it reflects the functional group density on the surface of the primary particles. This in turn validates the most basic hypotheses of this study, namely the importance of small molecule monomers for the synthesis of robust aerogels.

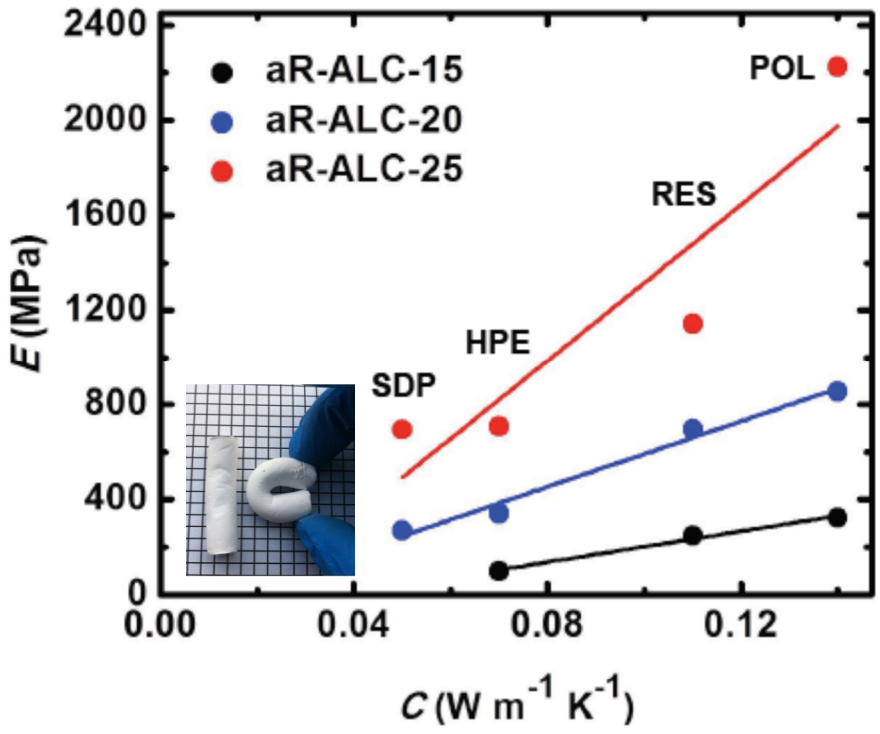

Figure 1.17 Young's modulus, E, under dynamic compression versus interconnectivity parameter C (via Eq. 6) for **aR-ALC-xx** aerogels. Those α and x parameters correlate linearly in Figure 1.14.

It is also noteworthy that the interconnectivity (*C*) and stiffness (*E*) of the two kinds of samples that are flexible at low densities (**aR-HPE-xx** and **aR-SDP-xx** - see Figure 1.17) are both numerically low and close to one another (Figure 1.17). Again, this is attributed to the functional group density on the surface of the particles.

1.7.3 Applications. Polyurethane aerogels are considered for thermal insulation.[60,64] At higher densities, **PU** aerogels absorb as much as 72-102 J g^{-1} falling between X-silica (ρ_b=0.548 g cm^{-3}) and X-vanadia (ρ_b=0.436 g cm^{-3}) of similar densities, and they far surpass materials typically considered strong such as acrylic polymers (8 J g^{-1} at 1.04 g cm^{-3}), Kevlar-49 epoxy (11 J g^{-1} at 1.04 g cm^{-3}), 4130 steel (15 J g^{-1} at 7.84 g cm^{-3}) and SiC ceramics (20 J g^{-1} at 3.02 g cm^{-3}).[46] **PU** aerogels are thus suitable for structural as well as ballistic applications. The rigidity of **PU** aerogels makes them suitable for civil related applications whereas their flexibility makes them suitable for acoustic insulation. Flexible aerogels can also be used as wrap-around thermal insulators in diverse applications from undersea oil pipes to space and planetary exploration.[69]

1.8 POLYUREAS

Polyurea aerogels were synthesized from both the routes as shown in Scheme 5 and 7.

1.8.1 Polyurea Aerogels. Biesmans has reported work on polyisocyanurate aerogels without chemical evidence.[60] Although polyurea aerogels have shown remarkable properties like high surface area and low thermal conductivity, there is no mechanical study. In 2009, Lee et. al. reported polyurea aerogels with an eye on thermal insulation.[64] Those polyurea aerogels were synthesized using commercially available methylene diisocyanates (MDI, for polyurea 1) and polymeric MDI (for polyurea 2) with

two different types of amine hardeners (Jeffamine-T3000 and T5000, Huntsman LLC). They have reported particulate morphology for all the polyurea aerogels (Figure 1.18)

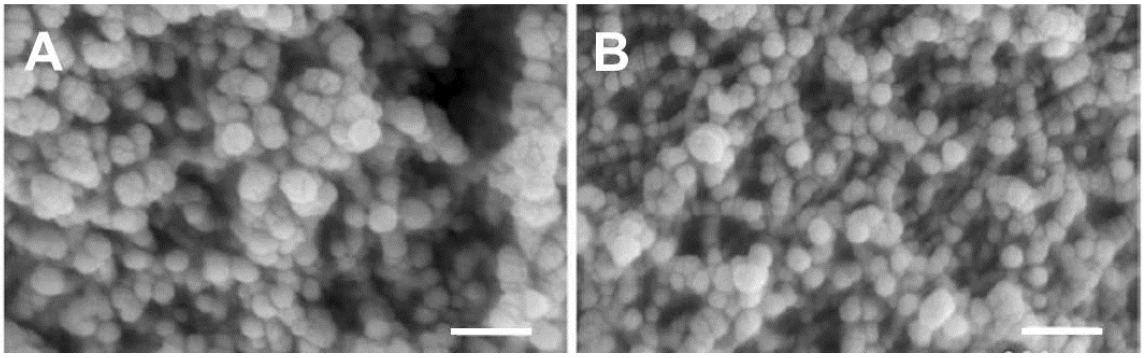

Figure 1.18 SEM (scale bar show 200 nm) of polyurea aerogels synthesized with constant EW ratio (equivalent weight of NH/equivalent weight of NCO) A: synthesized from pMDI and Jeffamine T3000 (ρ_b = 0.06 g cm^{-3}) B: synthesized from pMDI and Jeffamine T5000 (ρ_b = 0.1 g cm^{-3}).[64]

It was also shown that the small pore diameter and narrow size distributions were obtained with the aerogels synthesized from small molecule, in this case from MDI (Figure 1.19).

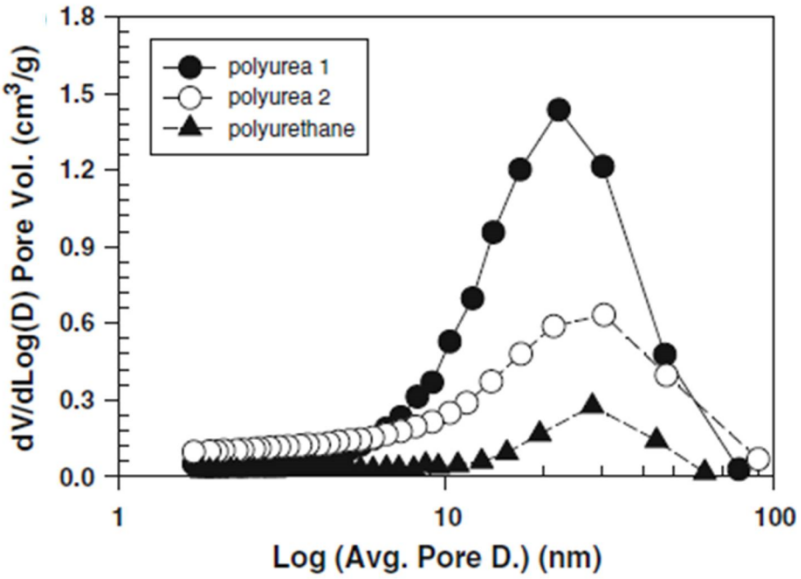

Figure 1.19 Pore size distribution of polyurea and polyurethane aerogels. Polyurea 1: synthesized from pMDI and Jeffamine T3000 ($\rho_b = 0.06$ g cm^{-3}), polyurea 2: synthesized from pMDI and Jeffamine T5000 ($\rho_b = 0.1$ g cm^{-3}). Polyurethane: synthesized from 4,4´-diphenylmethyldiisocyanate (MDI) and polyether polyol (Multranol 9185)[64]

Polyurea aerogels showed lower thermal conductivity than polyurethane aerogels (Figure 1.9). Though those aerogels showed a wide range of final densities (0.098 – 0.116 g cm^{-3}), high porosity (90-91 %), low shrinkage (f = 1.14-2.95, f – shrinkage factor calculated from final density (g cm^{-3})/target density (g cm^{-3})), low thermal conductivities (18-19 mW m^{-1} K^{-1}), good hydrophobicity, however, there is no report on mechanical behavior of those aerogels. A more inexpensive alternative of mechanically strong polyurea (**PUA**) aerogels was synthesized in acetone from Desmodur N3300A triisocyanate, water and triethylamine (TEA) as catalyst. Interestingly, the nanomorphology of our previously reported **PUA** aerogels varies from fibrous to particulate as the density increases (Figure 1.20).[46]

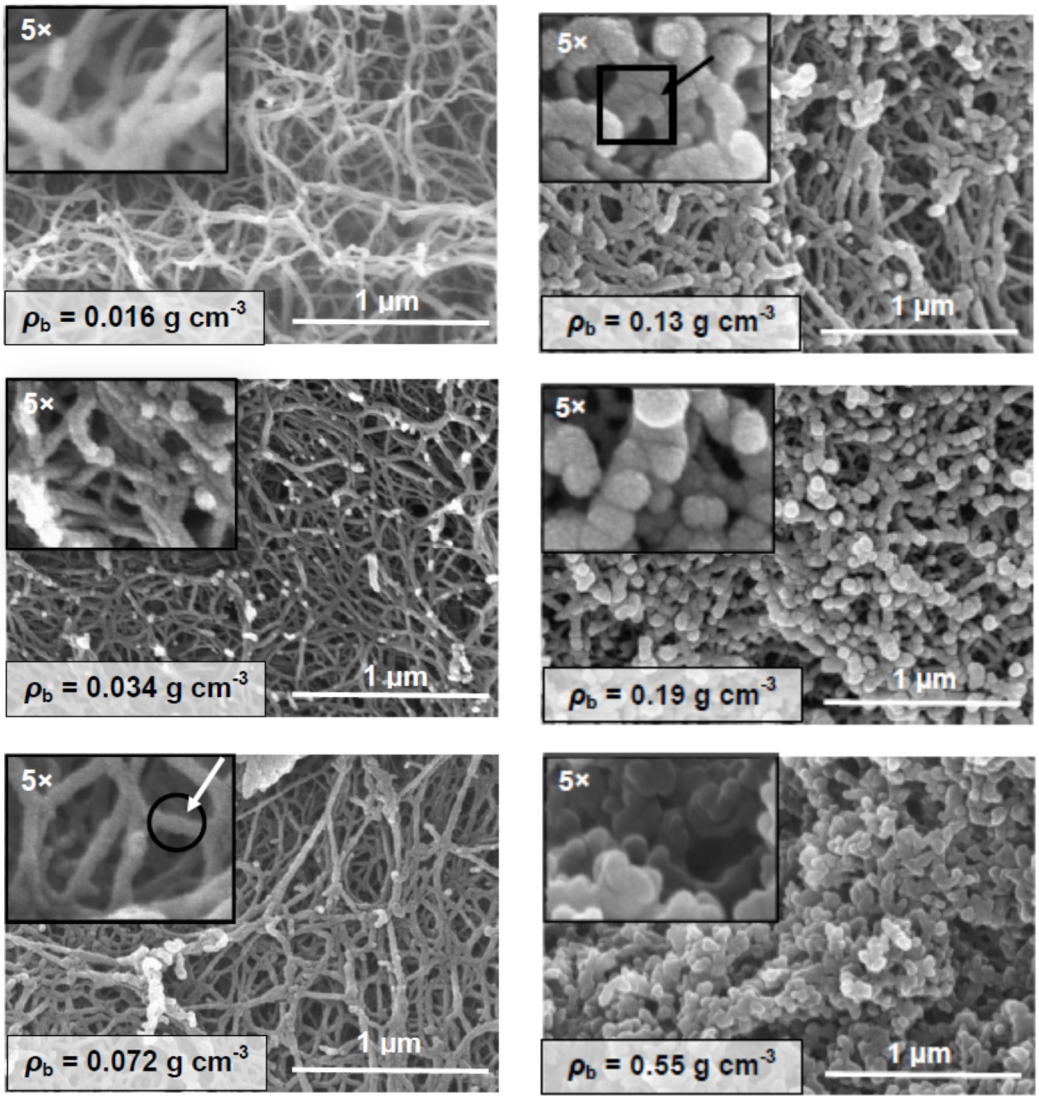

Figure 1.20 SEM as a function of density of **PUA** aerogels derived from Desmodur N3300A [46]

Simplified synthesis of PUA aerogels along with the exceptional mechanical properties and the expected low thermal conductivity from lower densities lead to the synthesis of density-gradient PUA aerogels monoliths by adopting the S. Jones method[70] as illustrated in Figure 1.21 and their characterization also summarized in Figure 1.22 which shows fibrous morphology obtained with low density end and particulate morphology obtained with high density end as already seen in Figure 1.20.

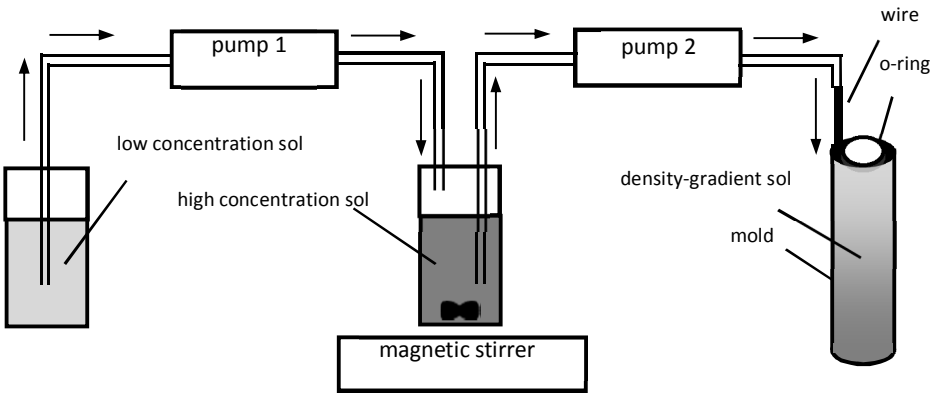

Figure 1.21 Synthesis of density-gradient PUA wet-gels.[70]

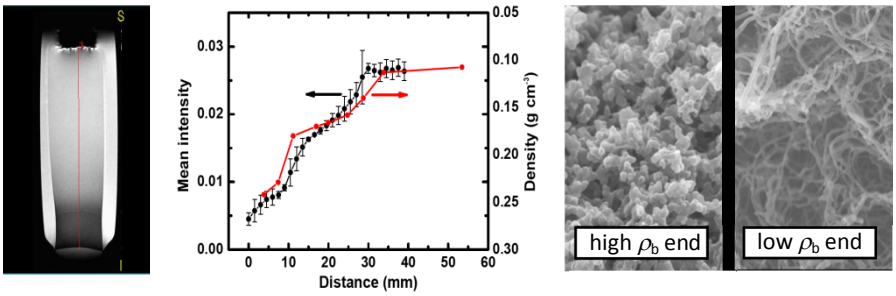

Figure 1.22 Density-gradient PUA aerogel monoliths. Left: MRI of a water filled sample; high rb at the bottom. Middle: Density variation by MRI and by direct measurement (by cutting disks along a monolith). Right: SEMs at the two ends, as noted, agree with the SEM data of Figure 1.20. [71]

Reasoning that higher monomer concentrations (as high as 0.52 M) change the dielectric properties of the medium, herein we study that effect by changing the solvent polarity, and we report synthesis of **PUA** aerogels with nanomorphologies varying from similar to those obtained in acetone (e.g., in ethyl acetate), to cocoon-like structures embedded in a fiber web in acetonitirile. Some of those materials are flexible, while others demonstrate low speed of sound wave propagation and are suitable for acoustic

insulation. **PUA** aerogels synthesized from acetonitrile are highly hydrophobic as compared to **PUA** aerogels synthesized from acetone which can also be attributed to their cocoon microstructure.

1.8.2 Characterization. The **PUA** aerogels synthesized from different solvents are chemically indistinguishable (by solid ^{13}C and ^{15}N CPMAS NMR). Figure 1.23 illustrated the ^{13}C and ^{15}N NMR comparison of **PUA** aerogels synthesized from acetone, acetonitirile (ACN) and dimethyl formamide (DMF). By ^{15}N NMR, they all show two peaks corresponding to urea resonance at 78 ppm (i) and isocyanurate resonance at 138 ppm (g). However, in terms of properties, these materials are vastly different.

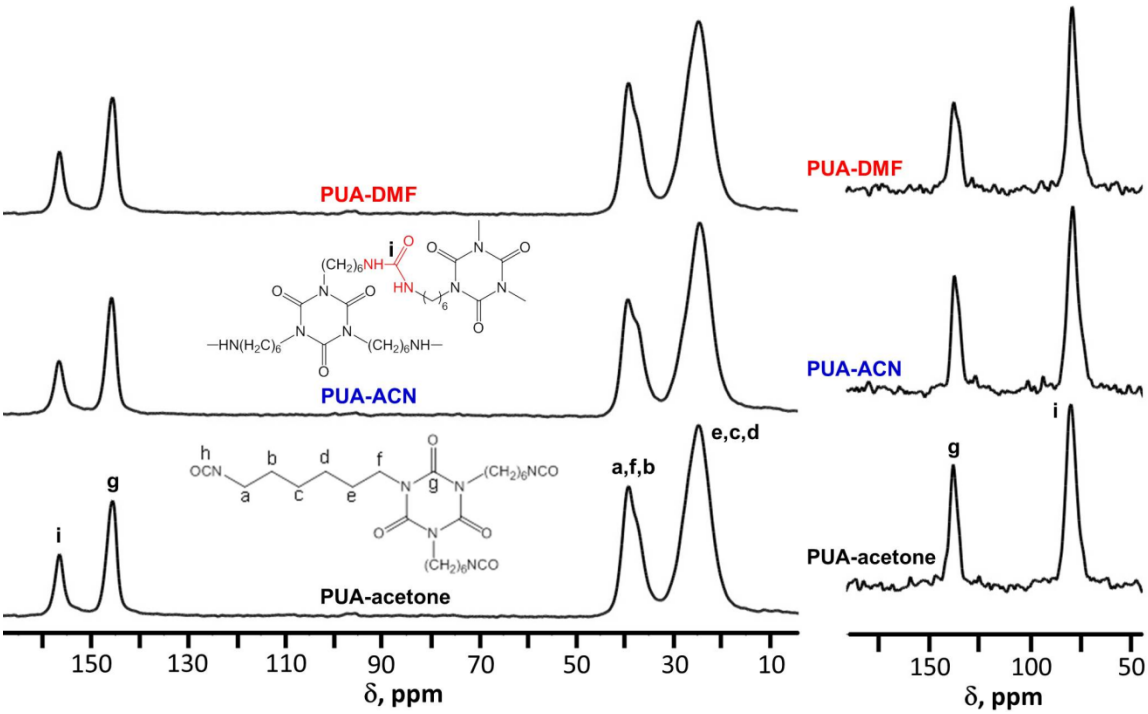

Figure 1.23 Solid ^{13}C (Left) and ^{15}N (Right) CPMAS spectra of polyurea (**PUA)** aerogels synthesized from different solvents as indicated.

General material characterization data are summarized in Table 1.2. Figure 1.24 compares the N_2 sorption isotherms of PUA aerogels synthesized with 5.5 g N3300A. All isotherms show rise above P/P_o=0.9 and do not reach saturation, which in combination with narrow hysteresis loops suggest both meso and macroporosity. BJH plots which reflect mesoporosity show all materials to be mesoporous.

Table 1.2 Selected material characterization data of polyurea aerogels

sample – g solvent	bulk density (ρ_b, g cm^{-3})	porosity (%)	BET surface area (σ, m^2 g^{-1})	particle radius (by $3/\rho_s\sigma$, nm)
PUA-5.5-acetone	0.075 ± 0.003	94	187	13.3
PUA-5.5-ACN	0.073 ± 0.002	94	55	45.5
PUA-5.5-DMF	0.076 ± 0.003	94	307	8.0

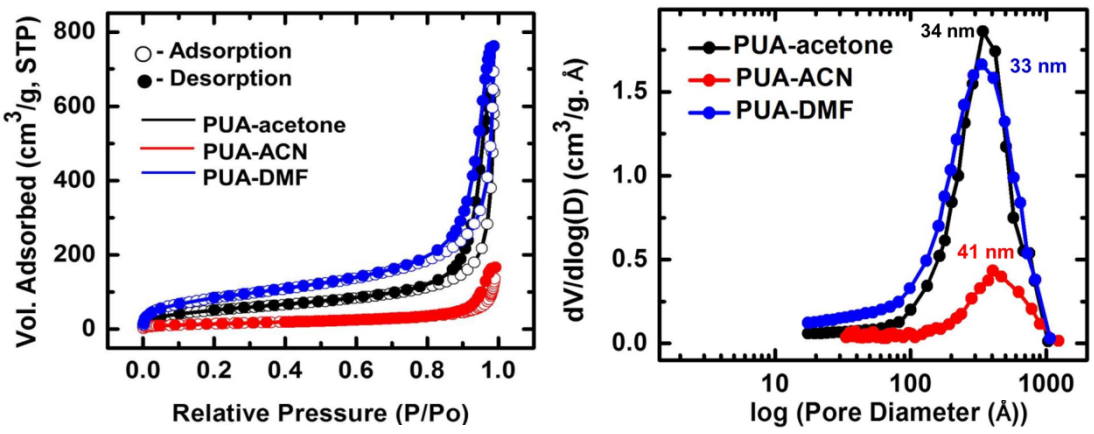

Figure 1.24 Left: N_2 sorption porosimetry and Right: BJH plots of polyurea aerogels synthesized in different solvents as indicated.

Figure 1.25 shows the morphological difference of **PUA** aerogels synthesized in different solvents using 0.11 M isocyanate concentration. Fibers were obtained in **PUA** aerogels synthesized in acetone as reported previously.[61] However, for similar concentration, cocoon-like morphology was obtained in acetonitrile and particles were obtained in DMF which show how polarity affects the morphology or aggregation of particles.

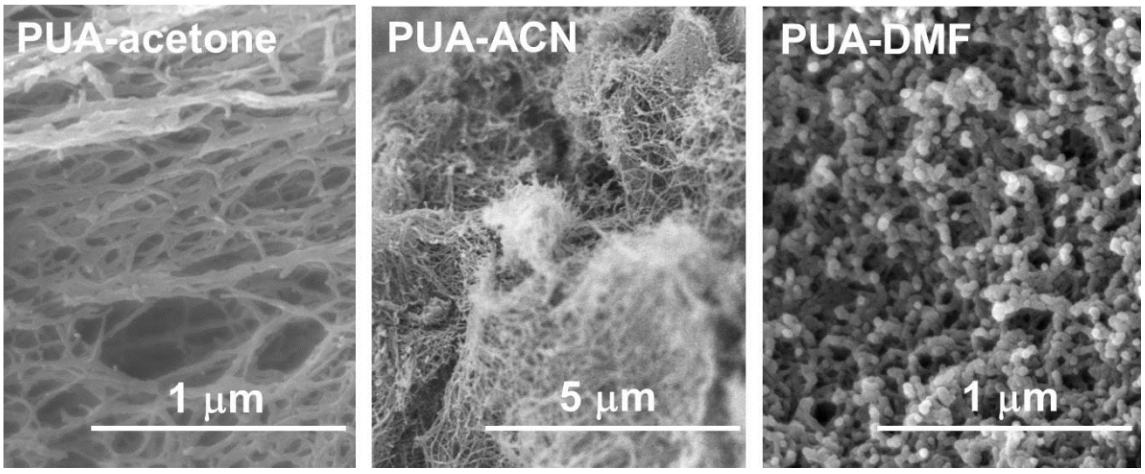

Figure 1.25 SEM comparisons of **PUA** aerogels for the similar density ($\rho_b \sim 0.07$ g cm^{-3}).

Also, mechanically they behave completely different at 0.11 M concentration. Aerogels synthesized in acetone are stronger compared to **PUA**-ACN and **PUA**-DMF. **PUA**-DMF are fragile whereas **PUA**-ACN are flexible as shown in Figure 1.26. Comparison of mechanical behavior of **PUA** aerogels synthesized from acetone and ACN at high isocyanate concentration, 0.52 M, also shown in Figure 1.26 and pertinent data corresponding to this figure are summarized in Table 1.3.

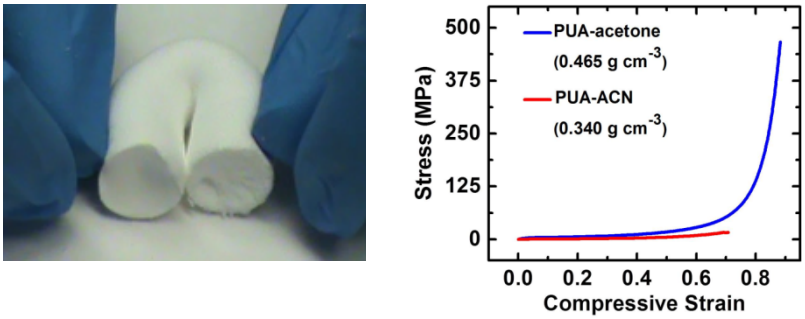

Figure 1.26 Mechanical characterization of **PUA** aerogels made in acetone and acetonitrile. Flexibility of **PUA**-ACN synthesized from 5.5 g N3300A (ρ_b = 0.072 g cm^{-3}) on left and comparison of **PUA** aerogels synthesized from acetone and ACN under quasi-static compression on right.

Table 1.3 Comparison of quasi-static compression of PUA aerogels synthesized from acetone and ACN

PUA sample	bulk density (g cm^{-3})	Young's modulus (MPa)	speed of sound (m s^{-1})	ultimate strength (MPa)	ultimate strain (%)	specific energy abs. (T, J g^{-1})
acetone	0.465 ± 0.002	148 ± 8	564	456 ± 10	88 ± 0	90 ± 5
ACN	0.340 ± 0.002	14.3 ± 1.8	198	14 ± 4	68 ± 2	7 ± 2

Overall, mechanically **PUA**-acetone aerogels are much stronger materials compared to **PUA**-ACN, and this can be attributed to their microstructure. **PUA**-ACN are macroporous and phase separated with higher particles as compared to their **PUA**-acetone counterparts as shown in Figure 1.27.

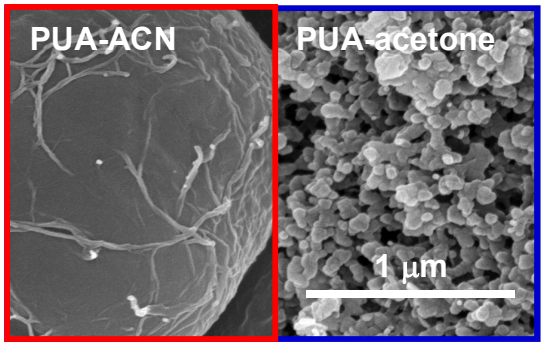

Figure 1.27 SEM comparison of **PUA** aerogels synthesized from 0.52 M N3300A.

The thermal conductivity, λ, was calculated from bulk density, ρ_b, thermal diffusivity, R, and heat capacity, c_p, according to $\lambda=\rho_b \times R \times c_p$. Specific heat capacity of PUA aerogels was taken as 1.255 ± 0.060 J g^{-1} K^{-1}.[72] With different solvents, the minimum thermal conductivity obtained was 34 mW m^{-1} K^{-1} and is comparable with other organic aerogels (Figure 1.28).

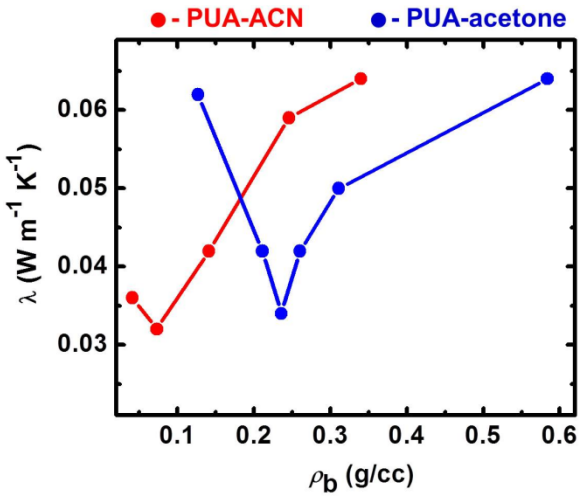

Figure 1.28 Thermal conductivity as a function of density for the **PUA** aerogels synthesized from acetone and ACN.

PUA aerogels synthesized from acetone and ACN are hydrophobic similar to Lee's findings. However, they show huge difference in their hydrophobicity. **PUA** aerogels synthesized from ACN show contact angle of 150° whereas **PUA**-acetone show 100° (Figure 1.29). This huge difference is attributed to a lotus leaf effect,[73] and underlines the importance of the microstructure.

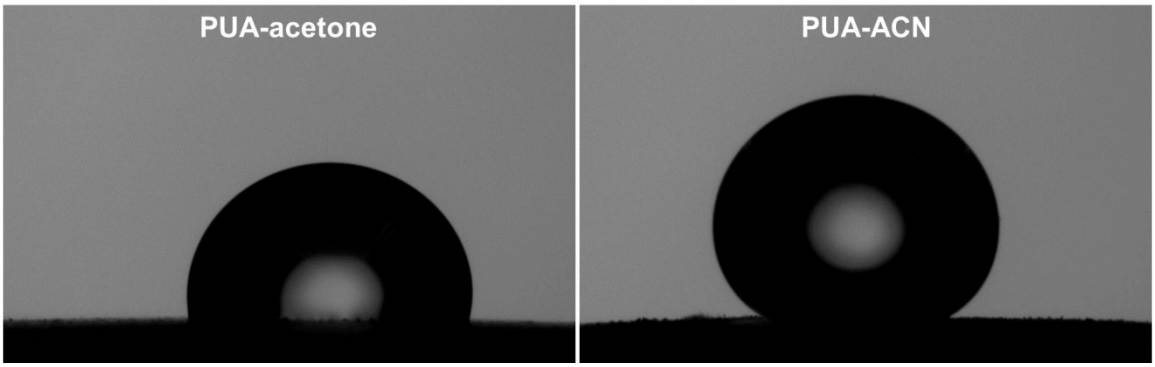

Figure 1.29 PUA-ACN is more hydrophobic than **PUA**-acetone for 16.5 g **PUA** samples

1.8.3 Applications. The flexibility of **PUA**-ACN aerogels combined with their low thermal conductivity, can be used in flexible thermal insulation where wrap-around is necessary.[69] The speed of sound in **PUA**-ACN aerogels is less than the speed of sound in open air, therefore they can be used for acoustic insulation. The flexible aerogels combined with their super-hydrophobicity can be used as shock absorbing materials and can also be used as efficient absorbents of oil and organic compounds.[74] In fact they show fast selective oil absorption as shown in Figure 1.30).

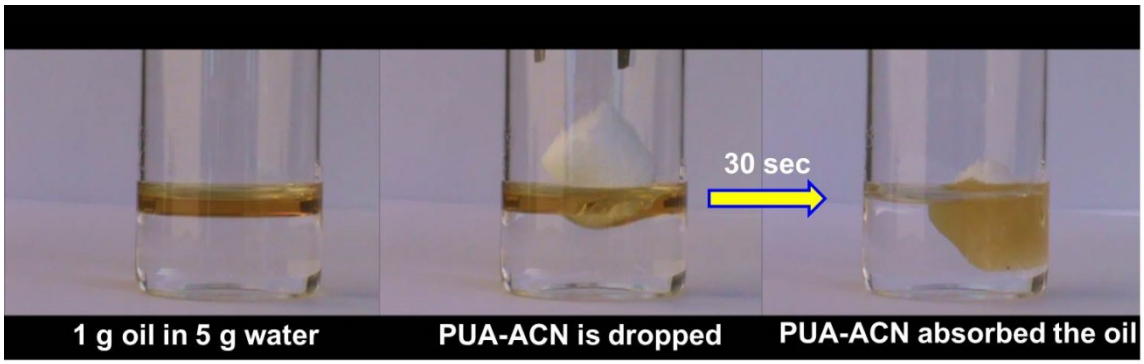

Figure 1.30 Ability of 0.087 g of **PUA**-ACN (ρ_b = 0.073 g cm^{-3}) to absorb oil completely. It absorbs ~11 times its own weight and almost selectively.

1.9 POLYAMIDES

Polyamides are a class of thermoplastics that have properties that vary broadly from relative flexibility to significant stiffness, strength and toughness.[75] Nylon was the first polyamide developed in 1929 using a condensation reaction (for e.g., nylon 6,6, a condensation product of adipic acid and hexamethylene diamine).[76] In current terminology the word "nylon" is a used to describe aliphatic and semiaromatic polyamides. The fully aromatic polyamides are called "aramids". Aramids are pursued as advanced materials, owing to their thermal stability, strong intermolecular forces, chain rigidity, and the inherent stability of the aromatic moiety. Better known commercial aramids are Kevlar (Scheme 24) and Nomex (*meta* variant of Kevlar, a condensation product of *m*-phenylene diamine and isophthaloyl chloride). Kevlar fibers have exceptional strength coupled with excellent resistant to high temperatures. They can replace steel and glass fibers in many applications particularly in the aerospace industry where the relatively low density is preferential.[77] When the properties of aromatic polyamides are combined with the inherent properties of aerogels, one should realize materials that are suitable for aerospace applications.

1.9.1 Synthesis of Polyamides. There are several well-established methods for preparing polyamides. A popular route involves the step-growth polymerization of a dicarboxylic acid with a diamine. This synthesis is typically a multi-step process at high reaction temperatures. For example, poly(hexamethylene adipamide) can be prepared from the corresponding dicarboxylic acid – diamine 1:1 salt followed by pre-polymerization of the salt at a lower temperature to produce a lower molecular weight polymer in order to prevent the diamine from sublimation, and further polymerization to

afford high molecular weight polyamide at 260-270 ^{o}C.[26] The high temperature treatment can be avoided by replacing acid with an acid halide. However, this process requires the removal of hydrogen halide, which is formed as a byproduct formed during polymerization (Scheme 24).

Scheme 24. Synthesis of Kevlar

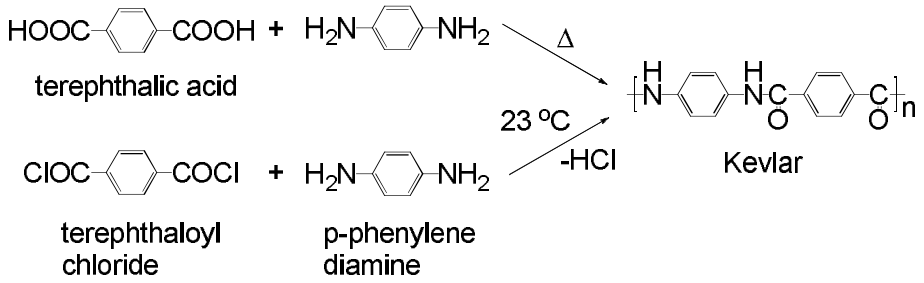

1.9.2 Synthesis of Polyamide Aerogels. Designing Kevlar aerogels from *p*-phenylenediisocyanate and terephthalic acid imposes several interrelated chemical and structural issues. Hence, designing Kevlar aerogels are not easy due to their linear chemical structure with limited chances for crosslinking. Therefore, we resort into hyperbranched structures based on trifunctional single aromatic core monomers. Realizing that classical methods for bulk polymer synthesis are not necessarily the most economical for polymeric aerogels,[46] here we report aramid aerogels from the underutilized reaction of isocyanates and carboxylic acids. That route offers several advantages, two of which stand out: (a) trifunctional aromatic isocyanates are low-cost bulk chemicals, while the corresponding aromatic amines are in general expensive; and, (b) the only by-product is CO_2. This process is implemented with a trifunctional isocyanate, tris(4-isocyanatophenyl)methane (**TIPM**, supplied by Bayer Corp. U.S.A. as

Desmodur RE) and 1,3,5-benzene tricarboxylic acid (**TMA**) in anhydrous DMF (Scheme) at 90 ^{o}C, referred to as **PA-ET** aerogels, and at 23 ^{o}C, referred to as **PA-RT** aerogels (Scheme 25).[78]

Scheme 25. Synthesis of polyamide (aramid) aerogels at both elevated (**PA-ET**) and room temperature (**PA-RT**)

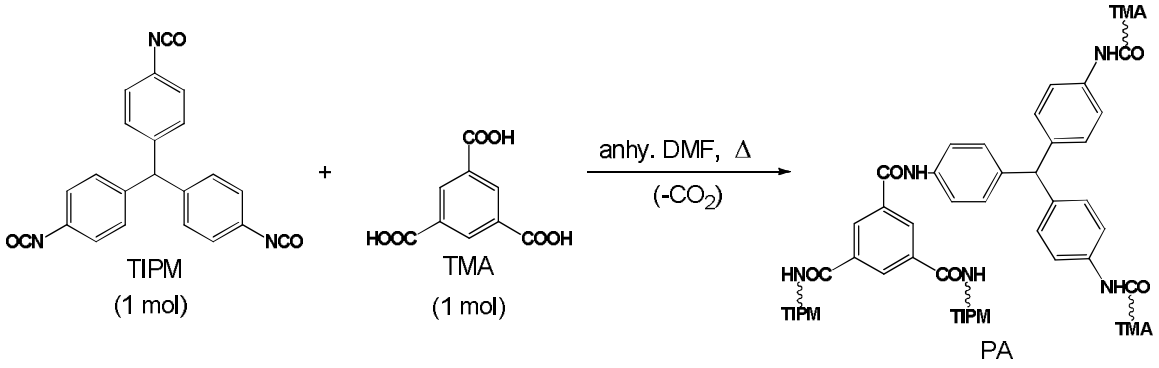

1.9.3 Characterization of PA-ET and PA-RT Aerogels. Figure 1.31 compares the ^{13}C NMR of polyamide aerogels synthesized and processed at three different temperatures as indicated. We can clearly observe the urea peak at 154 ppm, which is formed at room temperature by the side reaction shown in Scheme 13, once the carbamic carboxylic anhydride intermediate is formed, it disproportionates to urea and anhydride, which are fixed in the network and cannot diffuse and react to give amide. As the gelation temperature increases, the amount of urea decreases and the reaction proceeds through the four-membered intermediate (Scheme 14).

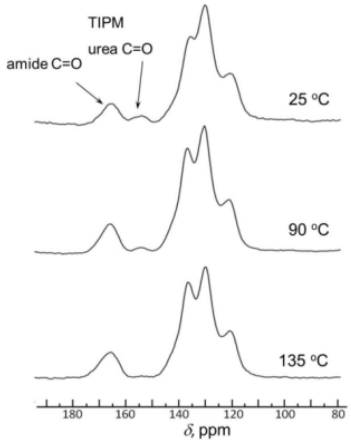

Figure 1.31 Solid ^{13}C CPMAS spectra of **PA** aerogels synthesized and processed at the three different temperatures indicated.[78]

Microscopically, both **PA-ET** and **PA-RT** aerogels show connectivity of smaller particles into larger agglomerates. **PA-RT** samples consist of larger particles than **PA-ET** aerogels (Figure 1.32).

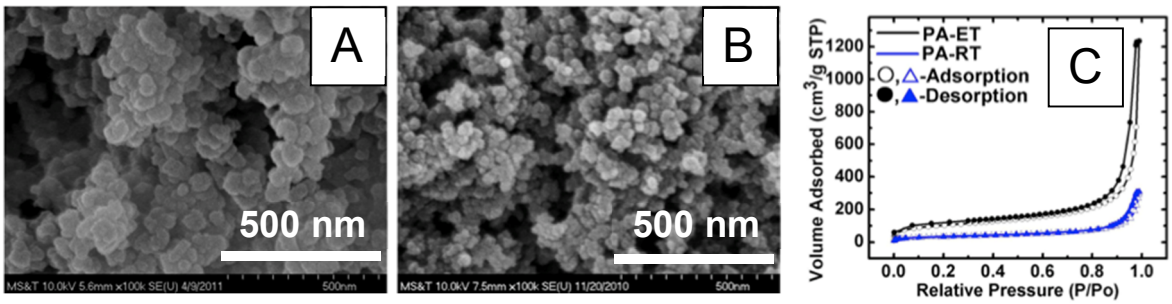

Figure 1.32 Left: SEM of (A) **PA-RT-15** and (B) **PA-ET-15**. Right (C): N_2 sorption isotherms of the same samples as indicated.[78]

In fact, the particle sizes in Figure 1.32 are similar to those calculated via $3/\rho_s\sigma$, hence are the smallest building blocks (primary particles). All N_2 sorption isotherms of **PA-ET** and **PA-RT** aerogels rise above relative pressure 0.9 and do not reach saturation, consistent again with the macroporosity observed in SEM. However, narrow desorption

loop and initial rise in the volume adsorbed indicate the presence of meso and microporosity. (Figure 1.32 C).

Figure 1.33 shows the stress-strain curve for both **PA-ET** and **PA-RT** aerogels. It shows a linear elastic region (<3% strain) followed by plastic deformation and hardening. The Young's modulus, *E*, is controlled by the amide interparticle bridges and is comparable to that of other isocyanate-derived organic aerogels of similar ρ_b. Specifically, the Young's modulus of **PA-ET** and **PA-RT** aerogels follows power-law relationships with bulk density of the type $E \sim \rho_b^{1.85}$ and $E \sim \rho_b^{4.35}$, respectively. Table 1.4 summarizes the data pertaining to aramid aerogels and provides a direct comparison with the percent of solids used in the sol.[78]

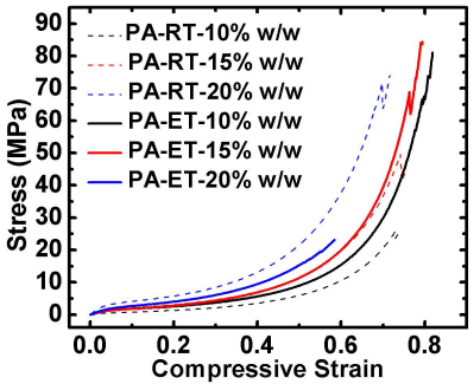

Figure 1.33 Quasi-static stress-strain curves of samples and formulations as indicated.[78]

Table 1.4 Mechanical characterization data of **PA-ET** and **PA-RT** aerogels.

sample – % w/w	ρ_b (g cm^{-3})	Young's Modulus (E, MPa)	Ultimate Strength (MPa)	Ultimate strain (%)	sp. energy abs. (J g^{-1})
PA-ET-10	0.288	33±4	71±9	80±2	37.0
PA-RT-10	0.256	15±0	24±2	74±0	18.4
PA-ET-15	0.324	46±12	77±10	74±2	36.5
PA-RT-15	0.315	36±4	49±2	74±1	26.8
PA-ET-20	0.361	50±0	23±1	61±3	14.6
PA-RT-20	0.384	88±11	78±8	72±2	37.0

The thermal conductivity, λ, was calculated from bulk density, ρ_b, thermal diffusivity, R, and heat capacity, c_p, data according to $\lambda=\rho_b \times R \times c_p$. Table 1.5 summarizes the relevant data.[78]

Table 1.5 Selected thermal conductivity data of polyamide aerogels

aerogel	**bulk density, ρ_b (g cm^{-3})**	**heat capacity, c_p (J g^{-1} K^{-1}) @ 23 °C**	**thermal diffusivity, R (mm^2 s^{-1})**	**thermal conductivity, λ (W m^{-1} K^{-1})**
PA-ET-10	0.280±0.009	0.913±0.028	0.111±0.005	0.028±0.002
PA-ET-15	0.310±0.023	1.114±0.034	0.112±0.002	0.038±0.003

Figure 1.34 shows the thermal stability of **PA-ET** aerogels both in N_2 and in air. In air, those materials are stable up to 350 °C, while in N_2 they carbonize (yield ≈ 40%

w/w) and may be considered as precursors for porous carbons. **PA-ET** aerogels (90 ^{o}C) were pyrolysed under Ar at 800 ^{o}C for 3 h, remaining sturdy monoliths. Microscopically (by SEM, Figure 1.34 B), we clearly observe that polyamide-derived C-aerogels consist of particles. Again, N_2 sorption indicates the presence of all three kinds of pores, while the BET surface area of carbon aerogels increased relative to the parent aramid aerogels. The BJH-desorption method reflects the mesoporsity and yields pore diameter of 28 nm.

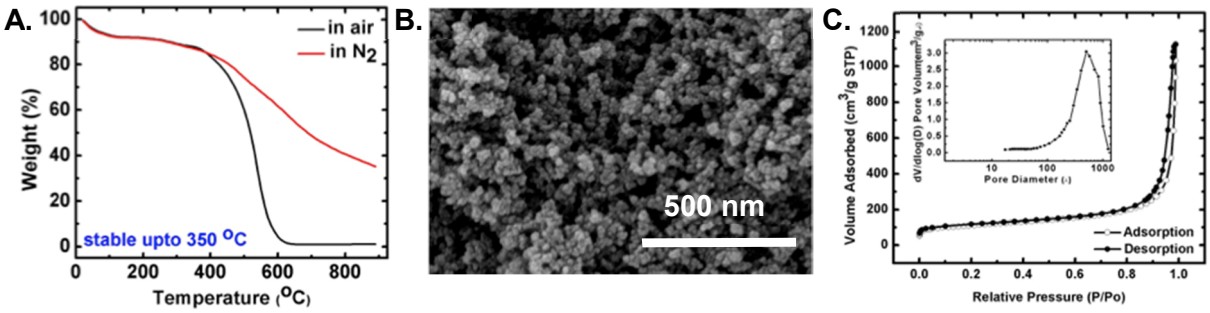

Figure 1.34 A: TGA analysis of **PA-ET** aerogels in air as well as in N_2 as indicated. B: SEM of **PA-ET** derived carbon aerogels. C: N_2 sorption isotherm and (inset) BJH desorption plot of **PA-ET** derived carbon aerogels. (ρ_b=0.319 g cm^{-3}; surface area σ=371 m^2 g^{-1}; micropore area = 121 m^2 g^{-1}; porosity = 80% v/v).[78]

Overall, polyamide (aramid) aerogels are synthesized successfully at both room temperature as well as elevated temperatures. Microscopically they consist of nanoparticles. However, the particle size for **PA-RT** aerogels is larger than that of their **PA-ET** counterparts, probably reflecting slower reaction. Mechanically, **PA-ET** aerogels are stronger indicating a higher degree of interparticle crosslinking. Upon pyrolysis, polyamide aerogels are converted to highly porous, electrically conducting C-aerogels.

1.9.4 Applications. These aramid aerogels are low density and showed high toughness, open air-like speed of sound and Styrofoam-like thermal conductivity. They

can be used in thermal and acoustic insulation and are suitable for a variety of civil, defense and transport related applications.[78]

1.10 POLYIMIDES

Among engineering plastics, polyimides demonstrate good chemical resistance, excellent mechanical properties and high thermal stability.[79]

1.10.1 Synthesis of Polyimides.

1.10.1.1 The DuPont route. Polyimides (**PI**) are generally synthesized via reaction of dianhydrides with diamines. For example, a commercially successful polyimide is referred to as Kapton® (trade name of DuPont Chemical Company) and is synthesized from pyromellitic dianhydride (PMDA) and oxydianiline (Scheme 26).[79]

Scheme 26. Synthesis of Kapton® polyimide via the DuPont route

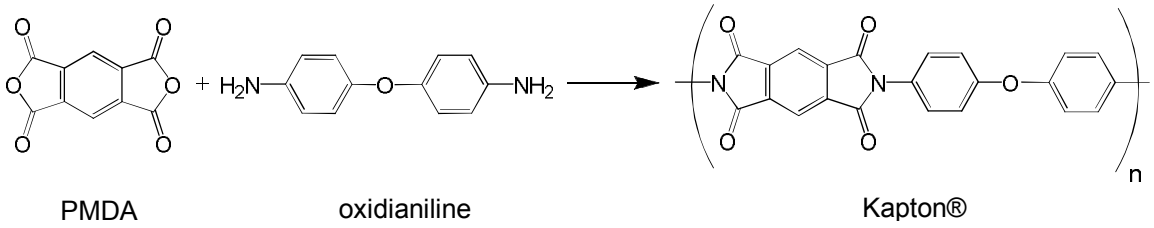

1.10.1.2 The PMR route (PMR, polymerization of monomeric reactants). There is also a second type of polyimides, exemplified by PMR-15, which have become an aerospace industry standard replacing metal components in jet engines. PMR-15 has an operating temperature of 290 ^{o}C and consists of ~1500 molecular weight, short-chain, norbornene-capped polyimide oligomers.[80] Crosslinking to the final (thermoset) resin is induced by polymerization of the norbornene double bonds,[80] by heating at >300 ^{o}C.

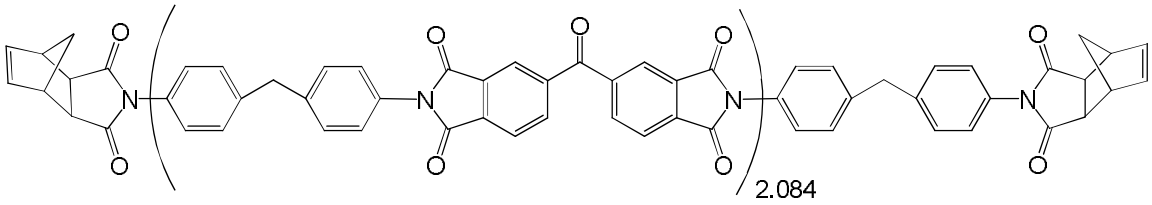

PMR-15

1.10.2 Synthesis of Polyimide Aerogels. Owing to their high temperature resistance, polyimide aerogels could be ideal materials for high-temperature thermal insulation. Although blown closed-cell macroporous polyimide-foams (Figure 1.35)[81] are already used for that purpose, as it becomes evident from above, mesoporous polyimide aerogels should have an edge.

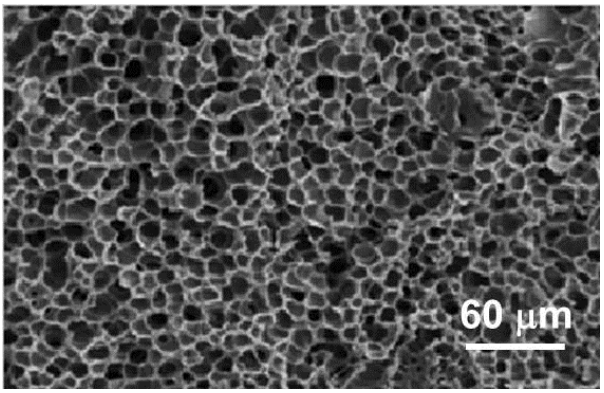

Figure 1.35 SEM of closed-cell macroporous polyimide foam.[82]

Thus, polyimide aerogels were first reported in 2006 in a US patent.[83] They were synthesized by the typical two-step DuPont polyamic acid route from a dianhydride and a diamine (Scheme 14). There have been various attempts to make robust polyimide aerogels by using anhydride end-capped polyamic acid solution and crosslinked using 1,3,5-triaminophenoxybenzene.[84] It was also observed that pore structure of the aerogels can be varied as a function of solvent as shown in Figure 1.36.

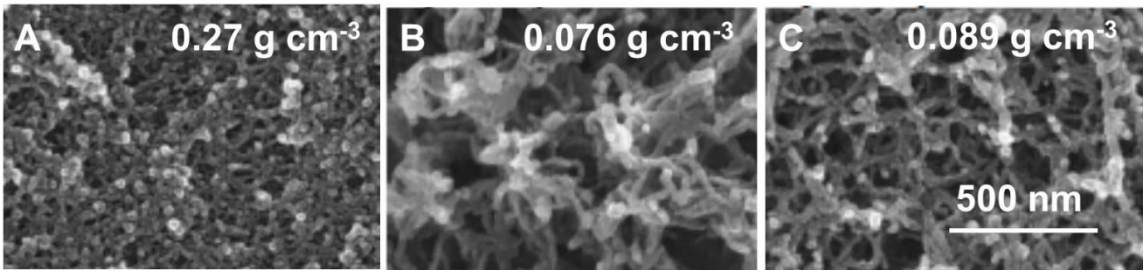

Figure 1.36 Different nanostructures obtained using different solvents for polyimide aerogels crosslinked with 1,3,5-triaminophenoxybenzene: A. NMP B. DMF C. DMAc.[84]

There are some organic-inorganic hybrid flexible polyimide aerogels also reported.[85] They are based on biphenyltetracarboxylic dianhydride (BPDA) and bisaniline-*p*-xylidene (BAX) and oligomers were formulated with 25 repeating units by taking the molar ratio of BPDA:BAX equal to (n+1):n, where n is the number of repeating units in the oligomers capped with anhydride (Scheme 27).[85]

Scheme 27. Synthesis of **PI** aerogels crosslinked with octa(aminophenyl)silsesquioxane (OAPS) where n is the number of repeat units in BPDA and BAX oligomers[85]

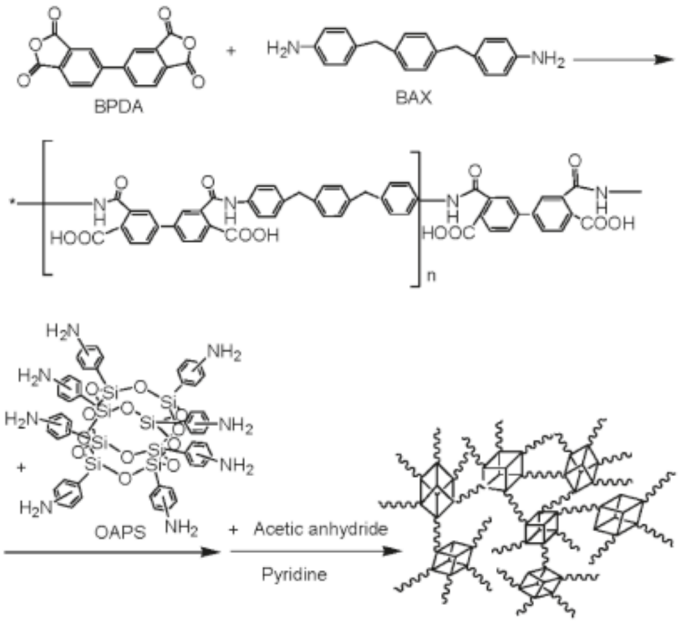

The anhydride end-capped oligomers were crosslinked with OAPS and the resultant aerogels are flexible (Figure 1.37).

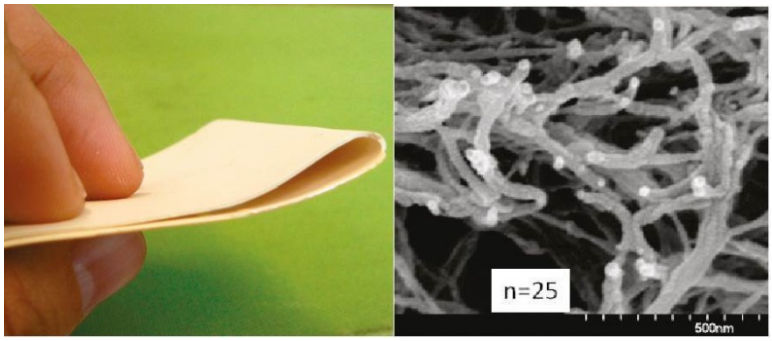

Figure 1.37 Flexible OAPS crosslinked polyimide aerogel thin film (n=25) on left and its typical microstructure on right.[85]

The robustness and the mechanical properties of those **PI** aerogels are completely dependent on the nature of the amine crosslinker.[85] We have also reported a low temperature process to polyimide aerogels via the PMR route, whereas the norbornene end-caps of a suitable bisnadimide, **bis-NAD**, were synthesized using classical DuPont-route imidization, and were polymerized via ring opening metathesis polymerization (ROMP) using the second-generation Grubbs' catalysts **GC-II** (Scheme 28).[86]

Scheme 28. Synthesis of bisnadimide and its crosslinking through ROMP using **GC-II**

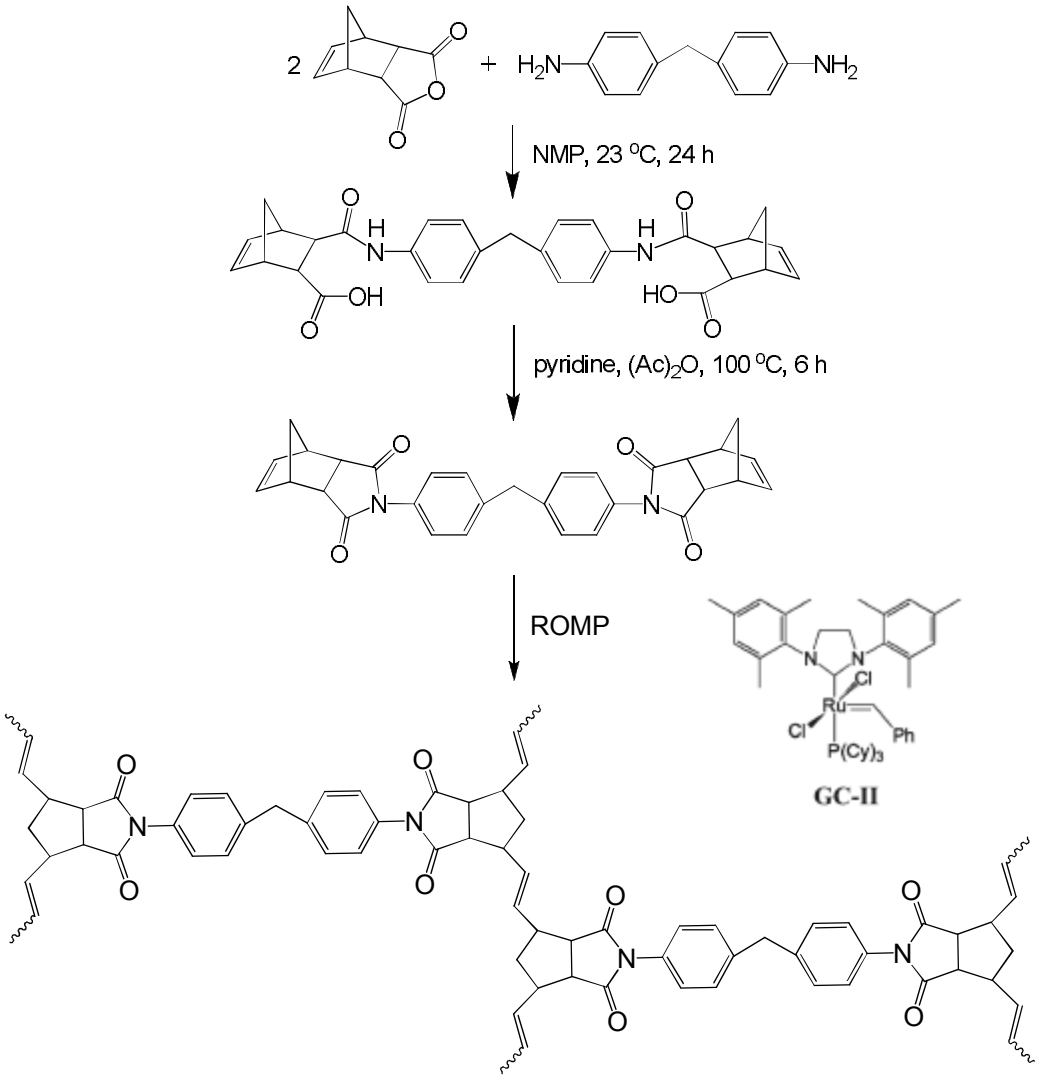

In this study we synthesized polypyromellitimide aerogels using monomers shown in the Scheme 29. Polyimide aerogels are synthesized through the isocyanate route (**PI-ISO**) in *N*-methyl pyrollidinone (NMP) as a solvent and compared their materials properties with a similar material synthesized from the DuPont route (**PI-AMN**) as exemplified in Scheme 30.[87]

Scheme 29. Compounds used in this study

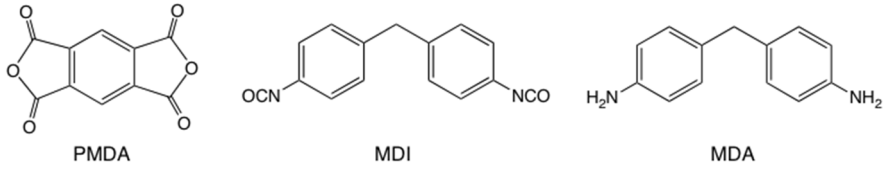

Scheme 30. Synthesis of polypyromellitimide from both routes

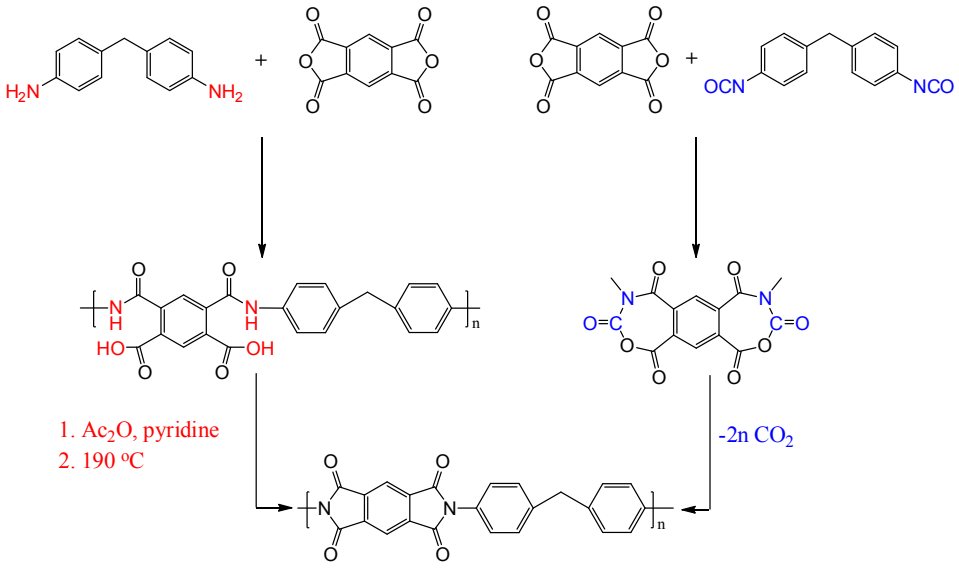

As it turns out, the isocyanate route has several distinct advantages for materials synthesis: (a) CO_2 is the only byproduct; (b) it does not require sacrificial dehydrating agents (e.g., acetic anhydride/pyridine) for gelation as is the case with the polyamic acid route; (c) it requires low gelation temperatures (from room to up to 90 ^{o}C), and it does not require post gelation curing at high temperatures (e.g., 190 ^{o}C) in order to complete imidization; and, (d) higher density aerogels for bifunctional structural and thermal

insulation applications are easily accessible, while the polyamic acid route encounters solubility issues at higher concentration sols.

1.10.3 Characterization of Polyimide Aerogels. The polyimide aerogels synthesized from the isocyanate route (**PI-ISO**) are chemically indistinguishable (Figure 1.38) from those synthesized via the polyamic acid route (**PI-AMN**). However, in terms of properties, the two materials are vastly different.

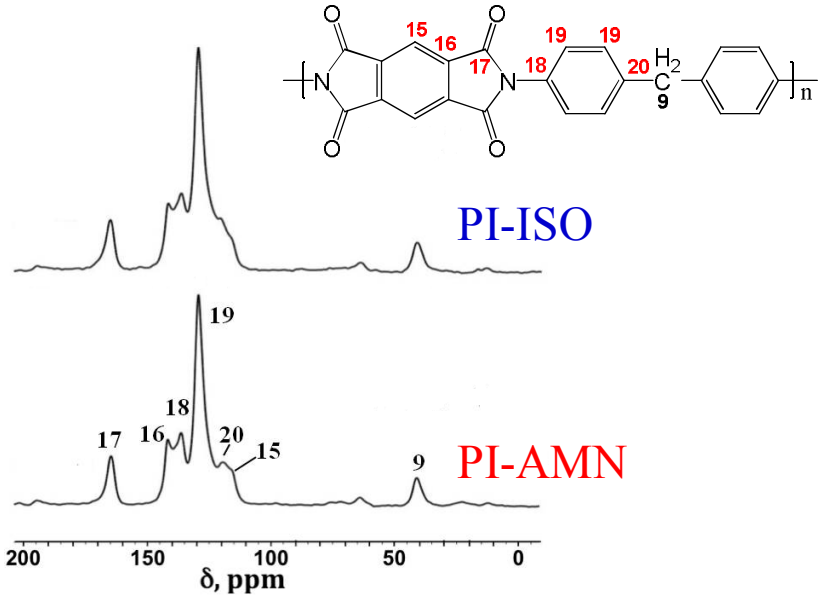

Figure 1.38 Solid ^{13}C CPMAS spectra of polyimide (**PI)** aerogels synthesized from both routes as indicated.[87]

Figure 1.39 shows the morphological difference of **PI-ISO** and **PI-AMN** synthesized using the same 15% w/w solids formulation. **PI-ISO** shows a fiber-like structure, which is completely different from the particulate nanomorphology of **PI-AMN**. **PI-AMN** and **PI-ISO** show similar size primary and secondary particles according to SANS (Figure 1.39).

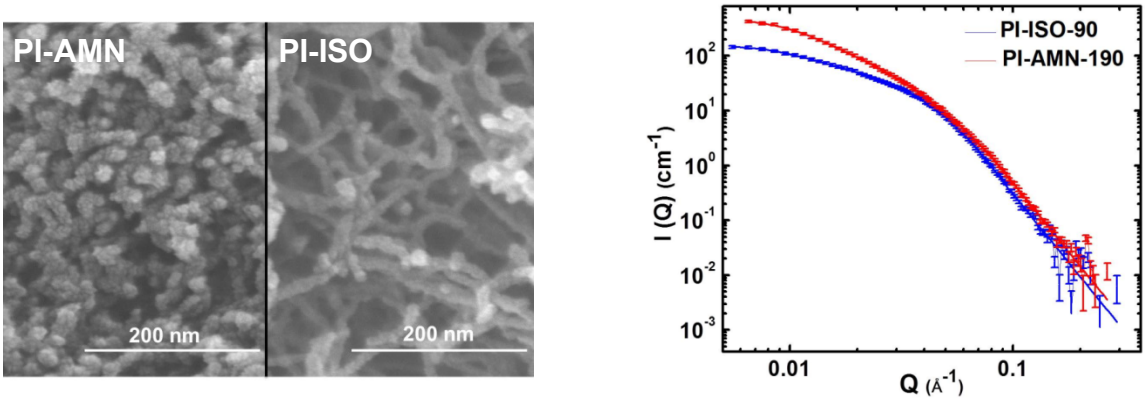

Figure 1.39 Left: SEM of **PI** aerogels as indicated. Right: Small angle neutron scattering (SANS) data of **PI-AMN-190** (red line, ρ_b= 0.23 g cm^{-3}, $R(1)$ = 5.8 nm and $R(2)$ = 35 nm) and of **PI-ISO-90** (blue line, ρ_b= 0.22 g cm^{-3}, $R(1)$ = 4.7 nm and $R(2)$ = 42 nm) both prepared in NMP using the 15% w/w solids formulation.[87]

Overall, chemically identical and structurally very similar primary particles seem to form secondary particles in the case of **PI-AMN**, and fibers in the case of **PI-ISO**. However, they behave very different upon quasi-static compression. Although the size of the primary particles is controlled by the common solvent (NMP), the only variable that remains different in the two systems is the actual chemistry of the two processes, which is translated into the surface functionality of the primary particles. The aerogels synthesized from the classic route are much stronger materials than the aerogels synthesized from the isocyanate route. This huge difference in mechanical strength can be attributed to the interfacial chemistry of primary particles. Figure 1.40 illustrates that the **PI-AMN** primary particles allow pivoting, closer packing and thus leading to a 3D growth resulting into secondary particles. On the other hand, the rigidity of the 7-member ring between **PI-ISO** primary particles, in combination with steric hindrance from neighboring particles, imposes growth at the exposed ends of the assembly resulting in directional growth and fibers.

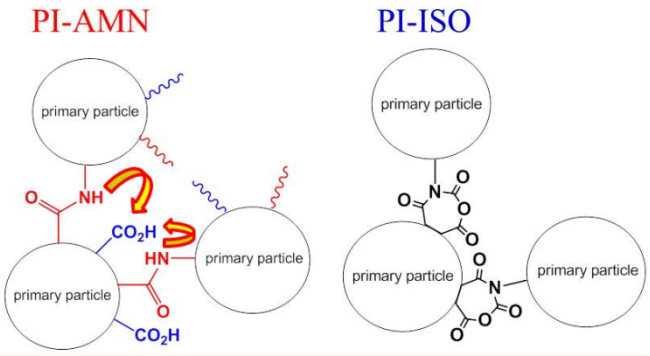

Figure 1.40 Interfacial chemistry of primary particles of polyimide aerogels synthesized from the amine route (**PI-AMN**) and the isocyanate route (**PI-ISO**).[87]

Though the failure of polyimide aerogels may be attributed to the phase separation mechanism, the 3D growth in **PI-AMN** should create numerous crosslinks between secondary particles while in the case of **PI-ISO**, crosslinking happens only at the contacts between fibers and therefore the **PI-ISO** weakness may also be due to their linear chemical structure. In order to validate, we should approach polyimide aerogels through multifunctional particles as shown in Figure 1.41.

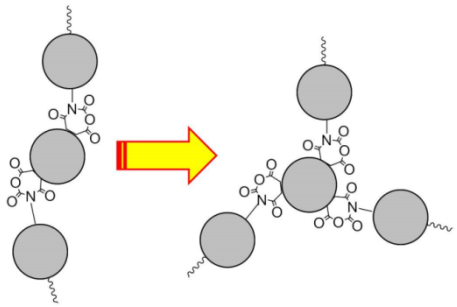

Figure 1.41 Proposed model for mechanically stronger polyimide aerogels from isocyanates and anhydrides.

Since multifunctional particles should originate from multifunctional monomers and realizing their importance in terms of imparting mechanical strength, we resort to a trifunctional isocyanate (**TIPM**). In order to investigate the role of dianhydride (**DANH**)

rigidity, we used two different anhydrides (Scheme 31). Resulting materials are called as **aR-DANH-xx** where aR indicates aromatic isocyanates **TIPM** in this case and xx indicates % w/w solids.

Scheme 31. Design of mechanically strong **PI** aerogels using two different anhydrides

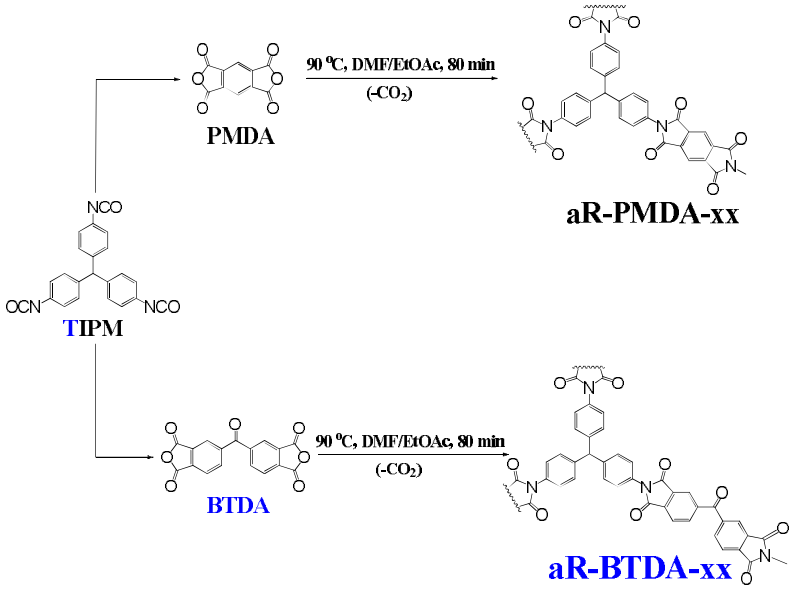

Figure 1.42 shows the typical stress-strain curve of polyimide aerogels. The polyimide aerogels are extremely robust materials with high energy absorption (*T*) capability, indicating that multifunctional particles lead to mechanically strong aerogels.

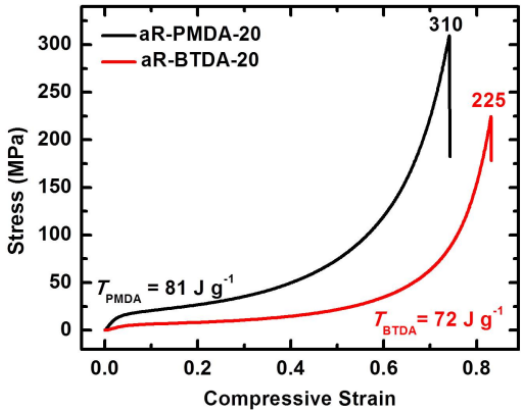

Figure 1.42 Stress-strain curves of selected **PI** samples under quasi-static compression.[88]

Table 1.6 summarizes data of polyimide aerogels synthesized with similar bulk density.[88]

Table 1.6 Selected quasi-static compression data for polyimide aerogels

sample-% w/w	bulk density, (ρ_b, g cm^{-3})	Young's modulus, (E, MPa)	specific energy absorption, (J g^{-1})
aR-PMDA-6	0.437±0.010	143±6	50±2
aR-BTDA-20	0.426±0.007	140±7	72±2

Both polyimide aerogels are stable up to 400 ^{o}C (by TGA), as expected from polyimides, while in N_2 they carbonize with yield ~ 50% w/w and can be considered as precursors to porous carbons. Porous carbons are pursued as electrodes for fuel cells and batteries.[89] Since polyimides generally have good carbonization yields,[90] these polyimides aerogels were subjected to pyrolysis. Carbonizable polymers are capable of either cyclizing or undergoing ring fusion and chain coalescence by heating. For this the chain should either contain aromatic moieties or be aromatizable usually by oxidation. In

the former case, there should be just one carbon atom between aromatic rings; otherwise, pyrolytic chain scission will prevail leading to loss of fragments.[91] Both monomers used here in the synthesis of polyimides fulfill the last criterion. Thus, upon pyrolysis at 800 ^{o}C under Ar, those aerogels are converted to carbon aerogels in high yields (52-59 % w/w).

Overall, we successfully have prepared polyimide aerogels at room temperature via reaction of an isocyanate with an anhydride. Mechanically, the materials synthesized from the isocyanate route are much weaker than the ones synthesized from the DuPont route. However, this has been addressed by using a multifunctional monomer and we demonstrate that the strength of nanoporous polymers (aerogels) can be increased by increasing the crosslinking density. We conclude that more rigid monomers lead to high stiffness and toughness as **aR-PMDA-xx** show ~7× higher Young's modulus than **aR-BTDA-xx** for similar monomer concentrations and higher specific energy absorption (twice as much as **aR-BTDA-xx**).

1.10.4 Applications. aR-PMDA-xx aerogels exhibit high thermal conductivities (0.074-0.089 W m^{-1} K^{-1}) due to the high shrinkage which in turn leads to high bulk densities. On the other hand, the conductivity values of **aR-BTDA-xx** aerogels fall between 0.052-0.084 W m^{-1} K^{-1}, which compare favorably with those of polyurea cross-linked silica aerogels (0.041 W m^{-1} K^{-1} at 0.451 g cm^{-3}), glass wool (0.040 W m^{-1} K^{-1}), corkboard (0.043 W m^{-1} K^{-1}) and fiberboard (0.048 W m^{-1} K^{-1}).[92] **aR-BTDA-xx** aerogels can be used in refrigerants, casing, building furnaces, piping sectors, cryogenic and heat exchangers.[93] These aerogels can be potentially used for high temperature thermal insulations. Polyimide aerogels can also be used as precursors to porous carbons.

PAPER

I. Fractal Multiscale Nanoporous Polyurethanes: Flexible to Extremely Rigid Aerogels from Multifunctional Small Molecules

Chakkaravarthy Chidambareswarapattar[1], Patrick M. McCarver[1], Huiyang Luo[2], Hongbing Lu[*,2], Chariklia Sotiriou-Leventis[*,1] and Nicholas Leventis[*,1]

1. Department of Chemistry, Missouri University of Science and Technology, Rolla, MO 65409, U.S.A. leventis@mst.edu, cslevent@mst.edu
2. Department of Mechanical Engineering, The University of Texas at Dallas, Richardson, TX 75080, U.S.A. hongbing.lu@utdallas.edu

Submitted for Publication as an Article to the *Chemistry of Materials*

Abstract: A large array of easily available small-molecule (as opposed to industrial oligomeric) triisocyanates and aromatic polyols render polyurethanes a suitable model system for a trend-based systematic study of structure-property relationships in nanoporous matter as a function of the monomer structure. Molecular parameters of interest include rigidity, number of functional groups per monomer (*n*) and functional group density (number of functional groups per phenyl ring, *r*). All systems were characterized from gelation to the bulk properties of the final aerogels. Molecular and nanoscopic features of interest, including skeletal composition, porous-structure, nanoparticle size and assembly, were probed with a combination of liquid- and solid-state ^{13}C and ^{15}N NMR, rheometry, N_2- and Hg-porosimetry, SEM and small angle x-ray scattering (SAXS). Macroscopic properties such as Styrofoam-like thermal conductivities (~0.030 W $m^{-1}K^{-1}$), foam-like flexibility or armor-grade energy absorption under compression (up to 100 J g^{-1}) were correlated with one another and serve as a top-down probe of the interparticle connectivity, which was again related to the monomer structure. Overall, both molecular rigidity and multifunctionality control phase-separation, hence particle size and by association porosity (e.g., meso versus macro) and internal surface

area. With sufficiently rigid monomers, skeletal frameworks include intrinsic microporosity, rendering the resulting materials hierarchically nanoporous over the entire porosity regime (micro to meso to macro). Most importantly, however, clear roles have been identified not only for the absolute number of functional groups per monomer, but also for parameter *r*. The latter is expressed onto the surface of the skeletal nanoparticles (controls the surface functional group density per unit mass) and becomes the dominant structure-directing as well as property-determining parameter. By relating the molecular functional group density with the functional group density on the nanoparticle surfaces, these results establish that for three-dimensional (3D) assemblies of nanoparticles to form rigid nanoporous frameworks, they have first and foremost to be able to develop strong *covalent bonding* with one another. These findings are relevant to the rational design of 3D nanostructured matter, not limited to organic aerogels.

1. Introduction

Aerogels are low-density nanoporous solids pursued for thermal and acoustic insulation, or as hosts for functional molecular or nanoparticulate guests.[1] They are prepared from suitable wet-gels by turning the pore-filling solvent into a supercritical fluid (SCF) that is vented off. Wet-gels that can be dried into aerogels consist of networks of nanoparticles, entangled fibers or a combination of both. Those wet-gels may be the result of what has been referred to as "chemical cooling,"[2] namely reaction of suitable monomers leading to phase-separation of small surface-reactive primary particles that undergo interparticle covalent bonding. That network-forming process points to the importance of multifunctional small-molecule monomers that undergo extended

molecular-level crosslinking, which in turn leads to an early phase separation of small primary particles with high surface functional group-to-volume ratios. Nevertheless, there is a lack of relevant systematic studies of those parameters, probably because of limited availability of a sufficiently wide variety of small-molecule monomers within the same class. Polyurethanes have the potential to rectify this situation.[3]

Polyurethanes are the reaction product of isocyanates and polyols.[4] Their bulk properties have been tailored by varying the chemical identity of the reagents with chain extenders and/or crosslinkers.[5] Polyurethane foams in particular have been extremely successful in thermal insulation.[6] Hence, polyurethane (**PU)** aerogels comprise a logical extension for those applications. **PU** aerogels were first reported in 1998 by Biesmans, using Suprasec^{TM} DNR (an aromatic polymeric isocyanate from ICI Polyurethanes) in CH_2Cl_2 and 1,4-diazabicyclo[2.2.2]octane (DABCO) as catalyst.[7,8] Curiously though, Biesmans' reports did not mention an alcohol, but instead emphasized the role of DABCO as a trimerization catalyst of isocyanates to isocyanurates. In 2001, Tan *et. al.* used toluene diisocyanate (TDI) to crosslink cellulose aerogels into materials with impact strength ten times higher than that of resorcinol-formaldehyde (RF) aerogels.[9] In 2002, Yim *et. al.* reported on the *co-gelation* of tetramethylorthosilicate (TMOS) and polymeric methylene diisocyanate (MDI) yielding silica-polyurethane hybrid aerogels.[10] In 2004, Rigacci *et. al.* revisited **PU** aerogels with emphasis on thermal superinsulation, using materials synthesized from Lupranat M20S [4,4´-methylenebis(phenylisocyanate)], two aliphatic polyols, saccharose and pentaerythritol, and DABCO as catalyst in DMSO/ethyl acetate mixtures.[11] Materials from both supercritical and subcritical drying were compared in terms of bulk density, pore volume, and thermal conductivity. The latter was

less than that of standard polyurethane foam (0.022 versus 0.030 W m^{-1} K^{-1} at room temperature and atmospheric pressure). It was further shown that the aerogel morphology depends on the solubility of the precursors, as well as the solubility parameter (δ_m) of the reaction medium. If $\delta_m<\delta_{PU}$ (the solubility parameter of the polyurethane), the aerogel consists of aggregates of micrometer-size particles; if $\delta_m>\delta_{PU}$ smaller-size particles and mesoporous structures were reported.[11] In 2009, Lee *et al.* reported on **PU** aerogels from 4,4´-diphenylmethyldiisocyanate (MDI) and polyether polyol (Multranol 9185) catalyzed with triethylamine.[12] The properties of those aerogels were compared with those of silica aerogels, as well as with polyurea aerogels from MDI or polyMDI and polyamines; at 0.128 g cm^{-3} Lee's aerogels had a surface area of 47 m^2 g^{-1}, an average pore diameter of 13 nm and a thermal conductivity of 0.027 W m^{-1} K^{-1}.[12]

All previously studied **PU** aerogels adopted "monomers" from bulk polyurethane synthesis, i.e., oligomeric isocyanates and/or high molecular weight (M_w) polyols. Although working with industrial materials has advantages in terms of availability and cost, from an aerogel perspective there are recognizable disadvantages as well: (a) given the importance of the relative solubilities suggested by Rigacci,[11] oligomeric reagents are expected to yield overall more-soluble products, which delays phase-separation and yields larger colloidal particles; (b) consequently, surface-to-volume ratios are expected relatively low, resulting in lower surface-area materials; and, (c) in general, oligomeric starting materials should yield low functional group densities on the surface of the nanoparticles, thus interparticle crosslinking should be also compromised, and the resulting aerogels are expected to be weak mechanically.

In view of the above, **PU** aerogels are synthesized herewith from inexpensive multifunctional small-molecule monomers. Morphostructural control is pursued through molecular parameters such as the rigidity vs. flexibility of the isocyanate. For this we employed two trifunctional isocyanates: aromatic **TIPM** (Desmodur RE) and aliphatic **N3300A** (Desmodur N3300A, see Scheme 1), both courtesy of Bayer Corp. U.S.A. Concurrently, we varied systematically the functionality as well as the molecular size and shape of the alcohols (Scheme 1). The basis for our selections was our intension to induce very early phase separation by adjusting the aromatic-to-functional group content of the monomer. Aromatic triols included phloroglucinol (**POL**) and 1,1,1-tris(hydroxyphenyl)ethane (**HPE**). Diols included resorcinol (**RES**), sulfonyl diphenol (**SDP**), bisphenol A (**BPA**), and dihydroxy benzophenone (**DHB**).

Scheme 1. Isocyanates and polyols used in this study

triisocyanates

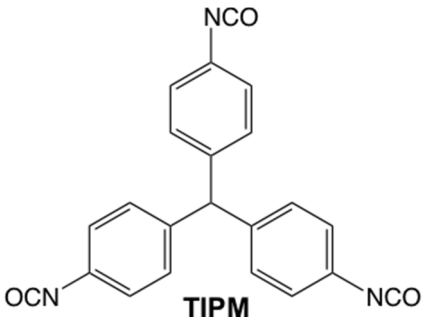

TIPM

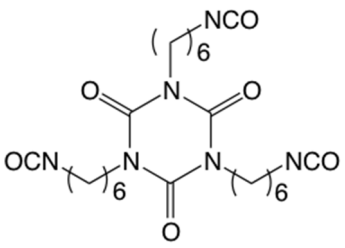

N3300A

triols

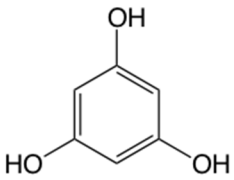

POL (n=3, r=3)

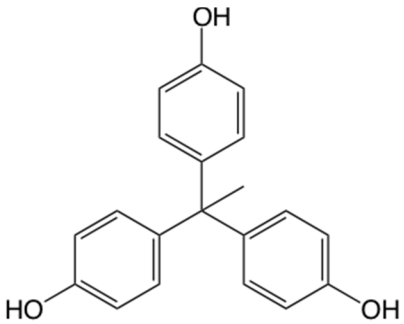

HPE (n=3, r=1)

diols

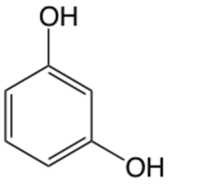

RES (n=2, r=2)

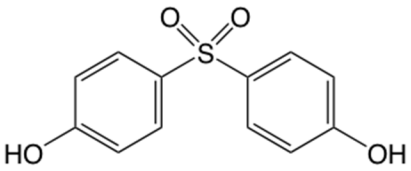

SDP (n=2, r=1)

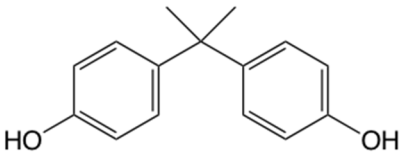

BPA (n=2, r=1)

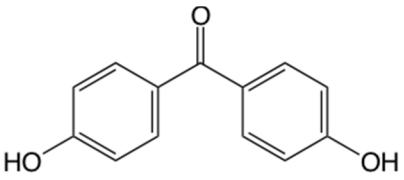

DHB (n=2, r=1)

With those alcohols we vary: (a) the absolute number of -OH groups, *n*, per monomer; (b) the ratio of -OH groups per aromatic ring, *r*; and (c) the "crowding" at the bridge between aromatic rings. Our basic hypothesis was that all three factors should be related to the solubility of the developing polymer, hence to the primary particle size. In

addition, parameters *n* and *r* should be expressed to the nanoparticle OH-group surface density, hence they should be related to the interparticle connectivity and mechanical strength. Samples based on aRomatic **TIPM** or aLiphatic **N3300A** are referred to as **aR-** or **aL-**, respectively. Overall, wet-gels and aerogls are abbreviated as **aR-ALC-xx** and **aL-ALC-xx**. **ALC** refers to the alcohol according to Scheme 1, and extension **–xx** refers to the weight percent of monomers in the sol.

Materials were characterized at the gel state, at the molecular level in terms of their chemical composition, at the nanoscopic level in terms of particle size, morphology of the hierarchical network and pore structure, and at the macroscopic level in terms of mechanical properties and thermal conductivity. Those bulk properties serve as proxies for investigating interparticle contact and bonding, which again are related to the monomer structure.

Scheme 2. Synthesis of polyurethane aerogels from small-molecule monomers (Letters serve as labels for the ^{13}C NMR peak assignment.)

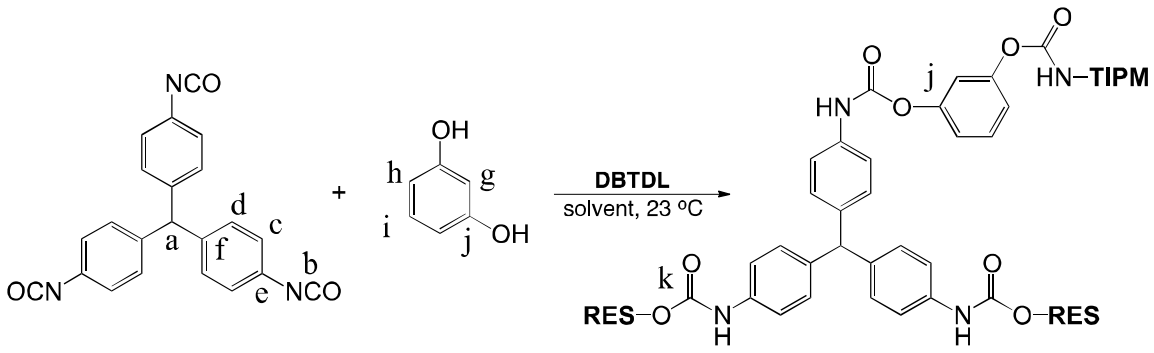

2. Results and Discussion

2.1. Synthesis of PU aerogels. Scheme 2 uses **TIPM** and **RES** to exemplify polyurethane wet-gel synthesis from small-molecule monomers under standard conditions.[5,13] Data, including phenomenological gelation times for all samples, are summarized in Tables S.1 and S.2 of Appendix I in the Supporting Information. The isocyanate/alcohol reaction is typically catalyzed either with tin salts (e.g., dibutyltin dilaurate: DBTDL), or with tertiary amines (e.g., DABCO). Although solid-state ^{13}C and ^{15}N NMR spectra show identical products with either DBTDL or DABCO (refer to Figures S.3 and S.4 in Appendix II of the Supporting Information), we opted for polyurethane-specific DBTDL,[14] because it is a several times more powerful catalyst than tertiary amines.[15] In order to accommodate short (10 min) and long gelation times (5.5 h) for high- and low-concentration sols, respectively, we opted for room temperature gelation and a constant monomer-to-catalyst ratio (**TIPM**:DBTDL equal to 120 mol/mol - see Experimental). Variable density samples were synthesized by just varying the amount of solvent (anhydrous acetone).

Scheme 3. Preparation of polyurethane (PU) aerogels from small molecule monomers

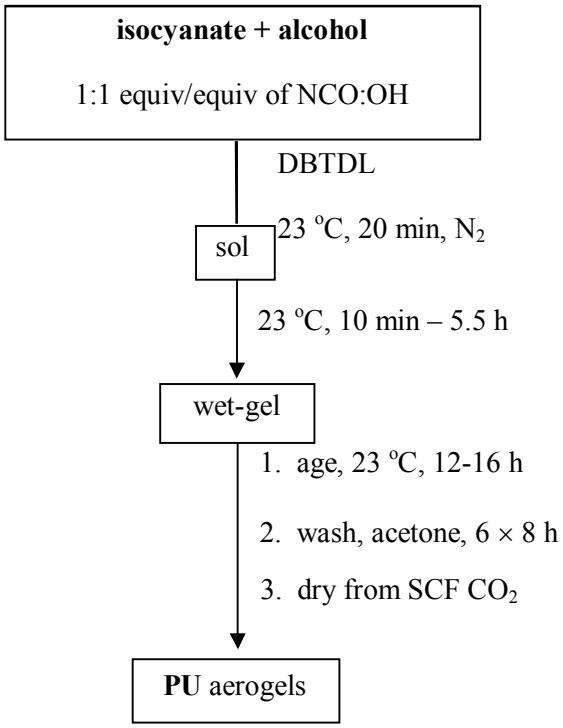

Scheme 3 summarizes the practical implementation of Scheme 2. Since **TIPM** is supplied as a solution in anhydrous ethyl acetate (EtOAc), **aR-ALC-xx** wet-gels were synthesized in EtOAc/acetone mixtures. **N3300A** is supplied in neat form. (For its full characterization refer to the Supporting Information of Ref. 16), and **aL-ALC-25** wet-gels were synthesized in pure acetone. In the case of **aR-ALC-xx**, the monomer weight percent in the sol (denoted by **-xx**) was varied in the 5-25 range (see Experimental). **aR-ALC-xx** samples missing from the 5-25 range signifies that those particular formulations would not gel. That was the case with the 5% w/w sols of all diols, while it is also noted that **aR-DHB-15** was the minimum **DHB** sol concentration that gelled. The ability to gel was a more acute issue with **aL-ALC-xx**. Thus, we report only on the **aL-ALC-25** samples, and we note that even with that constrain, sols based on **RES** and **DHB** diols

formed loose, grainy precipitates (flocs) rather than gels. Because those flocs seemed to possess some structural integrity and did not undergo any additional shrinking compared to other samples, they were processed further as regular wet-gels.

2.2. Monitoring the gelation process. Phenomenological gelation times (Tables S.1 and S.2 in the Supporting Information) were recorded from the addition of the catalyst (Scheme 3) to the point sols stopped flowing by inverting the molds. In general, other factors being equal, **aL-ALC-25** gel much more slowly (1 h 20 min to 5 h 30 min) than the corresponding (molar concentration-wise – refer to Tables S.1 and S.2) **aR-ALC-20** samples (10-40 min). That is attributed to the lower reactivity of aliphatic (**N3300A)** versus aromatic (**TIPM)** isocyanates.[5] On the other hand, within the **aR-**series, higher concentration sols gel faster, while by considering constant sol concentrations triol-based sols (e.g., **aR-HPE-20**, 15 min and **aR-POL-20**, 25 min) gel faster than most diol-based sols: **aR-RES-20** (25 min) > **aR-BPA-20** (30 min) > **aR-DHB-20** (40 min). **aR-SPD-xx** samples comprise an exception as they gel faster than all other **aR**-sols (e.g., **aR-SPD-20** gelled in 10 min).

The chemical fate of the monomers during the early phase of gelation, and the formal sol-gel transition were monitored with liquid ^{13}C NMR and rheometry, respectively.

All sols lose their ^{13}C NMR signals long before gelation. This is illustrated in Figure 1 with **aR-RES-10** whose sols gel relatively slowly (145 min – Table S.1) and early products are relatively more soluble, rendering observation of intermediates within the time scale of the ^{13}C NMR experiment possible. Twenty five (25) min after adding the catalyst (Figure 1B), the overall intensity of the ^{13}C NMR signal had decreased, and

numerous new resonances had appeared (referred to with primed labels) owing to soluble oligomers. For example, in addition to two new urethane carbonyl resonances, "k," in the 151-152 ppm range (Scheme 2), we also observe two new peaks (j′ at 158 ppm and j′′ at 152 ppm) corresponding respectively to the remaining unreacted phenolic C-OH carbon of a mono-reacted resorcinol and to the reacted phenolic C-OCONH. Thirty five (35) min after adding the catalyst (Figure 1C), the overall signal intensity had decreased further, and beyond that point all signals besides the solvent were lost (spectra not shown). It is concluded that the reaction starts immediately after addition of the catalyst, **PU** phase-separates quickly leading to the ^{13}C NMR signal loss, and all monomers are practically consumed completely much sooner than the gel point. That sequence of events suggests that the initial reaction among monomers switches quickly to monomer-oligomer, oligomer-oligomer and monomer/oligomer-cluster aggregation. Beyond the point of ^{13}C NMR signal loss, the process most probably turns to diffusion-limited cluster aggregation, which is expected to yield fractal assemblies.

Rheometry was conducted in the multi-wave mode superimposing four different oscillatory frequencies (see Experimental). Figure 2A shows the typical evolution of the storage (G') and the loss (G'') moduli of the sol at a single oscillatory frequency as a function of time. The two curves cross near the gelation point, beyond which the elastic properties of the newly formed rigid gel dominate over the viscous properties of the fluid sol. The formal (i.e., actual) gelation point is located at the inflection point of the tanδ ($=G''/G'$) versus time plot (included in Figure 2A). Since the gelation point is a physical property of the system, it is independent of the oscillation frequency of the cone, and can be obtained as the common crossing point of all the tanδ versus time curves,[17] or more

accurately, at the minimum of the statistical variable log(s/<tanδ>) versus time plot (see Figure 2B, whereas s is the standard deviation of the four tanδ from the four oscillatory frequencies, at every sampling time along gelation).[18] Results are summarized in Table 1, and are cited together with the corresponding phenomenological gelation times (reproduced from Table S.1). In general, the formal and the phenomenological gelation times are close; exception was the **aR-SDP-25** sol, which by rheology gelled at 1193 s, but it stopped flowing only 15 min (420 s) after adding the catalyst as mentioned above. Therefore, by rheometry the real gelation point of the **aR-SDP-25** sol is reached at a comparable time to that required for **aR-POL-25** (1396 s). (Those data strongly suggest that **aR-SDP-25** forms a thixotropic fluid, whereas the sol stops flowing because of high viscosity (a polymer gel) rather than because it reaches its percolation threshold.) Overall, parameter n seems to be an important factor controlling the gelation time: in general, higher-n sols gel faster than lower-n sols. Between equal-n **POL** and **HPE**, lower-r **HPE** gels faster than **POL**; this can be attributed to the electron-withdrawing deactivation brought about to the remaining –OH groups by the first urethane formation of one of the –OH groups of **POL**. However, that trend is generally reversed in the n=2 series; for example, **RES** sols gel faster than those based on **BPA** and **DHB**. The matter is a multivariable problem whereas n and r are not the only important parameters. The solubility of the developing polymer is expected to be also a critical one.

At the gel point, tanδ is related to the gel relaxation exponent 'z' via Eq. 1.[19] In turn,

$$\tan\delta = \tan(z\pi/2) \qquad (1)$$

considering the excluded volume of the (primary) particles forming the clusters, 'z' is related via Eq. 2 to the mass fractal dimension, D_f, of the clusters forming the gel (see Table 1).[20] (Note, for three-dimensional non-fractal clusters, D_f=D=3.[20])

$$z = \frac{D(D+2-2D_f)}{2(D+2-D_f)} \qquad (2)$$

Table 1. Rheometry data from the gelation of selected **PU** sols as indicated

formulation	aging time before loading into rheometer (s)	gelation point, t_{gel} [a] (s[s])	tanδ at t_{gel}	z [b]	D_f [c]
aR-POL-5	9000	10514 [10800]	0.079	0.051	2.45
aR -POL-10	2400	3290 [3600]	0.553	0.322	2.20
aR -POL-15	1200	2062 [2400]	0.395	0.240	2.28
aR -POL-20	900	1734 [1500]	0.572	0.331	2.19
aR -POL-25	660	1396 [1200]	0.463	0.276	2.24
aR -HPE-15	1200	1667 [1500]	0.263	0.164	2.35
aR-RES-10	6600	7930 [8700]	0.314	0.194	2.33
aR -SDP-25	60	1193 [420]	0.187	0.171	2.34

[a] Identified at the minimum of the statistical function as shown in Figure 2B. In brackets, phenomenological gelation times from Table S.1 [b] From Eq. 1. [c] From Eq. 2.

The D_f values of the selected **PU** formulations shown in Table 1 are in the 2.2-2.5 range, suggesting that the gel network is formed by mass-fractal particles via diffusion-limited cluster aggregation,[21] consistent with ^{13}C NMR.

2.3. Chemical characterization of PU aerogels. The chemical identity of the **PU** aerogels was confirmed with FTIR and solid state CPMAS ^{13}C NMR. The degree of molecular order within the solid framework was investigated with XRD.

The solid-state CPMAS ^{13}C NMR spectra of all **aR-ALC-xx** aerogels are shown in Appendix II of the Supporting Information. Strictly identical spectra were obtained for

all **–xx** within each **aR-ALC-xx**. In most cases no resonance peaks related to the gelation, or the wash solvent are visible in the spectra. A representative example (**aR-RES-10**) is shown in Figure 1D. The resonance at 54 ppm is assigned to the CH of **TIPM**. The resonances at 135 ppm (with shoulder at 140 ppm), 129 ppm and 118 ppm are assigned to the aromatic carbons from **TIPM** and **RES** (refer to Scheme 2). The intense broad resonance at 152 ppm is assigned to the overlapping urethane carbonyl and the phenolic C-O(CO)NH from **RES**. That assignment is partly based on the evolution of the liquid ^{13}C NMR spectra during gelation (Figures 1B and 1C), and partly on the spectrum of **aR-HPE-25** (see Figure S.2 in Appendix II of the Supporting Information), whereas the two resonances are close to one another but resolved: the urethane carbonyl appears at 150 ppm, while the aromatic (**HPE**) C-O- shows up at 154 ppm. It is noted, however, that owing to broadening, the solid-state ^{13}C NMR spectra are unclear on whether all –NCO or –OH groups have reacted.

Representative FTIR spectra of **PU** aerogels are shown in Figure 3. Neither a unreacted N=C=O stretch in the 2273-2000 cm^{-1} range, nor a urea carbonyl stretch in the 1600-1640 cm^{-1}range, nor the intense O-H stretch of the monomer in the 3200-3350 cm^{-1} range are detectable, supporting complete reaction of NCO with OH to urethane. The urethane carbonyl stretch is observed at 1740 cm^{-1}, the C-N stretch near 1204 cm^{-1}, the N-H bending coupled to the C-N stretching near 1510 cm^{-1}, while the band at 1595 cm^{-1} is due to aromatic C-C stretching. The absorptions at 1127 cm^{-1} and 1012 cm^{-1} are attributed to the urethane asymmetric and symmetric C-O-C stretching, respectively.[22] The free N-H stretch is observed at 3408 cm^{-1}, and the hydrogen-bonded N-H absorption near 3312 cm^{-1}.[23] In analogy to polyamides (e.g., Kevlar or Nylon),[24] H-

bonding in polyurethanes has been associated with crystallinity.[23]

Powder XRD spectra of all **aR-ALC-10** and **aL-ALC-25** samples are shown in Figure S.10 of the Supporting Information. Broad, but well-defined diffractions are observed at 2θ equal to 11°, 19°, and 44°, indicating nanocrystallinity. Increased rigidity produces a more intense diffraction at 2θ =11°,[25,26] which is the case for all **aL-ALC-25** aerogels. The degree of crystallinity, $cr_{\%}$, was calculated by subtracting the broad background from the entire diffraction profile and results are presented in footnotes [g] and [h] of Tables 2 and 3, respectively. As shown below, the degree of crystallinity is reflected in a subtle way upon the skeletal densities of the backbone nanoparticles, but otherwise it seems to be inconsequential in terms of particle size or microporosity (that is samples with comparable *cr%* may include significant microporosity or none).

2.4 Materials Characterization

2.4.1 General material properties. Relevant materials characterization data for **aR-ALC-xx** and **aL-ALC-25** aerogels are summarized in Tables 2 and 3, respectively. Discussion focuses on parameters *n*, *r* and the nature of the bridge between phenyl groups.

All **aR-**samples shrink 17-35% in diameter during aging, solvent-exchange and drying. Higher-concentration gels shrink during aging and solvent exchange. Lower-concentration gels shrink mostly during SCF drying. In particular, **aR-(POL**_or_**HPE)-5** and **-10** gels shrink exclusively during SCF drying. By comparison of **aR-ALC-20** and **aL-ALC-25** aerogels (i.e., samples synthesized from similar molar sol concentrations – see Tables S.1 and S.2), **aL-ALC-25** wet-gels shrink more than their **aR-ALC-20** counterparts, presumably due to the inherent flexibility of the $-(CH_2)_6-$ tethers, which

allows twisting and packing in order to maximize non-covalent interactions (van der Walls, hydrogen bonding) upon drying. A notable exception is **aL-BPA-25**, which actually *expands* (swells) during the SCF CO_2 drying process. (A photograph of such a sample is included in Figure S.24 of the Supporting Information.) To our knowledge, this behavior of **aL-BPA-25** is unique and, in the context of this discussion (Section 2.4.2b), is probably caused by swelling of the primary particles with liquid CO_2.

Within each **aR-ALC-xx** series, the largest shrinkage is observed when both *n* and *r* are high, (**aR-POL-xx**, *n*=3, *r*=3; and, **aR-RES-xx**, *n*=2, *r*=2), and within those two series, samples shrink somewhat less as the sol concentration increases, most probably signifying the higher concentration of elementary building block with higher functional group expression at their surfaces, which in turn rigidizes the framework more effectively. Among alcohols with equal *n* and *r* (i.e., **SDP**, **BPA** and **DHB**; *n*=2, *r*=1), the least shrinkage (17%-19%) is observed with the **aR-DHB-xx** aerogels, followed by **aR-SDP-xx** (25%-28%) and **aR-BPA-xx** (24%-30%). There seems to be no correlation of shrinkage with the number of atoms in the bridge, but rather with the hybridization of the bridging atom: sp^2 hybridization (case of **aR-DHB-xx**) seems to result in lower shrinkage than sp^3. In order to probe this further, we considered synthesis of **aR-**type aerogels with 4,4′-bisphenol. However, the solubility of that diol in acetone is low, not allowing synthesis of suitable aerogels for direct comparison.

Reflecting primarily higher shrinkage, **aL-ALC-25** aerogels are generally more dense than their **aR-ALC-20** counterparts. On the other hand, within each **aR-ALC-xx** series, differential shrinkage is not high enough to alter the intended trend, therefore samples from less concentrated sols are generally less dense. In the case of **aR-HPE-5**,

the combination of low concentration with low relative shrinkage yields aerogels with bulk density (ρ_b) less than 0.1 g cm^{-3}. A second noteworthy case is **aL-BPA-25** whereas, because of negative shrinkage (Table 3), the bulk density is also relatively low (0.16 g cm^{-3}). The finding might be of technological importance and renders the **aL-BPA-xx** series in need of further future investigation.

The skeletal density, ρ_s, of **aR-POL-xx** varies randomly with ρ_b and remains about constant. All other **aR-ALC-xx** show a systematic *increase* in ρ_s with increasing ρ_b. That upward trend in ρ_s excludes closed porosity, and its origin is discussed in Section 2.4.2b. By inspection, weak correlations seem to exist between the ρ_s values of **aR-ALC-xx** and: (a) the densities of the parent ALC, ρ_{ALC} (for the ρ_{ALC} values see Experimental); and, (b) the degree of crystallinity, $cr_{\%}$, of the samples (cited in footnote [g] of Table 2). A fully quadratic fit of the ρ_s values of **aR-ALC-xx** with ρ_{ALC} and $cr_{\%}$ yields: $\rho_s=6.839(\rho_{ALC})^2+0.00314(cr_{\%})^2-4.335(\rho_{ALC})(cr_{\%})-0.699(\rho_{ALC})+0.0322(cr_{\%})-4.700$ ($R^2=1.000$). That interplay of ρ_{ALC} and $cr_{\%}$ provides a reasonable explanation for the fact that the ρ_s values of **aL-ALC-25** and **aR-ALC-20** are comparable, despite the very different molecular structures of **N3300A** and **TIPM**.

Porosities, Π, as percent of empty space were calculated via $\Pi=100\times(\rho_s-\rho_b)/\rho_s$ and decrease as the sol concentration increases, as expected (see Tables 2 and 3). Without going to unnecessary detail, the total change of Π with ρ_b within each series of samples follows the same trend with shrinkage: the largest change was observed within the **aR-POL-xx** series and the lowest within the **aR-DHB-xx** samples. The porosities of the **aL-ALC-25** samples were generally lower than those of the corresponding **aR-ALC-20**. In particular, the porosities of **aL-RES-25** (28%) and **aL-DHB-25** (35%) were significantly

lower than those of **aR-RES-20** (57%) and **aR-DHB-20** (77%), presumably because the former two samples were actually produced from flocs. The porosity of **aL-BPA-25** was found higher than that of the corresponding (sol-concentration-wise) **aR-BPA-20** (88% versus 67%), because of swelling upon drying as mentioned above.

2.4.2 Bottom-up characterization: the porous structure and the skeletal framework.

2.4.2a The porous structure. That was probed with N_2-sorption and Hg-intrusion porosimetry. All data are provided in Appendix IV of the Supporting Information.

N_2-sorption isotherms of all lower-density **aR-**samples do not reach saturation and show narrow hysteresis loops, suggesting mostly macroporous structures. On the other hand, isotherms of higher-density **aR-**samples based on polyols with high either *n* or *r* (cases of **POL**, **HPE** and **RES**) are clearly Type IV, they reach saturation at $P/P_o \sim 1.0$ and show pronounced desorption hysteresis loops. Considered together, these data signify a macroporous-to-mesoporous transition as density increases. Representative data with **aR-POL-xx** and **aR-HPE-xx** are shown in Figure 4. It is noted further that: (a) all high-*n* or high-*r* samples, irrespective of density, show substantial volumes of N_2 absorbed at low relative pressures, meaning that they are also microporous; (b) at the high pressure end of the isotherms, the hysteresis loops are H2-type, characterizing ink-bottle shaped nanopores as those expected from close-packed spheres (see analysis of the skeletal framework in Section 2.4.2b); and, (c) as demonstrated with **aR-HPE-xx** in Figure 4B, the mesoporous space of all **aR-ALC-xx** except **aR-POL-xx** increases with density (see Appendix IV); the mesoporous space of **aR-POL-xx** decreases with ρ_b (Figure 4A).

The macroporous-to-mesoporous transition is supported by pore diameters calculated via the $4\times V_{Total}/\sigma$ method (σ: BET surface area, see below). For that calculation, V_{Total} was either taken from the highest point along the N_2-sorption isotherm (at $P/P_o\sim1.0$), or was calculated via $V_{Total}=(1/\rho_b)-(1/\rho_s)$. Pore diameters with V_{Total} calculated via the two methods diverge significantly for the lower-density samples (e.g., 18.9 nm versus 92.2 nm, respectively, for **aR-POL-5**) and converge as the density increases (e.g., 8.3 nm, versus 10.1 nm for **aR-POL-25**). Consistent with the macroporous-to-mesoporous evolution with ρ_b, pore size distributions calculated with the BJH method become narrower and move to lower values as ρ_b increases (see insets in Figure 4). From isotherms that reach saturation, the maximum along the BJH pore size distribution agrees well with the values calculated via the $4\times V_{Total}/\sigma$ method (e.g., 9.8 nm for **aR-POL-25**).

N_2-sorption isotherms of **aR-**samples based on polyols with lower *n* and *r* (cases of **SDP**, **BPA** and **DHB**) do not reach broad saturation plateaus at any density. The total volume of N_2-absorbed is generally low, and the desorption hysteresis loops are narrow. Therefore, the maxima of the BJH pore size distributions *do not* agree with values calculated via the $4\times V_{Total}/\sigma$ method (Table 2), although they should still represent accurately the small amount of mesopores present in the samples. In most of those cases the macroporous structure was probed with Hg-intrusion porosimetry as demonstrated in Figure 5 with **aR-SDP-15**; **-20**; and **-25**. The maxima of the Hg-intrusion-derived pore size distributions agree reasonably well with the average pore sizes calculated via the $4\times V_{Total}/\sigma$ method (Table 2), whereas V_{Total} is the true total pore volume calculated via $V_{Total}=(1/\rho_b)-(1/\rho_s)$; that confirms macroporosity and validates the Hg-intrusion data in

the sense that the pressure range required to force Hg in the pores does not alter the porous structure. In general, the macropore size distribution of **aR-SDP-xx**, **aR-BPA-xx** and **aR-DHB-xx** is quite narrow and moves to lower values as ρ_b increases. An exception is the low density **aR-SDP-10** sample that shows (see Figure S.16 in Supporting Information) a very broad macropore distribution and a sudden rush of Hg into the sample at only 40 psia, which might be related to the mechanical flexibility of those samples – see Section 2.4.3b below).

With **aL-ALC-25** aerogels, significant N_2 uptake (400-700 cm^3 g^{-1} under STP) and quasi-saturation plateaus were observed only with n=3 (**POL** or **HPE**). All other samples adsorb much less N_2 (<125 cm^3 g^{-1} under STP), and the isotherms do not reach saturation. Analysis of the pore structure was also conducted with Hg-intrusion (Appendix IV and Table 3).

Finally, the internal surface area of all **aR-ALC-xx** and **aL-ALC-25** samples, σ, determined with the BET method from the multilayer adsorption part of the N_2-sorption isotherms, seems completely unrelated to shrinkage or porosity (Tables 2 and 3). **aL-ALC-25** aerogels have significant lower surface areas than their **aR-ALC-20** counterparts; exceptions are **aL-SPD-25** and **aL-BPA-25**; the latter presumably because it swells upon drying. In **aR-ALC-xx** aerogels, surface areas seem to correlate strongly with the ability of isotherms of high-density samples to reach saturation plateaus. That is, whenever higher-density samples are strictly mesoporous (cases of **aR-POL-25**; **aR-HPE-25**; and, **aR-RES-25**) the surface area *of the entire series* is relatively high (200-241 m^2g^{-1}; 132-235 m^2g^{-1}; and, 33-119 m^2g^{-1}, respectively). In addition, the surface areas of those samples have notable contributions from micropores, roughly 5-10%, *including*

the low-density members of the series, which are mostly macroporous (micropore surface areas are included in Table 2). In contrast, whenever higher-density samples remain macroporous (cases of **aR-SPD-25**, **aR-BPA-25** and **aR-DHB-25**) the surface areas of the entire series are relatively small (<50 m^2g^{-1} and typically <10 m^2 g^{-1}). Microporosity in those cases is almost completely absent. Most importantly, the surface area of **aR-POL-xx** does not vary systematically as the mesoporous space decreases with increasing ρ_b (Figure 4A). In all other cases, whereas the total volume of N_2 adsorbed *increases* with ρ_b (e.g., **aR-HPE-xx**, see Figure 4B), so does the surface area: for example, for **aR-HPE-5**, σ=132 m^2g^{-1}, and for **aR-HPE-25**, σ=235 m^2g^{-1} (refer to Table 2).

Table 2. General materials characterization data for **aR-ALC-xx**

sample	linear shrinkage (%) [a,b]	bulk density, ρ_b (g cm^{-3}) [a]	skeletal density, ρ_s (g cm^{-3}) [c]	Π (%)	BET surface area, σ (m^2 g^{-1}) [d]	average pore diam. [Φ] (nm [nm]) [e]	BJH average pore diam. (nm)	particle radius (nm) [f]	R(1) from SAXS (nm) [m]
aR-POL-xx (*n*=3; *r*=3)									
aR-POL-5	34.8 ± 0.9	0.159 ± 0.006	1.361 ± 0.007	88	241 [19]	18.9 [92.2]	[j]	9.2	$10._7$±$2._6$
aR-POL-10	31.4 ± 0.2 [g]	0.298 ± 0.004	1.355 ± 0.008	78	239 [21]	22.4 [43.9]	53.6 [62.1] [h]	9.2	$11._4$±$2._3$
aR-POL-15	31.9 ± 0.3	0.477 ± 0.008	1.345 ± 0.010	65	234 [19]	18.0 [23.2]	29.8 [9.9] [h]	9.5	$11._4$±$1._4$
aR-POL-20	30.8 ± 0.3	0.640 ± 0.010	1.336 ± 0.007	52	200 [17]	12.0 [16.3]	15.2 [3.6] [h]	11.2	13.6±0.2
aR-POL-25	28.8 ± 0.4	0.760 ± 0.050	1.340 ± 0.006	43	225 [17]	8.3 [10.1]	9.8 [2.3] [h]	9.3	10.52±0.06
aR-HPE-xx (*n*=3; *r*=1)									
aR-HPE-5	22.4 ± 1.6	0.094 ± 0.004	1.232 ± 0.015	92	132 [14]	11.4 [297.7]	54.9 [80.8] [h]	18.5	$16._2$±$1._7$
aR-HPE-10	20.6 ± 0.4 [g]	0.184 ± 0.007	1.251 ± 0.007	85	165 [19]	13.1 [112.4]	47.3 [62.1] [h]	14.5	$12._8$±$2._3$
aR-HPE-15	23.9 ± 0.3	0.315 ± 0.003	1.260 ± 0.009	75	174 [19]	17.6 [54.7]	41.0 [69.1] [h] (56 [i])	13.7	$12._7$±$1._5$
aR-HPE-20	24.1 ± 0.2	0.426 ± 0.008	1.276 ± 0.002	66	192 [21]	31.9 [32.6]	43.2 [33.7] [h]	12.2	$13._3$±$1._6$
aR-HPE-25	22.1 ± 0.2	0.567 ± 0.002	1.260 ± 0.003	55	235 [20]	18.2 [16.5]	43.8 [41.4] [h]	9.3	7.1±0.8
aR-RES-xx (*n*=2; *r*=2)									
aR-RES-10	31.7 ± 0.4 [g]	0.244 ± 0.005	1.307 ± 0.010	81	33 [1.2]	22.9 [404]	59.5 [76.8] [h]	69.6	$55._6$±$5._4$
aR-RES-15	30.7 ± 0.1	0.404 ± 0.001	1.297 ± 0.022	69	83 [3.6]	20.7 [82.1]	50.6 [66.1] [h] (35 [i])	28.5	$39._9$±$5._8$
aR-RES-20	30.8 ±0.0_1	0.565 ± 0.004	1.319 ± 0.008	57	109 [5]	27.2 [37.1]	42.5 [27.6] [h]	20.9	$29._9$±$1._3$
aR-RES-25	28.6 ± 0.2	0.680 ± 0.003	1.316 ± 0.004	48	119 [5]	17.0 [23.9]	22.7 [7.4] [h]	19.2	21.8±0.4
aR-SDP-xx (*n*=2; *r*=1)									
aR-SDP-10	27.5 ± 0.7 [g]	0.190 ± 0.005	1.319 ± 0.005	86	2.8 [0.0]	11.3 [6436]	(5226 [i])	812	$98._1$±$2._7$
aR-SDP-15	27.6 ± 0.5	0.307 ± 0.007	1.319 ± 0.004	77	4.0 [0.6]	11.4 [2499]	(2035 [i])	569	89±13
aR-SDP-20	25.7 ± 0.1	0.422 ± 0.003	1.325 ± 0.005	68	9.0 [1.4]	13.1 [718]	(525 [i])	252	$69._9$±$3._3$

aR-SDP-25	24.9 ± 0.2	0.541 ± 0.004	1.345 ± 0.005	60	28 [2.3]	21.4 [158]	(115 [i])	74	$60._2 \pm 1._7$
aR-BPA-xx (*n*=2; *r*=1)									
aR-BPA-10	24.7 ± 0.3 [g]	0.194 ± 0.005	1.228 ± 0.003	84	1.0 [0.0]	[j] [17361]	(22763 [i])	2440	[l]
aR-BPA-15	23.7 ± 0.2	0.293 ± 0.005	1.240 ± 0.006	76	1.0 [0.0]	11.6[10426]	(8463 [i])	2420	$64._4 \pm 6._6$
aR-BPA-20	29.7 ± 0.2	0.460 ± 0.002	1.229 ± 0.004	67	4.0 [0.2]	12.1 [1360]	(1080 [i])	536	$79._6 \pm 5._1$
aR-BPA-25	26.3 ± 0.3	0.567 ± 0.005	1.232 ± 0.005	54	49 [0.2]	22.1 [78]	(53 [i])	49.5	$44._6 \pm 1._3$
aR-DHB-xx (*n*=2; *r*=1)									
aR-DHB-15	17.2 ± 0.8 [g]	0.243 ± 0.009	1.297 ± 0.008	81	0.09	[j] [148631]	(18587 [i])	[k]	[l]
aR-DHB-20	17.5 ± 0.2	0.309 ± 0.003	1.349 ± 0.009	77	0.5	[j] [19960]	(13917 [i])	[k]	[l]
aR-DHB-25	18.5 ± 0.4	0.432 ± 0.007	1.315 ± 0.003	70	1.0	[j] [6217]	(4559 [i])	2280	[l]

[a] Average of 5 samples. [b] Shrinkage = 100 × (mold diameter – sample diameter)/(mold diameter). [c] Single sample, average of 50 measurements. [d] First number indicates the BET surface area, the number in the square bracket indicates the micropore area given by t-plot. [e] By the $4 \times V_{Total}/\sigma$ method. For the first value, V_{Total} was calculated by the single-point adsorption method; for the value in brackets, (referred to as Φ), V_{Total} was calculated via $V_{Total} = (1/\rho_b)-(1/\rho_s)$. [f] Particle radius from gas sorption = $3/\rho_s\sigma$. [g] Samples whose degree of crystallinity, *cr%*, was determined with powder XRD; (sample, *cr%*): **aR-POL-10**, 42; **aR-HPE-10**, 35; **aR-RES-10**, 33; **aR-SDP-10**, 54; **aR-BPA-10**, 36; **aR-DHB-15**, 37. [h] From the BJH plots: the first number is the peak maximum; numbers in brackets are the widths at half maxima of the BJH plots. [i] In parentheses, maxima of pore distribution curves from Hg-intrusion porosimetry. [j] Non-reliable isotherms at high partial pressures. [k] Not reliable owing to small BET surface area. [l] Not tested. [m] From Table S.5.

Table 3. General materials characterization data for **aL-ALC-25**

sample	linear shrinkage (%) [a,b]	bulk density, ρ_b (g cm^{-3}) [a]	skeletal density, ρ_s (g cm^{-3}) [c]	Π (%)	BET surface area, σ (m^2 g^{-1})	average pore diameter (nm) [e]	pore diameter [f]	particle radius (nm) [g]	R(1) from SAXS (nm) [j]
aL-POL-25 [h]	30.5 ± 1.2	0.652 ± 0.028	1.284 ± 0.010	49	57	32.9 [53.0]	72 nm	41.0	31.9±0.4
aL-HPE-25 [h]	26.9 ± 0.3	0.563 ± 0.004	1.243 ± 0.009	55	99	36.7 [39.3]	46 nm	24.4	27.3±0.3
aL-RES-25 [h]	38.4 ± 0.3	0.872 ± 0.008	1.206 ± 0.003	28	[d]	[d]	70 nm	[d]	61.$_6$±1.$_6$
aL-SDP-25 [h]	32.5 ± 0.2	0.639 ± 0.005	1.324 ± 0.006	52	28	66.5 [116]	64 nm	80.9	53.$_2$±2.$_3$
aL-BPA-25 [h]	-11.6 ± 2.4 [i]	0.160 ± 0.013	1.281 ± 0.015	88	54	53.7 [405]	80 nm	43.4	19.7±0.8
aL-DHB-25 [h]	23.6 ± 1.6	0.694 ± 0.004	1.063 ± 0.006	35	[d]	[d]	1.2 and 3.3 μm	[d]	[k]

[a] Average of 5 samples. [b] Shrinkage = 100 × (mold diameter – sample diameter)/(mold diameter). [c] Single sample, average of 50 measurements. [d] Albeit monolithic, those samples came from flocs and the isotherms show that the samples undergo changes during N_2-sorption analysis. [e] By the $4 \times V_{Total}/\sigma$ method. For the first number, V_{Total} was calculated by the single-point adsorption method; for the number in brackets, V_{Total} was calculated via $V_{Total} = (1/\rho_b)-(1/\rho_s)$. [f] Maxima of pore distribution curves from Hg-intrusion porosimetry. [g] Particle radius from gas sorption = $3/\rho_s\sigma$. [h] Degree of crystallinity, *cr%*; (sample, *cr%*): **aL-POL-25**, 39; **aL-HPE-25**, 45; **aL-RES-25**, 39; **aL-SDP-25**, 45; **aL-BPA-25**, 42; **aL-DHB-25**, 38.[i] Sample swells during SCF CO_2 drying. [j] From Table S.5. [k] Not tested.

Considering together: (a) the decrease of mesoporous space in **aR-POL-xx** and its increase with ρ_b in all other cases; and, (b) the invariance of the surface area in **aR-POL-xx** with ρ_b, and the increase of the surface area in all other **aR-ALC-xx** with ρ_b, suggests an invariance of the fundamental building blocks of **aR-POL-xx**, and a change (decrease) in the particle size as ρ_b increases in all other cases. Particle radii calculated using the radius=$3/(\rho_s\sigma)$ method (Tables 2 and 3) follow exactly those trends and thus seem to support this conjecture, however, radii calculated by this method and σ are not linearly independent, compromising the strength of this argument. Therefore, to assess particle sizes independently of porosity, we resorted to SEM and small angle x-ray scattering.

2.4.2b The skeletal framework. Complete SEM data for all samples are grouped together with the porosimetry data in Appendix IV of the Supporting Information. Figure 6 compares morphostructural features for **aR-** and **aL-**aerogels at the two extremes of high (ALC: **POL** and **HPE**) and low (ALC: **BPA** and **DHB**) *n* and *r* values. It is noted that at similar monomer molar concentrations in the sol, **aR-ALC-20** aerogels consist of discrete particles, whereas in most cases of **aL-ALC-25** aerogels skeletal nanoparticles are coated with and fused by polymer (cases of ALC: **POL**, **HPE** and **BPA**). In the same context, it is noted that **aL-DHB-25** consists of flake-like objects similar in appearance to some clay aerogels reported by Schiraldi.[27] It is reminded that the **aL-DHB-25** sol did not actually gel, but rather formed a grainy floc. In turn, Figure 7 shows representative SEMs of low and high density **aR-**aerogels at two different magnifications for the four highest *n* and *r* samples (for the remaining two samples see Appendix IV). Semi-quantitatively, the three major observations are: (a) as suggested based on the N_2-sorption data above, there is a clear tendency for the particle size in **aR-HPE-xx**, **aR-RES-xx** and

aR-SPD-xx to decrease as ρ_b increases; that trend is not as clear in **aR-POL-xx**; (b) samples whose isotherms reach saturation plateaus at high ρ_b (i.e., **aR-POL-25**, **aR-HPE-25** and **aR-RES-25** - see Figures 4 and S.14) consist of smaller particles that assemble into larger globules, which in turn form even higher aggregates; and, (c) despite their vast difference in size, elementary building blocks in the lowest density **aR-HPE-5** and **aR-SDP-10** aerogels seem to be arranged in strings of beads in the former and bundles of strings in the latter. Those fibrous arrangements are lost in the corresponding higher-density samples, which consist of globules of smaller particles. At high magnification though, we note that the string-of-beads-like structure of **aR-HPE-5** consists of secondary aggregates of the tiniest nanoparticles. The cause of the string-of-beads arrangement is probably electrostatic (as opposed to kinetic) similar to that noted for strings of certain inorganic nanoparticles;[28] evidence for this argument lies with the fact that while the size of the primary and secondary particles remains about the same, the structure switches back to globular clusters similar to those observed with higher-ρ_b samples as soon as the gelation solvent is changed from acetone to THF or DMF (see Figure S.13 in the Supporting Information). (Complete characterization of the **aR-HPE-5** samples synthesized in THF and DMF, in comparison to those prepared in acetone, is provided in Tables S.3 and S.4.)

Quantitatively, the make-up of the skeletal framework was probed with SAXS. Typical data for the scattering intensity, I, versus scattering vector, Q, are exemplified with several **aR-POL-xx** and the **aL-POL-25** aerogel in Figure S.22 of Appendix V of the Supporting Information. Data were analyzed with the Beaucage Unified Model[29,30] and results are summarized in Table S.5. At the high-Q range, all aerogels show a power

law region (marked as Region I in Figure S.22) with slope >4.0 signifying that the smallest (primary) skeletal particles have density-gradient (fuzzy) interfaces. At lower *Q*s, adjacent to Region I, all samples show a Guinier knee (Region II) that gives the radius of gyration, $R_G(1)$, of the primary particles.[31] The actual radius, $R(1)$, is related to $R_G(1)$ via $R_G(1)=0.77\times R(1)$. $R(1)$ values are included in Tables 2 and 3 for direct comparison with values obtained via the $3/\rho_s\sigma$ method. The smallest primary particles are observed in the **aR-POL-xx** aerogels ($R(1)$ in the 11-14 nm range). The next size up is observed with **aR-HPE-xx** ($R(1)$ in the 7-16 nm range) followed by **aR-RES-xx** (in the 22-56 nm range). It is also noted that in those three cases the $R(1)$ values match well with the radii of the smaller entities on the framework calculated from N_2-sorption data. The SAXS radii of **aR-SDP-xx** and **aR-BPA-xx** aerogels are larger than those of the previous three samples, yet much smaller (60-100 nm) than the radii calculated from the N_2-sorption data (up to 812 nm and 2.4 μm for **aR-SDP-xx** and **aR-BPA-xx**, respectively). (An analogous comparison with **aR-DHB-xx** was not attempted, because the particle radius by gas sorption was not reliable, owing to the extremely small surface areas.) It is also noted that the $R(1)$ values of **aR-POL-xx** do not vary with the sol concentration (i.e., with ρ_b), while in all other cases $R(1)$ decreases with increasing ρ_b. That is in agreement both with the SEM data of Figure 7, and with conclusions drawn from the variation of the mesoporous volume and the BET surface area with ρ_b. In one instance, (**aR-POL-5**) SAXS was also conducted on wet-gels (see Appendix V, Table S.5). The high-*Q* slope was found ≈4.00 signifying abrupt interfaces; the radius of the primary particles was found equal to 22 nm (versus 11 nm after drying), suggesting that primary particles in the wet-gel state are swollen with solvent; upon drying particles loose solvent and de-swell in

order to maximize non-covalent interactions among polymeric chains. As primary particles shrink, their surfaces curl-up and become rough, yielding a power-law slope for Region I >4.0. Since during processing, **aR-POL-5** wet-gels shrink *only* during SCF CO_2 drying, macroscopic shrinkage is thus directly linked to solvent-loss de-swelling of primary particles.

At even lower Qs, i.e., below the first Guinier knee, some samples show a second power-law region (Region III, exemplified with **aR-POL-5** in Figure S.22 of the Supporting Information), followed by a second Guinier knee (Region IV). For most samples though, the low-Q scattering profile flattens out into a plateau (e.g., **aR-POL-25** and **aL-POL-25** in Figure S.22) signifying that larger structural features fall outside the Q-range of our SAXS capability. Whenever observed, the slope of the second power-law Region III is generally ≥3.0 (Table S.5), indicating that primary particles form densely-packed surface fractal secondary particles. (The surface fractal dimensions, D_s, can be calculated via D_s=6-(high-Q slope).) The radii of the secondary particles (R(2), Table S.5) are calculated via $R_G(2)=0.77\times R(2)$, whereas the radii of gyration, R_G(2), are obtained from the second Guinier knees. Because gel-network forming particles are mass fractals (D_f<3.0 from rheology - Table 1), while primary particles assemble into surface fractals, it is concluded that the network is formed by higher aggregates of closed-packed secondary particles as illustrated in Scheme 4.

Scheme 4. The proposed structure of **PU** aerogels

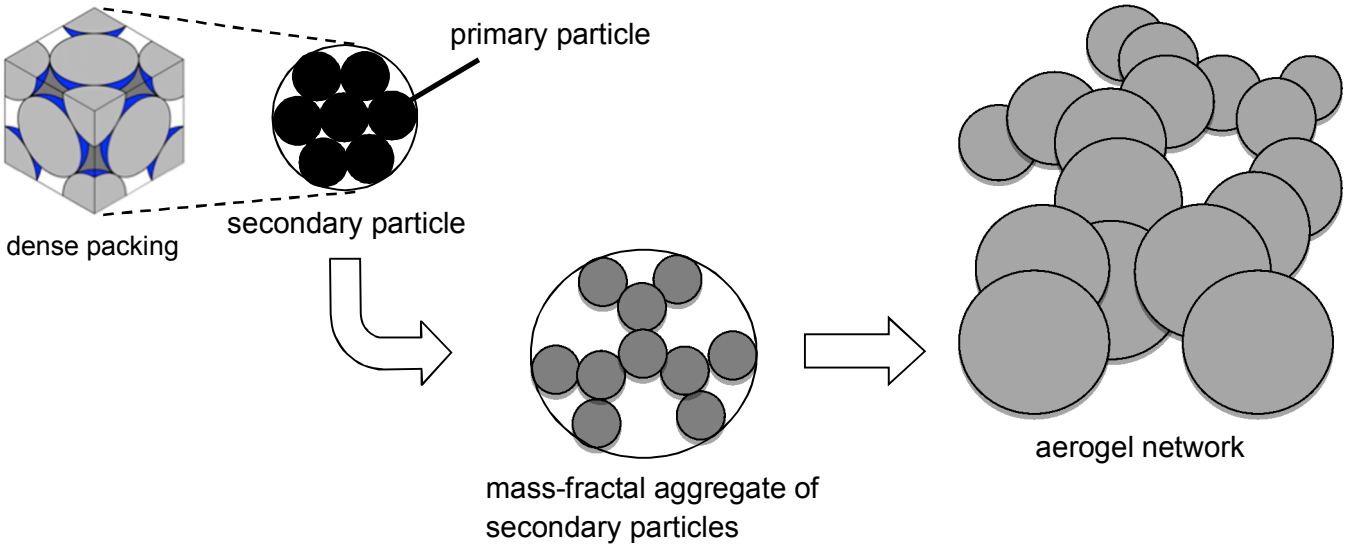

With high n and r (cases of ALC = **POL**, **HPE**, and **RES**, $n+r \geq 4$), putting together (a) the early loss of the ^{13}C NMR signal of the monomer; (b) the very small particle size in **aR-POL-xx**; (c) the reduction of $R(1)$ with increasing ρ_b in **aR-HPE-xx** and **aR-RES-xx**; and, (d) the general formation of surface rather than mass fractal secondary particles, we concluded that a fast reaction consumes all monomer long before the sol gels, yielding polymer of decreasing solubility with increasing $n+r$. The gelation process continues through primary particle aggregation into closely-packed secondary particles, followed by diffusion-limited aggregation of the larger secondary particles into larger mass-fractal aggomerates that meet the percolation threshold and the sol gels.

With lower n and r, (cases of ALC = **SDP**, **BPA** and **DHB**, $n+r=3$) the situation is markedly different: at lower densities (e.g., **aR-SPD-10**) skeletal building blocks are large and featureless (~1 μm in diameter - Figure 7), however SAXS shows that they still consist of smaller particles (~200 nm in diameter – Table 2). At higher densities (e.g., **aR-SDP-25**) particle sizes by SEM, N_2-sorption and SAXS converge. These data are consistent with small primary particles embedded in a medium of different density. This is supported by the increase in skeletal densities as ρ_b increases as noted in Section 2.4.1. In turn, that suggests that when $n+r$ is low, oligomers are more soluble, phase separation is delayed, particles are generally larger and start aggregating while a significant amount of monomer (or small oligomers) remain in solution. (In this context, it is reminded that in at least one occasion (**aR-SDP-25**) there is evidence for polymer gels – see Section 2.2.) Unreacted monomer binds to surface functional groups of aggregated particles, and new polymer (of somewhat higher density) accumulates and closes the interparticle pores; consequently, mesoporosity is lost, skeletal particles appear larger and smoother

by SEM, yet smaller particles are still "visible" by SAXS. That glazing effect is more prominent in **aL-POL-25** and **aL-HPE-25** (Figure 6), whereas apparently the interplay among the monomer concentration, oligomer solubility and reaction rate is fine-balanced to the point that skeletal particles are fused by, yet still clearly visible under a thin conformal polymer layer.

A final point in need of discussion in terms of the skeletal nanostructure is the origin of microporosity. According to Table 2, the percent of micropore surface area in **aR-POL-xx** is ~7.6-8.8%, somewhat higher in **aR-HPE-xx** (8.5-11.5%) and lower in **aR-RES-xx** (3.6-4.6%). Closely-packed primary particles leave an open accessible 25-36% v/v empty space (depending on whether the packing is orderly –cubic or hexagonal– or random).[32] The size of those voids depends on the size of the spheres and, for sufficiently small primary particles, can fall in the micropore range. However, **aR-POL-xx**, which posses the smallest primary particles, do not possess the largest micropore areas. Furthermore, although the particle size in **aR-HPE-xx** and **aR-RES-xx** decreases with increasing ρ_b, the percent micropore area does not increase. Thus, microporosity is not related to the empty space between closely-packed primary particles, but rather to an inherent property of the polymer itself (intrinsic microporosity),[33] which in turn can be attributed to the molecular rigidity of the monomers (**TIPM**, **POL**, **HPE** and **RES**).

2.4.3 Top-down characterization: the interparticle connectivity. In the previous section, **PU**aerogels were described as static assemblies, whereas individual nanoparticles have no knowledge of one another. However, desirable macroscopic properties such as low thermal conductivity and high mechanical strength depend on the nature of the interface between skeletal nanoparticles. Owing to lack of formal bottom-up

methods to probe interparticle connectivity (contact area and extent of interparticle bonding), the very macroscopic properties that render aerogels useful are utilized herewith in a top-down fashion in order to assess interparticle bonding and connectivity and correlate them to monomer structure.

2.4.3a Thermal Conductivity. Total thermal conductivities, λ, of **aR-ALC-xx** samples were calculated from their thermal diffusivities (R), heat capacities (c_P) and bulk densities (ρ_b), using Eq. 3.

$$\lambda = \rho_b \times c_P \times R \qquad (3)$$

Thermal diffusivities were measured using a heat-flash method (see Experimental).[34] Typical data are shown in Figure 8A. The time required by the detector voltage (proportional to temperature) to reach its half-maximum value (denoted as t_{50}) is used as the initial value for iterative fitting of the experimental data to the heat-transfer equation via the pulse-corrected Cowan model.[35,36] Results are summarized in Table 4.

In general, with increasing density, thermal conductivities first decrease, reach a minimum and then increase (Figure 8B). The lowest λ values (e.g., 0.031 W m^{-1} K^{-1} for **aR-POL-10** at 0.298 g cm^{-3}) compare favorably with values reported for glass wool (0.040 W m^{-1} K^{-1}) and Styrofoam (0.030 W m^{-1} K^{-1}),[34] as well as values found for other related aerogels, for example polyurea-crosslinked silica aerogels (0.041 W m^{-1} K^{-1} at 0.451 g cm^{-3}),[37] pure polyurea aerogels (0.034 W m^{-1} K^{-1} at 0.236 g cm^{-3}),[38] ROMP-derived polyimide aerogels (0.031 W m^{-1} K^{-1} at 0.338 g cm^{-3}),[39] and other polyurethane aerogels reported previously (0.027 W m^{-1} K^{-1} at 0.451 g cm^{-3}).[12] In the search for unifying trends we notice a weak correlation between λ and r, i.e., the number of functional groups per aromatic ring: e.g., for samples of analogous micromorphology and

about constant thermal diffusivity (0.111-0.113 $mm^2\ s^{-1}$, cases of **aR-POL-20**, **aR-HPE-20** and **aR-RES-20**), λ increases with increasing r: from 0.052 W m^{-1} K^{-1} for r=1 (**HPE**), to 0.059 W m^{-1} K^{-1} for r=2 (**RES**), to 0.074 W m^{-1} K^{-1} for r=3 (**POL**). That underlines the importance of heat conduction through the skeletal framework.

Assuming no coupling of the heat transfer modes in monolithic aerogels, λ can be considered as the sum of three contributors (Eq. 4):

$$\lambda = \lambda_g + \lambda_s + \lambda_{irr} \tag{4}$$

whereas λ_g is the non-convective thermal conductivity through the pore-filling gas, λ_s is the thermal conductivity through the solid framework and λ_{irr} is the radiative heat transfer. The latter was minimized experimentally (see Experimental), and the remaining portion was removed from the data digitally (see Figure 8A). The minima in Figure 8B occur because λ_s is expected to increase with ρ_b (all other things been equal – see below), while λ_g decreases with decreasing pore-size, which in turn decreases at higher densities.[40] Quantitatively, the relative contributions of λ_g and λ_s to the total λ can be assessed by calculating λ_g using Knudsen's equation (Eq. 5):[41]

$$\lambda_g = \frac{\lambda_{g,o}\Pi}{1+2\beta(l_g/\Phi)} \tag{5}$$

where $\lambda_{g,o}$ is the intrinsic conductivity of the pore-filling gas (for air at 300 K at 1 bar , $\lambda_{g,o}$=0.02619 W m^{-1} K^{-1}),[42] Π is the porosity in decimal notation (data from Table 2), β is a parameter that accounts for the energy transfer between the pore-filling gas and the aerogel walls (for air β=2), l_g is the mean free path of the gas molecules (for air at 1 bar pressure, $l_g \approx 70$ nm) and Φ is the pore diameter, calculated via the $4\times V_{Total}/\sigma$ method, (V_{Total}=(1/ρ_b)-(1/ρ_s)) (see Table 2). In this context, it is noted also that $\lambda_{g,o}$ is the upper

limit of λ_g for Π=1 and $\Phi \rightarrow \infty$; as ρ_b increases, both Π and Φ decrease, hence λ_g decreases from $\lambda_{g,o}$ monotonically. Therefore, at some point the solid framework becomes the main conductor of heat. Both λ_g and λ_s values are included in Table 4, and representative curves of λ, λ_g and λ_s as a function of the bulk density are exemplified with the **aR-HPE-xx** system in Figure 9A.

The variation of λ_s with ρ_b has been modeled via an exponential expression, Eq. 6.[40,43]

$$\lambda_s = C(\rho_b)^a \qquad (6)$$

Exponent α depends on how matter fills space. The pre-exponential factor *C* depends on the particle chemical composition and the interparticle coupling (neck area and extent of interparticle bonding). For foams, which are non-mass-fractal objects, α=1. For base-catalyzed silica aerogels α has been found equal to 1.5 (for bulk densities in the 0.070-0.230 g cm^{-3} range).[44] With base-catalyzed RF aerogels synthesized with low resorcinol:catalyst ratios (e.g., R/C~50; smaller particles) α=1.2; with high resorcinol:catalyst ratios (R/C~200; fewer, larger particles) α=1.5.[40] Recently, it was reported α=1 for fibrous polyurea aerogels.[38] On the other hand, regarding *C*, smaller RF particles (R/C~50) connected by more numerous and wider necks (by TEM) have a higher *C* value than that of RF aerogels with larger particles (R/C~200) connected by fewer, narrower necks (also by TEM).[40] Importantly, in the RF system the particle size is fixed with the R/C ratio, i.e., it does not vary with density.

Exponent α and coefficient *C* for the **aR-ALC-xx** aerogels were calculated from Log-Log plots (e.g., Figure 9B). Results are included in Table 4. In the case of **aR-POL-**

xx, whereas particle size and microstructure do not vary with ρ_b, α=1.41, i.e., close to the RF value for similar-size particles. On the other hand, exponent α for the other **aR-ALC-xx** varies from a negative value (-0.22, case of **aR-SDP-xx** aerogels) to an extremely positive value (3.06, case of **aR-BPA-xx**) probably in some cases reflecting the dramatic change of particle size and micromorphology as ρ_b varies. *C* values vary also widely, the highest (0.625 W m^{-1} K^{-1}) corresponding to **aR-BPA-xx** (although it is also noted that within that series of samples we have observed one of the lowest overall thermal conductivities: 0.031 W m^{-1} K^{-1}). Further interpretation of α and *C* needs to be deferred until the reliability of those values is cross-checked via a second, experimentally independent macroscopic property, the elastic modulus (see next Section), which also depends on similar microscopic parameters such as the network structure and the interparticle connectivity.[40,43]

Table 4. Thermal conductivity data of the **aR-ALC-xx** aerogels at 23 ^{o}C

sample	ρ_b (g cm^{-3})	c_p (J g^{-1} K^{-1})	R (mm^2 s^{-1})	λ (W m^{-1} K^{-1})	average pore diameter [a] Φ (nm)	λ_g [b] (W m^{-1} K^{-1})	λ_s [c] (W m^{-1} K^{-1})	a, C (W m^{-1} K^{-1})
aR-POL-xx								
aR-POL-5	0.159 ± 0.006	1.007 ± 0.016	0.319 ± 0.008	0.051±0.002	92.2	0.006	0.045	
aR-POL-10	0.298 ± 0.004	0.840 ± 0.038	0.125 ± 0.001	0.031±0.001	43.9	0.003	0.028	
aR-POL-15	0.477 ± 0.008	0.977 ± 0.019	0.102 ± 0.002	0.047±0.001	23.2	0.001	0.046	1.41, 0.14
aR-POL-20	0.640 ± 0.010	1.028 ± 0.037	0.113 ± 0.006	0.074±0.004	16.3	0.001	0.073	
aR-POL-25	0.760 ± 0.050	1.000 ± 0.032	0.136 ± 0.002	0.103±0.007	10.1	0.0004	0.103	
aR-HPE-xx								
aR-HPE-5	0.094 ± 0.004	1.019 ± 0.019	0.424 ± 0.018	0.041 ± 0.002	297.7	0.012	0.029	
aR-HPE-10	0.184 ± 0.007	0.997 ± 0.017	0.221 ± 0.018	0.040 ± 0.003	112.4	0.006	0.034	
aR-HPE-15	0.315 ± 0.003	1.022 ± 0.026	0.136 ± 0.011	0.044 ± 0.003	54.7	0.003	0.041	0.43, 0.074
aR-HPE-20	0.426 ± 0.008	1.009 ± 0.079	0.112 ± 0.002	0.052 ± 0.003	32.6	0.002	0.05	
aR-HPE-25	0.567 ± 0.002	0.932 ± 0.037	0.128 ± 0.001	0.067 ± 0.002	16.5	0.001	0.066	
aR-RES-xx								
aR-RES-10	0.244 ± 0.005	0.616 ± 0.047			404			
aR-RES-15	0.404 ± 0.001	0.926 ± 0.038	0.114 ± 0.009	0.042 ± 0.003	82.1	0.004	0.038	
aR-RES-20	0.565 ± 0.004	0.955 ± 0.012	0.111 ± 0.001	0.059 ± 0.001	37.1	0.002	0.057	1.18, 0.11
aR-RES-25	0.680 ± 0.003	0.901 ± 0.041	0.117 ± 0.002	0.071 ± 0.003	23.9	0.001	0.07	

aR-SDP-xx								
aR-SDP-10	0.190 ± 0.005	0.954 ± 0.035	0.487 ± 0.013	0.088 ± 0.004	6436	0.022	0.066	
aR-SDP-15	0.307 ± 0.007	1.009 ± 0.015	0.262 ± 0.013	0.081 ± 0.004	2499	0.018	0.063	-0.22, 0.047
aR-SDP-20	0.422 ± 0.003	0.849 ± 0.043	0.191 ± 0.008	0.068 ± 0.004	718	0.013	0.055	
aR-SDP-25	0.541 ± 0.004	0.943 ± 0.003	0.143 ± 0.003	0.072 ± 0.001	158	0.006	0.066	
aR-BPA-xx								
aR-BPA-10	0.194 ± 0.005	1.098 ± 0.021						
aR-BPA-15	0.293 ± 0.005	0.883 ± 0.025	0.127 ± 0.001	0.032 ± 0.001	10426	0.019	0.013	
aR-BPA-20	0.460 ± 0.002	1.053 ± 0.069	0.201 ± 0.006	0.097 ± 0.006	1459	0.015	0.082	3.06, 0.625
aR-BPA-25	0.567 ± 0.005	1.169 ± 0.009	0.134 ± 0.004	0.088 ± 0.002	78	0.002	0.086	
aR-DHB-xx								
aR-DHB-15	0.243 ± 0.009	0.949 ± 0.065	0.396 ± 0.003	0.091 ± 0.006	148631	0.021	0.07	
aR-DHB-20	0.309 ± 0.003	0.807 ± 0.092	0.349 ± 0.015	0.087 ± 0.009	19960	0.020	0.067	
aR-DHB-25	0.432 ± 0.007	0.849 ± 0.028	0.243 ± 0.009	0.089 ± 0.004	6558	0.018	0.071	

[a] Via the $4\times V_{Total}/\sigma$ method using $V_{Total}=(1/\rho_b)-(1/\rho_s)$; from Table 2. [b] From Knudsen's equation. [c] From $\lambda_s=\lambda-\lambda_g$.

2.4.3b Mechanical properties. The **PU** aerogels of this study show an extremely diverse response to mechanical stress. Qualitatively, most aerogels with **–xx** extensions -5, -10 or -15 show some sort of reversible compliance to stress, however **aR-HPE-5**, **aR-HPE-10**, and **aR-SPD-10** are outright flexible (Figure 10A). Higher-density samples are extremely rigid. Stress-strain curves under compression, obtained either under quasi-static (low strain rates) or dynamic loading conditions (using the split Hopkinson pressure bar (SHPB) at UTD) show a short elastic range up to ~3% strain, followed by plastic deformation until ~40-60% strain, and then by densification and plastic hardening (Figure 10B), in analogy to other organic and polymer-crosslinked silica aerogels under similar conditions.[16,39,45,46] Overall, samples do not buckle during compression and expand laterally only during the hardening stage, presumably because most pores have been closed. The porosity at the end of the compression process is reduced down to the 18-36% v/v range (values by dynamic testing – **aR-ALC-25** samples). Mechanical properties of interest include the stiffness (quantified by the Young's modulus, *E*), the ultimate compressive strength at maximum strain (*UCS*), and the toughness (quantified by the specific energy absorption obtained by integration of the area under the stress-strain curves). Selected data are summarized comparatively for quasi-static and dynamic loading conditions in Table S.6. The complete data sets are shown in Tables S.7 and S.8.

aL-ALC-25 aerogels were tested only under quasi-static conditions. The relevant discussion concerns **aL-**samples based on **POL**, **HPE**, **SDP** and **BPA**. (Originating from flocs, **aL-RES-25** and **aL-DHB-25** were brittle and were not tested.) Although, sol-concentration-wise **aL-ALC-25** correspond to **aR-ALC-20**, a fair comparison should be based on equal densities. Referring to Table S.6, **aL-POL-25** corresponds to **aR-POL-**

20, **aL-HPE-25** and **aL-SDP-25** to **aR-HPE-25** and **aR-SDP25**, respectively. Owing to swelling, **aL-BPA-25** (ρ_b=0.160 g cm^{-3}) corresponds roughly to **aR-BPA-15** (ρ_b=0.293 g cm^{-3}). With the exception of the latter sample, **aL-**aerogels are about as stiff as their **aR-** counterparts, but they fail at ~10% higher strains, which generally translates into stronger and tougher materials (Table S.6). In turn, **aL-BPA-25** appears moderately stiff (E=49 MPa), but extremely strong (UCS=230 MPa) and tough (55 J g^{-1}) for its low density, competing favorably with the best **aR-** aerogels. It is noted that **aL-**samples show well-defined glass transitions (in the range 100-150 ^{o}C, see Figure S.26); **aR-** samples do not. Thus, in analogy to previous reasoning concerning the mechanical behavior of polyurea[16] and polyurea-crosslinked vanadia aerogels,[47] it is speculated that work done by compression on **aL-**samples is stored as thermal energy that causes local softening of the polymer and facilitates its "absorption" within its own porosity, effectively extending the useful strain range.

aR-ALC-xx aerogels appear stiffer (higher Young's moduli) under dynamic loading, consistent with the increase of the Young's modulus of polymers with increasing strain rate.[48,49] Surprisingly, however, in contrast to the typical behavior of porous materials under compression,[50] most **PU** aerogels show lower ultimate strength and specific energy absorption under dynamic loading than under quasi-static conditions. By inspection (Table S.6), that observation can be attributed to the fact that all other things being equal, samples fail at higher strains (often by >10%) under quasi-static conditions. In turn, that is related to the failure mode: under quasi-static compression samples shutter in fragments, while under dynamic loading they just develop cracks, only small portions peel-off their surfaces, and otherwise are held together (Figure S.24). It is speculated that

low strain-rates give the structure time to rearrange, and thus it can take higher loads and store more energy. In fact, most **PU** samples show a multiple of the specific energy absorption of Kevlar-49 epoxy and of armor-grade SiC (11 J g^{-1} at 1.04 g cm^{-3} and 20 J g^{-1} at 3.02 g cm^{-3}, respectively).[51] When **PU** samples fail at their maximum stains, the energy stored is released suddenly producing a loud, gun-shot-like sound (Movie S.1 in Supporting Information).

Figure 11 summarizes all *E*, *UCS* and specific energy absorption data for the **aR-** samples under quasi-static compression. (Qualitatively, similar data under dynamic loading conditions are shown in Figure S.25 of the Supporting Information.) It is noted that as the bulk density increases, the *UCS* and specific energy absorption converge, irrespective of the chemical identity of the ALC (Figures 11A and 11B). Beyond the point of convergence, *UCS* and energy absorption remain constant as can be seen clearly in the case of **aR-POL-xx** and **aR-HPE-xx**. Those findings signify that at sufficiently high densities (low porosities) both the *UCS* and specific energy absorption of nanostructured **PU** aerogels are controlled by the amount of material, not its chemical composition. By the same token, it is also noted that despite the convergence observed at high ρ_b, both *UCS* and specific energy absorption do start from very different values at lower densities. Hence, the slopes with which those properties converge are vastly different among **aR-**aerogels. This is not difficult to reconcile based on the skeletal microstructures identified and discussed in Section 2.4.2b: although at lower densities the structural morphology (and particle size) varies widely among different **aR-ALC-xx**, at higher densities all samples converge to more-or-less similar morphostructural networks

(for instance refer to **aR-SDP-xx** in Figure 7, or more dramatically to **aR-BPA-xx** in Figure S.17).

The most identifiable trend among the lower-density samples in Figures 11A and 11B is that trifunctional ALC yield materials with higher *UCS* and specific energy absorptions. This is not difficult to reconcile either, based on the fact that higher *n* introduces the energy of more chemical bonds per unit mass, hence the materials are more robust. However, it is also noted that the *UCS* and specific energy absorption are cumulative properties of the continuous structural evolution along compression, hence cannot be correlated with the interparticle connectivity in pristine samples. In that regard, it is more instructive to look into the Young's (elastic) modulus, *E*, which, like solid thermal conductivity, λ_s, depends on the skeletal interparticle connectivity of uncompressed samples.[40] According to the Log-Log plots of Figure 11C, all *E* vary exponentially with ρ_b according to Eq. 7:

$$E = A(\rho_b)^x \tag{7}$$

As with Eq 6, exponent *x* depends on how matter fills space. Data for **aR-ALC-xx** under quasi-static loading conditions are summarized in Table 5. (Whenever available, data under dynamic loading conditions are also included for comparison. The two sets agree with one another, as expected.) Typically, for base-catalyzed silica aerogels *x* has been found in the 3.2-3.8 range,[43,52] while for base-catalyzed RF aerogels at ~2.7 (and independent on particle size).[53] Here, in most **aR-ALC-xx** aerogels, *x* takes higher values than those reported for silica or RF aerogels. That, as in the case of the unusually high values of the exponent α in Eq. 6, probably reflects the change in particle size/nanomorphology with ρ_b, and is investigated further. In general α (Eq. 6) and *x* (Eq.

7) do not agree numerically, because of the "higher tensorial order of the elastic problem."[43] Nevertheless, as shown in Figure 12A, the two sets of data correlate linearly with one another. This finding underlines the common physical property controlling both α and x, i.e., how matter fills space. To our knowledge, such correlation has not been shown before, probably because of lack of a simultaneous availability of λ_s and E data for a wide array of related materials. Curiously, **aR-BPA-xx**, whose α and x exponents are both the highest among all others (again validating one another), comprises an exception in the sense that its (α,x) point does not correlate with the those from the other **aR-ALC-xx**.

Table 5. Young's modulus (E) sensitivity on the bulk density from compression testing

aerogel	Exponent x (Eq. 7) loading conditions	
	quasi-static	dynamic
aR-POL-xx	3.73 ± 0.35	4.00 ± 0.27
aR-HPE-xx	5.16 ± 1.13	4.74 ± 0.13
aR-RES-xx	3.49 ± 0.02	3.62 ± 0.02
aR-SDP-xx	6.57 ± 1.36	
aR-BPA-xx	7.75± 1.59	
aR-DHB-xx	4.25 ± 1.41	

Subsequently, we turn into how interconnectivity, expressed through parameter C (Eq. 6), actually controls the Young's modulus, and from that relationship we seek to understand how molecular structure relates to interconnectivity. The analysis focuses on those materials that participate in the linear correlation between α and x (Figure 12A), because that indicates a structural similarity (or more accurately, a similar structural evolution with density). In this context, Figure 12B shows the variation of E with C for three different **–xx** formulations, as indicated. Interestingly, it appears that the most important molecular parameter for increasing stiffness through improved interparticle

connectivity (i.e., higher *C*) is the functional group density of the monomer (*r*). Thus, despite that both **HPE** and **POL** have *n*=3, interconnectivity and stiffness of **aR-HPE-xx** are both much lower not only than those of **aR-POL-xx**, but also than those of **aR-RES-xx** (*n*=2) at all densities. Considering this together with the fact that particle sizes of **aR-POL-xx** and **aR-HPE-xx** are not very different, and certainly smaller than those in all other **PU** aerogels (including **aR-RES-xx** - Table 2), leads to the conclusion that *r* is important in terms of interconnectivity and stiffness, because it translates the functional group density of the monomer into the functional group density on the surface of the primary particles. In turn, this validates the most basic hypotheses of this study, namely the importance of multifunctional small molecule monomers for the synthesis of robust aerogels.

Finally, flexibility is a sought-after property for wrap-around thermal insulation in diverse applications from undersea oil pipes to space and planetary exploration.[54] In that regard, it is noteworthy that the interconnectivity (*C*) and stiffness (*E*) of the two kinds of flexible samples (**aR-HPE-xx** and **aR-SDP-xx** – see Figure 10A) are also overall the lowest numerically (see Figure 12B). Again, this is attributed to the functional group density on the surface of the particles. However, although a low *r*-value seems to be a necessary condition for flexibility, it is not a sufficient one: for example, although low-density **aR-BPA-10** and **aR-DHB-15** (for both *r*=1) are somewhat compliant to stress, they are nowhere nearly as flexible as **aR-HPE-5**, **aR-HPE-10**, or **aR-SDP-10**. As discussed in Section 2.4.2b, flexible **aR-HPE-5** and **aR-SDP-10** consist of nanostrings of beads, or bundles of strings, respectively. But again, strictly fibrous polyurea aerogels synthesized with **N3300A** (Scheme 1) and water are not even nearly as flexible as **aR-**

HPE-5 or **aR-SDP-10**.[16] It is speculated that the fiber aspect ratio (i.e., length_between_fiber_contacts : string-diameter) is also important.

3. Conclusion

Polyurethane aerogels based on two monomeric triisocyanates, one flexible aliphatic and one rigid aromatic, in combination with two aromatic triols and four diols have been prepared and their structure-property relationships have been examined. Molecular rigidity was correlated with primary particle size as well as with the presence of intrinsic microporosity in certain samples. A correlation was shown between the monomer structure and the properties of the resulting nanostructured network. It was found out that in general the primary particle size decreases with increasing concentration, leading to the conclusion that phase separation is rate-limited. Primary particles condense into densely-packed secondary particles that, owing to their size, assemble via a diffusion-limited cluster aggregation process into higher fractal agglomerates that form the gel. Macroscopically, samples range from flexible to extremely rigid. Reasoning that bulk behavior cannot be rationalized through a static description of the framework in which individual nanoparticles have no knowledge of one another, we used a top-down characterization approach, whereas we correlated solid thermal conduction with the elastic modulus. It was concluded that the controlling parameter of interparticle connectivity is the functional group density of the monomer. That parameter is expressed as functional group density at the surface of primary particles and controls the efficiency of interparticle bonding. Overall, the findings of this study comprise a blueprint for further materials design, while the properties of the

specific materials described herewith fit well into an extremely wide array of possible aerogel applications, ranging from robust thermal insulation, to acoustic insulation and ballistic protection.

4. Experimental

4.1 Materials. All reagents and solvents were used as received unless noted otherwise. Tris(4-isocyanatophenyl)methane (**TIPM**) and 1,3,5-tris(6-isocyanatohexyl)-1,3,5-triazinane-2,4,6-trione (**N3300A**) were donated generously by Bayer Corp. U.S.A. **TIPM** is supplied as a 27% w/w solution in anhydrous ethyl acetate (Desmodur RE). **N3300A** is supplied as a neat compound (Desmodur N3300A). Polyols (**ALC**; density): Resorcinol (**RES**; ρ_{RES}=1.270 g cm^{-3}), 1,1,1-tris(hydroxyphenyl)ethane (**HPE**; ρ_{HPE}=1.252 g cm^{-3}), phloroglucinol (**POL**; ρ_{POL}=1.488 g cm^{-3}), 4,4′-sulfonyldiphenol **(SDP**; ρ_{SDP}=1.432 g cm^{-3}) and 4,4′-dihydroxy benzophenone (**DHB**; ρ_{BHB}=1.302 g cm^{-3}) were purchased from Aldrich Chemical Co. U.S.A.; 4,4′-isopropylidenediphenol (**BPA**; ρ_{BPA}=1.195 g cm^{-3}), anhydrous acetone, dimethylformamide (DMF), dibutyltin dilaurate (DBTDL), tetrahydrofuran (THF) and HPLC grade acetone were purchased from Acros Chemicals, U.S.A. Deuterated chloroform ($CDCl_3$), dimethylsulfoxide (DMSO-d_6) and acetone (acetone-d_6) were obtained from Cambridge Isotope Laboratories, Inc.

4.2 Preparation of polyurethane (PU) aerogels

*4.2.1 Synthesis of **PU** aerogels from **TIPM (aR-ALC-xx)**.* All formulations and gelation times are summarized in Table S.1 of Appendix I in the Supporting Information. Samples are referred to as **aR-ALC-xx**, whereas **aR-** stands for aRomatic **TIPM**, **ALC-** is the abbreviation used for the alcohol (see Scheme 1) and **–xx** refers to the solids %

w/w content (**TIPM**+alcohol) in the sol. Typically, "**xx**" was varied from 5 to 25. For this, a solution of **TIPM** as received (Desmodur RE, 1.33 mL, containing 0.367 g (1.00 mmol) of **TIPM**), and the respective polyol in a 1.0:1.0 mol ratio to **TIPM** for trifunctional alcohols (**POL** and **HPE**), or in a 1.5:1.0 mol ratio for difunctional alcohols (**RES**, **SDP**, **BPA** and **DHB**) in variable amounts of anhydrous acetone (depending on the desirable percent weight of solids, **–xx**, in the sol; see Table S.1) was stirred for 10 min in a three-neck round-bottom flask at 23 ^{o}C under N_2. At that point, DBTDL (5 μL) was added, and the resulting sol was stirred for 5 min. Subsequently, the sol was poured into polypropylene molds (Polypropylene Scintillation Vials, General Purpose, 6.5 mL, Sigma-Aldrich Catalogue No. Z376825, 1.27 cm inner diameter), which were sealed with their caps, wrapped with Parafilm^{TM} and kept at room temperature for 12-16 h for gelation and aging. The gelation temperature and catalyst amount were selected based on a low-concentration sol, **aR-POL-5**, as the model system, using three different amounts of DBTDL at two different temperatures (refer to Table 6). The phenomenological gel-point was observed visually by inverting the molds. To accommodate both reasonably fast, and practically long gelation times for low- and high-concentration sols, respectively, we opted for room temperature gelation using the 119 **TIPM**:DBTDL mol:mol catalyst ratio. (The latter translates into 5 μL of DBTDL into 1.00 mmol of **TIPM**, as mentioned above.)

Table 6. Phenomenological gelation time of **aR-POL-5** with different catalyst amounts at two different temperatures

TIPM:DBTDL	Gelation time	
(mol/mol)	@ 23 ^{o}C	@ 60 ^{o}C
588	no gelation	no gelation
119	3 h	30 - 40 min
59	1 h 30 min	15 - 20 min

After aging, gels were removed from the molds, washed with acetone (6×, using 4× the volume of the gel) and dried in an autoclave with CO_2 taken out as a supercritical fluid (SCF).

*4.2.2 Synthesis of **PU** aerogels from **N3300A (aL-ALC-25)**.* All formulations and gelation times are summarized in Table S.2 of Appendix I in the Supporting Information. Low solid concentration sols (5% and 10% w/w) did not gel with any alcohol either at room or elevated temperatures, yielding at best viscous solutions. Thus, we opted for higher solids concentrations, and we report on **aL-ALC-25** aerogels samples, whereas **aL-** stands for aLiphatic **N3300A** and **-25** designates 25% w/w monomer (**N3300A**+alcohol) in the sol. The molar concentration of **N3300A** in those sols corresponds approximately to that of **TIPM** in the 20% w/w **aR-ALC-20** samples (compare data in Tables S.1 and S.2). In a typical process, **N3300A** as received (Desmodur N3300A, 0.504 g, 1.00 mmol), and the respective polyol (e.g., 1.00 mmol of **HPE,** or **POL**; or, 1.50 mmol for **RES**, **SDP**, **BPA** and **DHB**) were dissolved in the correct amount of anhydrous acetone (see Table S.2). The solution was stirred in a three-neck round-bottom flask at 23 ^{o}C under N_2 for 10 min and DBTDL (5 μL) was added. The resulting sol was stirred for another 20 min, and was poured into polypropylene molds as above, which were sealed and kept at room temperature. The gelation time

varied from 1 h 20 min to 5 h 30 min depending on the chemical identity of the polyol. All **aL-ALC-25** gels were aged for 24 h in their molds at room temperature, observing significant shrinkage (syneresis). After aging, gels were removed from the molds, washed with acetone (6×, using 4× the volume of the gel) and dried with CO_2 taken out as a supercritical fluid (SCF). It is noted that even under those conditions, **aL-RES-25** and **aL-DHB-25** did not actually gel, but rather formed loose precipitates (flocs). Since those precipitates hold themselves together, they were processed and analyzed as regular aerogels.

4.3 Methods.

The sol-gel transition: The rheological behavior of selected **PU** sols was recorded with a TA Instruments AR 2000ex Rheometer employing an aluminum cone (60 mm diameter, 2^o angle) and a Peltier plate using a 1 mm gap, at 20 ^oC. The instrument was operated in the continuous oscillation mode and time-sweep experiments were performed with fixed-strain amplitude. The gel-point was determined using a dynamic multiwave method with four superimposed harmonics (1, 2, 4, and 8 rad s^{-1}). The strain of the fundamental oscillation (1 rad s^{-1}) was set at 5%.

SCF drying: Drying with supercritical fluid (SCF) CO_2 was carried out in an autoclave (Spe-ed SFE system, Applied Separations, Allentown, PA).

Physical Characterization: Bulk densities, ρ_b, were calculated from the sample weight and dimensions. Skeletal densities, ρ_s, were determined with helium pycnometry using a Micromeritics AccuPyc II 1340 instrument.

Chemical Characterization: IR spectra were obtained in KBr pellets with a Nicolet-FTIR Model 750 Spectrometer. Liquid ^1H and ^{13}C NMR was recorded with a 400

MHz Varian Unity Inova NMR instrument (100 MHz carbon frequency). Solid-state ^{13}C NMR spectra were obtained with samples ground into fine powders on a Brucker Avance 300 Spectrometer with a 75.475 MHz carbon frequency using magic angle spinning (at 7 kHz) with broadband proton suppression and the CPMAS-TOSS pulse sequence for spin sideband suppression. Solid-state ^{15}N NMR spectra were obtained on a Bruker Avance 400 Spectrometer with a 40.557 MHz nitrogen frequency using magic angle spinning (at 5 kHz). All other conditions were similar to those used for solid-state ^{13}C NMR.

Structural Characterization: The pore structure was probed with N_2 sorption porosimetry at 77 K using a Micromeritics ASAP 2020 Surface Area and Porosity Analyzer. Data were converted and are reported under standard conditions of temperature and pressure (STP). In preparation for surface area analysis and skeletal density determination, **aR-ALC-xx** and **aL-ALC-25** samples were outgassed for 24 h under vacuum at 80 ^oC and 40 ^oC, respectively. Pore size distributions were determined with the Barret-Joyner-Halenda (BJH) equation applied to the desorption branch of the N_2-sorption isotherm.[55a] Micropore surface areas were calculated via t-plot analysis using the Harkins and Jura Model.[55b] Average pore diameters were determined by the $4\times V_{Total}/\sigma$ method, where V_{Total} is the total pore volume per gram of sample and σ, the surface area determined by the Brunauer-Emmett-Teller (BET) method from the N_2 adsorption isotherm. The value of V_{Total} can be calculated either from the single highest volume of N_2 adsorbed along the adsorption isotherm (at $P/P_o \sim 1$), or via $V_{Total} = (1/\rho_b) - (1/\rho_s)$. Average pore diameter values, calculated with V_{Total} by both methods, are cited herewith; the two values converge for mostly mesoporous materials. If the average pore diameter calculated using $V_{Total} = (1/\rho_b) - (1/\rho_s)$ is significantly higher, it is taken as evidence for

macroporosity, and the pore structure was further investigated with Hg-intrusion porosimetry (whenever feasible) using a Micromeritics AutoPore IV 9500 instrument.

The structural morphology of **PU** aerogels was determined with scanning electron microscopy (SEM) using Au-coated samples on a Hitachi S-4700 field emission microscope.

The degree of crystallinity of the samples, $cr_{\%}$, was determined with powder x-ray diffraction on a PANalytical X'Pert Pro Multipurpose Diffractometer (MPD) using Cu Kα radiation ($\lambda_{Cu\_K\alpha}$=1.54 Å). The fundamental building blocks of the skeletal framework was probed with small-angle X-ray scattering (SAXS) using 2-3 mm-thick disks, 0.7-1.0 mm in diameter. SAXS was carried out with the PANalytical X'Pert Pro MPD, configured for SAXS with a 1/32^o SAXS slit and a 1/16^o anti-scatter slit on the incident beam side, and a Ni 0.125 mm automatic beam attenuator and a 0.1 mm anti-scatter slit on the scattered beam side. Samples were placed in circular holders between thin Mylar^{TM} sheets and scattering intensities were measured with a point detector in transmission geometry by 2 Theta (2θ) scans ranging from -0.1 up to 5^o. All scattering data are reported in arbitrary units as a function of Q ($=4\pi\sin\theta/\lambda_{Cu\_K\alpha}$), the momentum transferred during a scattering event. Scattering intensity versus Q data were fitted to the Beaucage Unified Model[29,30] using the *Irena SAS* tool for modeling and analysis of small angle scattering,[56] within the commercial *Igor Pro* application (scientific graphing, image processing, and data analysis software from WaveMetrics, Portland, OR).

Mechanical Characterization: Quasi-static compression testing was performed according to the ASTM D1621-04a (Standard Test Method for Compressive Properties of Rigid Cellular Plastics) on cylindrical specimens using a Instron 4469 universal testing

machine frame, following the testing procedures and specimen length (2.0 cm) to diameter (1.0 cm) ratio specified in the ASTM standard. The recorded force as a function of displacement (machine-compliance corrected) was converted to stress as a function of strain. Compression experiments at high strain rates (969-1,491 s^{-1}) were conducted on a long split-Hopkinson pressure bar (SHPB) under ambient conditions at room temperature. The SHPB consists of 304 L stainless steel striker bar, a 304 L stainless steel incident bar (8.810 mm length, 19 mm outer diameter), a solid 7075-T651 aluminum transmission bar (3660 mm long, 19 mm in diameter), and a strain data acquisition system. Disk-shaped **PU** samples (5-7 mm thick, 9.6-10 mm in diameter) were sandwiched between the incident and transmission bars. The use of an aluminum transmission bar took advantage of the low Young's modulus of aluminum (~1/3 of steel) in order to reach high signal-to-noise ratios for the weak transmitted signal through aerogels.[3,57,58] and attain similar functions to those accessible with hollow transmission steel tubes.[46c,47b,48,59] A Cu disk pulse shaper (1.6 mm thick, 7.4 mm in diameter) was used to reach a dynamic stress equilibrium state and constant strain rates, which is necessary for a valid SHPB experiment.[60a] The working principle of SHPB has been well documented in literature, including formulas for the stress, strain and strain rate for a valid experiment.[60]

Thermal Characterization: Thermogravimetric analysis (TGA) was conducted with a TA Instrument, model Q50, under air or N_2 at a heating rate of 10 $^oC\ min^{-1}$. Glass transition temperatures (T_g) of **aL-ALC-25** samples and heat capacities (c_P) of all samples were determined with a TA Instruments Modulated Differential Scanning Calorimeter (MDSC) Model Q2000 instrument calibrated with a sapphire standard. For

T_g determination, samples were subjected sequentially to a first heating scan, one cooling scan and a second heating scan from 0 °C to 170 °C at 10 °C min^{-1}. T_gs were determined from the second heating scan. For heat capacities at 23 °C we used powders (4-8 mg), and the MDSC instrument was run from 0 °C to 40 °C at 0.5 °C min^{-1} in the modulated T4P mode. Raw c_P data were multiplied by a calibration factor equal to 1.10 determined from heat capacity measurements and comparison with literature data for rutile, graphite and corundum, just before running our samples.

Thermal conductivities, λ, were determined via $\lambda=\rho_b\times c_P\times R$, whereas the thermal diffusivity, R, was measured with a Netzsch NanoFlash Model LFA 447 flash diffusivity instrument using disk samples ~1 cm in diameter, 1.8-2.5 mm thick.[34a] Samples were first sputter-coated with gold and then spray-coated with carbon on both faces to minimize radiative heat transfer and ensure complete absorption of the heat pulse.[34b] Samples were heated with a heat pulse from one side and the temperature rise was observed as a function of time on the other. Subsequently, data were fitted with the pulse-corrected Cowan model to approximate the heat-transfer equation, using an initial value for the thermal diffusivity estimated from the time it takes the detector voltage (proportional to the temperature) to reach its half-maximum value (denoted as t_{50}).[35,36]

Supporting Information Available. Appendix I: Formulations of all PU aerogels (Tables S.1 and S.2); Appendix II: Solid-state NMR data for **aR-ALC-xx** and **aL-ALC-25** aerogel samples (Figures S.1-S.9); Appendix III: X-Ray diffraction data for selected **aR-ALC-xx** and **aL-ALC-25** aerogel samples (Figure S.10); Appendix IV: SEM, N_2-sorption and Hg-intrusion porosimetry data for all **PU** aerogels (Figures S.11-S.21, Tables S.3 and S.4); Appendix V: SAXS data (case of **aR-POL-xx**: Figure S.22,

cumulative data: Table S.5); Appendix VI: Mechanical characterization data under compression (Tables S.6-S.8, and Figures S.23-S.25); Appendix VII: Representative modulated differential scanning calorimetry (MDSC) data for selected **aL-ALC-xx** (Figure S.26). Appendix VIII: Compression video (Movie S.1). This information is available free of charge via the Internet at http://pubs.acs.org.

Acknowledgements. This project was supported by the Army Research Office under Award No. W911NF-10-1-0476. Initial funding was provided by the National Science Foundation under Agreement No.s CHE-0809562, DMR-0907291, CMMI-1031829, CMMI-1132174 and ECCS-1307997. We also thank the Bayer Corporation U.S.A for the generous supply of Desmodur RE and Desmodur N3300A, the Materials Research Center of MS&T for support with materials characterization and Dr. Wei Wycoff of the University of Missouri Columbia for her assistance with solid state NMR.

5. References

1. Pierre, A. C.; Pajonk, G. M. *Chem. Rev.* **2002**, *102*, 4243-4265.

2. See for example: Nakanishi, K.; Tanaka, N. *Acc. Chem. Res.* **2007**, *40*, 863-873.

3. Chidambareswarapattar, C.; Loebs, J. M.; Larimore, Z.; Dharani, L.; Luo, H.; Lu, H.; Sotiriou-Leventis, C.; Leventis, N. *MRS Proceedings* **2012**, *1403*, 35-40.

4. Bayer, O. *Angew. Chem.* **1947**, A59, 257-272.

5. Saunders, J. H.; Frisch, K. C. *Polyurethane Chemistry and Technology I. Chemistry*, Interscience Publishers, New York, N.Y. 1962.

6. Jarfelt, U.; Ramnäs, O. "Thermal conductivity of polyurethane foam - best performance," *In 10th International Symposium on District Heating and Cooling* **2006**, pp. 1-11.

7. Biesmans, G.; Randall, D.; Francais, E.; Perrut, M. *J. Non-Cryst. Solids* **1998**, *225*, 36-40.

8. Biesmans, G.; Mertens, A.; Duffours, L.; Woignier, T.; Phalippou, J. *J. Non-Cryst. Solids* **1998**, *225*, 64-68.

9. Tan, C.; Fung, B. M.; Newman, J. K.; Vu, C. *Adv. Mater.* **2001**, *13*, 644-646.

10. Yim, T. J.; Kim, S. Y.; Yoo, K. P. *Korean J. Chem. Eng.* **2002**, *19*, 159-166.

11. Rigacci, A.; Marechal, J. C.; Repoux, M.; Moreno, M.; Achard, P. *J. Non-Cryst. Solids* **2004**, *350*, 372-378.

12. Lee, J. K.; Gould, G. L.; Rhine, W. *J. Sol-Gel Sci Technol* **2009**, *49*, 209-220.

13. Gao, C.; Yan, D. *Prog. Polym. Sci.* **2004**, *29*, 183-275.

14. Schauerte, K.; Dahm, M.; Diller, W.; Uhlig, K. "Raw Materials." In *Polyurethane Handbook;* Oertel, G. Ed.; Hanser Publisher: New York, N.Y., 1985, pp 42-116.

15. Britain, J. W.; Gemeinhardt, P. G. *J. Appl. Polym. Sci.* **1960**, *4*, 207-211.

16. Leventis, N.; Sotiriou-Leventis, C.; Chandrasekaran, N.; Mulik, S.; Larimore, Z. J.; Lu, H.; Churu, G.; Mang, J. T. *Chem. Mater.* **2010**, *22*, 6692-6710.

17. Winter, H. H. *Polym. Eng. Sci.* **1987**, *27*, 1698-1702.

18. Kim, S.-Y.; Choi, D.-G.; Yang, S.-M. *Korean J. Chem. Eng*. **2002**, *19*, 190-196.

19. Raghavan, S. R.; Chen, L. A. ; McDowell, C.; Khan, S. A., Hwang, R.; White, S. *Polymer* **1996**, *37*, 5869-5875.

20. Muthukumar, M. *Macromolecules* **1989**, *22*, 4656-4658.

21. Kolb, M.; Botet, R.; Jullien, R. *Phys. Rev. Lett.* **1983**, *51*, 1123-1126.

22. McCarthy, S. J.; Meijs, G. F.; Mitchell, N.; Gunatillake, P. A.; Heath, G.; Brandwood, A.; Schindhelm, K. *Biomaterials* **1997**, *18*, 1387-1409.

23. Saito, Y.; Nansai, S.; Kinoshita, S. *Polym. J.* **1972**, *3*, 113-121.

24. Iyer, R. V.; Sooryanarayana, K.; Guru Row, T. N.; Vijayan, K. *J. Mater. Sci.* **2003**, *38*, 133-139.

25. Feng, W.; Sun, E.; Fujii, A.; Wu, A.; Nihara, K.; Yoshino, K. *Bull. Chem. Soc. Jpn.* **2000**, *73*, 2627-2633.

26. Trovati, G.; Sanches, E. A.; Neto, S. C.; Mascarenhas, Y. P.; Chierice, G. O. *J. Appl. Polym. Sci.* **2010**, *115*, 263-268.

27. (a) Bandi, S.; Bell, M.; Schiraldi, D. A. *Macromolecules* **2005**, *38*, 9216-9220. (b) Hostler, S. R.; Abramson, A. R.; Gawryla, M. D.; Bandi, S. A.; Schiraldi, D. A. *Int. J. Heat Mass Transfer* **2009**, 52, 665-669.

28. (a) Zhang, H.; Wang, D. *Angew. Chem. Int. Ed.* **2008**, *47*, 3984-3987. (b) Landfester, K. *Annu. Rev. Mater. Res.* **2006**, *36*, 231-279. (c) Taden, A.; Landfester, K.; Antonietti, M. *Langmuir* **2004**, *20*, 957-961.

29. Beaucage, G. *J. Appl. Cryst*. **1995**, *28*, 717-728.

30. Beaucage, G. *J. Appl. Cryst*. **1996**, *29*, 134-146.

31. Guinier, A.; Fournet, G. *Small-Angle Scattering of X-Rays*, John Wiley and Sons: New York, N.Y., 1955.

32. (a) Feder, J. *Fractals*, Plenum Press, New York, 1988; (b) Lee, D. G.; Bonner, J. S.; Garton, L. S.; Ernest, A. N. S.; Autenrieth, R. L. *Water Res.* **2000**, *34*, 1987–2000.

33. (a) McKeown, N. B.; Budd, P. M.; Msayib, K. J.; Ghanem, B. S.; Kingston, H. J.; Tattershall, C. E.; Makhseed, S.; Reynolds, K. J.; Fritsch, D. *Chem. Eur. J.* **2005**, *11*, 2610-2620. (b) Mckeown, N. B.; Budd, P. M. *Macromolecules* **2010**, *43*, 5163-5176. (c) Jiang, S.; Jones, J. T. A.; Hasell, T.; Blythe, C. E.; Adams, D. J.; Trewin, A.; Cooper, A. I. *Nature Commun.* **2011**, *2:207*, doi: 10.1038/ncomms1207.

34. (a) Parker, W. J.; Jenkins, R. J.; Butler, C. P.; Abbott, G. L. *J. Appl. Phys.* **1961**, *32*, 1679-1684. (b) Lee, D.; Stevens, P. C.; Zeng, S. Q.; Hunt, A. J. *J. Non-Cryst. Solids* **1995**, *186*, 285-290.

35. Cowan, R. D. *J. Appl. Phys.* **1961**, *32*, 1363-1369.

36. Cowan, R. D. *J. Appl. Phys.* **1963**, *34*, 926-927.

37. Katti, A.; Shimpi, N.; Roy, S.; Lu, H.; Fabrizio, E. F.; Dass, A.; Capadona, L. A.; Leventis, N. *Chem. Mater.* **2006**, *18*, 285-296.

38. Weigold, L.; Mohite, D. P.; Mahadik-Khanolkar, S.; Leventis, N.; Reichenauer, G. *J. Non-Cryst. Solids* **2013**, *368*, 105-111.

39. Leventis, N.; Sotiriou-Leventis, C.; Mohite, D. P.; Larimore, Z. J.; Mang, J. T.; Churu, G.; Lu, H. *Chem. Mater.* **2011**, *23*, 2250-2261.

40. Lu, X.; Caps, R.; Fricke, J.; Alviso, C. T.; Pekala, R. W. *J. Non-Cryst. Solids*, **1995**, *188*, 226-234.

41. (a) Lu, X.; Arduini-Schuster, M. C.; Kuhn, J.; Nilsson, O.; Fricke, J.; Pekala, R. W. *Science* **1992**, *255*, 971-972. (b) Reichenauer, G.; Heinemann, U.; Ebert, H.-P. *Colloids Surf. A* **2007**, **300**, 204-210.

42. Stephan, K.; Laesecke, A. *J. Phys. Chem. Ref. Data* **1985**, *14*, 227-234.

43. Lu, X.; Nilsson, O.; Fricke, J.; Pekala, R. W. *J. Appl. Phys.* **1993**, *73*, 581-584.

44. Fricke, J.; Lu, X.; Wang, P.; Büttner, D.; Heinemann, U. *Int. J. Heat Mass Transfer* **1992**, *35*, 2305-2309.

45. (a) Chidambareswarapattar, C.; Larimore, Z.; Sotiriou-Leventis, C.; Mang, J. T.; Leventis, N. *J. Mater. Chem.* **2010**, *20*, 9666-9678. (b) Leventis, N.; Chidambareswarapattar, C.; Mohite, D. P.; Larimore, Z. J.; Lu, H.; Sotiriou-Leventis, C. *J. Mater. Chem.* **2011**, *21*, 11981-11986.

(c) Sadekar, A. G.; Mahadik, S. S.; Bang, A. N.; Larimore, Z. J.; Wisner, C. A.; Bertino, M. F.; Kalkan, A. K.; Mang, J. T.; Sotiriou-Leventis, C.; Leventis, N. *Chem. Mater.* **2012**, *24*, 26-47.

46. (a) Leventis, N. *Acc. Chem. Res*. **2007**, *40*, 874-884. (b) Leventis, N.; Lu, H. "Polymer-Crosslinked Aerogels." In *Aerogels Handbook*; Aegerter, M. A.; Leventis, N.; Koebel, M. M. Eds.; Springer: New York, N.Y., 2011, Chapter 13, pp 251-285. (c) Lu, H.; Luo, H.; Leventis, N. "Mechanical Characterization of Aerogels." In *Aerogels Handbook*; Aegerter, M. A.; Leventis, N.; Koebel, M. M. Eds.; Springer: New York, N.Y., 2011, Chapter 22, pp 499-535.

47. (a) Leventis, N.; Sotiriou-Leventis, C.; Mulik, S.; Dass, A.; Schnobrich, J.; Hobbs, A.; Fabrizio, E. F.; Luo, H.; Churu, G.; Zhang, Y.; Lu, H. *J. Mater. Chem.* **2008**, *18*, 2475-2482. (b) Luo, H.; Churu, G.; Fabrizio, E. F.; Schnobrich, J.; Hobbs, A.; Dass, A.; Mulik, S.; Zhang, Y.; Grady, B. P.; Capecelatro, A.; Sotiriou-Leventis, C.; Lu, H.; Leventis, N. *J. Sol-Gel Sci. Technol.* **2008**, *48*, 113-134.

48. Luo, H.; Zhang, Y.; Wang, B.; Lu, H. *J. Offshore Mech. Arct. Eng.* **2010**, *132*, 021301.

49. Chen, W. W.; Song, B. *Split Hopkinson (Kolsky) Bar: Design, Testing and Applications*, Springer, New York, N.Y., **2010**.

50. Lu, H.; Tan, G.; Chen, W. *Mech. Time-Depend. Mater.* **2001**, *5*, 119-129.

51. (a) American Society for Metals. ASM Engineering Materials Handbook, Composites; ASM International: Materials Park, OH, 1998; Vol. 1, p 178, Table 2. (b) Luo, H.; Chen, W. *Int. J. Appl. Ceram.Technol.* **2004**, *1*, 254–260. (c) Luo, H.; Chen, W.; Rajendran, A. M. *J. Am. Ceram. Soc.* **2006**, *89*, 266–273.

52. (a) Gross, J.; Fricke, J.; Pekala, R. W.; Hrubesh, L. W. *Phys. Rev. B* **1992**, *45*, 12774-12777. (b) Gross, J.; Fricke, J. *J. Non-Cryst. Solids* **1992**, *145*, 217-222.

53. Pekala, R. W.; Alviso, C. T.; Lemay, J. D. *J. Non-Cryst. Solids* **1990**, *125*, 67-75.

54. See for example: (a) Meador, M. A. B.; Malow, E. J.; Silva, R.; Wright, S.; Quade, D.; Vivod, S. L.; Guo, H.; Guo, J.; Cakmak, M. *ACS Appl. Mater. Interfaces* **2012**, *4*, 536-544. (b) Meador, M. A. B. "Improving Elastic Properties of Polymer-Reinforced Aerogels." In *Aerogels Handbook*; Aegerter, M. A.; Leventis, N.; Koebel, M. M. Eds.; Springer: New York, N.Y., 2011, Chapter 15, pp 191-214. (c) Jin, C. "Aerogels Super Thermal Insulation Material by Nano Hi-tech." In *Aerogels Handbook*; Aegerter, M. A.; Leventis, N.; Koebel, M. M. Eds.; Springer: New York, N.Y., 2011, Chapter 40, pp 865-877. (d) Jones, S. M.; Sakamoto, J. "Applications of Aerogels in Space Exploration." In *Aerogels Handbook*; Aegerter, M. A.; Leventis, N.; Koebel, M. M. Eds.; Springer: New York, N.Y., 2011, Chapter 32, pp 721-746.

55. Webb, P. A.; Orr, C. Analytical Methods in Fine Particle Technology, Micromeritics Instrument Corporation, Norcross, GA, USA, 1997; (a) p 80; (b) pp 67-68.

56. Ilavsky, J.; Jemian, P. R. *J. Appl. Cryst*. **2009**, *42*, 347-353.

57. (a) Mohite, D. P.; Mahadik-Khanolkar, S.; Luo, H.; Lu, H.; Sotiriou-Leventis, C.; Leventis, N. *Soft Matter* **2013**, *9*, 1516-1530. (b) Mohite, D. P.; Mahadik-Khanolkar, S.; Luo, H.; Lu, H.; Sotiriou-Leventis, C.; Leventis, N. *Soft Matter* **2013**, *9*, 1531-1539.

58. Luo, H.; Roy, S.; Lu, H. *Compos. Sci. Technol.* **2012**, *72*, 159-166.

59. Luo, H.; Lu, H.; Leventis, N. *Mech. Time-Depend. Mater.* **2006**, *10*, 83-111.

60. (a) Frew, D. J.; Forrestal, M. J.; Chen, W. *Exp. Mech.* **2002**, *42*, 93-106. (b) Gray, G. T. *Mech. Test. Eval. ASM Handbook* **2000**, *8*, 462-476. (c) Gama, B. A.; Lopatnikov, S. L.; Gillespie, J. W. *Appl. Mech. Rev.* **2004**, *57*, 223-250.

6. Figures

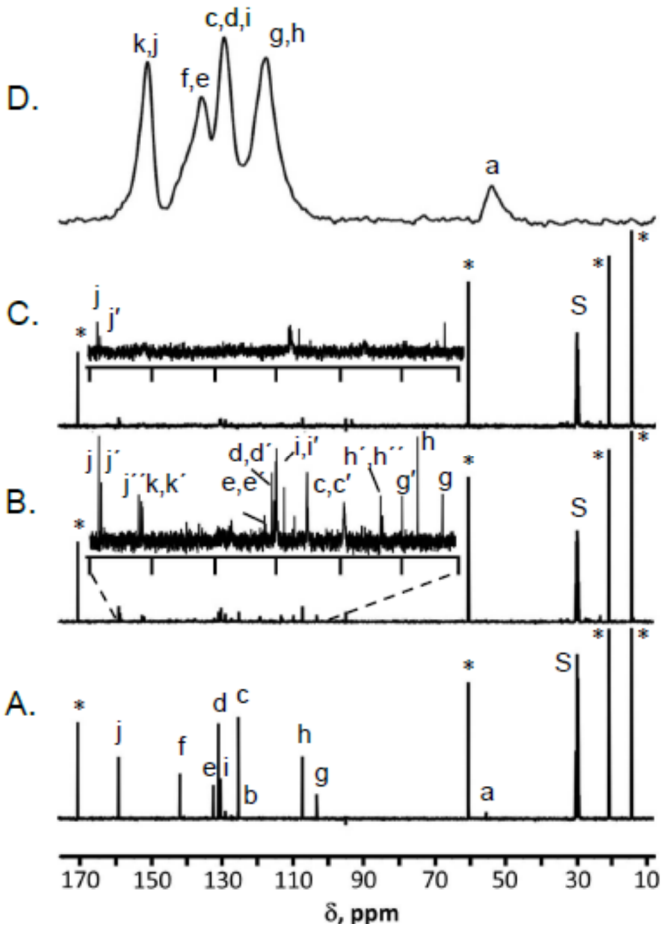

Figure 1. Representative ^{13}C NMR data. (All liquid spectra at the same attenuation, except insets). A. Room temperature liquid ^{13}C NMR in acetone-d_6 (marked with S) of a **TIPM**/**RES** mixture (1:1.5 mol:mol, at the 10% w/w solids formulation). For resonance assignments refer to Scheme 2. B. Liquid ^{13}C NMR of the mixture in A, 25 min after adding the catalyst. C. Liquid ^{13}C NMR of the mixture in A, 35 min after adding the catalyst. (Note, the formal gelation point -by rheology- is at 132 min; see Table 1.) D. Solid-state CPMAS ^{13}C NMR spectrum of the resulting **aR-RES-10** aerogel. (Resonances of ethyl acetate introduced with **TIPM** are denoted with asterisks. Data for the other **aR-ALC-xx** aerogels are provided in Appendix II of the Supporting Information.)

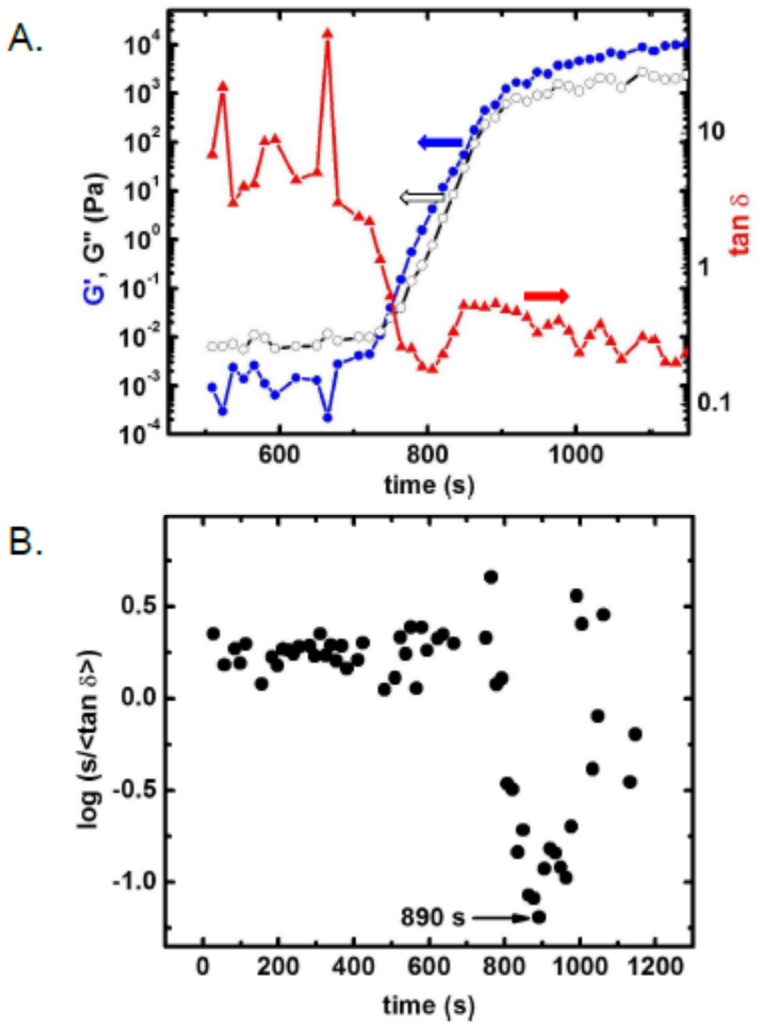

Figure 2. Typical rheological data during gelation at 20 ^{o}C, exemplified with the **aR-POL-10** sol. A. Evolution of the storage (G´ - dark circles) and loss (G´´ - open circles) moduli and tanδ (triangles) versus time. Oscillation frequency ω=1 rad s^{-1}. Monitoring started 2400 s after adding the catalyst (Table 1). B. Statistical variable versus time (see text). The formal gelation point is defined at the minimum. (Incubation time before loading to the rheometer: 2400 s (Table 1).

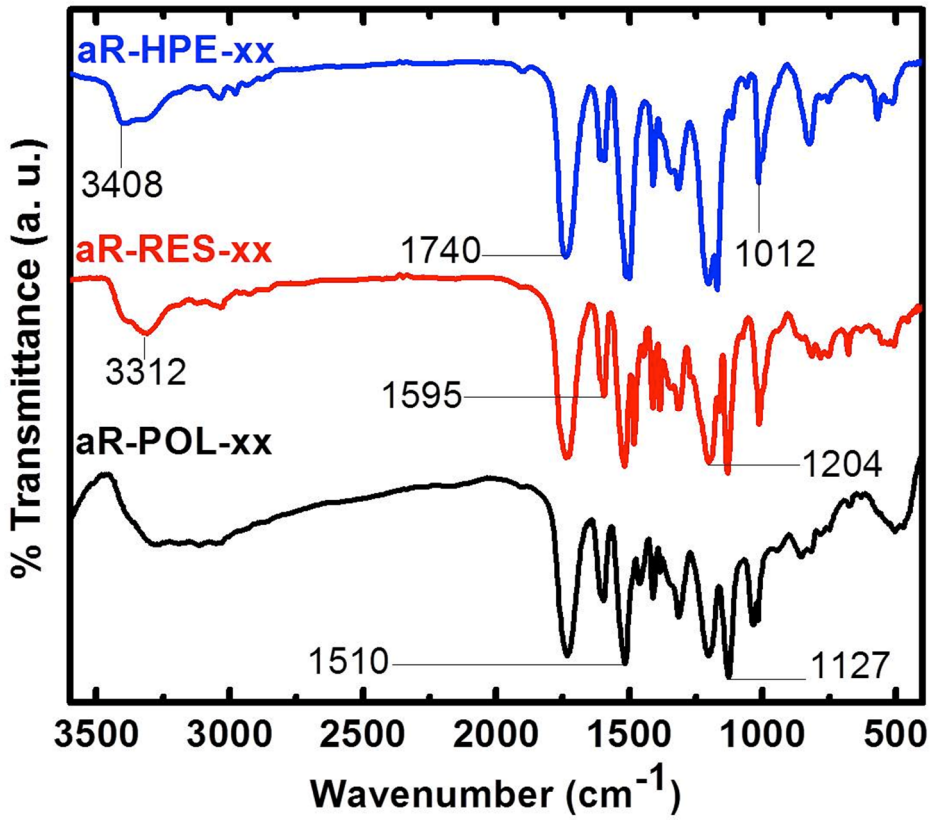

Figure 3. Representative infrared absorption data for samples as shown. Peaks marked explicitly are discussed in the text.

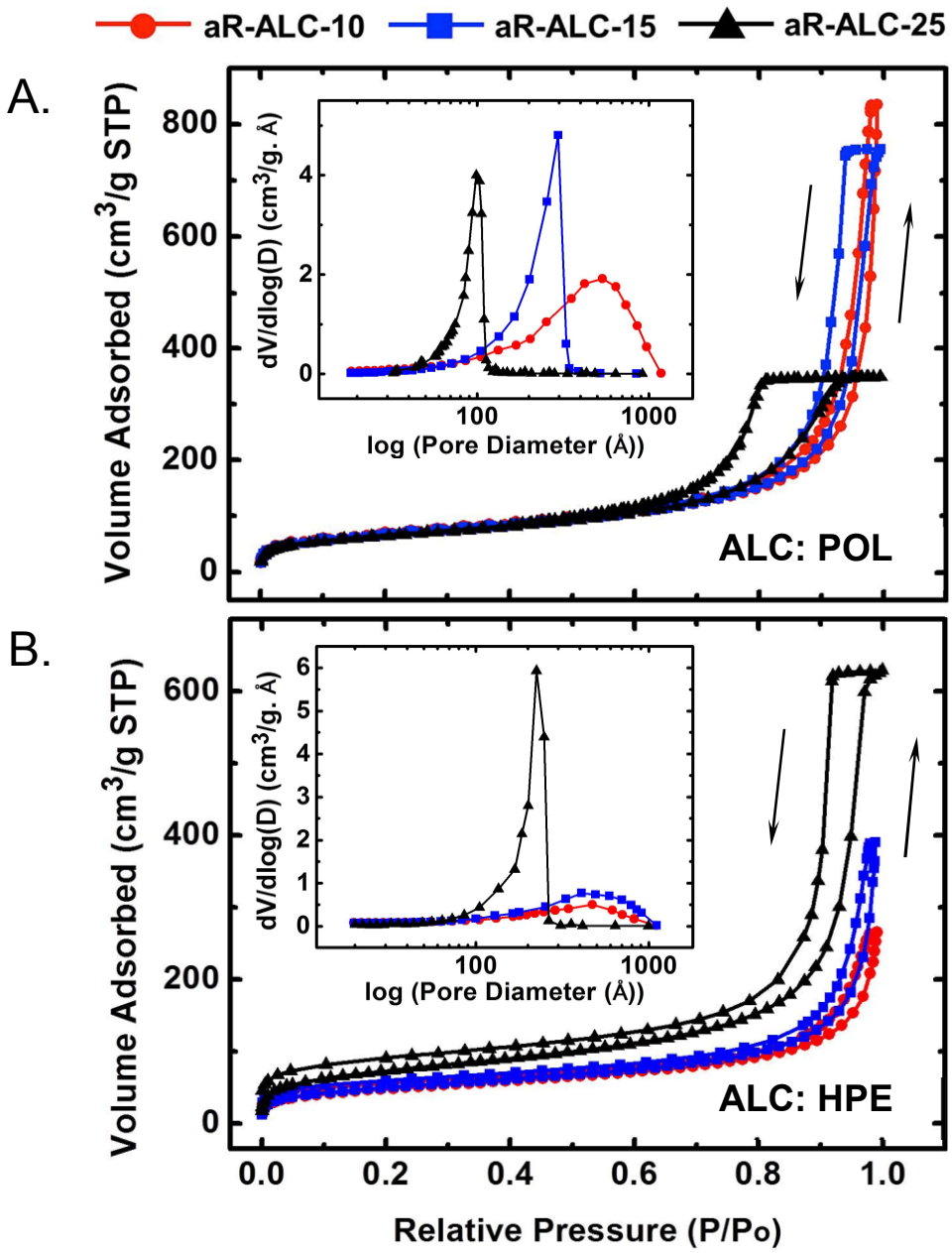

Figure 4. A. Typical N_2-sorption data for a system whereas the volume of N_2 adsorbed decreases with density (**aR-POL-xx**). B. Similarly, for a system whereas the volume of N_2 adsorbed increases with density (**aR-HPE-xx**). Insets: pore size distributions via the BJH equation applied to the desorption branch of the isotherms. For other systems refer to Appendix IV in the Supporting Information. Data are summarized in Table 2.

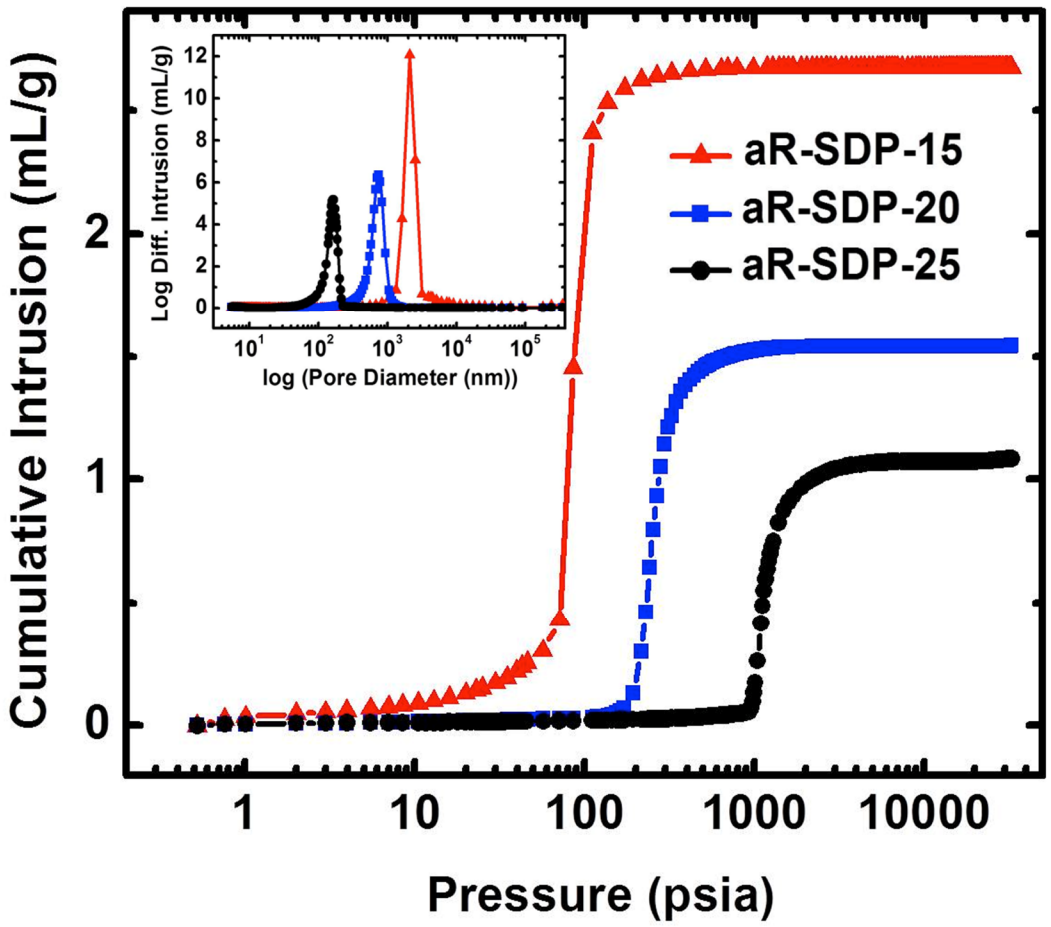

Figure 5. Representative Hg-intrusion porosimetry data exemplified with **aR-SDP-xx** aerogels. Inset: pore size distributions. For other systems refer to Appendix IV in the Supporting Information. Data are summarized in Tables 2 and 3.

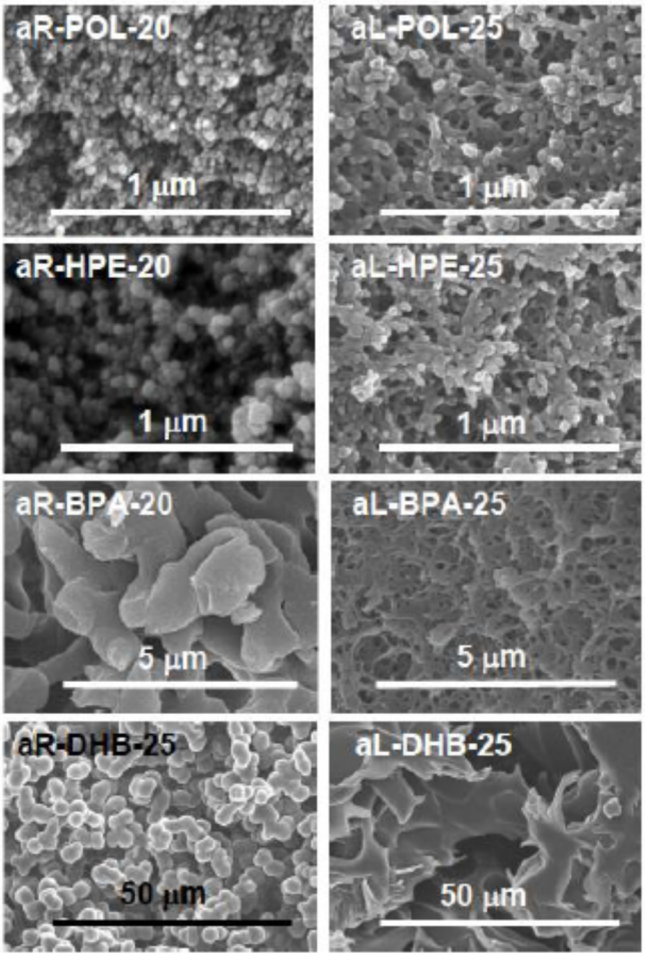

Figure 6. Scanning electron microscopy (SEM) data of selected **aR-ALC-20** aerogels and the corresponding (in terms of molar concentration of the sol) **aL-ALC-25** aerogels at the same magnifications. (For the complete list, as well as different magnifications refer to Appendix IV in the Supporting Information.)

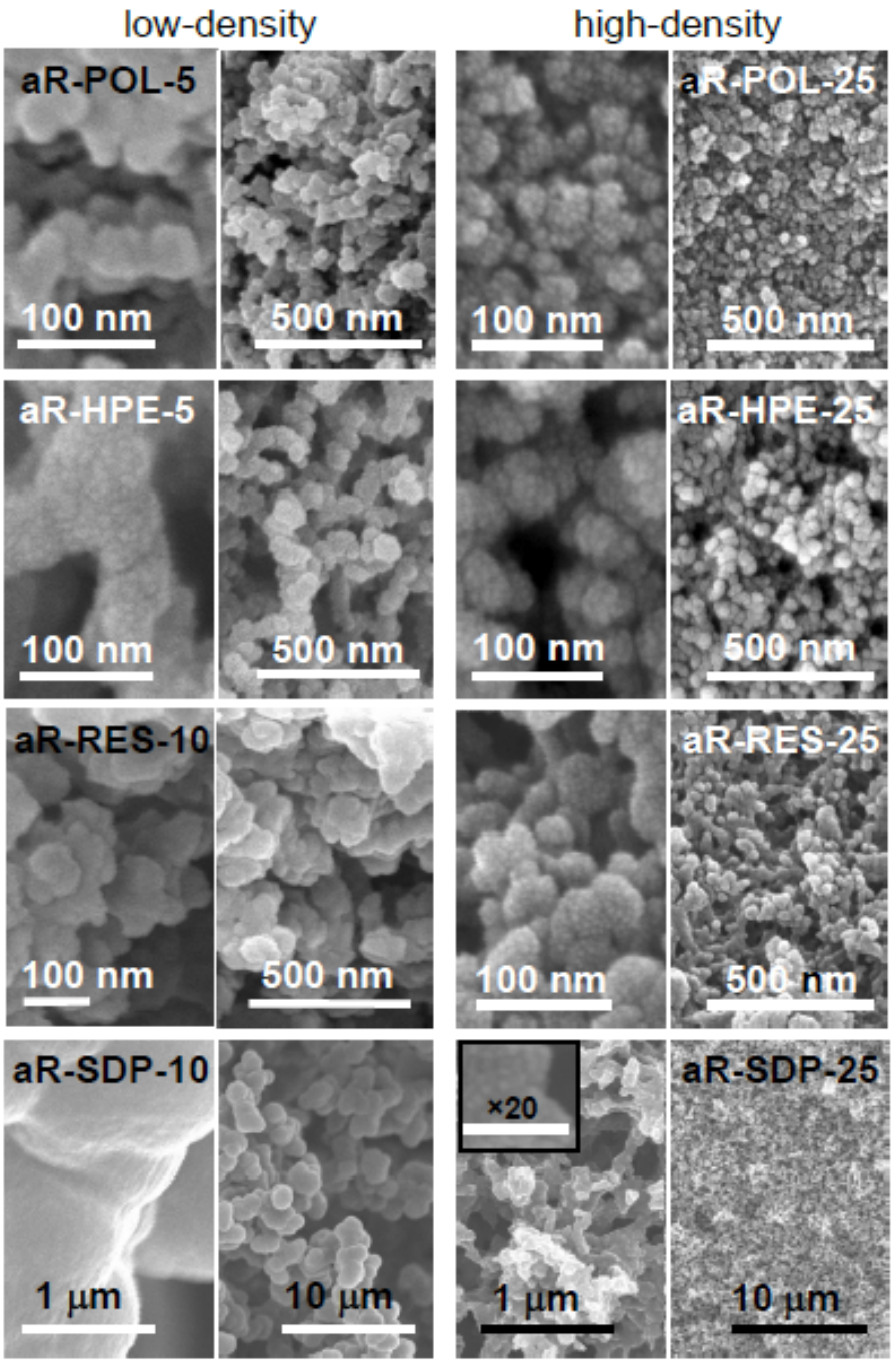

Figure 7. Selected scanning electron microscopy (SEM) data for **aR-ALC-xx** aerogels at two density extremes, at low and high magnification. Length scales have been selected to capture the relative sizes of the building blocks and the morphology of the networks.

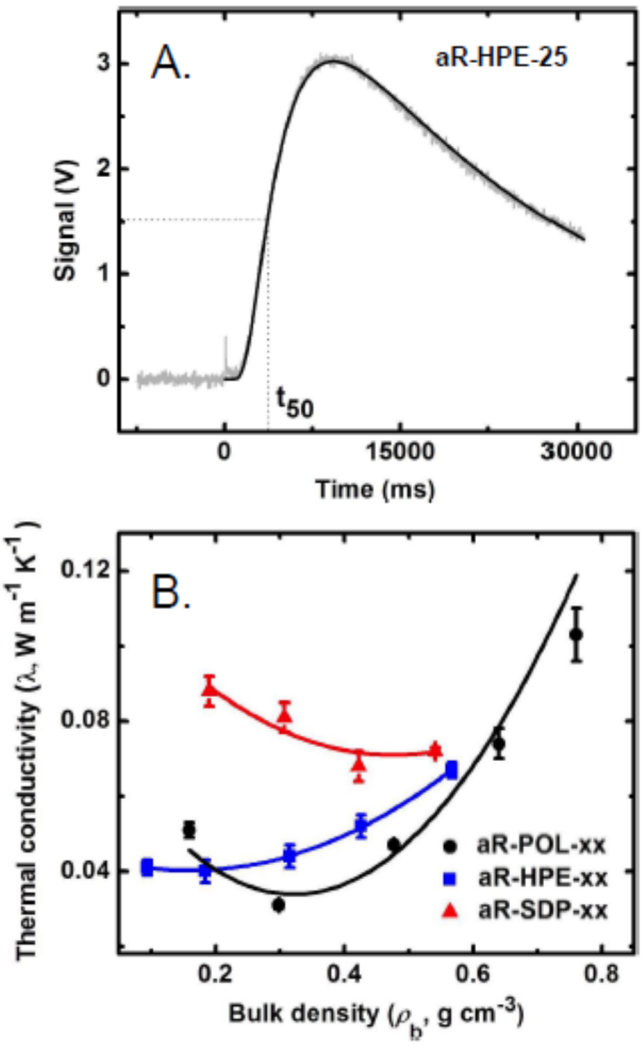

Figure 8: A. Rise of the detector voltage (proportional to temperature) on the back face of a **aR-HPE-25** aerogel disk following a heat pulse incident to the front face (see Experimental). The dashed lines mark t_{50}, the time required for the detector voltage to reach half its maximum value. The analysis software eliminates the radiative spike visible just before the smooth temperature rise. Data have been fitted to the pulse-corrected Cowan model.[35,36] B. Representative variation of the thermal conductivity, λ, of three **aR-ALC-xx** aerogels (as indicated), as a function of their bulk density. Data are summarized in Table 4.

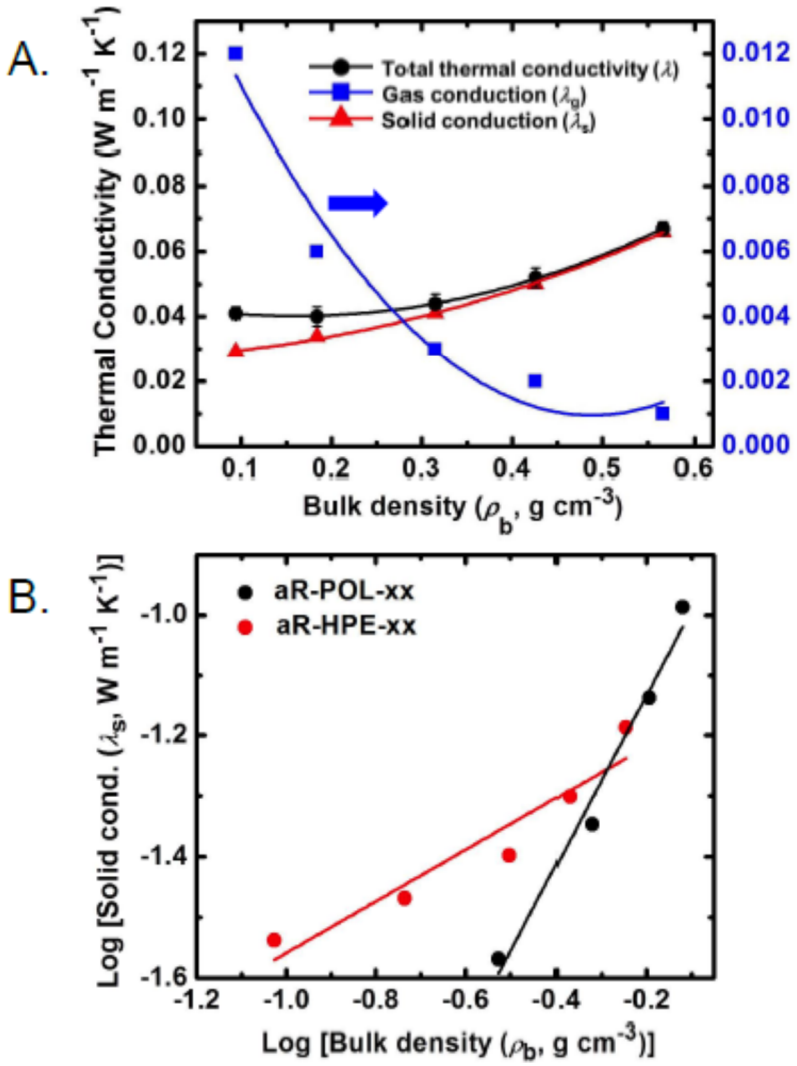

Figure 9. A. Typical deconvolution, exemplified with **aR-HPE-xx**, of the total thermal conductivity, λ, into through-gas (λ_g) and through-the-solid (λ_s) thermal conduction. B. Log-Log plot of λ_s versus bulk density, ρ_b, of **aR-HPE-xx**. Data from similar curves for the remaining **aR-ALC-xx** aerogels are summarized in Table 4.

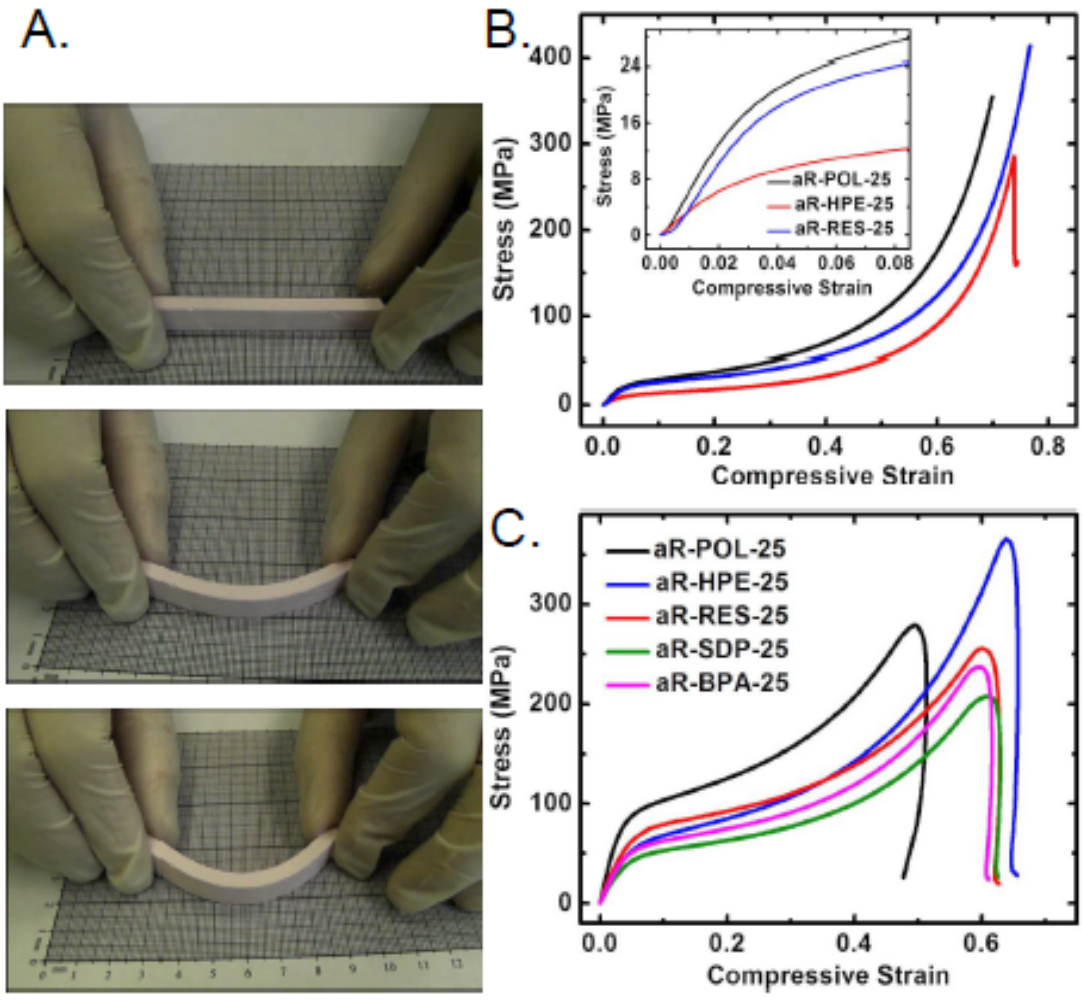

Figure 10. A. **aR-HPE-10** (ρ_b= 0.18 g cm^{-3}): a flexible sample at various stages of bending (last frame: right before failure). **aR-HPE-5** and **aR-SDP-10** are even more flexible, allowing 180^o bending (see TOC Graphic). B. Representative stress-strain curves of selected **aR-ALC-25** samples under quasi-static compression. Inset: Magnification of the low-strain linear region whose slope gives the Young's modulus. C. Stress-strain curves of **aR-ALC-25** samples under dynamic loading conditions. (Strain rates are cited in Table S.8 of the Supporting Information.) Note the increased stiffness, but also the lower *UCS* relative to the data in part B of this figure.

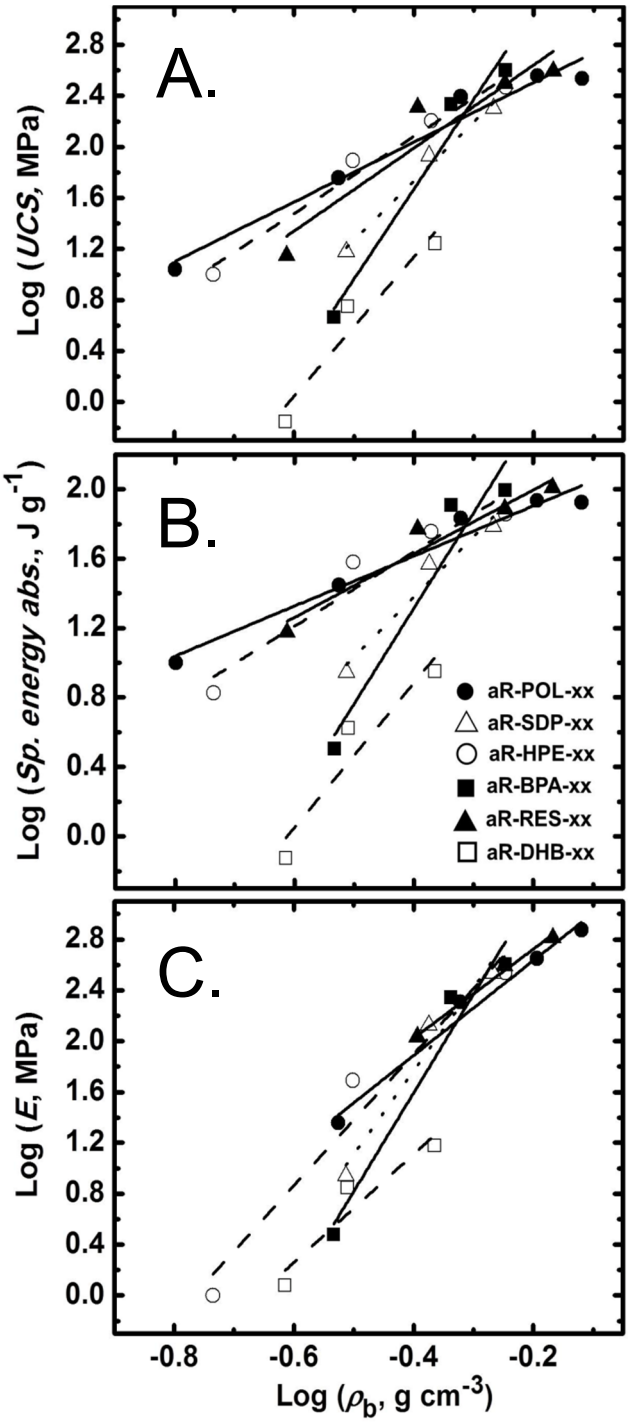

Figure 11. Log-Log plots from the quasi-static compression data of **aR-ALC-xx** aerogels: A. Ultimate compressive strength (*UCS*) versus bulk density. B. Specific energy absorption versus bulk density. C. Young's modulus (*E*) versus bulk density.

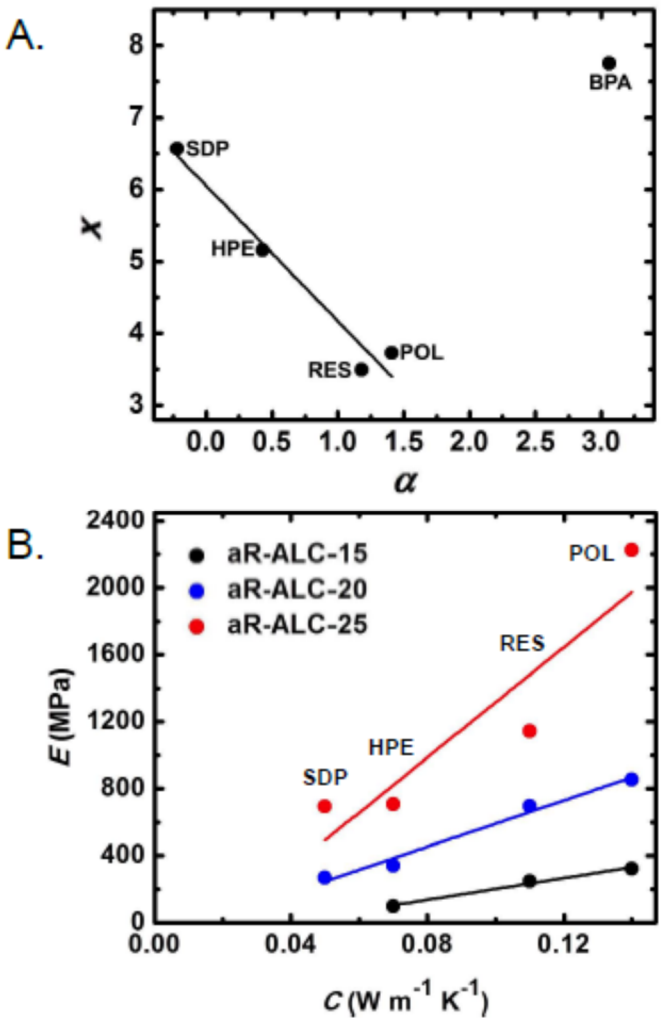

Figure 12. A. Exponent α for the dependence of the solid thermal conduction (λ_s) on the bulk density (via Eq. 6), versus exponent x for the dependence of the Young's modulus (E) on the bulk density (via Eq. 7). Data shown concern the **aR-ALC-xx** aerogels. B. Young's modulus, E, under dynamic compression (see Figure 10C, data from Table S.8), versus the interconnectivity parameter C (via Eq. 6, from Table 4). Data shown concern **aR-ALC-xx** aerogels whose α and x parameters correlate linearly in part A of this figure.

7. Supporting Information

Appendix I. Formulations of all **PU** aerogels

Table S.1. Formulations and gelation times of **TIPM**-based **aR-ALC-xx** aerogels [a]

Sample	Alcohol [b]				Desmodur RE [c]		**TIPM**			acetone		gelation time (min)
	mass (g)	volume (mL)	mmol	C (M)	volume (mL)	mass (g)	mass [d] (g)	mmol	C (M)	mass (g)	volume (mL)	
aR-POL-5	0.126	0.0847	1.00	0.0834	1.33	1.359	0.367	1.00	0.0834	8.37	10.58	180
aR-POL-10	0.126	0.0847	1.00	0.1735	1.33	1.359	0.367	1.00	0.1735	3.44	4.35	60
aR-POL-15	0.126	0.0847	1.00	0.2714	1.33	1.359	0.367	1.00	0.2714	1.8	2.27	40
aR-POL-20	0.126	0.0847	1.00	0.3767	1.33	1.359	0.367	1.00	0.3767	0.98	1.24	25
aR-POL-25	0.126	0.0847	1.00	0.4939	1.33	1.359	0.367	1.00	0.4939	0.49	0.61	20
aR-HPE-5	0.306	0.2444	1.00	0.0607	1.33	1.359	0.367	1.00	0.0607	11.8	14.9	90
aR-HPE-7.5	0.306	0.2444	1.00	0.0925	1.33	1.359	0.367	1.00	0.0925	7.31	9.24	70
aR-HPE-10	0.306	0.2444	1.00	0.1254	1.33	1.359	0.367	1.00	0.1254	5.06	6.4	50
aR-HPE-15	0.306	0.2444	1.00	0.1944	1.33	1.359	0.367	1.00	0.1944	2.82	3.57	25
aR-HPE-20	0.306	0.2444	1.00	0.2685	1.33	1.359	0.367	1.00	0.2685	1.7	2.15	15
aR-HPE-25	0.306	0.2444	1.00	0.3479	1.33	1.359	0.367	1.00	0.3479	1.03	1.3	4
aR-RES-10	0.165	0.1299	1.50	0.2396	1.33	1.359	0.367	1.00	0.1597	3.8	4.8	145
aR-RES-15	0.165	0.1299	1.50	0.3731	1.33	1.359	0.367	1.00	0.2488	2.02	2.56	25
aR-RES-20	0.165	0.1299	1.50	0.5173	1.33	1.359	0.367	1.00	0.3448	1.14	1.44	25
aR-RES-25	0.165	0.1299	1.50	0.6757	1.33	1.359	0.367	1.00	0.4505	0.6	0.76	15
aR-SDP-10	0.375	0.2619	1.50	0.1710	1.33	1.359	0.367	1.00	0.1140	5.69	7.18	25
aR-SDP-15	0.375	0.2619	1.50	0.2635	1.33	1.359	0.367	1.00	0.1757	3.21	4.1	15
aR-SDP-20	0.375	0.2619	1.50	0.3666	1.33	1.359	0.367	1.00	0.2444	1.98	2.5	10

aR-SDP-25	0.375	0.2619	1.50	0.4759	1.33	1.359	0.367	1.00	0.3173	1.23	1.56	7
aR-BPA-10	0.342	0.2862	1.50	0.1780	1.33	1.359	0.367	1.00	0.1187	5.39	6.81	90
aR-BPA-15	0.342	0.2862	1.50	0.2759	1.33	1.359	0.367	1.00	0.1840	3.03	3.82	55
aR-BPA-20	0.342	0.2862	1.50	0.3801	1.33	1.359	0.367	1.00	0.2534	1.84	2.33	30
aR-BPA-25	0.342	0.2862	1.50	0.4924	1.33	1.359	0.367	1.00	0.3283	1.13	1.43	15
aR-DHB-15	0.321	0.2465	1.50	0.2859	1.33	1.359	0.367	1.00	0.1906	2.91	3.67	60
aR-DHB-20	0.321	0.2465	1.50	0.3951	1.33	1.359	0.367	1.00	0.2634	1.76	2.22	40
aR-DHB-25	0.321	0.2465	1.50	0.5125	1.33	1.359	0.367	1.00	0.3417	1.07	1.35	15

[a] Catalyst 5 μL in all formulations. [b] Volumes of the alcohols were calculated based on their densities: **POL**: 1.488 g cm^{-3}; **HPE**: 1.252 g cm^{-3}; **RES**: 1.270 g cm^{-3}; **SPD**: 1.432 g cm^{-3}; **BPA**: 1.195 g cm^{-3}; **DHB**: 1.302 g cm^{-3}. [c] The mass of the commercial Desmodur RE was calculated based on the density of the ethyl acetate solution as measured by us (1.022 g cm^{-3}). [d] The mass of **TIPM** in Desmodur RE was calculated based on the 27% w/w concentration noted by the supplier.

Table S.2. Formulations and gelation times of **N3300A**-based **aL-ALC-25** aerogels [a]

Sample	Alcohol [b]				Desmodur N3300A [c]				acetone		gelation time
	mass (g)	volume (mL)	mmol	C (M)	mass (g)	volume (mL)	mmol	C (M)	mass (g)	volume (mL)	
aL-POL-25	0.126	0.0847	1.00	0.3442	0.504	0.4308	1.00	0.3442	1.89	2.39	3 h
aL-HPE-25	0.306	0.2444	1.00	0.2670	0.504	0.4308	1.00	0.2670	2.43	3.07	1 h 20 min
aL-RES-25	0.165	0.1299	1.50	0.4838	0.504	0.4308	1.00	0.3225	2.01	2.54	5 h 30 min
aL-SDP-25	0.375	0.2619	1.50	0.3729	0.504	0.4308	1.00	0.2486	2.64	3.33	1 h 20 min
aL-BPA-25	0.342	0.2862	1.50	0.3820	0.504	0.4308	1.00	0.2546	2.54	3.21	5 h 15 min
aL-DHB-25	0.321	0.2465	1.50	0.3940	0.504	0.4308	1.00	0.2627	2.48	3.13	5 h 30 min

[a] Catalyst 5 μL in all formulations. [b] Volumes of the alcohols as in footnote b of Table S.1. [c] The volume of **N3300A** was calculated based on its density (1.170 g cm^{-3}) provided by the supplier.

Appendix II. Solid-state NMR data for aR-ALC-xx and aL-ALC-25 aerogel samples

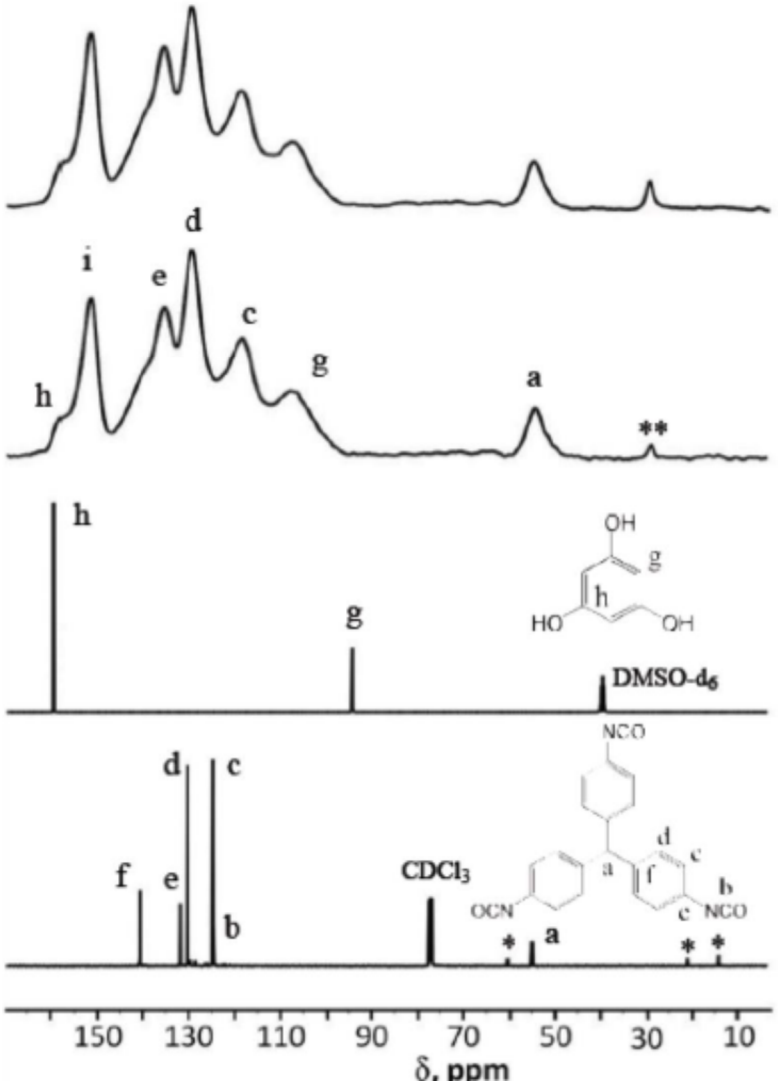

Figure S.1 Liquid ^{13}C-NMR spectra of **TIPM** (Desmodur RE) in $CDCl_3$ (bottom), **POL** in DMSO-d_6 (second from bottom), and solid CPMAS ^{13}C-NMR spectra of **aR-POL-5** aerogel (second from top) and **aR-POL-25** aerogel (top). (*: ethyl acetate; **: acetone)

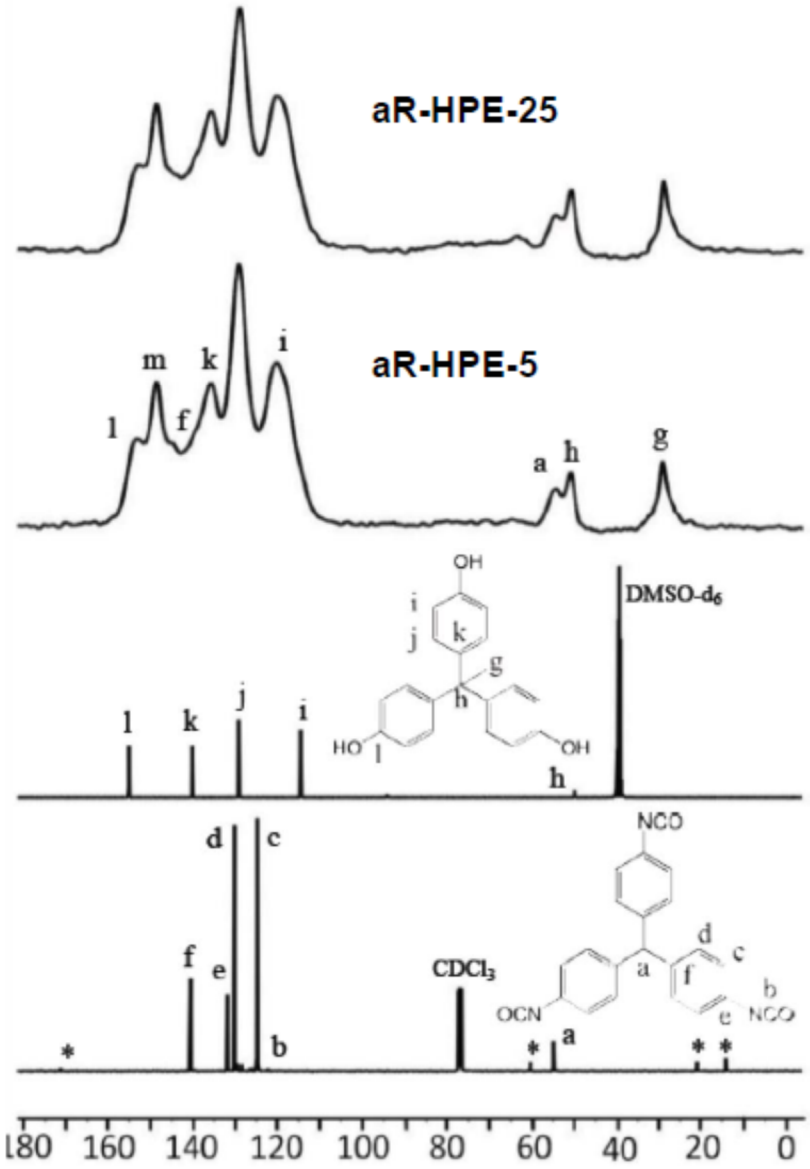

Figure S.2 Liquid ^{13}C-NMR spectra of **TIPM** (Desmodur RE) in $CDCl_3$ (bottom), **HPE** in DMSO-d_6 (second from bottom), and solid CPMAS ^{13}C-NMR spectra of **aR-HPE-5** aerogel (second from top) and **aR-HPE-25** aerogel (top). (*: ethyl acetate)

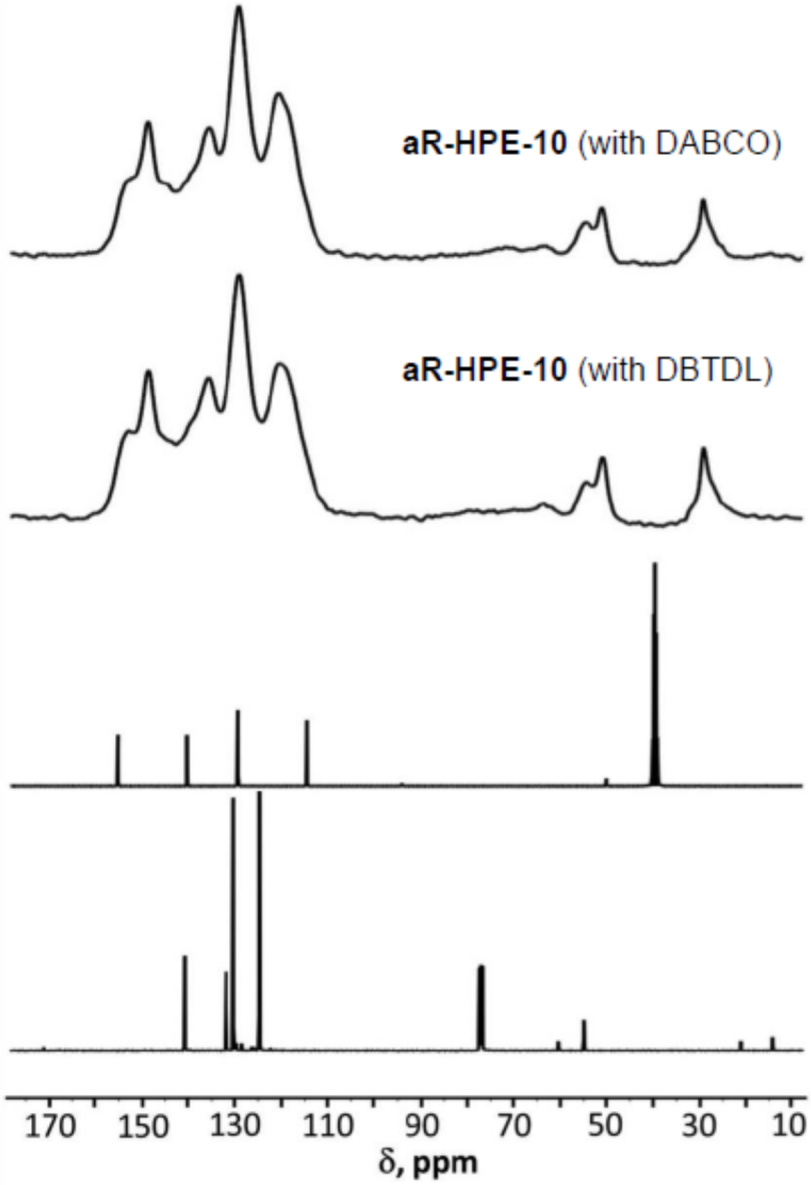

Figure S.3 Liquid ^{13}C-NMR spectra of **TIPM** (Desmodur RE) in $CDCl_3$ (bottom), **HPE** in DMSO-d_6 (second from bottom), and solid CPMAS ^{13}C-NMR spectra of **aR-HPE-10** aerogel synthesized with DABCO catalyst (top) and DBTDL (second from top as marked). For peak assignments see Figure S.2.

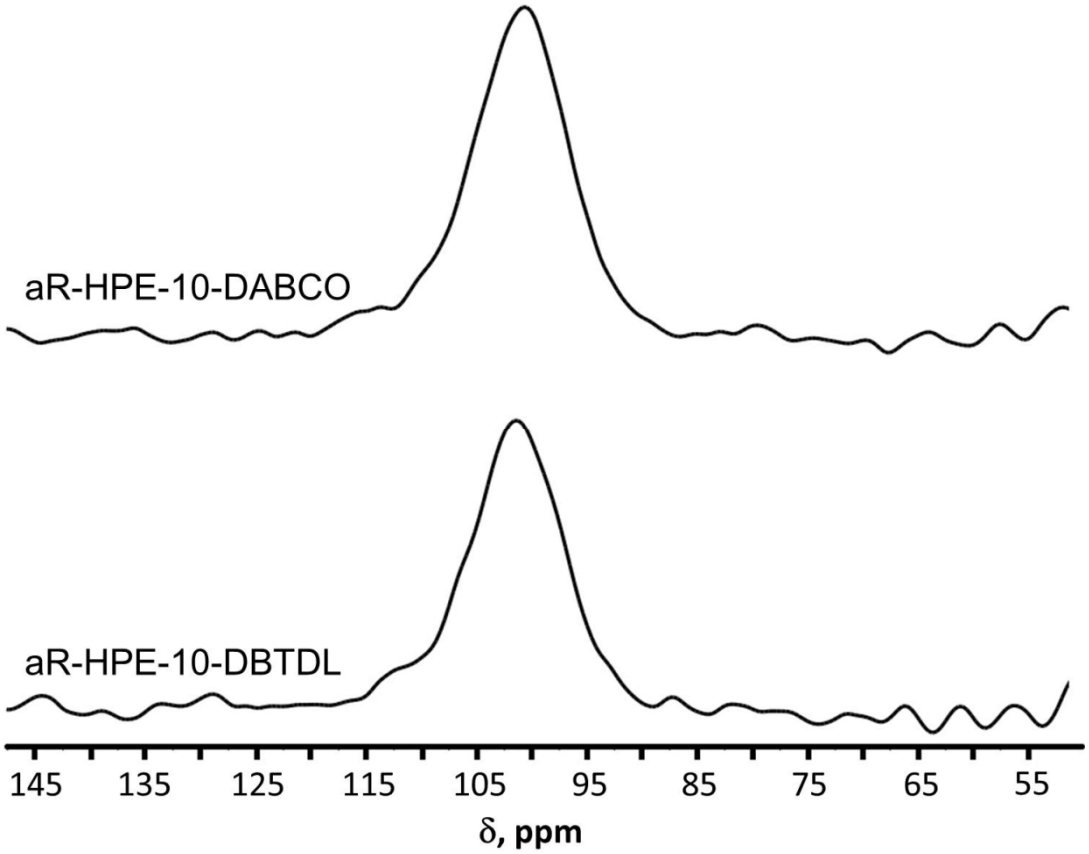

Figure S.4 Solid-state CPMAS ^{15}N-NMR spectra of **aR-HPE-10** aerogel synthesized with DABCO (top) and DBTDL (bottom).

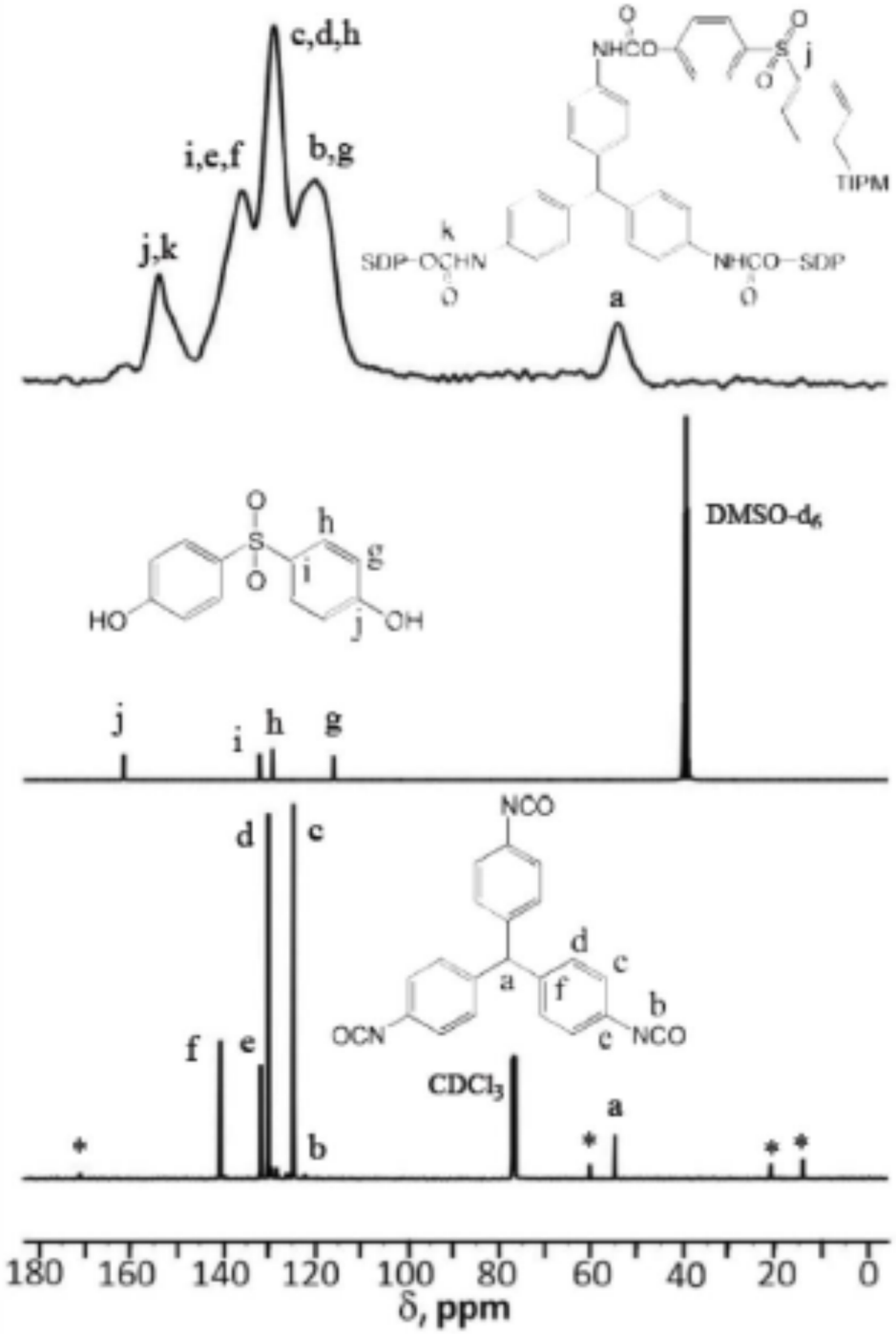

Figure S.5 Liquid ^{13}C-NMR spectra of **TIPM** (Desmodur RE) in $CDCl_3$ (bottom), **SDP** in DMSO-d_6 (middle), and solid-state CPMAS ^{13}C-NMR spectrum of **aR-SDP-25** aerogel (top). (*: ethyl acetate for Desmodur RE)

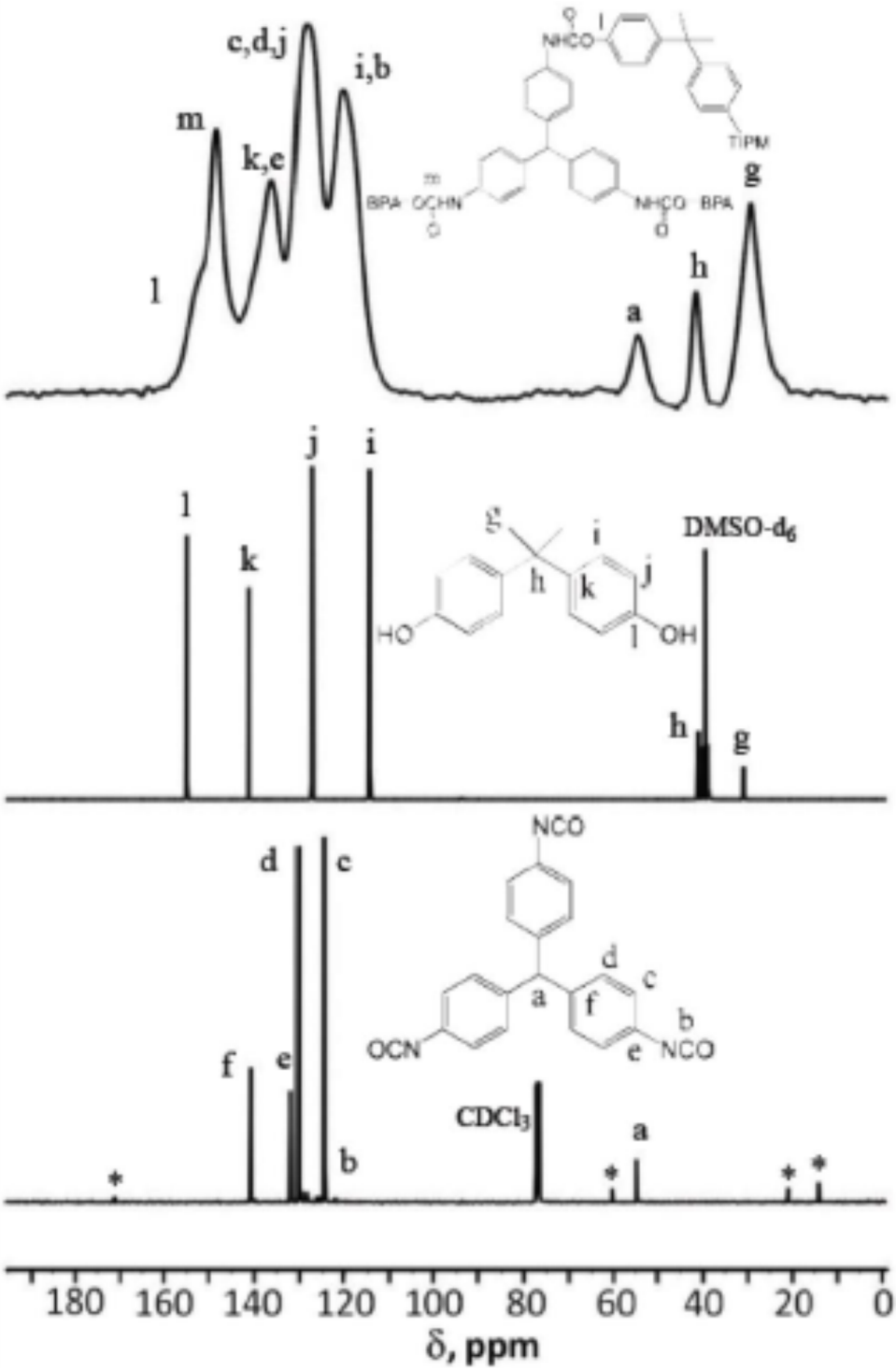

Figure S.6 Liquid ^{13}C-NMR spectra of **TIPM** (Desmodur RE) in $CDCl_3$ (bottom), **BPA** in DMSO-d_6 (middle), and solid-state CPMAS ^{13}C-NMR spectrum of **aR-BPA-25** aerogel (top). (*: ethyl acetate from Deesmodur RE)

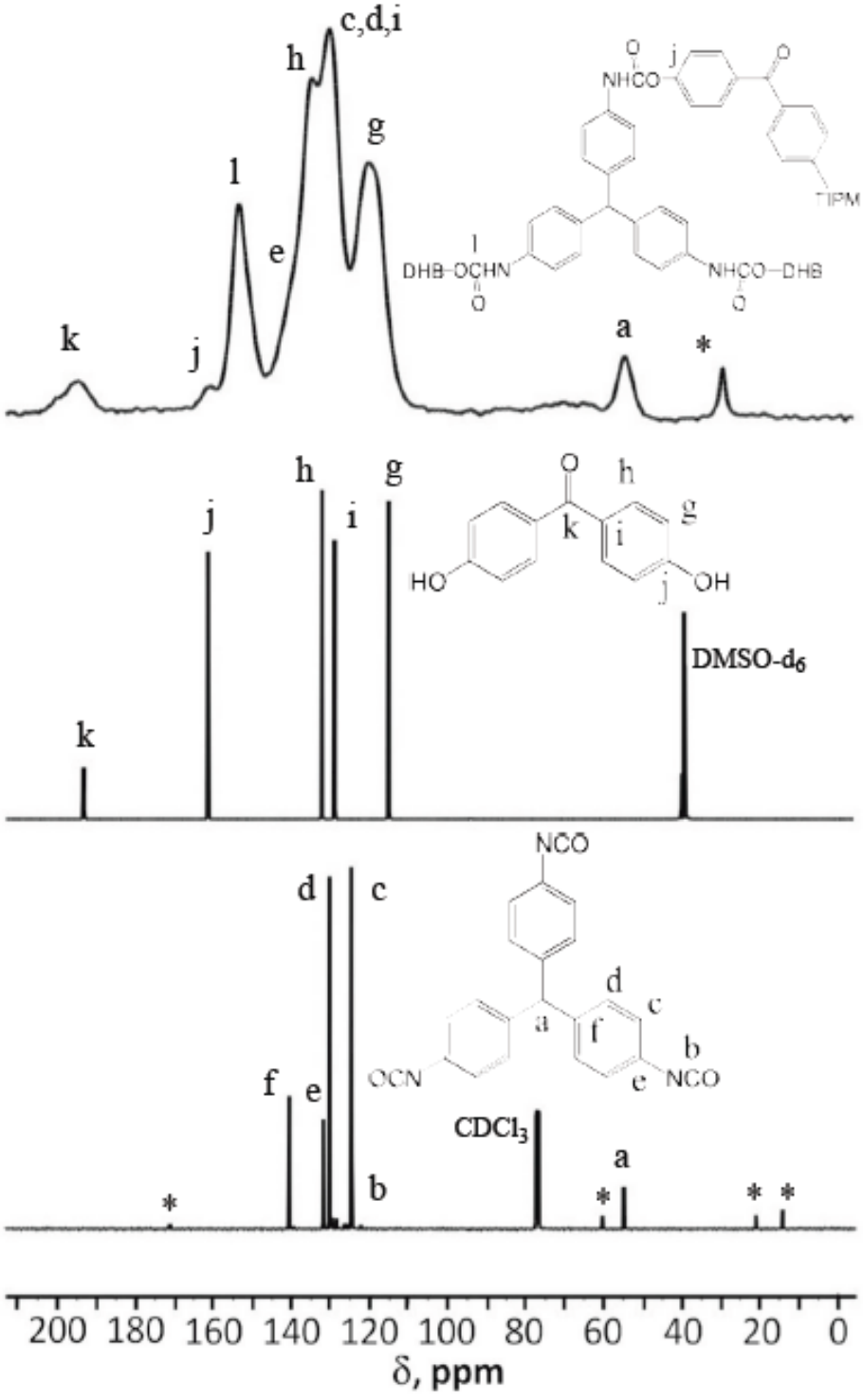

Figure S.7 Liquid ^{13}C-NMR spectra of **TIPM** (Desmodur RE) in $CDCl_3$ (bottom), **DHB** in DMSO-d_6 (middle), and solid-state CPMAS ^{13}C-NMR spectrum of **aR-DHB-25** aerogel (top). (*: ethyl acetate from Desmodur RE; **: acetone from processing)

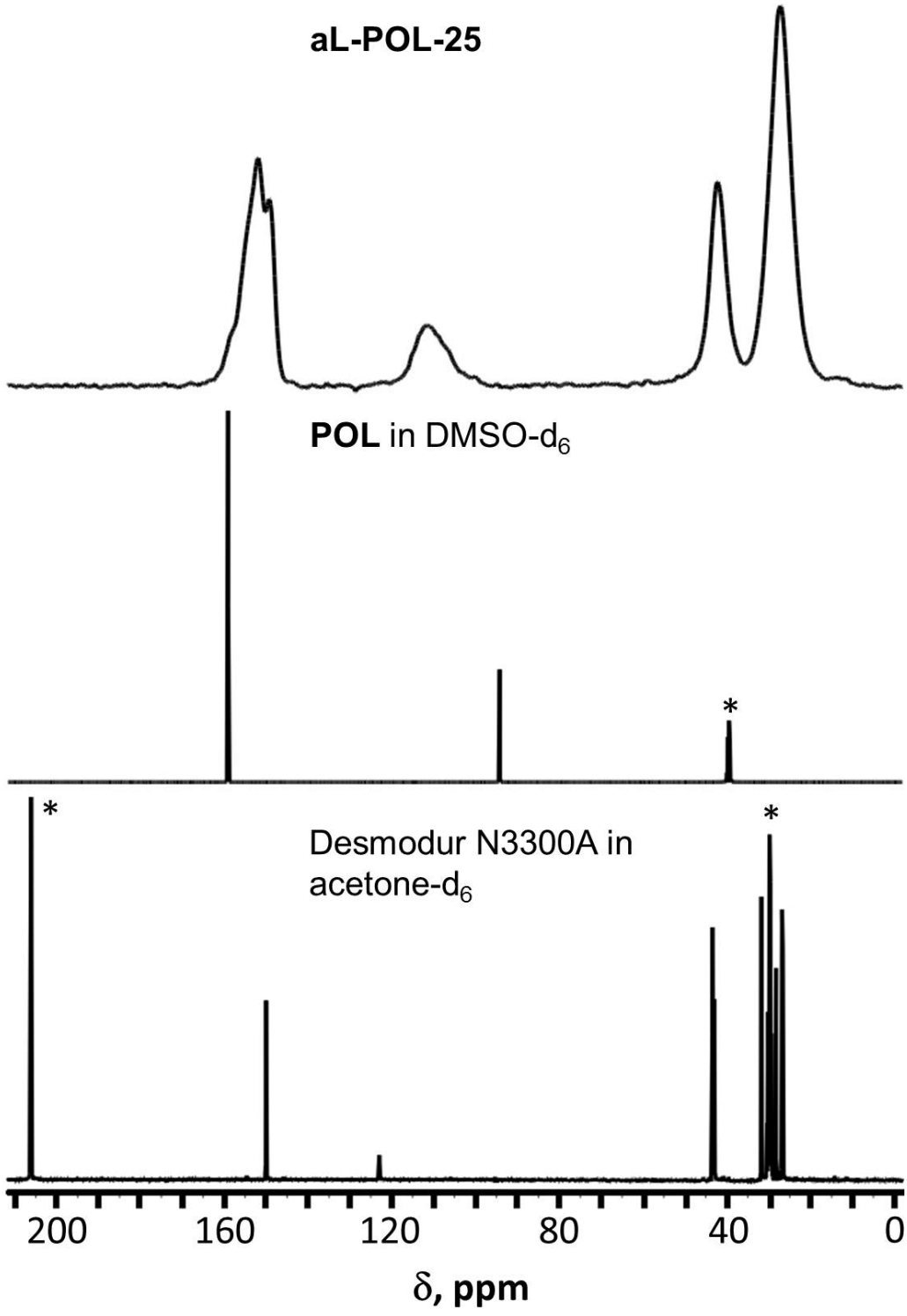

Figure S.8 Liquid ^{13}C-NMR spectra of **N3300A** (Desmodur N3300A) in acetone-d_6 (bottom), **POL** in DMSO-d_6 (middle), and solid-state CPMAS ^{13}C-NMR spectrum of **aL-POL-25** aerogel (top). (*: corresponding solvent)

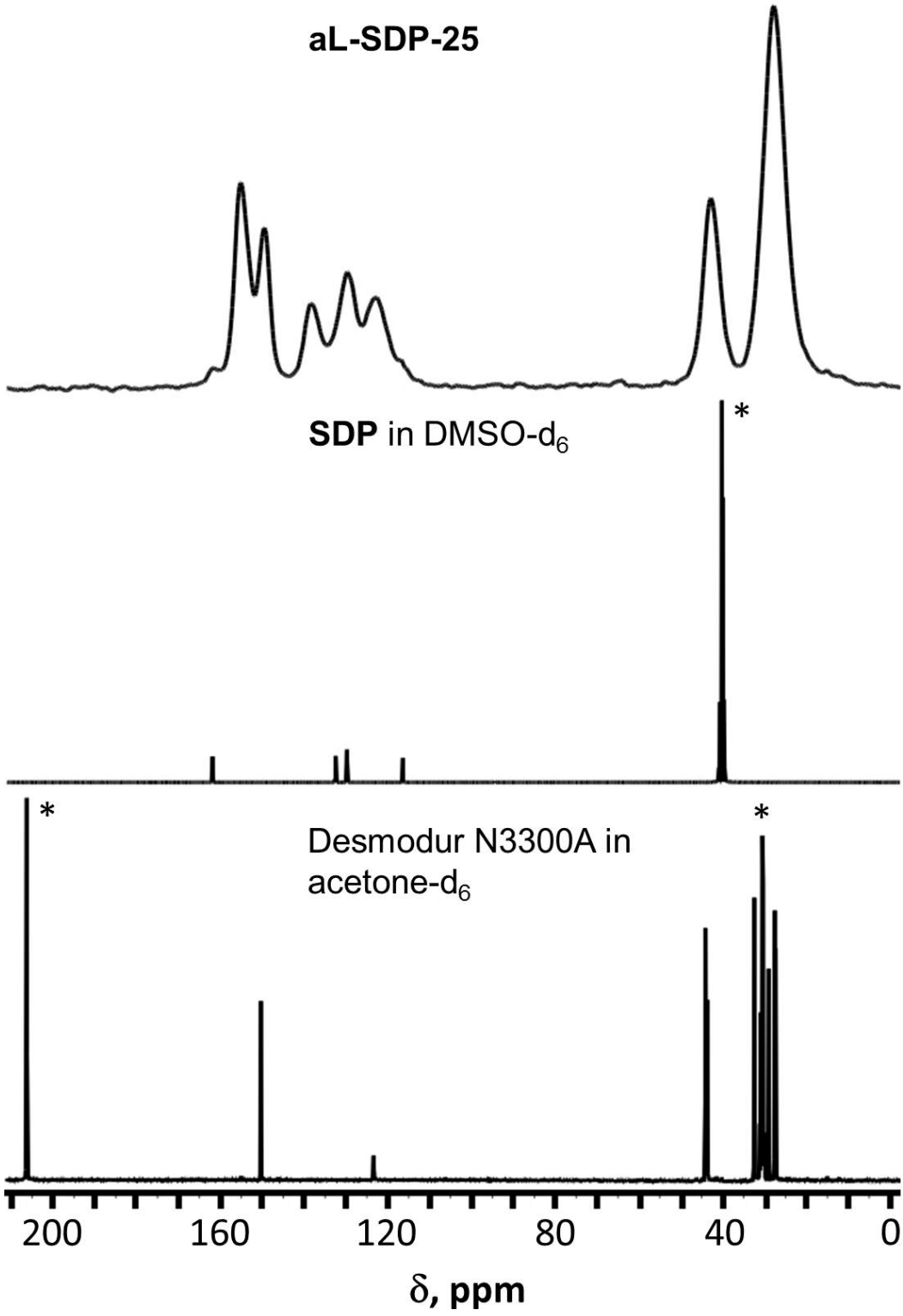

Figure S.9 Liquid ^{13}C-NMR spectra of **N3300A** (Desmodur N3300A) in acetone-d_6 (bottom), **SDP** in DMSO-d_6 (middle), and solid-state CPMAS ^{13}C-NMR spectrum of **aL-SDP-25** aerogel (top). (*: corresponding solvent)

Appendix III. X-Ray diffraction data for selected aR-ALC-xx and aL-ALC-25 aerogel samples

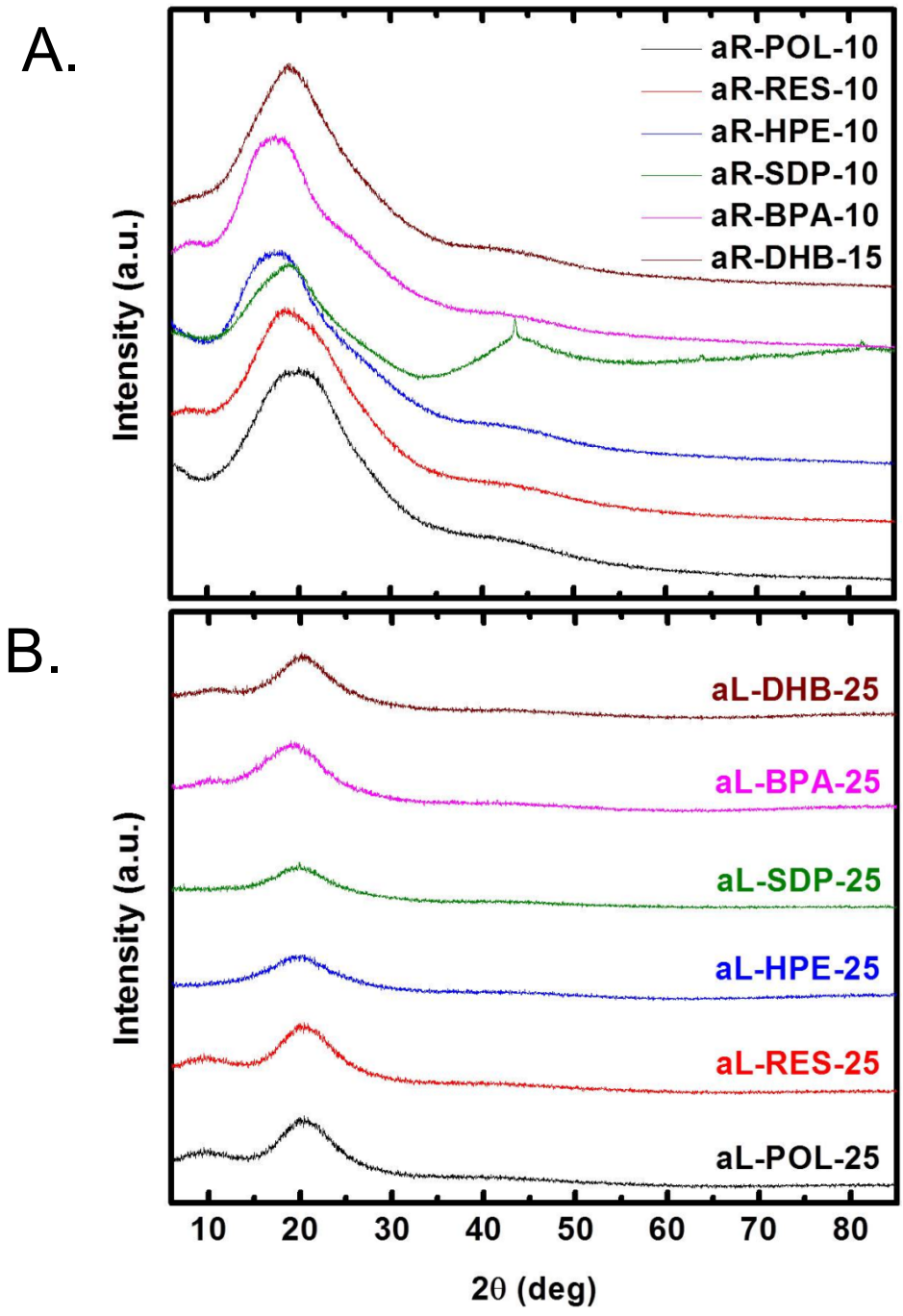

Figure S.10 A. XRD of **aR-ALC-xx** aerogels (as indicted). B. XRD of **aL-ALC-25** aerogels.

Appendix IV. SEM, N_2-sorption and Hg-intrusion porosimetry data for all PU aerogels

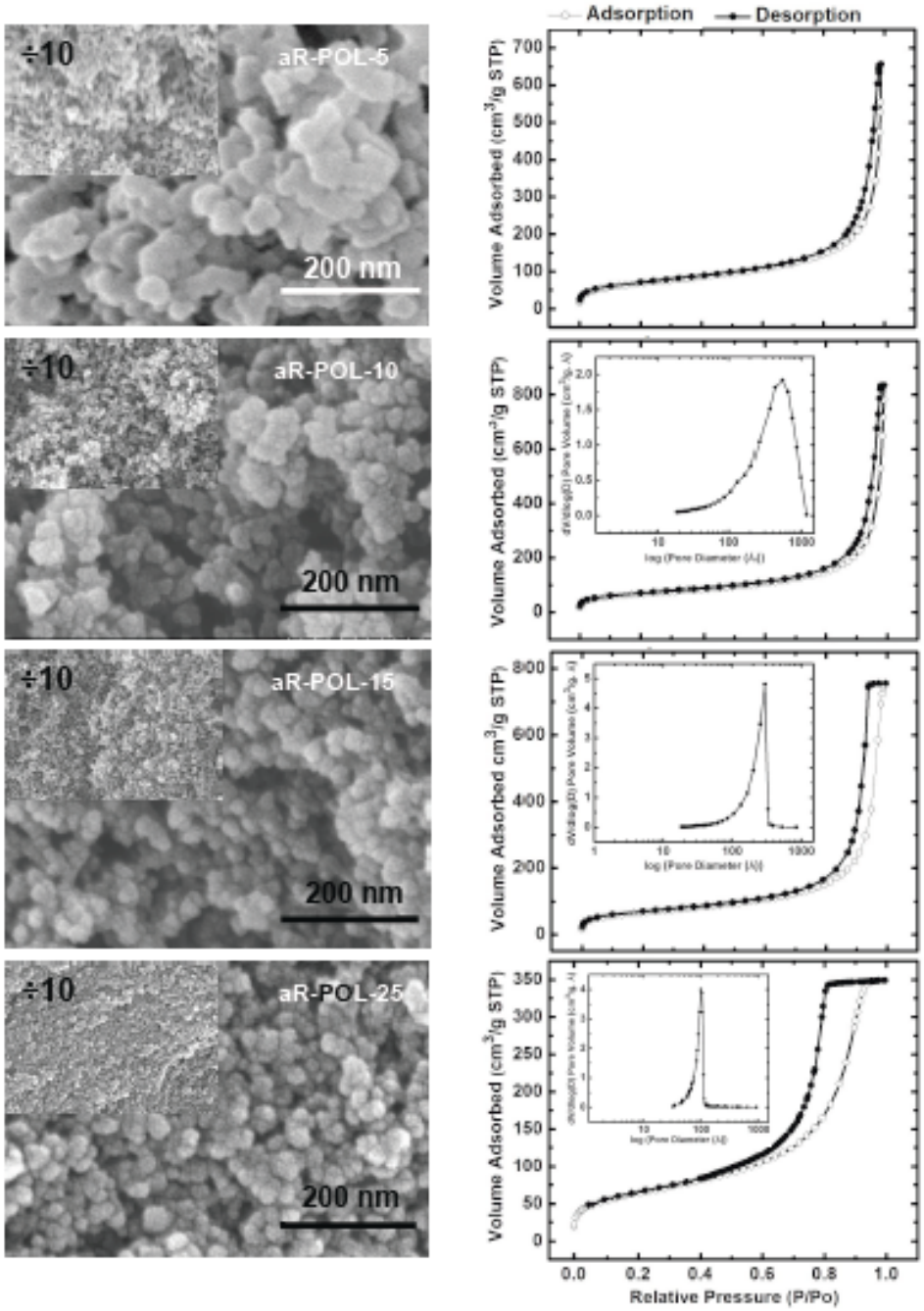

Figure S.11 SEM and N_2 sorption porosimetry data for the **aR-POL-xx** aerogels. (Insets: BJH plots.)

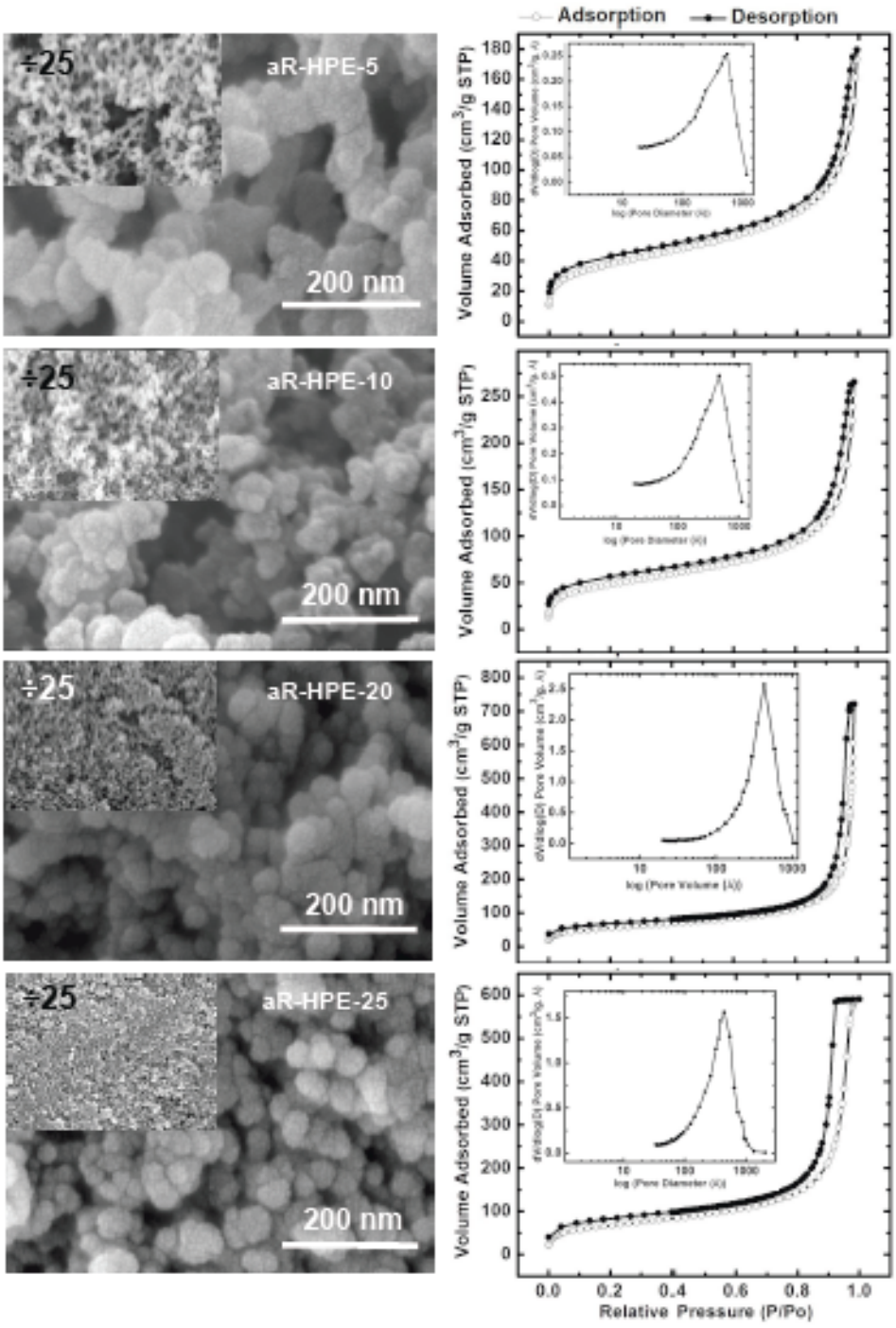

Figure S.12 SEM and N_2 sorption porosimetry data for the **aR-HPE-xx** aerogels. (Insets: BJH plots.)

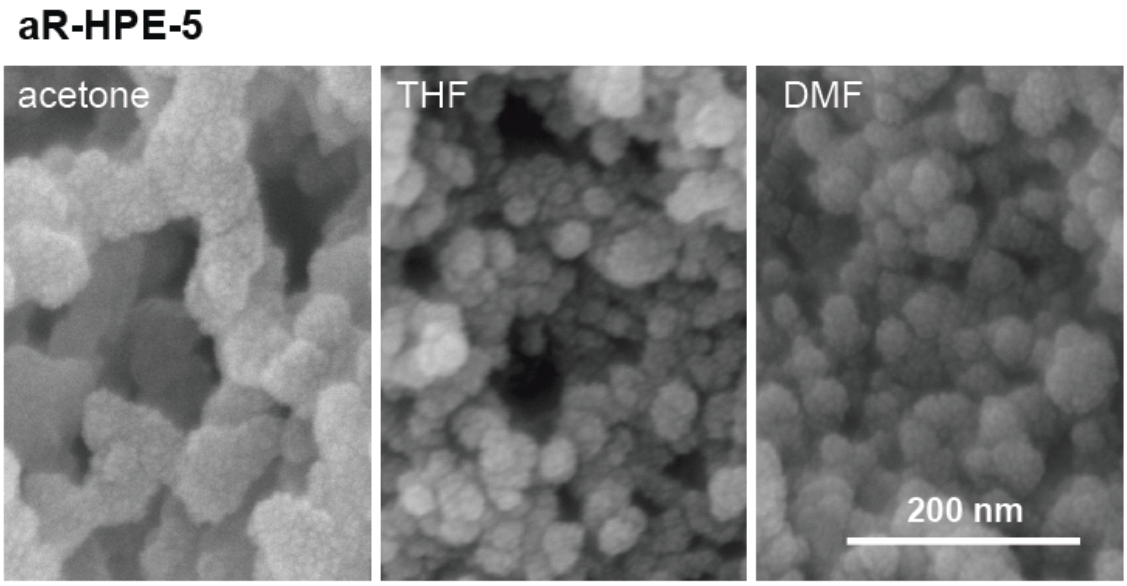

Figure S.13 High-magnification SEM of **aR-HPE-5** aerogels synthesized in the three solvents as shown. From acetone, aggregates of smaller particles form strings. From THF or DMF aggregates of the smallest particles form larger clusters. Material characterization data for the three samples are shown in Table S.3 below. Quantitative particle size analysis was conducted with small angle x-ray scattering (SAXS) and data are shown in Table S.4.

Table S.3. General materials characterization data for **aR-HPE-5** aerogels synthesized in the three solvent systems as indicated

aR-HPE-5	linear shrinkage (%) [b]	bulk density, ρ_b (g cm^{-3}) [a, h]	skeletal density, ρ_s (g cm^{-3}) [c]	Π (%)	BET surface area, σ (m^2 g^{-1}) [d]	average pore diam. Φ (nm [nm]) [e]	BJH average pore diam. (nm) [f]	particle radius (nm) [g]
acetone [a]	22.4 ± 1.6	0.094 ± 0.004	1.232 ± 0.015	92	132 [14]	11.4 [297.7]	54.9 [80.8]	18.5
THF [h]	49.8 ± 0.7	0.364 ± 0.003	1.266 ± 0.019	71	312 [14]	27.2 [25.1]	43.6 [23.1]	7.6
DMF [h]	54.2 ± 1.3	0.513 ± 0.020	1.260 ± 0.004	59	270 [18]	17.3 [17.1]	19.9 [12.0]	8.8

[a] Average of 5 samples; data from Table 2. [b] Shrinkage = 100 × (mold diameter – sample diameter)/(mold diameter). [c] Single sample, average of 50 measurements. [d] First number indicates the BET surface area, the number in the square bracket indicates the micropore area given by t-plot analysis. [e] By the $4 \times V_{Total}/\sigma$ method. For the first value, V_{Total} was calculated by the single-point adsorption method; for the value in brackets, (referred to as Φ), V_{Total} was calculated via $V_{Total} = (1/\rho_b)-(1/\rho_s)$. [f] From the BJH plots: the first number is the peak maximum; numbers in brackets are the widths at half maxima of the BJH plots. [g] Particle radius = $3/\rho_s\sigma$. [h] Average of 3 samples

Table S.4. Quantitative particle size analysis with small angle x-ray scattering (SAXS) for **aR-HPE-5** aerogels synthesized in the three solvent systems as indicated

sample	Primary Particles			Secondary Particles			$3/\rho_s\sigma$
	high-Q slope [a]	$R_G(1)$ [b] (nm)	$R(1)$ [c] (nm)	low-Q slope [d]	$R_G(1)$ [e] (nm)	$R(2)$ [c] (nm)	radius [f] (nm)
aR-HPE-5							
acetone	4.11±0.03	$12._5$±$1._3$	$16._2$±$1._7$	3.9±0.4	$48._5$±$1._9$	$63._0$±$2._5$	18.5
THF	4.53±0.06	3.95±0.90	5.12±0.01	2.8±0.2	21.1±0.53	27.4±0.7	7.6
DMF	4.70±0.03	4.99±0.21	6.48±0.27	2.3±0.2	16.5±0.23	21.4±.29	8.8

Referring to Figure S.22 below: [a] From power-law Region I. [b] From Guinier Region II. [c] Particle radius $R = R_G/0.77$. [d] From power-law Region III. [e] From Guinier Region IV. [f] From Tables S.3 above.

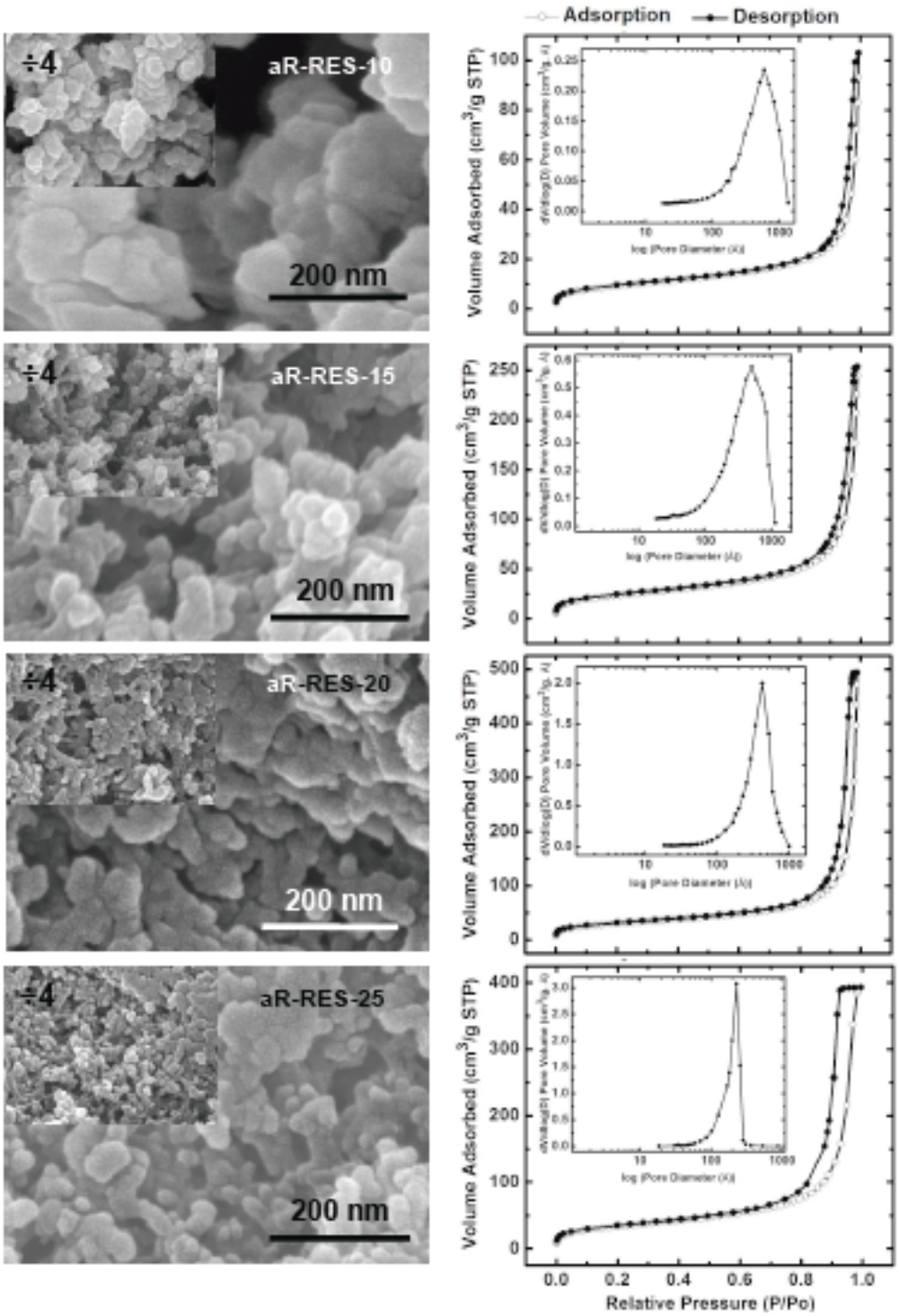

Figure S.14 SEM and N_2 sorption porosimetry data for the **aR-RES-xx** aerogels. (Insets: BJH plots.)

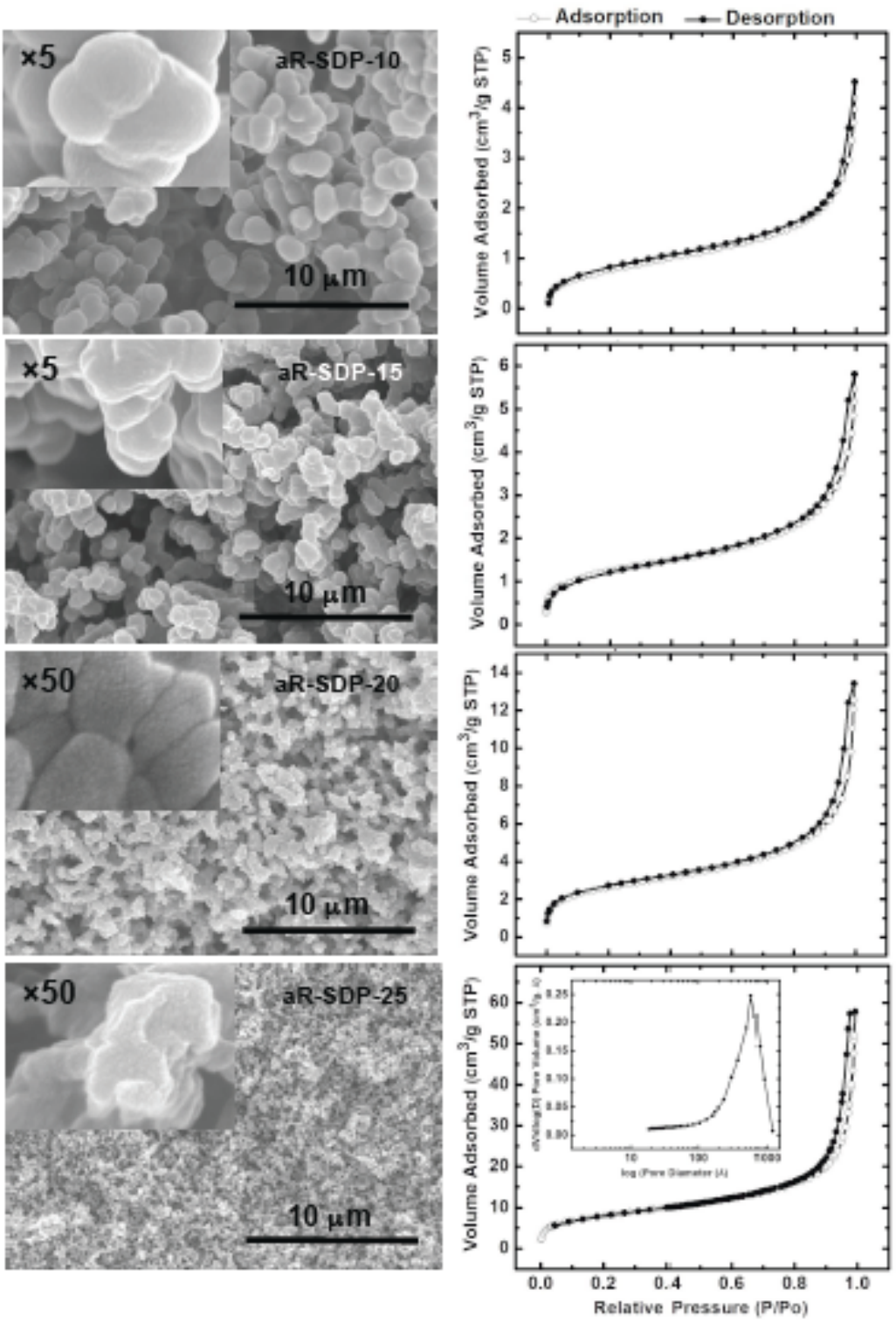

Figure S.15 SEM and N_2 sorption porosimetry data for the **aR-SDP-xx** aerogels. (Inset: BJH plot.)

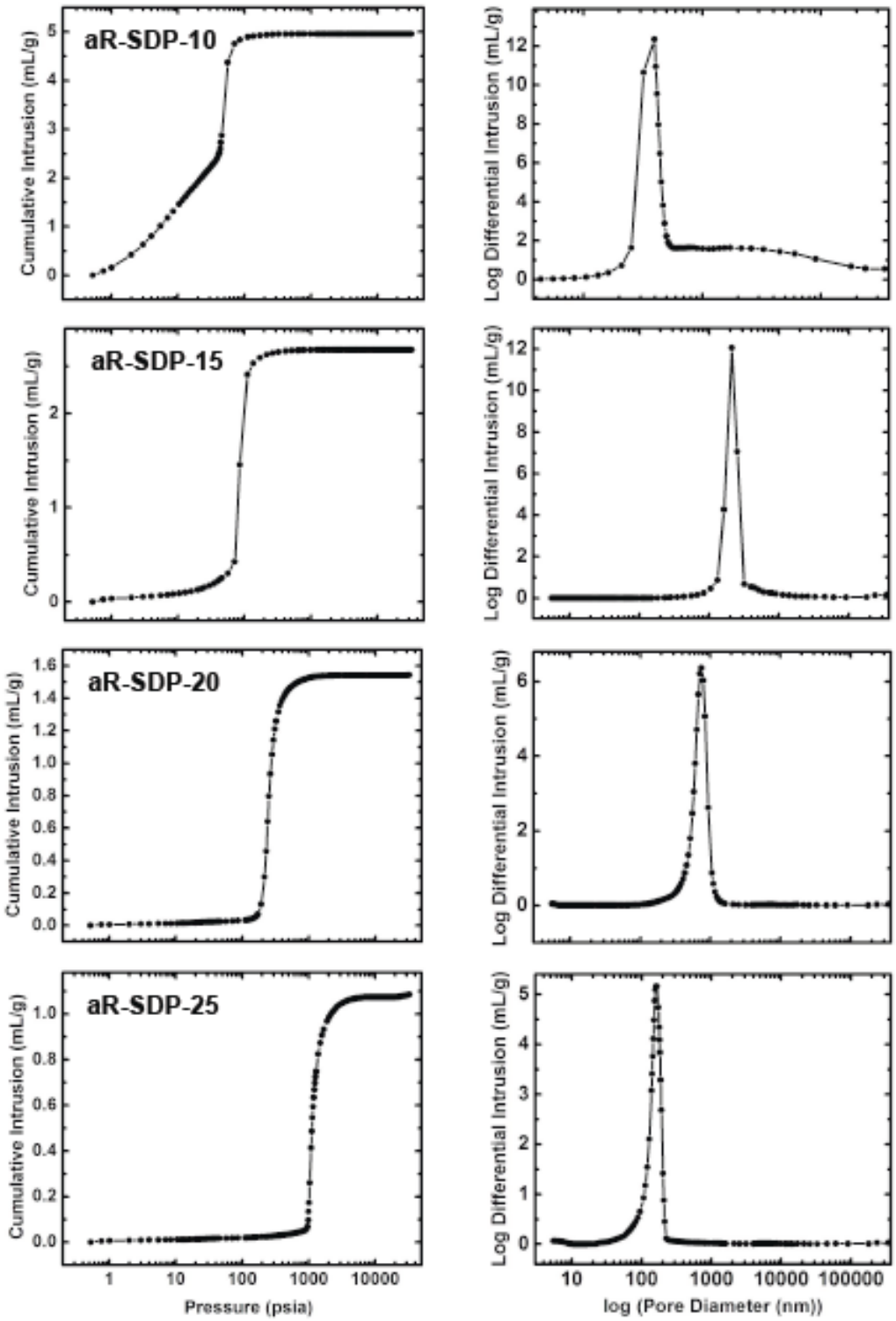

Figure S.16 Hg-porosimetry data (left) and corresponding pore size distribution curves (right) for **aR-SDP-xx** aerogels.

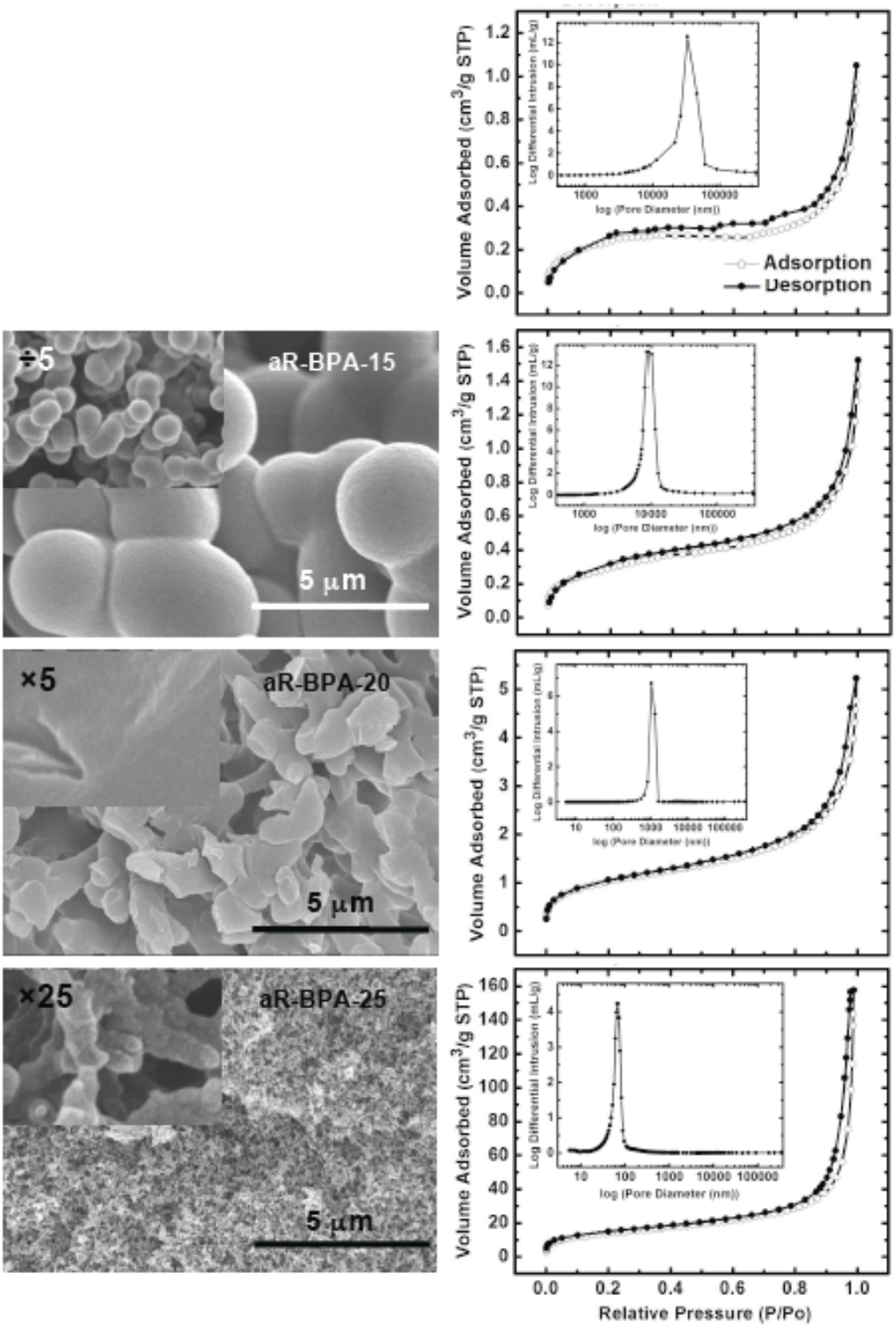

Figure S.17 SEM and N_2 sorption porosimetry data for the **aR-BPA-xx** aerogels. (Insets: pore size distributions from Hg-intrusion porosimetry data.)

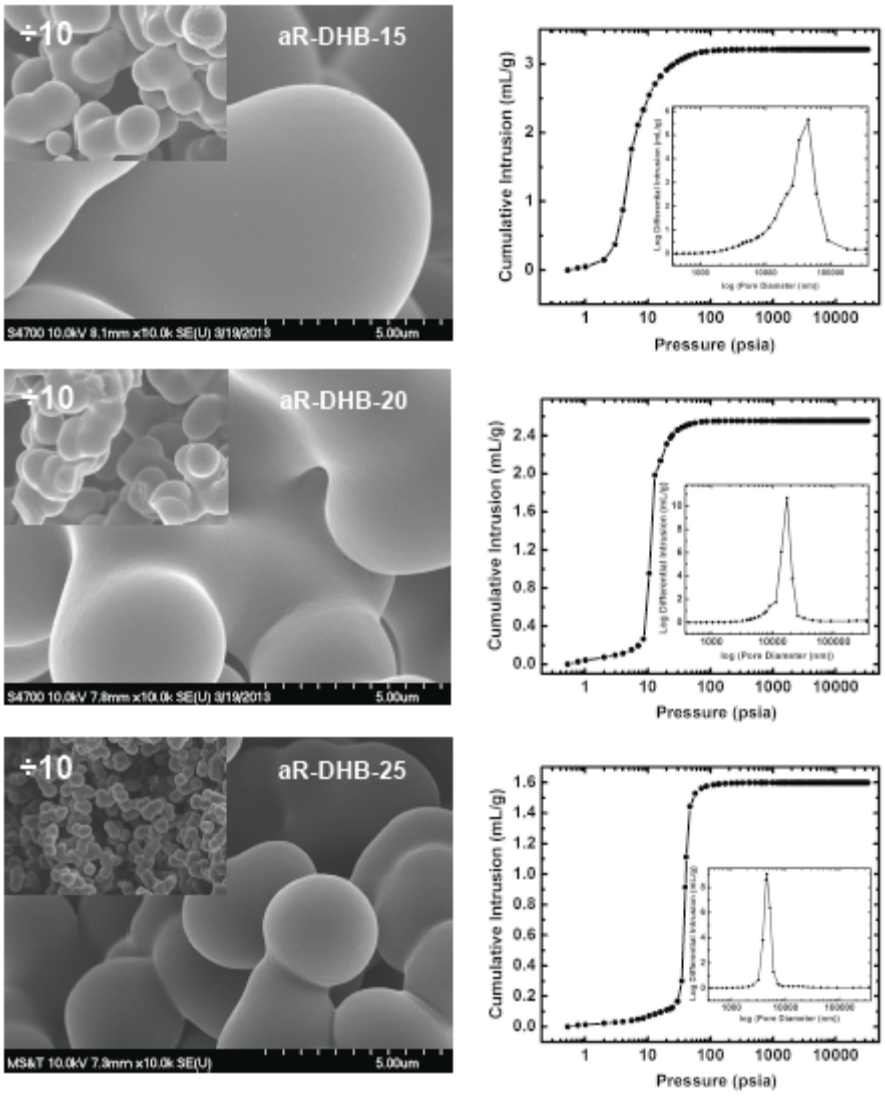

Figure S.18 SEM and Hg-intrusion porosimetry data for the **aR-DHB-xx** aerogels. (Insets: pore size distributions from the Hg-intrusion porosimetry data.)

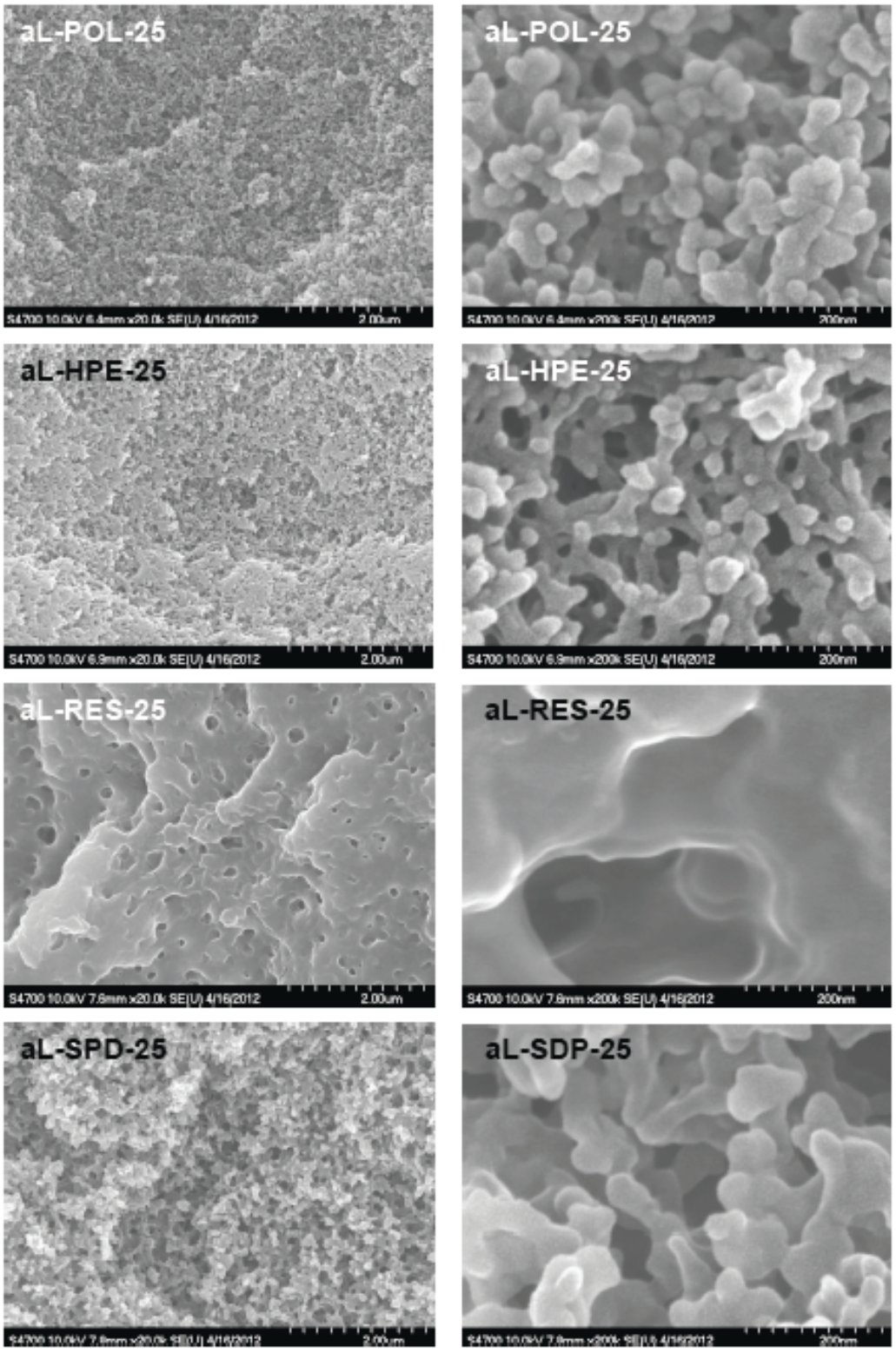

Figure S.19 SEM at two different magnifications of **aL-ALC-xx** aerogels (as indicated).

(Continued on next page.)

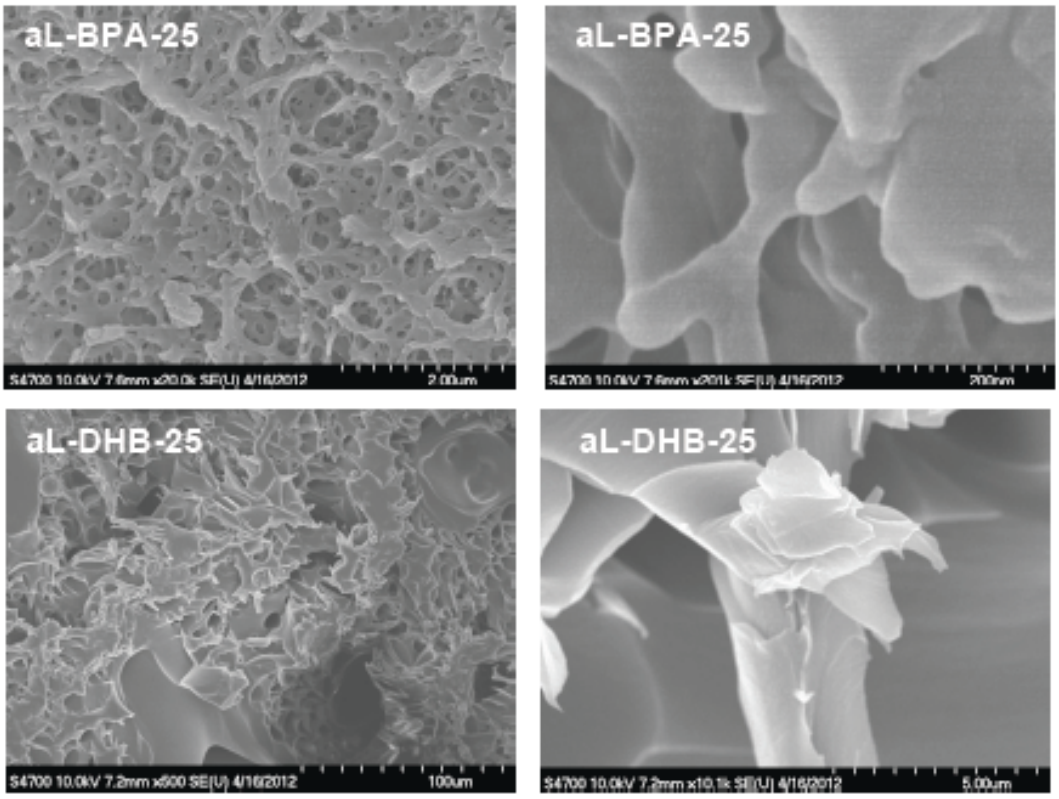

Figure S.19 (Continued) SEM at two different magnifications of **aL-ALC-xx** aerogels (as indicated).

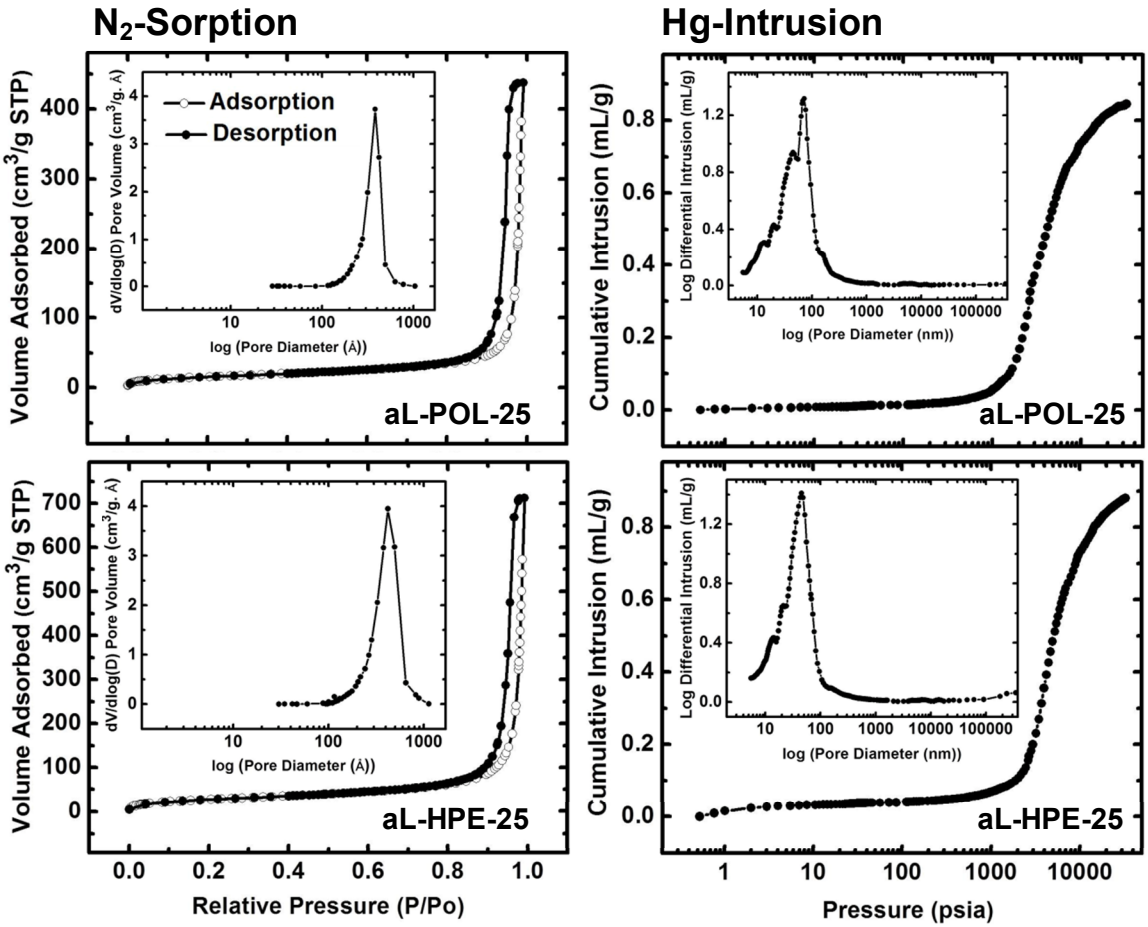

Figure S.20 Porosimetry data for **aL-POL-25 and aL-HPE-25** aerogels via N_2-sorption and Hg-intrusion. (Insets: Corresponding pore size distributions as indicated).

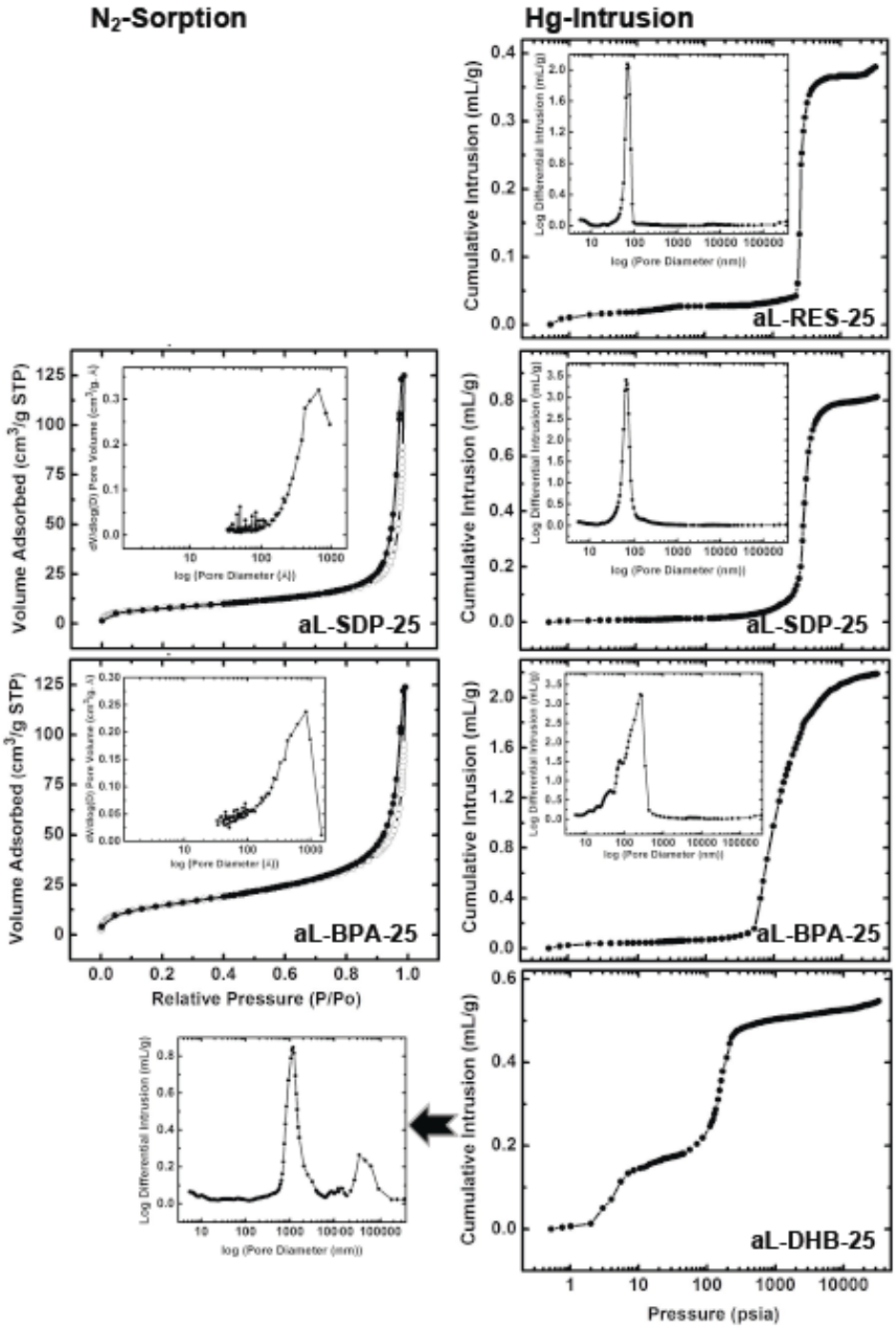

Figure S.21 Porosimetry data for **N3300A**-based **aL**-aerogels via N_2-sorption and Hg-intrusion. (Insets: Corresponding pore size distributions as indicated).

Appendix V. Representative SAXS data – case of aR-POL-xx

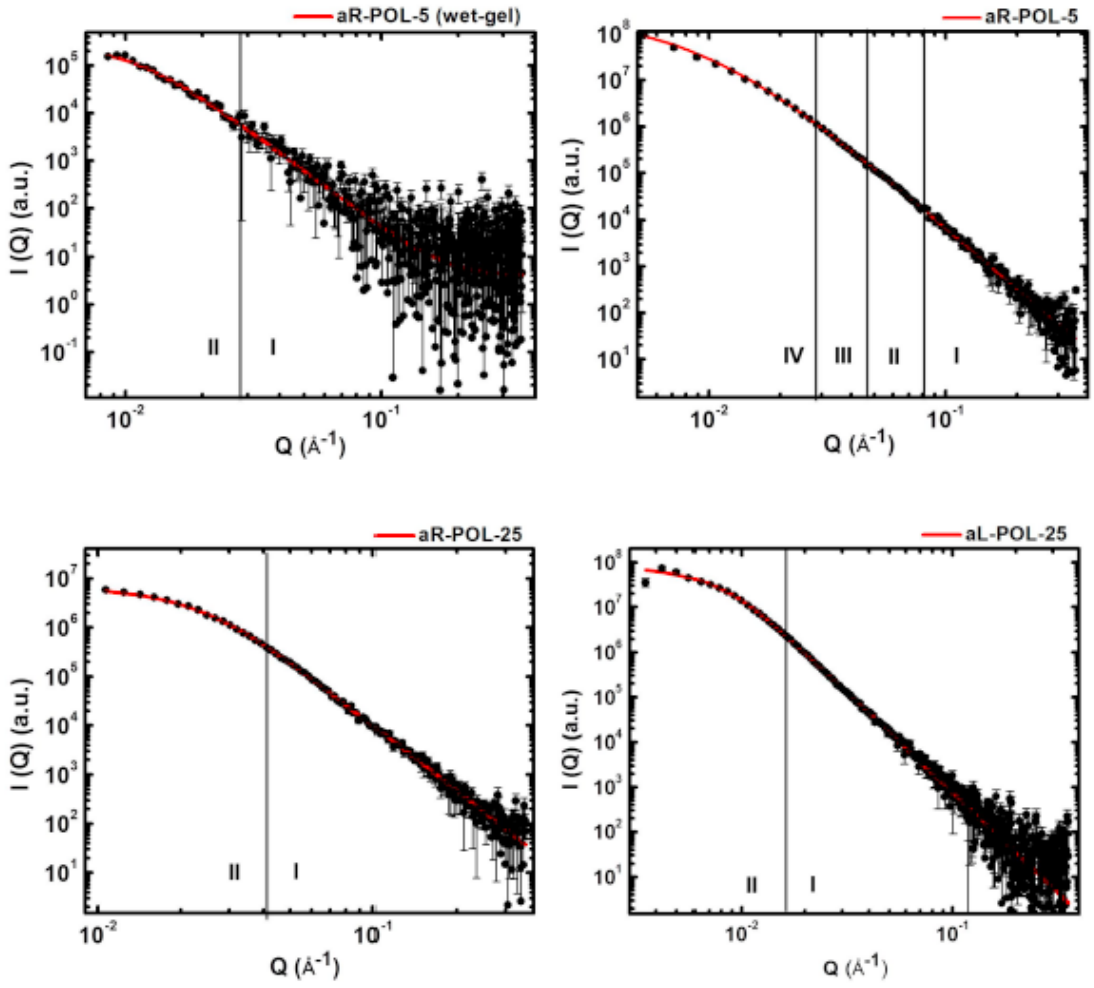

Figure S.22 Representative small angle X-ray scattering (SAXS) depicted with selected **aR-POL-xx** samples, including a wet-gel (of **aR-POL-5)** as shown. Data have been fitted with the Beaucage Unified Model. Results are summarized in Table S.5 below.

Table S.5. Small angle x-ray scattering (SAXS) data of **PU** aerogels

sample	Primary Particles			Secondary Particles			$3/\rho_s\sigma$
	high-Q slope [a]	$R_G(1)$ [b] (nm)	$R(1)$ [c] (nm)	low-Q slope [d]	$R_G(1)$ [e] (nm)	$R(2)$ [c] (nm)	radius [f] (nm)
aR-POL-xx							
aR-POL-5 (gel)	3.97±0.07	16.9±0.7	22.0±0.9				
aR-POL-5	4.29±0.03	$8._8$±$2._0$	$10._7$±$2._6$	3.6±0.4	$27._3$±$6._5$	$35._5$±$8._4$	9.2
aR-POL-10	4.33±0.03	$8._8$±$1._8$	$11._4$±$2._3$	3.1±0.4	$31._5$±$9._1$	41±12	9.2
aR-POL-15	4.28±0.03	$9._1$±$1._1$	$11._4$±$1._4$				9.5
aR-POL-20	4.30±0.01	10.5±0.1	13.6±0.2				11.2
aR-POL-25	4.39±0.02	8.10±0.05	10.52±0.06				9.3
aR-HPE-xx							
aR-HPE-5	4.11±0.03	$12._5$±$1._3$	$16._2$±$1._7$	3.9±0.4	$48._5$±$1._9$	$63._0$±$2._5$	18.5
aR-HPE-10	4.21±0.04	$10._0$±$1._8$	$12._8$±$2._3$	4.1±0.5	34±21	45±27	14.5
aR-HPE-15	4.16±0.03	$9._9$±$1._2$	$12._7$±$1._5$	4.0±0.5	$32._6$±$7._1$	$42._4$±$9._3$	13.7
aR-HPE-20	4.19±0.02	$10._3$±$1._2$	$13._3$±$1._6$	3.4±0.7	33±23	43±30	12.2
aR-HPE-25	4.27±0.04	5.4±0.6	7.1±0.8	3.3±0.5	15.9±0.5	$20._6$±$0._6$	9.3
aR-RES-xx							
aR-RES-10	4.18±0.02	$42._8$±$4._2$	$55._6$±$5._4$				69.6
aR-RES-15	4.16±0.01	$30._7$±$4._5$	$39._9$±$5._8$				28.5
aR-RES-20	4.11±0.01	$23._0$±$1._0$	$29._9$±$1._3$				20.9
aR-RES-25	4.19±0.01	16.8±0.3	21.8±0.4				19.2
aR-SDP-xx							
aR-SDP-10	4.25±0.02	$75._5$±$2._1$	$98._1$±$2._7$				
([g])	(3.97±0.05)	(16.6±0.9)	(21.5±1.1)	(4.4±0.5)	(76.7±2.4)	($99._7$±$3._1$)	812
aR-SDP-15	4.29±0.02	$68._9$±$9._8$	89±13				
([g])	(4.37±0.07)	($13._8$+$1._9$)	($17._7$±$2._5$)	(4.2±0.5)	($60._1$±$8._7$)	($78._1$±$1._1$)	569
aR-SDP-20	4.28±0.02	$53._8$±$2._5$	$69._9$±$3._3$				
([g])	(4.19±0.03)	($15._1$±$1._1$)	($19._7$±$1._5$)	(4.0±0.3)	(66±15)	(86±20)	252
aR-SDP-25	4.27±0.01	$46._3$±$1._3$	$60._2$±$1._7$				74
aR-BPA-xx							
aR-BPA-15	4.28±0.03	$49._6$±$5._1$	$64._4$±$6._6$				2420
aR-BPA-20	4.20±0.02	$61._3$±$4._0$	$79._6$±$5._1$	(4.2±0.4)	($59._0$±$3._9$)	($76._6$±$5._1$)	536

([g])	(4.19±0.06)	($12._6$±$1._1$)	($16._4$±$1._4$)				
aR-BPA-25	4.20±0.01	$34._3$±$1._0$	$44._6$±$1._3$				49.5
aR-DHB-xx							
aR-DHB-15	4.25±0.06	$66._9$±$3._1$	$86._9$±$4._1$				
aR-DHB-20	4.22±0.04	$68._4$±$4._2$	$88._8$±$5._5$				
aR-DHB-25	4.27±0.03	$63._2$±$6._9$	$82._1$±$9._0$				
aL-POL-25	4.43±0.01	24.6±0.3	31.9±0.4				41.0
aL-HPE-25	4.35±0.01	21.0±0.2	27.3±0.3				24.4
aL-RES-25	4.42±0.01	$47._4$±$1._2$	$61._6$±$1._6$				
aL-SDP-25	4.39±0.01	$41._0$±$1._8$	$53._2$±$2._3$				80.9
aL-BPA-25	4.27±0.02	15.2±0.7	19.7±0.8	3.9±0.2	$51._6$±$5._7$	$67._1$±$7._4$	43.4

Referring to Figure S.22 above: [a] From power-law Region I. [b] From Guinier Region II. [c] Particle radius $R = R_G/0.77$. [d] From power-law Region III. [e] From Guinier Region IV. [f] From Tables 2 and 3 of the main article. [g] Without affecting the discussion or the conclusions, those data could be also fitted to two length scales; the criterion was a small error (typically ≤10%) in the second power-law slope (Region III). In some instances that operation results in very large errors in $R(2)$.

Appendix VI. Mechanical characterization data for PU aerogels under compression

Table S.6. Comparative compression data under quasi-static and under dynamic loading conditions at room temperature (23 °C) for all polyurethane (**PU**) aerogels of this study (data selected from Tables S.7 and S.8 below) [a]

sample	bulk density ρ_b (g cm^{-3})	Young's modulus (E, MPa)		ultimate strain (%)		ultimate strength (MPa)		specific energy absorption (J g^{-1})	
		quasi-static	dynamic	quasi-static	dynamic	quasi-static	dynamic	quasi-static	dynamic
aR-POL-xx									
aR-POL-5	0.159 ± 0.006	[b]	[c]	80 ± 4	[c]	11 ± 5	[c]	10 ± 4	[c]
aR-POL-10	0.298 ± 0.004	22.7 ± 1.2	37 ± 3	76 ± 2	84 ± 4	57 ± 7	149 ± 86	28 ± 1	71 ± 6
aR-POL-15	0.477 ± 0.008	203 ± 4	325 ± 8	76 ± 1	69 ± 5	247 ± 4	142 ± 60	68 ± 10	69 ± 3
aR-POL-20	0.640 ± 0.010	447 ± 12	855 ± 23	76 ± 0	56 ± 3	360 ± 18	181 ± 45	86 ± 7	68 ± 9
aR-POL-25	0.760 ± 0.050	750 ± 0	2224 ± 437	69 ± 1	50 ± 1	342 ± 10	224 ± 30	84 ± 2	74 ± 10
aL-POL-25	0.652 ± 0.028	380 ± 28	[c]	84 ± 1	[c]	339 ± 23	[c]	66 ± 1	[c]
aR-HPE-xx									
aR-HPE-10	0.184 ± 0.007	1.0 ± 0.2	[c]	75 ± 0	[c]	10 ± 1	[c]	6.7 ± 0.7	[c]
aR-HPE-15	0.315 ± 0.003	49 ± 2	99 ± 12	79 ± 1	74 ± 3	78 ± 15	55 ± 9	38 ± 5	43 ± 5
aR-HPE-20	0.426 ± 0.008	1.4 ± 0.0	342 ± 20	75 ± 1	65 ± 4	160 ± 17	109 ± 19	57 ± 3	61 ± 4
aR-HPE-25	0.567 ± 0.002	343 ± 12	708 ± 27	74 ± 1	64 ± 3	292 ± 10	187 ± 29	72 ± 7	89 ± 3
aL-HPE-25	0.563 ± 0.004	363 ± 18	[c]	82 ± 1	[c]	505 ± 40	[c]	103 ± 3	[c]
aR-RES-xx									
aR-RES-10	0.244 ± 0.005	[b]	[c]	68 ± 5	[c]	14 ± 1	[c]	15 ± 5	[c]
aR-RES-15	0.404 ± 0.001	108 ± 12	248 ± 68	82 ± 1	68 ± 4	204 ± 5	101 ± 21	59 ± 10	59 ± 14
aR-RES-20	0.565 ± 0.004	390 ± 14	697 ± 65	76 ± 3	63 ± 1	313 ± 10	137 ± 20	77 ± 6	67 ± 6
aR-RES-25	0.680 ± 0.003	650 ± 0	1145 ± 129	77 ± 1	60 ± 2	390 ± 24	172 ± 39	102 ± 10	75 ± 8

aL-RES-25 [d]									
aR-SDP-xx									
aR-SDP-15	0.307 ± 0.007	8.7 ± 1.5	[c]	71 ± 1	[c]	15 ± 3	[c]	8.8 ± 0.7	[c]
aR-SDP-20	0.422 ± 0.003	133 ± 6	270 ± 32	74 ± 2	75 ± 1	85 ± 14	86 ± 11	37 ± 3	55 ± 6
aR-SDP-25	0.541 ± 0.004	340 ± 17	695 ± 75	76 ± 2	61 ± 3	200 ± 18	123 ± 21	61 ± 6	56 ± 6
aL-SDP-25	0.639 ± 0.005	315 ± 15	[c]	85 ± 2	[c]	493 ± 30	[c]	91 ± 6	[c]
aR-BPA-xx									
aR-BPA-15	0.293 ± 0.005	3.0 ± 0.7	[c]	60 ± 1	[c]	4.6 ± 0.5	[c]	3.2 ± 0.5	[c]
aR-BPA-20	0.460 ± 0.002	220 ± 17	116 ± 14	79 ± 1	77 ± 2	214 ± 16	68 ± 5	81 ± 8	41 ± 2
aR-BPA-25	0.567 ± 0.005	400 ± 0	857 ± 22	80 ± 1	60 ± 3	396 ± 30	146 ± 21	98 ± 6	64 ± 2
aL-BPA-25	0.160 ± 0.013	49 ± 9	[c]	76 ± 3	[c]	230 ± 8	[c]	55 ± 1	[c]
aR-DHB-xx									
aR-DHB-15	0.243 ± 0.009	1.2 ± 0.2	[c]	52 ± 4	[c]	0.70 ± 0.07	[c]	0.75 ±0.03	[c]
aR-DHB-20	0.309 ± 0.003	7 ± 2	[c]	59 ± 3	[c]	5.6 ± 0.7	[c]	4.2 ± 0.8	[c]
aR-DHB-25	0.432 ± 0.007	15 ± 1	[c]	57 ± 2	[c]	17.5 ± 1.5	[c]	8.9 ± 0.8	[c]
aL-DHB-25 [d]									

[a] Average of five samples each formulation. Quasi-static loading: strain rate in the range 0.003-0.006 s^{-1}; dynamic loading: strain rate in the range 1000-1500 s^{-1} (see Table S.8 below). [b] Low stress, could not be determined reliably with the load-cell employed. [c] Sample was not tested. [d] Sample came from a floc, brittle, not-tested.

Table S.7. Comprehensive mechanical characterization data under quasi-static compression at room temperature (23 ^{o}C) of both **aR-** and **aL-** polyurethane (**PU**) aerogels

bulk density ρ_b (g cm^{-3})	strain rate (s^{-1})	Young's modulus *E* (MPa)	speed of sound (m s^{-1}) [a]	yield stress at 0.2% offset strain (MPa)	ultimate strength *UCS* (MPa)	ultimate strain (%)	specific energy absorption (J g^{-1}) [b]
aR-POL-xx							
0.159 ± 0.006	0.006	--			11.3±4.5	80±4	10±4
0.298 ± 0.004	0.006	22.7±1.2	276	0.27±0.04	57±7	76±2	28±1
0.477 ± 0.008	0.006	203±4	652	3.42±0.97	247±4	76±1	68±10
0.640 ± 0.010	0.006	447±12	836	9.10±0.14	360±18	76±0	86±7
0.760 ± 0.050	0.006	750±0	993	14.00±1.32	342±10	69±1	84±2
aL-POL-25							
0.652 ± 0.028	0.006	380±28	763	10.06±0.64	339±23	84±1	66±1
aR-HPE-xx							
0.184 ± 0.007	0.005	1.0±0.2	74	0.04±0.01	10±1	75±0	6.7± 0.7
0.315 ± 0.003	0.005	48.8±1.8	394	0.72±0.10	78±15	79±1	38±5
0.426 ± 0.008	0.005	1.4±0.0	57		160±17	75±1	57± 3
0.567 ± 0.002	0.005	343±12	778	5.25±1.09	292±10	74±1	72±7
aL-HPE-25							
0.563 ± 0.004	0.006	363±18	803	5.50±0.70	505±40	82±1	103± 3
aR-RES-xx							
0.244 ± 0.005	0.005	--			14±1	68±5	14.54 ±
0.404 ± 0.001	0.005	108±12	517	2.75±0.48	204±5	82±1	59 ± 10
0.565 ± 0.004	0.005	390±14	831	6.05±0.77	313±10	76±3	77 ± 6
0.680 ± 0.003	0.005	650±0	978	13.75±1.06	390±24	77±1	102±10
aR-SDP-xx							
0.307 ± 0.007	0.006	8.7±1.5	168	0.24±0.01	15±3	71±1	8.8 ± 0.7
0.422 ± 0.003	0.006	133±6	561	2.63±0.40	85±14	74±2	37±3
0.541 ± 0.004	0.005	340±17	793	5.50±1.50	200±18	76±2	61±6
aL-SDP-25							
0.639 ± 0.005	0.006	315±15	702	4.93±0.23	493±30	85±2	91± 6

Table S.5 (Continued)

aR-BPA-xx							
0.293 ± 0.005	0.005	3.0±0.7	101	0.12±0.01	4.6±0.5	60±1	3.2 ± 0.5
0.460 ± 0.002	0.005	220±17	692	5.83±0.40	214±16	79±1	81±8
0.567 ± 0.005	0.005	400±0	840	9.88±0.53	396±30	80±1	98±6
aL-BPA-25							
0.160 ± 0.013	0.003	49±9	553	0.58±0.08	230±8	76±3	55±1
aR-DHB-xx							
0.243 ± 0.009	0.005	1.2±0.2	70	0.07±0.01	0.70±0.07	52±4	0.75±0.03
0.309 ± 0.003	0.005	7±2	151	0.25±0.04	5.6±0.7	59±3	4.2 ± 0.8
0.432 ± 0.007	0.005	15±1	186	0.85±0.02	17.5±1.5	57±2	8.9 ± 0.8

[a] The speed of sound through the various samples is calculated from the Young's modulus, E, and the bulk density, ρ_b, via: speed of sound = $(E/\rho_b)^{0.5}$. In some cases the speed of sound is much lower than the speed of sound in the open air, rendering those materials viable candidates for acoustic insulation. [b] From the integrated area under the stress-strain curves

Table S.8. Comprehensive compression data at room temperature (23 °C) for selected **aR-ALC-xx** polyurethane aerogels at high strain rates using the split Hopkinson pressure bar at the University Texas-Dallas (For definitions and interpretation of E_2, $\sigma_{0.2}$ and σ_y see Figure S.23 below.)

bulk density ρ_b (g cm^{-3})	strain rate (s^{-1})	Young's modulus E_1 (MPa)	plastic modulus E_2 (MPa)	yield strength at 0.2% offset strain $\sigma_{0.2}$ (MPa)	yield strength σ_y (MPa)	ultimate strength (MPa)	ultimate strain (%)	intercept σ_0 (MPa)	specific energy absorption (J g^{-1})
aR-POL-xx									
0.298±0.004	1491±257	37±3	16±2	2.7±1.1	2.8±1.1	149±86	84±4	1.1±0.6	71±6
0.477±0.008	1220±168	325±8	60±1	10.3±1.0	13.4±1.2	142±60	69±5	10.9±1.1	69±3
0.640±0.010	1053±75	855±23	123±18	30±1	40±2	181±45	56±3	34±1	68±9
0.760±0.050	969±39	2224±437	171±12	48±8	71±9	224±30	50±1	66±9	74±10
aR-HPE-xx									
0.315±0.003	1121±41	99±12	24±3	3.7±0.4	4.6±0.5	55±9	74±3	3.4±0.4	43±5
0.426±0.008	1139±61	342±20	47±3	8.9±0.6	13.5±0.9	109±19	65±4	11.7±0.8	61±4
0.567±0.002	1218±114	708±27	85±3	19±1	31±1	187±29	64±3	26.4±1.2	89±3
aR-RES-xx									
0.404±0.001	1132±90	248±68	41±11	9±2	11.4±2.5	101±21	68±4	10.1±2.2	59±14
0.565±0.004	1064±53	697±65	73±7	21±2	30±2	137±20	63±1	27±2	67±6
0.680±0.003	1095±82	1145±129	88±10	30±3	48±5	172±39	60±2	45±4	75±8
aR-SDP-xx									
0.422±0.003	1196±24	270±32	29±3	8.2±0.6	11.4±0.8	86±11	75±1	10.1±0.7	55±6
0.541±0.004	1036±60	695±75	60±7	19±2	27±3	123±21	61±3	25±3	56±6
aR-BPA-xx									
0.460±0.002	1143±38	116±14	42±5	4.2±0.4	5.4±0.5	68±5	77±2	3.3±0.3	41±2
0.567±0.005	1049±82	857±22	74±2	22.5±0.2	34.1±0.3	146±21	60±3	31.1±0.3	64±2

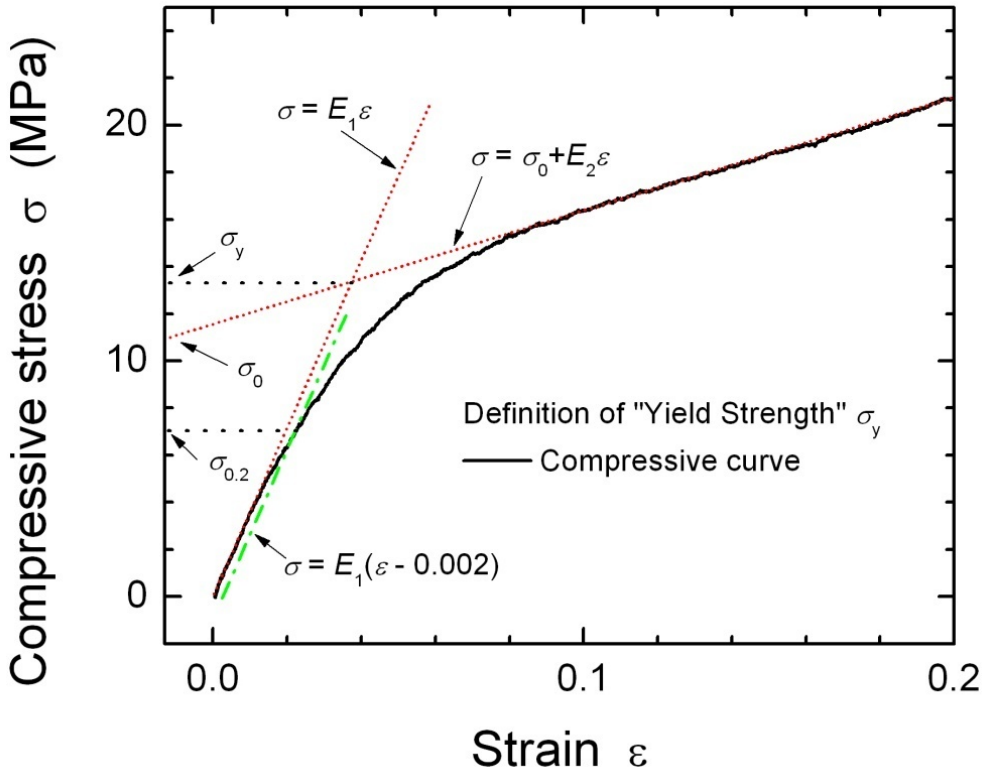

Figure S.23 Definition of yield strength, σ_y, for aerogels using the dynamic compression data for **aR-HPE-20**. The yield strength calculated at the 0.2% offset strain ($\sigma_{0.2}$ - see Table S.8) seems to be too low: the materials seem able to work reproducibly at higher stresses. Therefore, we consider defining the yield strength in a different way. Looking at the intersection of two tangents (the one from the loading portion in the elastic range, and the one from the hardening portion in the plastic hardened stage), as well as the 0.2% offset yield strength, *we define a new yield strength (σ_y) especially for aerogels*. Here the initial part of the plastic hardened stage can be considered as linearly plastic, therefore $\sigma=\sigma_0+E_2\varepsilon$, whereas σ_0 is the intercept stress of the linear plastic stage, and E_2 is the plastic modulus in the hardened stage. The linear elastic stage is described as usually by $\sigma=E_1\varepsilon$; E_1 is the Young's modulus. Physically, the yield strength σ_y is the preconsolidation pressure, a similar definition of compression as used in soil mechanics. The "new" yield strength increases with increasing bulk density and is a more useful quantity than $\sigma_{0.2}$ because it more accurately represents both the linear elastic and the non-linear elastic regimes.

A.

B.

Pristine **aR-HPE-25** **aR-HPE-20** **aR-HPE-15**

Figure S.24 Photographs of pristine samples and after compression (A) Quasi-static; (B) Dynamic. (Notice the barreling in the pristine **aL-BPA-25** sample, due to swelling upon drying. Samples for compression were machined out of pristine samples.)

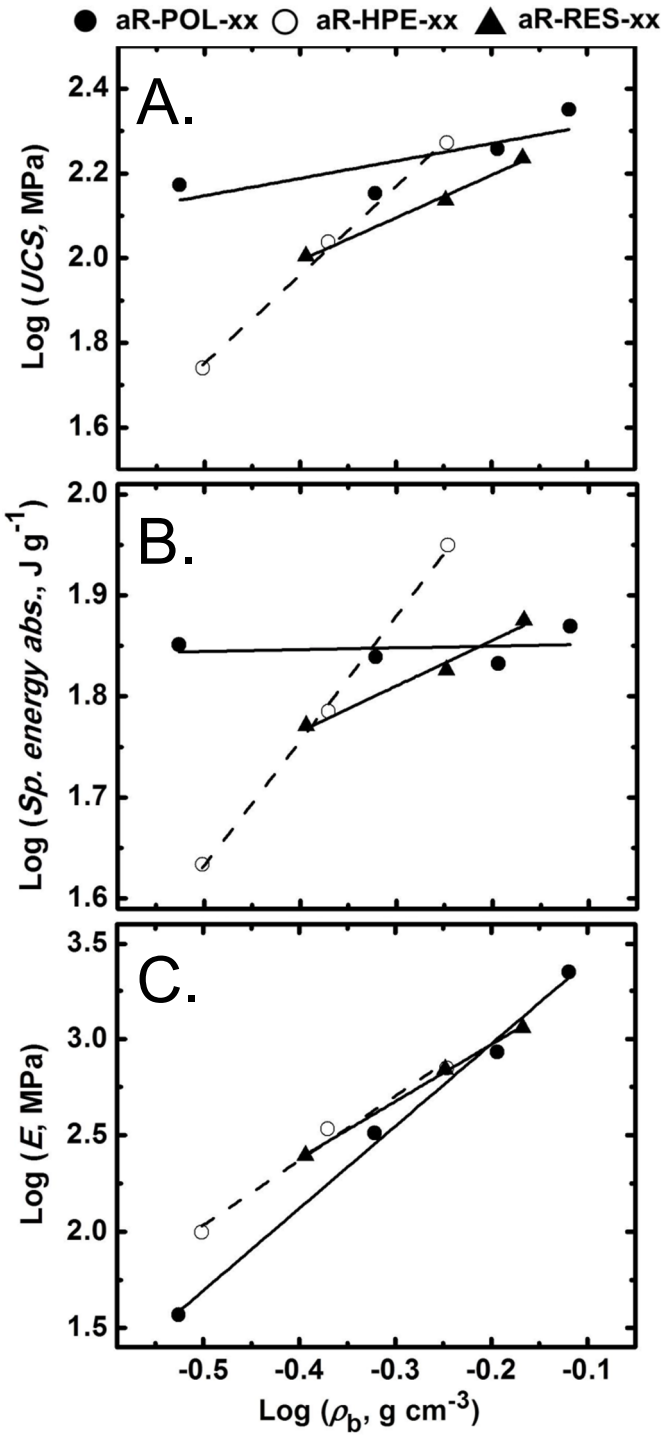

Figure S.25 Log-Log plots from the dynamic compression data of **aR-ALC-xx** aerogels: (A) Ultimate compressive strength (*UCS*) versus bulk density. (B) Specific energy absorption versus bulk density. (C) Young's modulus (*E*) versus bulk density.

Appendix VII. Representative MDSC data for selected aL-ALC-xx aerogels

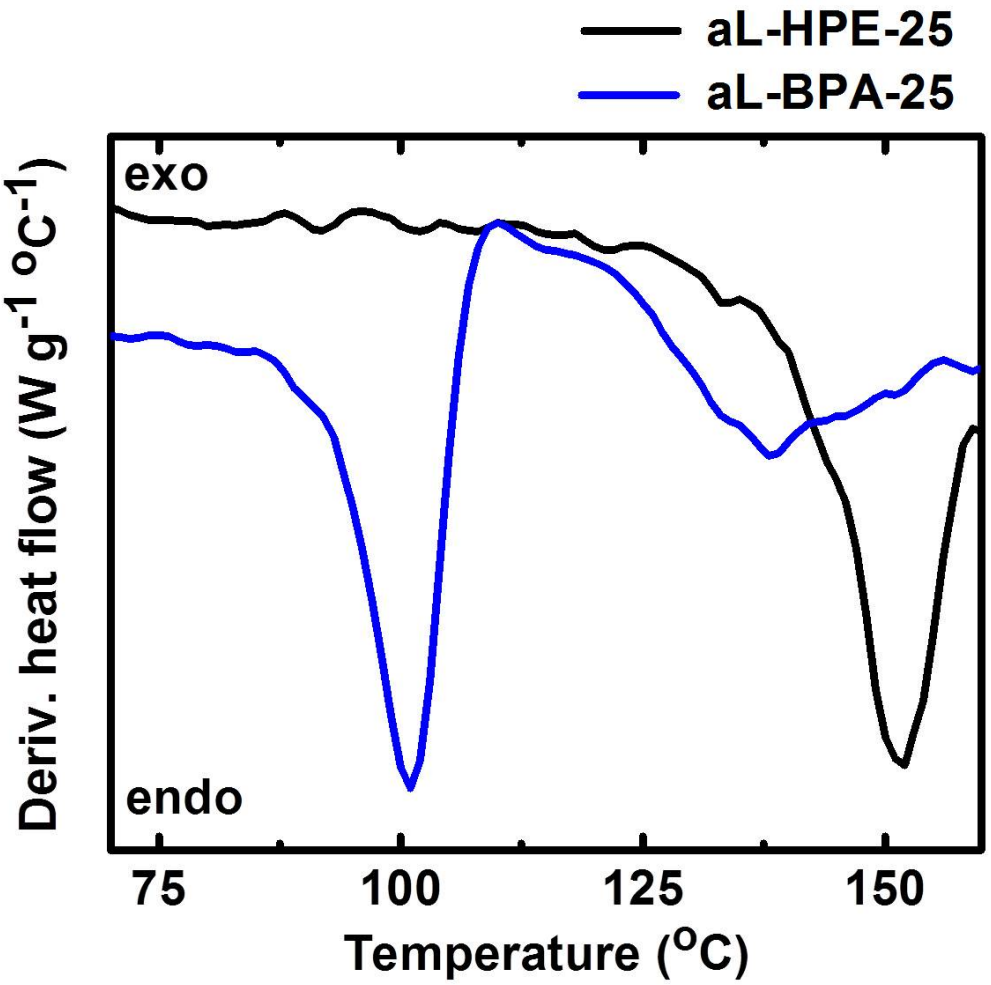

Figure S.26 Modulated differential scanning calorimetry (MDSC) under N_2 at 10 ^{o}C min^{-1} showing the T_g of two representative **aL-**aerogels as indicated.

II. Introducing Petal-Effect Superhydrophobicity in Hydrophilic Polyurea: Flexible Nanofibrous Aerogels with Applications in Environmental Remediation

Nicholas Leventis*, Chakkaravarthy Chidambareswarapattar and Chariklia Sotiriou-Leventis*

Department of Chemistry, Missouri University of Science and Technology, Rolla, MO 65409, U.S.A. leventis@mst.edu, cslevent@mst.edu

Submitted for Publication as a communication to the *J. Am. Chem. Soc.*

Abstract: Polyurea aerogels were prepared in one-step via the sol-gel reaction of an aliphatic triisocyanate and water. Notwithstanding the inherent hydrophylicity of the dense polymer (water contact angle θ=69.1±0.2^o), texture-related super-hydrophobicity was imparted with no use of templates via rational design of the gelation process. Morphostructurally, the material consists of solid polymeric microspheres entrapped in nanofiber web. Water droplets (5 μL) form contact angles up to 150^o and stick to the surface when the substrate is turned upside-down (Petal effect). Monoliths display texture-related oleophilicity in inverse order to hydrophobicity, hold a high capacity for oil absorption (>10:1 w/w), float on water, can be harvested and reused.

Aerogels are inherently nanostructured highly porous solids, thereby reasonable platforms for economic access to texture-related superhydrophobicity. The design parameters set forth below call for particles entrapped in fibers. This is exemplified with polyurea aerogels synthesized in one step at room temperature from an inexpensive aliphatic triisocyanate (N3300A) and water, using triethylamine (Et_3N) as catalyst (Scheme 1, and Experimental in Appendix S.1 of the Supporting Information).

Scheme 1. Synthesis of Polyurea (PUA) Aerogels

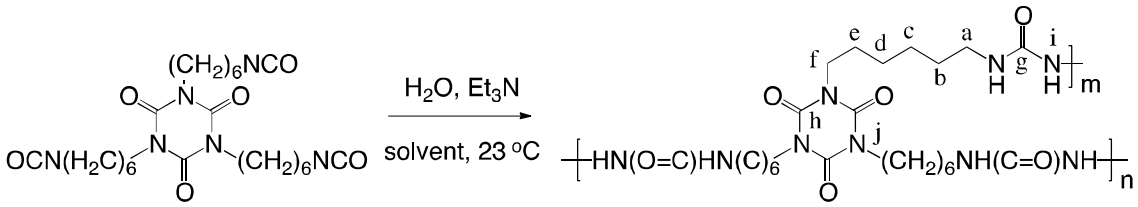

Hydrophobicity is important for applications in self-cleaning materials, corrosion and biofouling prevention, drag reduction in microfluidic devices, and environmental remediation e.g., in oil-spill clean up.[1] Hydrophobicity is introduced via either chemical or textural modification and is quantified with the contact angle, θ, of water droplets on flat surfaces. The upper theoretical limit of θ on smooth close hexagonally-packed low-energy $-CF_3$ groups is 119^o.[2] Textured surfaces on the other hand may yield much higher θ values, often $>150^o$, in which case they are classified as superhydrophobic. There are two main models for texture-related hydrophobicity. The Wenzel model considers the surface roughness (r, always >1) and assumes that water enters the crevices between surface features under the droplet. The contact angle on a flat texture surface, θ', is given by eq. 1, where θ is Young's contact angle on the smooth non-textured material.

$$\cos \theta' = r \cos \theta \qquad (1)$$

Clearly, the Wenzel model predicts superhydrophobicity only for already hydrophobic materials (i.e., $\theta>90^o$).[3] In the Cassie-Baxter model, water does not enter the crevices between surface features; the droplet is "suspended" over the surface, touching only at the apexes of the roughness (the fakir state).[4] The model is quantified by eq 2, whereas f is the fraction of the actual contact area between droplet and substrate.

$$\cos \theta' = f(\cos \theta + 1) - 1 \qquad (2)$$

Oftentimes, mention is made about the air trapped in the crevices underneath the droplet, however, as demonstrated herewith, presence of air is not relevant. Importantly, the Cassie-Baxter model predicts hydrophobic behavior ($\cos\theta' < 0$) even for *hydrophilic* materials ($\cos\theta > 0$) as long as $f < 1/(\cos\theta + 1)$. That property is embedded implicitly in several literature reports,[5] but is explicitly possible only within the Cassie-Baxter model, and comprises a basic design parameter of this study.

Inspired from Nature, there are two limiting cases for superhydrophobicity. The Lotus effect (from the leaves of the plant[6]) is expected intuitively from superhydrophibic surfaces, and describes situations whereas water droplets run off by the slightest tilt of the surface (typically by $< 5^{o}$); it is used by many plants (to stay clean), insects (to stand on water) and animals (to stay dry). In the more subtle Petal effect (from the petals of red rose) a droplet that seemingly barely touches the superhydrophobic surface underneath, sticks to it and oftentimes stays in place when the substrate is turned upside-down.[7] The Petal effect has been attributed to non-covalent interactions (e.g., van der Waals) and capillary effects, and possible applications are in lab-on-a-chip devices.[8] Both the lotus leaf and the red rose petal are rough, bearing regular patterns of micron-sized protrusions, and have been replicated by molding.[7,9] Imitating superhydrophobic surfaces artificially typically involves elaborate multi-step processing.[10] For example, Lotus-effect surfaces of particular interest bear microfabricated patterns with microbeads or grass-like nanopillars;[11] by increasing the aspect ratio of the latter, the surface layer evolves into entangled nanofibers, e.g., of carbon or polymer.[12] In that regard, owing to the inherent relevance of Lotus-effect fibers to textiles, a significant body of research has focused on electrospinning nanofiber webs.[13] This is also a rather complex process hampered by low

rates of production and high raw material cost, however, a persistent observation has been that if electrospun fiber webs include 'knots' (normally considered defects) they display higher contact angles.[14] Hence, efforts met with considerable success have been made to introduce nanoparticles (e.g., TiO_2) deliberately.[15]

In contrast, aerogels are prepared easily from wet-gels, which in turn are obtained from suitable sols via simple physical or chemical cooling. Rendering silica aerogels hydrophobic via surface-modification with $-CH_3$ groups, [16] has allowed ambient-pressure drying and has had an economic impact in terms of mass production.[17] Similarly, polystyrene-crosslinked silica aerogels are hydrophobic ($\theta = 121^o$) and their poly(pentafluorostyrene)-analogues are superhydrophobic ($\theta = 151^o$),[18] which, according to the above, is the result of both low surface energy and texture. More recently, co-gelation by physical cooling of solutions of linear polystyrene and high molecular weight polyethylene oxide led to phase-separation yielding micron-size hydrophilic macropores with sub-micron hydrophobic wells. Those materials were Petal-effect superhydrophobic.[19]

Based on the above, our goal was set at inducing Petal-effect superhydrophobicity by *self-doping* a fibrous hydrophilic polymer with particles. Polyurea (PUA) was chosen as a viable candidate because running the gelation process of Scheme 1 in acetone (η=0.36 cP, dielectric constant ε=20.7) yields concentration-dependent nanostructures: fibrous at low densities (Figure 1A) turning to particulate as density increases (Figure 1B).[20] Materials are abbreviated as **PUA-solvent-xxx**, whereas **–xxx** stands for the molar concentration of N3300A in the sol (i.e., [N3300A]=0.xxx M). Reasoning that N3300A, a viscous (η=2,500 cP) nonpolar (ε=7.8 at 220 Hz) liquid, modifies the properties of the

medium significantly, we kept its concentration low (at 0.109 M), and switched the gelation solvent to the more viscous, more polar, stronger hydrogen-bonding DMF (η=0.92 cP, ε=36.7). The nanostructure of low-densiy **PUA-DMF-109** is better described as strings-of-beads (Figure 1C). By going to DMSO (η=2.24 cP, ε=46.7) the nanostructure consists exclusively of clusters of particles (Figure 1D). Based on those findings, we moved to low-viscosity, highly polar but weakly hydrogen-bonding acetonitrile (ACN, η=0.38 cP, ε=37.5). Gelation times decreased drastically (to <30 min) at all concentrations. More importantly though, apparent and formal gelation times (the latter by rheometry – Appendix S.2 in Supporting Information) match each other extremely well in **PUA-acetone-xxx** and **PUA-DMF-xxx**, but somewhat less so in **PUA-ACN-xxx,** implying that the sol evolved differently, probably passing through thixotropic states with different compositions.

Microstructurally, ACN-derived aerogels are hybrids between the two extremes (acetone and DMSO), consisting of spherical moieties trapped in fiber web. Varying the concentration of N3300A has a profound effect on the relative ratio of spheres to fibers (Figure 2): **PUA-ACN-109** (ρ_b=0.073 g cm^{-3}) is mostly fibrous, **PUA-ACN-296** (ρ_b=0.172 g cm^{-3}) consists of spheres entangled in a fiber web, and **PUA-ACN-517** (ρ_b=0.347 g cm^{-3}) is mostly spherical. Thus, **PUA-acetone-xxx** and **PUA-ACN-xxx** are similar in that both move from fibrous to particulate as [N3300A] increases. The two key differences between the two materials though are that in **PUA-ACN-xxx**: (a) particles and fibers coexist at all densities, and (b) particles are much larger (micron size) than any of those observed in any other solvent (nm size). The question is whether spheres are hollow, solid or particulate, and how they relate to fibers.

Spheres and fibers are chemically identical as all materials, irrespective of solvent and [N3300A], have identical solid-state ^{13}C and ^{15}N CPMAS NMR spectra (Figure 3A). Macroscopically, corresponding **PUA-ACN-xxx** and **PUA-acetone-xxx** shrink similarly during processing and all monoliths look alike. Consequently, bulk densities, ρ_b, and porosities, Π, track each other closely between materials from the two solvents (Table 1). As a further probe of interconnectivity, the solid thermal conduction, λ_s (in W m^{-1} K^{-1}, Appendix S.3), through the **PUA-ACN-xxx** network scales with ρ_b as $\lambda_s=0.13\times(\rho_b)^{0.99}$, i.e., very similarly to **PUA-acetone-xxx** ($\lambda_s=0.10\times(\rho_b)^{1.00}$ – Figure 3B),[21] supporting the overall similar structural evolution identified with SEM in both materials, from fibers to particles, as ρ_b increases. However, (a) the BET surface areas of **PUA-ACN-xxx** (5-25 m^2 g^{-1}) are much lower than those of **PUA-acetone-xxx** (56-187 m^2 g^{-1}, Table 1); and, (b) at lower densities, **PUA-ACN-109** are flexible, while **PUA-acetone-109** are much more rigid (Figure 3C and Movies S.1 and S.2 in Supporting Information).

Table 1. Materials characterization for PUA aerogels prepared in three different solvents, as indicated.

Sample [a]	Bulk density ρ_b (g cm^{-3}) [b]	Skeletal density ρ_s (g cm^{-3}) [c]	Porosity Π (% v/v) [d]	BET surface area σ (m^2 g^{-1})	Particle radius (nm) [e]	$R(1)$ (nm) [f]	Water contact angle θ' (^{o})	C-B fraction f [g]
PUA-ACN-109	0.073 ± 0.002	1.19_7± 0.013	94	25	100	9.9 ± 0.9	116.2 ± 0.1	0.41
PUA-ACN-207	0.126 ± 0.002	1.17_7 ± 0.099	89	18	142	13.1 ± 0.1	133.0 ± 0.1	0.23
PUA-ACN-296	0.172 ± 0.007	1.201 ± 0.009	86	11	227	$16._6$ ± $3._2$	150.2 ± 0.5	0.097
PUA-ACN-517	0.347 ± 0.001	1.180 ± 0.004	70	5.1	509	$10._4$ ± $1._9$	127.6 ± 0.2	0.29
PUA-DMF-109	0.076 ± 0.002	1.210 ± 0.006	94	307	8.07	6.5 ± 0.3	104.4 ± 0.1	0.55
PUA-DMF-207	0.426 ± 0.004	1.270 ± 0.009	66	237	10.0	12.5 ± 0.0_3	102.3 ± 0.1	0.58
PUA-acetone-109	0.075 ± 0.003	1.201 ± 0.008	94	187	13.4	11.3 ± 0.6	$102._4$ ± $1._3$	0.58
PUA-acetone-207	0.126 ± 0.001	1.265 ± 0.006	90	169	14.0	11.9 ± 0.4	97.3 ± 0.1	0.64
PUA-acetone-296	0.172 ± 0.001	1.215 ± 0.002	86	68	36.3	19.4 ± 0.1	101.9 ± 0.0_4	0.59
PUA-acetone-517	0.465 ± 0.002	1.200 ± 0.001	61	56	44.6	$47._6$ ± $1._3$	100.1 ± 0.1	0.61

[a] Numerical extensions denote the [N3300A] in mM. [b] Average of 5 samples. [c] Single sample, average of 50 measurements. [d] Via: $\Pi=100\times(\rho_s-\rho_b)/\rho_s$. [e] Particle radii from gas sorption and skeletal density data = $3/\rho_s\sigma$. [f] Primary particle radii from SAXS data, see Appendix S.4 in the Supporting Information. [g] Cassie-Baxter fraction of contact area with the substrate, calculated via eq. 2 using $\theta=69.1^o$ and the measured θ' for each sample.

The composition at the nanoscopic level was probed quantitatively with small angle x-ray scattering (SAXS, Appendix S.4) showing that *all* materials contain similar-size primary and secondary nanoparticles. However, while in **PUA-acetone-xxx** and **PUA-DMF-xxx** radii of primary particles agree extremely well with particle sizes calculated from gas sorption (Appendix S.5) and skeletal density data (Table 1), by the same token they are very far off in all **PUA-ACN-xxx**. Considering those data together with the similar porosities but lower BET surface areas of **PUA-ACN-xx** relative to those of **PUA-acetone-xxx** supports that: (a) spheres in all **PUA-ACN-xxx** samples are dense objects comprising thermal shorts that justify the 30% higher pre-exponential factors of λ_s in those materials; and, (b) since most of the polymer goes to spheres, the weight percent contribution of entangled fibers to the structure is low, hence ACN materials are more flexible. Because spheres are dense solid objects falling beyond the Q-range of our SAXS capability, SAXS data concern fibers, which, therefore, are formed by secondary nanoparticles, which in turn are densely-packed surface-fractal assemblies of primary nanoparticles (see Table S.4 in Appendix S.4). Hence, we speculate that dense spheres are formed because of lack of strong hydrogen bonding between the developing polymer and ACN. Thus, soluble PUA oligomers are stabilized by H-bonding to one another and grow into large particles. Support for this hypothesis is found in the higher degree of crystallinity in **PUA-ACN-109** samples (67%, by XRD), as opposed to 50% and 40% in the corresponding materials from acetone and DMF, respectively (see Appendix S.6). Closer to the gel point, the monomer concentration gets low and an acetone-like process sets in; PUA particles start forming aggregates in solution that, probably for electrostatic/polarizability reasons,[22] form fiber-like strings that eventually accumulate on

reactive protrusions on the surface of spheres. Support for this argument comes from higher magnification SEM, whereas fibers consistently seem to emanate from the surface and grow out of spheres (Figure 2). Entanglement of those fibers forms the gel network.

All materials are hydrophobic relative to dense polurea (θ=69.1±0.2^o). Contact angles of 5 μL water droplets, θ', on flat internal surfaces of **PUA-ACN-xxx** were measured in the 116^o-150^o range, but only between 97^o and 102^o, and between 102^o and 104^o on **PUA-acetone-xxx** and **PUA-DMF-xx**, respectively. Clearly, all cases are Cassie-Baxter states, whereas the startling performance of ACN-samples cannot be attributed to anything but the presence of both fibers and spheres. The largest contact angle (150.2±0.5^o) was observed on **PUA-ACN-296**, which, qualitatively, shows a more equal balance between the two forms (see Figure 2). The Cassie-Baxter contact fractions, *f*, were calculated via eq 2 and for acetone or DMF samples vary in the 0.5-0.6 range; for ACN samples between 0.1 and 0.4. Setting, as has been suggested,[19] f=1-(Π/100) for **PUA-ACN-296** (Π=86%, Table 1) predicts θ'=144^o, which is close to the experimental value. However, experimental *f* values do not vary monotonically with porosity, hence Π cannot be used as a reliable predictor of θ', which, therefore, depends on texture.

All samples float on water indefinitely. Pulling vacuum does not force water in the pores; in other words, a Cassie-Baxter to Wenzel transition is not observed. Indeed, that would happen at a contact angle where, according to eqs 1 and 2, cos θ=(1-*f*)/(*r*-*f*). Calculating the roughness, *r*, from cos (69.1^o) and *f* yields *negative* values for all samples, which is not meaningful, hence that transition cannot take place. In spite of the large contact angles, droplets adhere to the PUA surfaces even when the substrate is turned upside-down (Petal effect – see TOC graphic). Since the latter is observed irrespective of

texture, it is attributed to H-bonding between water and PUA.

Hydrophobic PUA aerogel monoliths are ideal for soaking non-polar organic liquids. For example, they remove oil from water fast (Figure 4 and Movie S.3) and can be harvested afterwards easily. Interestingly, as demonstrated by the bottom part of Figure 4, that oleophilic effect is also texture-related: **PUA-ACN-xxx** and **PUA-acetone-xxx** behave opposite in terms of oil absorption; low-density fibrous/particulate **PUA-ACN-109** absorb about 11× their weight in oil (Figure 4-Bottom(left), which fills 91% of the available porosity (Figure 4-Bottom(right); exclusively-fibrous and less hydrophobic **PUA-acetone-109** absorb *only* 2× their weight in oil, filling only 25% of their porosity. By going to more dense, less porous, but also in both cases particulate **PUA-acetone-517** and **PUA-ACN-517**, oil fills 97% and 100% of the porous space, respectively; however, owing to the higher density of those monoliths, the oil:aerogel ratio falls to 1.3 w/w versus 1.9 w/w, respectively (see Figure 4-Bottom(left), and data in Table S.5 of Appendix S.7). The oil absorption capability of **PUA-ACN-109** (>11× w/w) competes favorably with that of polymethyl-silsesquioxane aerogels (6.2 w/w for hexane),[23] and polystyrene aerogels (5-6× w/w for oil),[24] with the additional advantage over the latter being the dimensional stability owing to crosslinking. Recently reported ultra-low-density (0.16 mg cm^{-3}) graphene-derived aerogels absorb about 900× w/w of oil,[25] yet **PUA-ACN-109** absorbs more oil per volume (by 6×).

In conclusion, aerogels are particularly attractive platforms for imparting texture-induced superhydrophobicity. As demonstrated herewith with polyurea, careful selection of the monomers and rational adjustment of the gelation conditions (solvent) yields high-value-added materials in one easy step. The specific PUA aerogels of this study are

suitable for environmental remediation. Owing to their low cost, it is envisioned that oil-soaked samples may be used directly as fuel.

Supporting Information Appendix S.1: Experimental Section; Appendix S.2: rheometry; Appendix S.3: thermal conductivity; Appendix S.4: SAXS; Appendix S.5: N_2-sorption; Appendix S.6: XRD; Appendix S.7: oil absorption data; Appendix S.8: Movies: S.1-S.3 (separate files).

AUTHOR INFORMATION

Corresponding Author

leventis@mst.edu; cslevent@mst.edu

Notes The authors declare no competing financial interest.

Acknowledgements. We thank the Army Research Office for financial support (Award No. W911NF-10-1-0476), and Bayer Corporation U.S.A for the generous supply of Desmodur N3300A triisocyanate.

References

1. See for example: (a) Bocquestt, L.; Lauga, E. *Nature Mater.* **2011**, *10*, 334-337. (b) Shirtcliffe, N. J.; McHale, G.; Newton, M. I. *J. Polym. Sci. Part B: Polym. Phys.* **2011**, *49*, 1203-1217. (c) Callies, M.; Quéré, D. *Soft Matter* **2005**, *1*, 55-61. (d) Zhang, L.; Wu, J.; Wang, Y.; Long, Y.; Zhao, N.; Xu, J. *J. Am. Chem. Soc.* **2012**, *134*, 9879-9881.

2. Ma, M.; Hill, R. M.; Rutledge, G. C. *J. Adhes, Sci. Technol.* **2008**, *22*, 1799-1817.

3. Wenzel, R. N. *Ind. Eng. Chem.* **1936**, *28*, 988-994.

4. Cassie, A. B. D.; Baxter, S. *Trans. Faraday Soc.* **1944**, *40*, 546-551.

5. See for example: Levkin, P. A.; Svec, F.; Frechet, J. M. *Adv. Funct. Mater.* **2009**, *19*, 1993-1998.

6. Barthlott, W.; Neinhuis, C. *Planta* **1997**, *202*, 1-8.

7. Feng, L.; Zhang, Y.; Xi, J.; Zhu, Y.; Wang, N.; Xia, F.; Jiang, L. *Langmuir* **2008**, *24*, 4114-4119.

8. Dawood, M. K.; Zheng, H.; Liew, T. H.; Leong, K. C.; Foo, Y. L.; Rajagopalan, R.; Khan, S. A.; Choi, W. K. *Langmuir* **2011**, *27*, 4126-4133.

9. Sun, M.; Luo, C.; Xu, L.; Ji, H.; Ouyang, Q.; Yu, D.; Chen, Y. *Langmuir* **2005**, *21*, 8978-8981.

10. See for example: Tuteja, A.; Choi, W.; McKinley, G. H.; Cohen, R. E.; Rubner, M. *MRS Bull.* **2008**, *33*, 752-758.

11. (a) Gu, Z. Z.; Uetsuka, H.; Takahashi, K.; Nakajima, R.; Onishi, H.; Fujishima, A.; Sato, O. *Angew. Chem., Int. Ed.* **2003**, *42*, 894-897. (b) Öner, D.; McCarthy, T. J. *Langmuir* **2000**, *16*, 7777-7782. (c) Bico, J.; Marzolin, C.; Quéré, D. *Europhys. Lett.* **1999**, *47*, 220-226.

12. Li, H.; Wang, X.; Song, Y.; Liu, Y.; Li, Q.; Jiang, L.; Zhu, D. *Angew. Chem., Int. Ed.* **2001**, *40*, 1743-1746.

13. Sas, I.; Gorga, R. E.; Joines, J. A.; Thoney, K. A. *J. Polym. Sci. Part B; Polym. Phys.* **2012**, *50*, 824-845.

14. Zhu, Y.; Zhang, J.; Zheng, Y.; Huang, Z.; Feng, L.; Jiang, L. *Adv. Funct. Mater.* **2006**, *16*, 568-574.

15. Ogawa, T.; Ding, B.; Sone, Y.; Shiratori, S. *Nanotechnology* **2007**, *18*, 165607-165615.

16. Prakash, S. S.; Brinker, C. J.; Hurd, A. J.; Rao, S. M. *Nature* **1995**, *374*, 439-443.

17. Thorne-Banda, H.; Miller, T. "Aerogels by Cabot Corporation: Versatile Properties for Many Applications," in *Aerogels Handbook, Advances in Sol-Gel Derived Materials and Technologies*, Aegerter, M. A.; Leventis, N.; Koebel, M. Ed.s Springer, New York, N.Y., pp 847-856.

18. Ilhan, U. F.; Fabrizion, E. F.; McCorkle, L.; Scheiman, D. A.; Dass, A.; Palczer, A.; Meador, M. A. B.; Johnston, J. C.; Leventis, N. *J. Mater. Chem.* **2006**, *16*, 3046-3054.

19. Wang, X.; Jana, S. C. *Langmuir* **2013**, *29*, 5589-5598.

20. Leventis, N.; Sotiriou-Leventis, C.; Chandrasekaran, N.; Mulik, S.; Larimore, Z. J.; Lu, H.; Churu, G.; Mang, J. T. *Chem. Mater.* **2010**, *22*, 6692-6710.

21. Weigold, L.; Mohite, D. P.; Mahadik-Khanolkar, S.; Leventis, N.; Reichenauer, G. *J. Non-Cryst. Solids* **2013**, *368*, 105-111.

22. (a) Zhang, H.; Wang, D. *Angew. Chem. Int. Ed.* **2008**, *47*, 3984-3987. (b) Taden, A.; Landfester, K.; Antonietti, M. *Langmuir* **2004**, *20*, 957-961.

23. Hayase, G.; Kanamori, K.; Fukuchi, M.; Kaji, H.; Nakanishi, K. *Angew. Chem. Int. Ed.* **2013**, *52*, 1986-1989.

24. Daniel, C.; Alfano, D.; Venditto, V.; Cardea, S.; Reverchon, E.; Larobina, D.; Mensitieri, G.; Guerra, G. *Adv. Mater.* **2005**, *17*, 1515-1518.

25. Sun, H.; Xu, Z.; Gao, C. *Adv. Mater.* **2013**, *25*, 2554-2560.

Figures

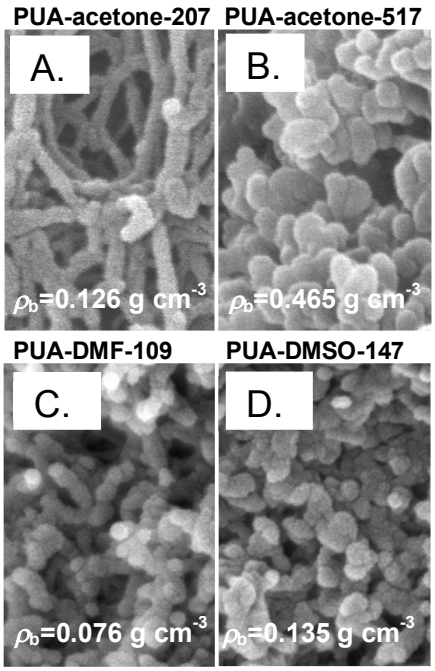

Figure 1. Micromorphology of PUA aerogels prepared from the solvents and at the bulk densities (ρ_b) indicated. Common scale bar at 200 nm. (Numerical extensions at the sample names indicate the monomer concentration (in mM) in the sol.)

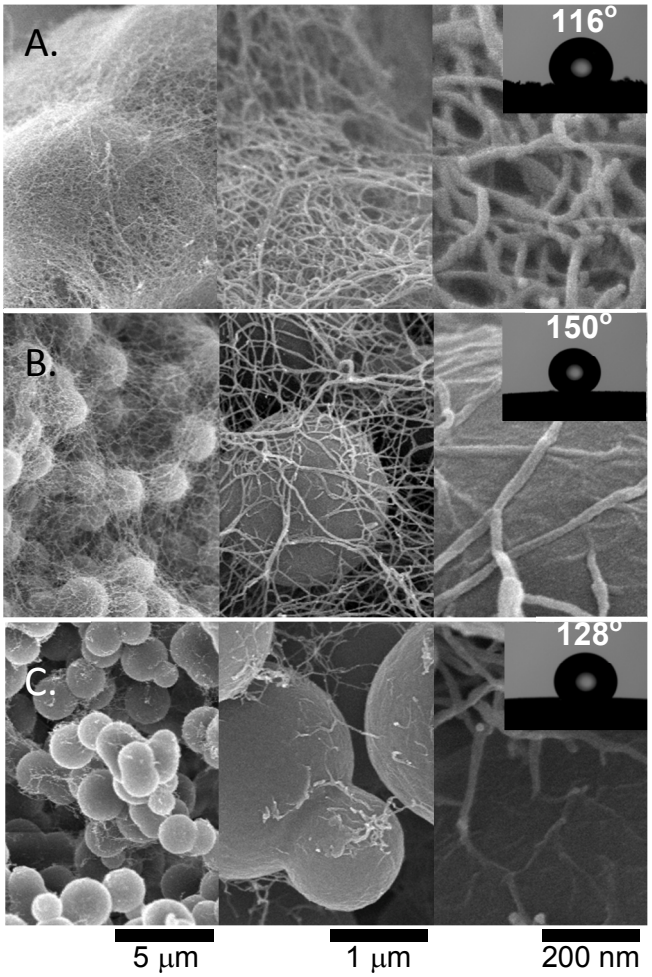

Figure 2. SEM of polyurea aerogels from CH_3CN sols at three different densities and magnifications: (A) **PUA-ACN-109** (ρ_b=0.073 g cm^{-3}); (B) **PUA-ACN-296** (ρ_b=0.172 g cm^{-3}); (C) **PUA-ACN-517** (ρ_b=0.347 g cm^{-3}). Insets: water droplets on flat surfaces and contact angles.

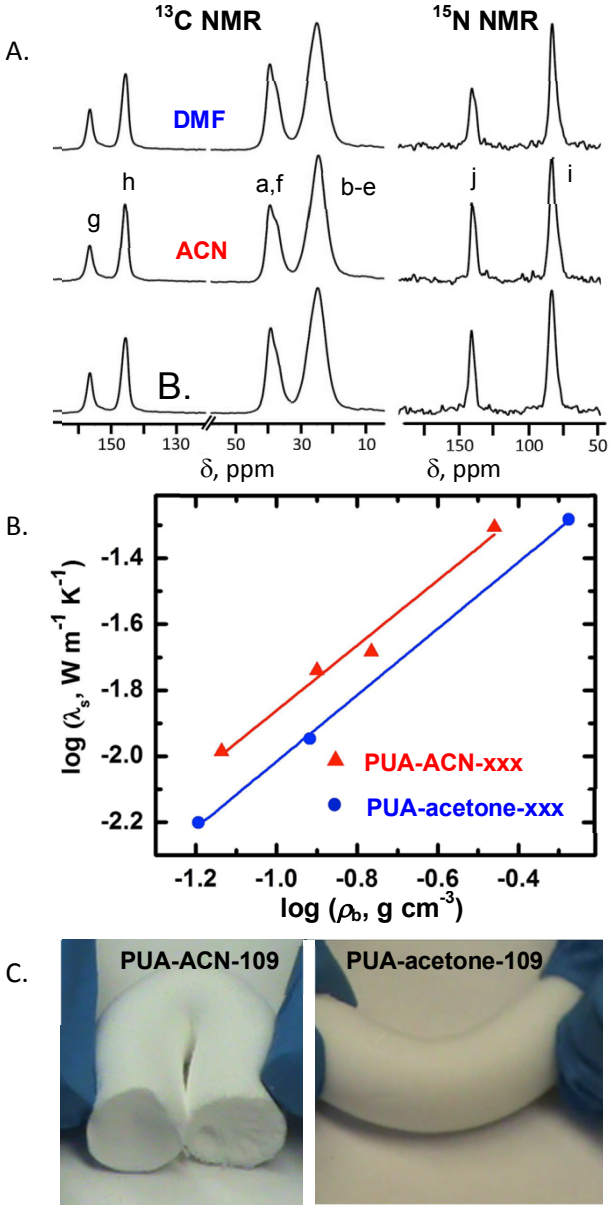

Figure 3. (A) Solid state NMR of PUA samples from different solvents as indicated. (For the peak assignment, refer to Scheme 1.) (B) Log-Log plot of solid thermal conductivity (λ_s) versus bulk density (ρ_b). (**PUA-acetone-xxx** data from Ref. 21.) (C) Bending of low-density samples as indicated (see Movies S.1 and S.2 in Supporting Information). Photograph of **PUA-acetone-109** at the break point

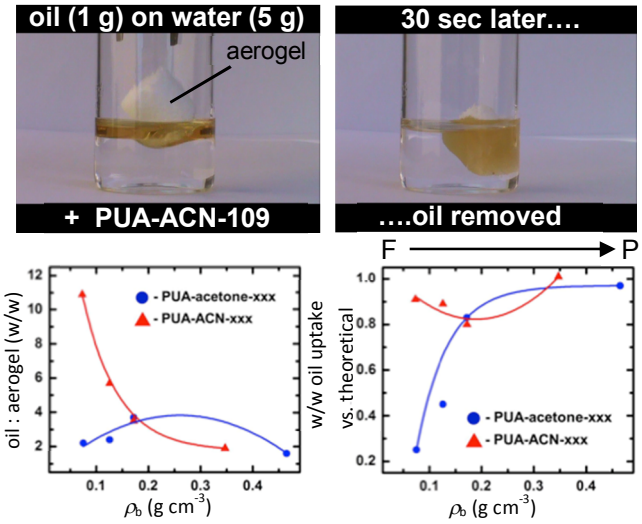

Figure 4. Top: oil absorption from the surface of water as shown (aerogel weight=0.087 g; aerogel volume=1.19 cm^{-3}; oil:aerogel=11.5 w/w). Bottom: *Left*, gravimetric oil absorption as a function of density for samples as shown. *Right*, experimental oil uptake versus calculated oil uptake based on sample porosities (see Table 1) and ρ_{oil}= 0.924 g cm^{-3}. Arrow above: transition from F (fibers) to P (particles).

Supporting Information

Appendix S.1 Experimental Section and Summary of Material Properties

Appendix S.2 Rheometry

Appendix S.3 Thermal conductivity

Appendix S.4 Small angle X-ray scattering (SAXS)

Appendix S.5 N_2-Sorption

Appendix S.6 X-ray Diffraction (XRD)

Appendix S.7 Oil absorption data

Appendix S.1 Experimental Section and Summary of Material Properties

Materials

All reagents and solvents were used as received unless noted otherwise. 1,3,5-tris(6-isocyanatohexyl)-1,3,5-triazinane-2,4,6-trione was donated generously as a pure chemical (Desmodur N3300A) by Bayer Corp. U.S.A. Triethylamine, anhydrous acetonitrile (ACN), anhydrous dimethylformamide (DMF), HPLC grade acetone, ACN and DMF were purchased from Aldrich Chemical Co. U.S.A. Anhydrous acetone was purchased from Acros Chemicals, U.S.A.

***Preparation of polyurea (PUA) aerogels*:** Polyurea aerogels at different densities were prepared by varying the concentration of Desmodur N3300A. In a typical procedure, 5.5 g of Desmodur N3300A was dissolved in 94 mL of dry solvent (acetone, ACN, DMF or DMSO); 3 mol equivalents of water (589 mL) was added, and finally the sol was obtained by adding 654 mL of triethylamine (0.6% w/w relative to the N3300A plus solvent). Subsequently, the sol was poured into polypropylene molds (Polypropylene Scintillation Vials, General Purpose, 6.5 mL, Sigma-Aldrich Catalogue No. Z376825, 1.27 cm inner diameter), which were sealed with their caps, wrapped with Parafilm^{TM} and kept at room temperature for 12 h for gelation and aging. Phenomenological gelation times were recorded by inverting the vials. After aging, gels were removed from the molds, washed with acetone (4×, using 4× the volume of the gel each time) and dried in an autoclave with CO_2 taken out as a supercritical fluid (SCF).

Methods

***The sol-gel transition*:** The rheological behavior of selected PUA sols was recorded with a TA Instruments AR 2000ex Rheometer employing an aluminum cone (60 mm diameter, 2^o angle) and a Peltier plate using a 1 mm gap, at 20 ^oC. The instrument was operated in the continuous oscillation mode and time-sweep experiments were performed with fixed-strain amplitude. The gel-point was determined using a dynamic multiwave method with four superimposed harmonics (1, 2, 4, and 8 rad s^{-1}). The strain of the fundamental oscillation (1 rad s^{-1}) was set at 5%.

***SCF drying*:** Supercritical fluid (SCF) CO_2 drying was carried out in an autoclave (Spe-ed SFE system, Applied Separations, Allentown, PA).

***Physical Characterization*:** Bulk densities, ρ_b, were calculated from the sample weight and dimensions. Skeletal densities, ρ_s, were determined by helium pycnometry using a Micromeritics AccuPyc II 1340 instrument. Porosities, Π, were determined from ρ_b and ρ_b via $\Pi=(\rho_s-\rho_b)/\rho_s$.

***Chemical Characterization*:** Full characterization of the monomer, Desmodur N3300A, has been reported elsewhere.[SI-R.1] Solid-state ^{13}C NMR spectra were obtained with samples ground into fine powders on a Brucker Avance 300 Spectrometer with a 75.475 MHz carbon frequency using magic angle spinning (at 7 kHz) with broadband proton suppression and the CPMAS-TOSS pulse sequence for spin sideband suppression. Solid-state ^{15}N NMR spectra were obtained on a Bruker Avance 400 Spectrometer with a 40.557 MHz nitrogen frequency using magic angle spinning (at 5 kHz). All other conditions were similar to those used for solid-state ^{13}C NMR.

The degree of crystallinity of all PUA aerogels was determined using powder X-ray diffraction (XRD) with a PANalytical X'Pert Pro Multi-Purpose Diffractometer (MPD) with a Cu Kα radiation source (λ= 1.54 Å).

***Structural Characterization*:** N_2 sorption porosimetry was conducted with a Micromeritics ASAP 2020 surface area and porosity analyzer. In preparation for surface area and skeletal density determination, samples were outgassed for 24 h at 40 ^oC under vacuum. Average pore diameters were determined via the $4\times V_{Total}/\sigma$ method, where V_{Total} is the total pore volume per gram, and s, the specific surface area determined via the Brunauer-Emmett-Teller (BET) method from the N_2 adsorption data. V_{Total} can be calculated either from the single highest volume of N_2 adsorbed along the adsorption isotherm, or via $V_{Total} = (1/\rho_b) - (1/\rho_s)$. Average pore diameter values calculated by both methods are cited in Table 1 of the article; when those values converge, the material includes mesoporosity. If the average pore diameter calculated using $V_{Total} = (1/\rho_b) - (1/\rho_s)$ is significantly higher, that is taken as evidence for macroporosity.

Hg-intrusion porosimetry was conducted with a Micromeritics AutoPore IV 9500 instrument.

The morphology of PUA aerogels was determined with scanning electron microscopy (SEM) using Au-coated samples on a Hitachi S-4700 field emission microscope.

The structure of the fundamental building blocks of the materials was probed with small-angle X-ray scattering (SAXS) using 2-3 mm-thick disks, ~7-10 mm in diameter. SAXS was carried out with a PANalytical X'Pert Pro multipurpose diffractometer (MPD), configured for SAXS using Cu Kα radiation (λ= 1.54 Å) and a 1/32^o SAXS slit and a 1/16^o anti-scatter slit on the incident beam side, and 0.1 mm anti-scatter slit and Ni 0.125 mm automatic beam attenuator on the diffracted beam side. Samples were placed in circular holders between thin Mylar^{TM} sheets and scattering intensities were measured with a point detector in transmission geometry by 2 Theta (2θ) scans ranging from -0.1^o up to 5^o. All scattering data are reported in arbitrary units as a function of Q (=$4\pi\sin\theta/\lambda$), the momentum transferred during a scattering event. Data analysis was conducted with the Beaucage Unified Model,[SI-R.2] using the *Irena SAS* tool for modeling of small angle scattering,[SI-R.3] within the commercial *Igor Pro* application (WaveMetrics, Portland, OR).

***Thermal Conductivity Characterization*:** Thermal conductivity, l, was calculated at 23 ^{o}C via $\lambda = R \times c_P \times \rho_b$. Thermal diffusivity, R, was determined with a Netzsch NanoFlash Model LFA 447 flash diffusivity instrument using disk samples ~1 cm in diameter, 2-3 mm thick. Heat capacities, c_P, at 23 ^{o}C were measured with powders (5-10 mg) using a TA Instruments Differential Scanning Calorimeter Model Q2000 calibrated against a sapphire standard and run from 0 ^{o}C to 30 ^{o}C at 0.5 ^{o}C min^{-1} in the modulated T4P mode. Raw c_P data were multiplied by a factor of 1.10 based on measuring the heat capacities of rutile, graphite and corundum just before running our samples and compared with literature values.

***Contact Angle Measurements*:** Water contact angles were measure using a Rame-Hart Model 250 standard goniometer equipped with a high resolution camera. In the static sessile drop method, an approximately 5 μL droplet of water was placed on the sample surface, the image was capture with the instrument camera and the contact angle was determined using the DROPimage Advanced v2.4 software. Ten measurements were taken for each specimen and the results reported as averages. Aerogel samples were prepared by cutting disks with a knife, surfaces, if necessary, were smoothened using the 3M Abrasives® (320 grit) sand paper (part No. 32541) and were blown over with dry N_2.

***Oil Absorption*:** Oil uptake from aerogels was determined gravimetrically. Excess of used pump oil (Duo Seal® Pump oil, density = 0.924 g cm^{-3}) was placed on water, a pre-

weighted aerogel monolith was dropped on top, left to soak for 12 h, was removed with a pair of tweezers, strained on paper for 10 min and weighted. Results are presented in Appendix S.7 below.

***Determination of the Dielectric Constant of Desmodur N3300A*:** That was determined with a calibration curve from capacitance measurements using an interdigitated electrode array dipped in several solvents of known capacitance and a METEX M-4650 digital multimeter operated at 220 Hz in the pulse mode.

SI-R.1 Leventis, N.; Sotiriou-Leventis, C.; Chandrasekaran, N.; Mulik, S.; Larimore, Z. J.; Lu, H.; Churu, G.; Mang, J. T. *Chem. Mater.* **2010**, *22*, 6692-6710.

SI-R.2 (a) Beaucage, G. *J. Appl. Cryst*. **1995**, *28*, 717-728.
(b) Beaucage, G. *J. Appl. Cryst*. **1996**, *29*, 134-146.

SI-R.3 Ilavsky, J.; Jemian, P. R. *J. Appl. Cryst.* **2009**, *42*, 347-353.

Table S.1. System and property summary for all aerogels of this study. (Numerical extensions in sample names represent the mM concentration of the monomer (Desmodur N3300A) in the sol.)

sample	gelation time (min) [a]	linear shrinkage (%) [b,c]	bulk density ρ_b (g cm^{-3}) [b]	skeletal density ρ_s (g cm^{-3}) [d]	porosity Π (% v/v)	BET surface area σ (m^2 g^{-1})	pore diameter (nm) [e]	particle radius (nm) [f]	R(1) (nm) [g]	R(2) (nm) [h]	contact angle θ' (°)
PUA-ACN-109	22 [28.3]	12.4 ± 0.2	0.073 ± 0.002	1.197 ± 0.013	94	25	19.4 [2058] (3949)	100	9.9 ± 0.9	56.8 ± 3.8	116.2 ± 0.1
PUA-ACN-207	15	11.5 ± 0.1	0.126 ± 0.002	1.177 ± 0.009	89	18	16.5 [1575]	142	13.1 ± 0.1	43.1 ± 2.1	133.0 ± 0.1
PUA-ACN-296	10 [6.35]	10.8 ± 0.1	0.172 ± 0.007	1.201 ± 0.009	86	11	17.0 [1811]	227	16.6 ± 3.2	43.4 ± 2.9	150.2 ± 0.5
PUA-ACN-517	7	9.6 ± 0.1	0.347 ± 0.001	1.180 ± 0.004	70	5	18.7 [1627] (1330)	509	10.4 ± 1.9	71.3 ± 4.9	127.6 ± 0.2
PUA-DMF-109	180 [177.3]	19.4 ± 0.2	0.076 ± 0.002	1.210 ± 0.006	94	307	16.0 [161]	8.1	6.5 ± 0.3	21.3 ± 0.3	104.4 ± 0.1
PUA-DMF-207	50	39.2 ± 0.3	0.426 ± 0.004	1.270 ± 0.009	66	237	14.9 [26.3]	10.0	12.5 ± 0.0$_3$	[i]	102.3 ± 0.1
PUA-acetone-109	180 [177.4]	5.7 ± 0.2	0.075 ± 0.003	1.201 ± 0.008	94	187	20.6 [267]	13.4	11.3 ± 0.6	28.4 ± 0.8	102.4 ± 1.3
PUA-acetone-207	75	9.8 ± 0.1	0.126 ± 0.001	1.265 ± 0.006	90	169	41.6 [169]	14.0	11.9 ± 0.4	27.2 ± 0.8	97.3 ± 0.1
PUA-acetone-296	30	13.4 ± 0.2	0.172 ± 0.001	1.215 ± 0.002	86	68	40.7 [293]	36.3	19.4 ± 0.1	[i]	101.9 ± 0.0
PUA-acetone-517	20	19.2 ± 0.1	0.465 ± 0.002	1.200 ± 0.001	61	56	28.3 [94.1]	44.6	47.6 ± 1.3	[j]	100.1 ± 0.1

[a] Phenomenological [via rheometry] gelation times (see Appendix S.2). [b] Average of 5 samples. [c] Linear shrinkage = 100 × [1-(sample diameter/mold diameter)]. [d] Single sample, average of 50 measurements. [e] By the $4 \times V_{Total}/\sigma$ method using N_2-sorption data (Appendix S.5 below), V_{Total} by the single-point adsorption method; in [brackets], V_{Total} via $V_{Total} = (1/\rho_b)-(1/\rho_s)$]; in (parentheses), via Hg intrusion porosimetry. [f] Particle radius from gas sorption data = $3/\rho_s\sigma$. [g] Primary particle radius, from SAXS data, first Guinier knee (Region II; refer to Fig. S.3 in Appendix S.4 below). [h] Secondary particle radius, from second Guinier knee (Region IV in Fig. S.3). [i] Not measured. [j] Beyond our accessible Q-range.

Appendix S.2 Rheometry

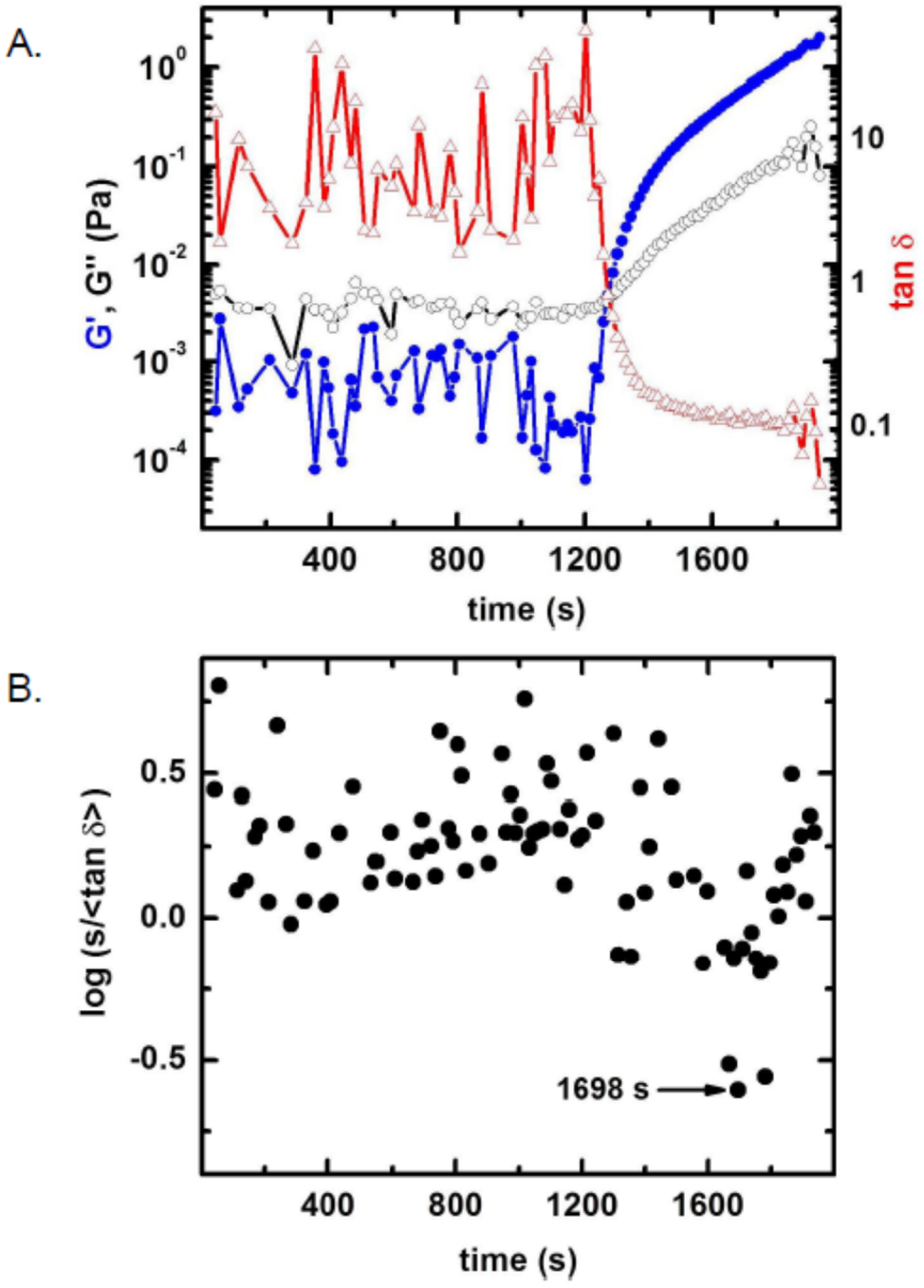

Figure S.1 Typical rheometry data during gelation of PUA sols. (A) Evolution of the storage (G´ – dark circles) and loss (G´´- open circles) moduli and tanδ (triangles) vs. time of a **PUA-ACN-109** sol ([N3300A]=0.109 M). Oscillation frequency ω=1 rad s^{-1}. (B) Statistical variable versus time (see Table S.2). Formal gelation point at the minimum.

Table S.2. Rheometry data from the gelation of selected PUA sols as indicated

sol formulation	aging time before loading to rheometer (s)	gelation point, t_{gel} [a] (s[s])	tanδ at t_{gel}	n [b]	D_f [c]
PUA-acetone-109	9000	10641 [10800]	0.078	0.050	2.46
PUA-DMF-109	7200	10640 [10800]	0.070	0.044	2.46
PUA-ACN-109	0	1698 [1320]	0.120	0.240	2.44
PUA-ACN-296	0	381 [600]	0.101	0.063	2.45

[a] Identified at the minimum of the statistical function, log(s/tan δ),[SI-R.4] as shown in Figure S.1 (s: standard deviation of tan δ between the four frequencies employed (see Experimental Section), at each time point.) In brackets, phenomenological gelation times.

At the gel point, tan δ is related to the gel relaxation exponent 'n' via Eq. S.1.[SI-R.5]

$$\tan\delta = \tan(n\pi/2) \qquad \text{(S.1)}$$

considering the excluded volume of the (primary) particles forming the clusters, 'n' is related via Eq. S.2 to the mass fractal dimension, D_f, of the clusters forming the gel.[SI-R.6] (Note, for three-dimensional non-fractal clusters, D_f=D=3.[SI-R.6])

$$n = \frac{D(D+2-2D_f)}{2(D+2-D_f)} \qquad \text{(S.2)}$$

[b] From Eq. S.1.

[c] From Eq. S.2. The D_f values of the selected PUA formulations (Table S.2) are in the 2.2-2.5 range, suggesting that the gel network is formed by mass-fractal particles.[SI-R.7]

SI-R.4 Kim, S.-Y.; Choi, D.-G.; Yang, S.-M. *Korean J. Chem. Eng.* **2002**, *19*, 190-196.

SI-R.5 Raghavan, S. R.; Chen, L. A.; McDowell, C.; Khan, S. A.; Hwang, R.; White, S. *Polymer* **1996**, *37*, 5869-5875.

SI-R.6 Muthukumar, M. *Macromolecules* **1989**, *22*, 4656-4658.

SI-R.7 Kolb, M.; Botet, R.; Jullien, R. *Phys. Rev. Lett.* **1983**, *51*, 1123-1126.

Appendix S.3 Thermal conductivity

Total thermal conductivities, λ, were determined using a laser flash method for all **PUA-ACN-xxx** aerogels from their thermal diffusivities (R), heat capacities (c_P) and bulk densities (ρ_b), via Eq. S.3, as described previously.[SI-R.8] Table S.3 summarizes the data,

$$\lambda = \rho_b \times c_P \times R \qquad \text{(S.3)}$$

and Figure S.2A shows the variation of λ with ρ_b. Thermal conductivities fall in the range 0.032-0.065 W m^{-1} K^{-1}, that is similar to that of **PUA-acetone-xxx** aerogels.[SI-R.9]

Table S.3. Thermal conductivity data of the **PUA-ACN-xxx** aerogels at 23 °C

Sample	Bulk density ρ_b (g cm^{-3})	Thermal diffusivity R (mm^2 s^{-1})	Total thermal conductivity λ (W m^{-1} K^{-1})	Gaseous thermal conductivity λ_g (W m^{-1} K^{-1}) [a]	Solid thermal conductivity λ_s (W m^{-1} K^{-1}) [b]
PUA-ACN-056	0.041 ± 0.008	0.709 ± 0.009	0.036 ± 0.002	0.023	0.013
PUA-ACN-109	0.073 ± 0.002	0.361 ± 0.005	0.032 ± 0.001	0.022	0.010
PUA-ACN-207	0.126 ± 0.002	0.244 ± 0.007	0.038 ± 0.001	0.020	0.018
PUA-ACN-296	0.172 ± 0.007	0.196 ± 0.001	0.040 ± 0.004	0.019	0.021
PUA-ACN-517	0.347 ± 0.001	0.154 ± 0.007	0.065 ± 0.007	0.016	0.049

[a] From Knudsen's equation (Eq. S.5).

[b] From $\lambda_s=\lambda-\lambda_g$ (Eq. S.4).

Assuming no coupling of the heat transfer modes, λ can be considered as the sum of three contributors (Eq. S.4), whereas λ_g is the non-convective thermal conductivity

$$\lambda = \lambda_g + \lambda_s + \lambda_{irr} \qquad \text{(S.4)}$$

through the pore-filling gas, λ_s is the thermal conductivity through the solid framework and λ_{irr} is the radiative heat transfer. The latter was minimized experimentally, and the remaining portion was removed from the data digitally.[SI-R.8] Quantitatively, the relative contributions of λ_g and λ_s to the total λ can be assessed by calculating λ_g using Knudsen's equation (Eq. S.5).[SI-R.10] where $\lambda_{g,o}$ is the intrinsic conductivity of the pore-

$$\lambda_g = \frac{\lambda_{g,o}\Pi}{1+2\beta(l_g/\Phi)} \qquad \text{(S.5)}$$

filling gas (for air at 300 K at 1 bar , $\lambda_{g,o}$=0.02619 W m^{-1} K^{-1}),[SI-R.11] Π is the porosity in decimal notation (data from Table 1), β is a parameter that accounts for the energy transfer between the pore-filling gas and the aerogel walls (for air β=2), l_g is the mean free path of the gas molecules (for air at 1 bar pressure, $l_g \approx 70$ nm) and Φ is the pore diameter, calculated via the $4\times V_{Total}/\sigma$ method, (V_{Total}=(1/ρ_b)-(1/ρ_s)) (see Table 1). In this context, it is noted also that $\lambda_{g,o}$ is the upper limit of λ_g for Π=1 and $\Phi\rightarrow\infty$; as ρ_b increases, both Π and Φ decrease, hence λ_g decreases from $\lambda_{g,o}$ monotonically. Therefore, at some point the solid framework becomes the main conductor of heat. Both λ_g and λ_s values for **PUA-ACN-xxx** aerogels are included in Table S.3.

The variation of λ_s with ρ_b has been modeled with an exponential expression, Eq. S.6.[SI-R.12, SI-R.13]

$$\lambda_s = C(\rho_b)^a \qquad \text{(S.6)}$$

Exponent α depends on how matter fills space. For foams α=1; for silica aerogels α~1.5. The pre-exponential factor C depends on the particle chemical composition and the interparticle coupling (neck area and extent of interparticle bonding). Exponent α and coefficient C for the **PUA-ACN-xxx** aerogels were calculated from Log-Log plots; results are shown in Figure S.2B and are compared with results obtained with **PUA-acetone-xxx** using the hot-wire method in Figure 2 of the main article.[SI-R.9]

SI-R-8 Parker, W. J.; Jenkins, R. J.; Butler, C. P.; Abbott, G. L. *J. Appl. Phys.* **1961**, *32*, 1679-1684.

SI-R.9 Weigold, L.; Mohite, D. P.; Mahadik-Khanolkar, S.; Leventis, N.; Reichenauer, G. *J. Non-Cryst. Solids* **2013**, *368*, 105-111.

SI-R.10 (a) Lu, X.; Arduini-Schuster, M. C.; Kuhn, J.; Nilsson, O.; Fricke, J.; Pekala, R. W. *Science* **1992**, *255*, 971-972. (b) Reichenauer, G.; Heinemann, U.; Ebert, H.-P. *Colloids Surf. A* **2007**, *300*, 204-210.

SI-R.11 Stephan, K.; Laesecke, A. *J. Phys. Chem. Ref. Data* **1985**, *14*, 227-234.

SI-R.12 Lu, X.; Caps, R.; Fricke, J.; Alviso, C. T.; Pekala, R. W. *J. Non-Cryst. Solids* **1995**, *188*, 226-234.

SI-R.13 Lu, X.; Nilsson, O.; Fricke, J.; Pekala, R. W. *J. Appl. Phys.***1993**, *73*, 581-584.

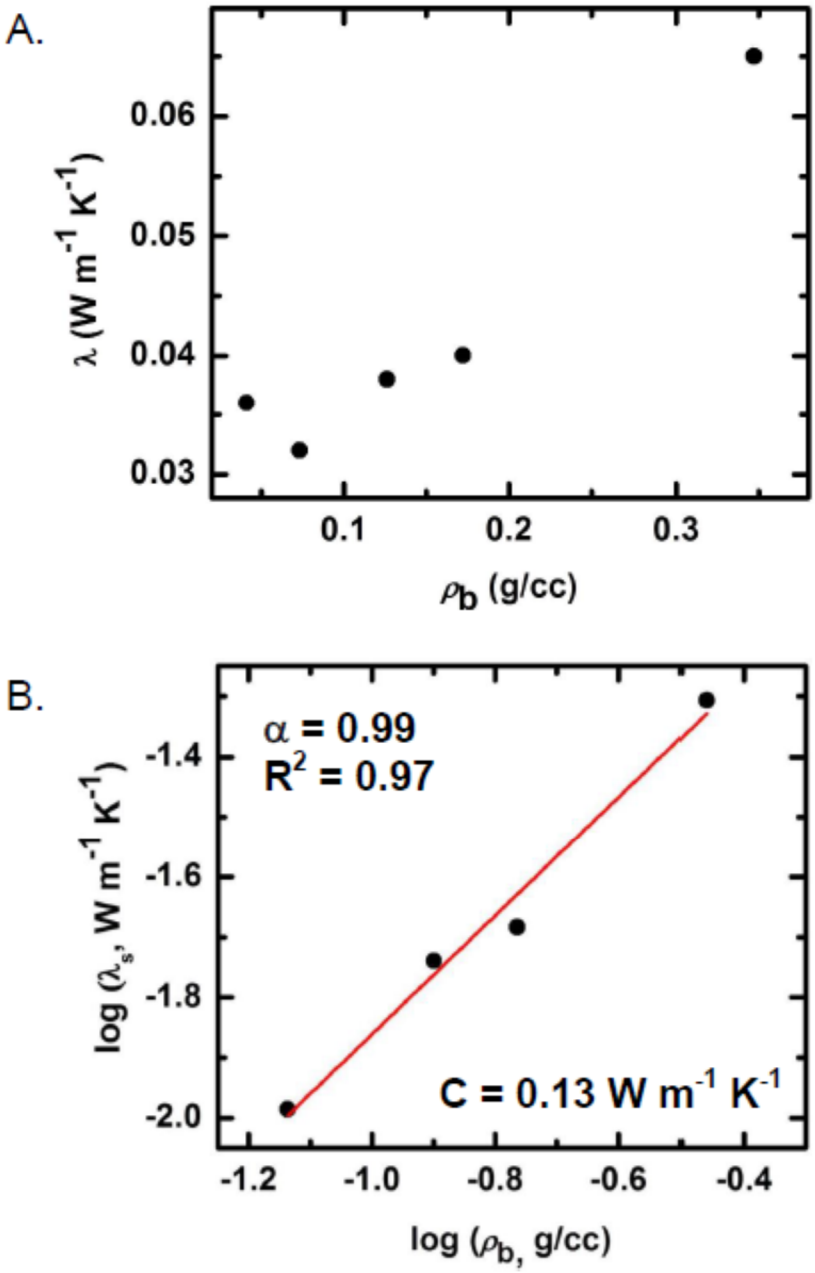

Figure S.2 (A) Total thermal conductivity, λ, of **PUA-ACN-xxx** aerogels as a function of density. (B) Log-Log plot of the solid thermal conductivity, λ_s, versus bulk density of **PUA-ACN-xxx** aerogels.

Appendix S.4 Small angle X-ray scattering (SAXS)

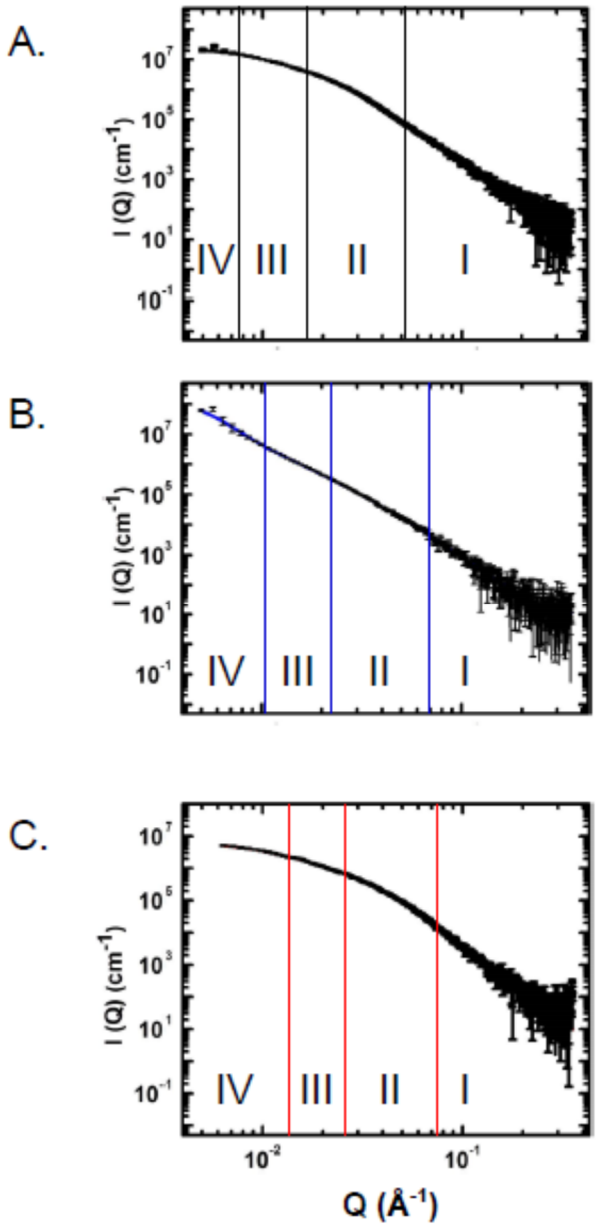

Figure S.3 Representative small angle X-ray scattering (SAXS) data for PUA aerogels synthesized in different solvents, (A) **PUA-acetone-109**. (B) **PUA-ACN-109**. (C) **PUA-DMF-109** (i.e., in all cases the monomer concentration in the sol [N3300A]=0.109 M). Data were fitted to the Beaucage Unified Model (see references in Appendix S.1, above). Results are summarized in Table S.4. (Region I: high-Q power low; Region II: first Guinier knee; Region III: second (low-Q) power law; Region IV: second Guinier knee.

Table S.4. SAXS characterization data of PUA aerogels

		Primary Particles			Secondary Particles		
sample	bulk density ρ_b (g cm^{-3})	high-Q slope [a]	$R_G(1)$ (nm) [b]	R_1 (nm) [c]	low-Q slope [d]	$R_G(2)$ (nm) [e]	R_2 (nm) [f]
in acetonitrile							
PUA-ACN-109	0.073 ± 0.002	-4.51 ± 0.09	7.6 ± 0.7	9.9 ± 0.9	-3.27 ± 0.10	43.7 ± 2.9	56.8 ± 3.8
PUA-ACN-207	0.126 ± 0.002	-4.52 ± 0.01	10.1 ± 0.1	13.1 ± 0.1	-3.32 ± 0.10	33.2 ± 1.6	43.1 ± 2.1
PUA-ACN-296	0.172 ± 0.007	-4.10 ± 0.09	12.8 ± 2.5	16.6 ± 3.2	-3.20 ± 0.19	33.4 ± 2.2	43.4 ± 2.9
PUA-ACN-517	0.347 ± 0.001	-4.46 ± 0.22	8.0 ± 1.5	10.4 ± 1.9	-3.82 ± 0.16	54.9 ± 3.8	71.3 ± 4.9
in DMF							
PUA-DMF-109	0.076 ± 0.002	-4.70 ± 0.03	5.0 ± 0.2	6.5 ± 0.3	-2.31 ± 0.23	16.4 ± 0.2	21.3 ± 0.3
PUA-DMF-207	0.426 ± 0.004	-4.67 ± 0.01	9.6 ± 0.0_2	12.5 ± 0.0_3	[g]	[g]	[g]
in acetone							
PUA-acetone-109	0.075 ± 0.003	-4.45 ± 0.01	8.7 ± 0.5	11.3 ± 0.6	-2.20 ± 0.40	21.9 ± 0.6	28.4 ± 0.8
PUA-acetone-207	0.126 ± 0.001	-4.39 ± 0.01	9.2 ± 0.3	11.9 ± 0.4	-2.52 ± 0.70	21.0 ± 0.6	27.2 ± 0.8
PUA-acetone-296	0.172 ± 0.001	-4.47 ± 0.01	14.9 ± 0.1	19.4 ± 0.1	[g]	[g]	[g]
PUA-acetone-517	0.465 ± 0.002	-4.21 ± 0.00_1	36.7 ± 1.0	47.6 ± 1.3	[g]	[g]	[g]

Referring to Figure S.3:

[a] From power-law Region I. Slopes<-4.0, signifying primary particles with density-gradient boundaries.

[b] First radius of gyration $R_G(1)$, from Guinier Region II.

[c] Primary particle radius = $R_G(1)/0.77$.

[d] From power-law Region III. Slopes>-3.0 signify mass-fractal assemblies with mass fractal dimensions, D_m=|slope|. Slopes<-3.0 signify close-packed surface-fractal assemblies, with surface fractal dimensions, D_s=6-|slope|.

[e] Second radius of gyration $R_G(2)$, from Guinier Region IV.

[f] Secondary particle radius = $R_G(2)/0.77$.

[g] Not within the accessible low-Q range.

Appendix S.5 N_2**-Sorption data**

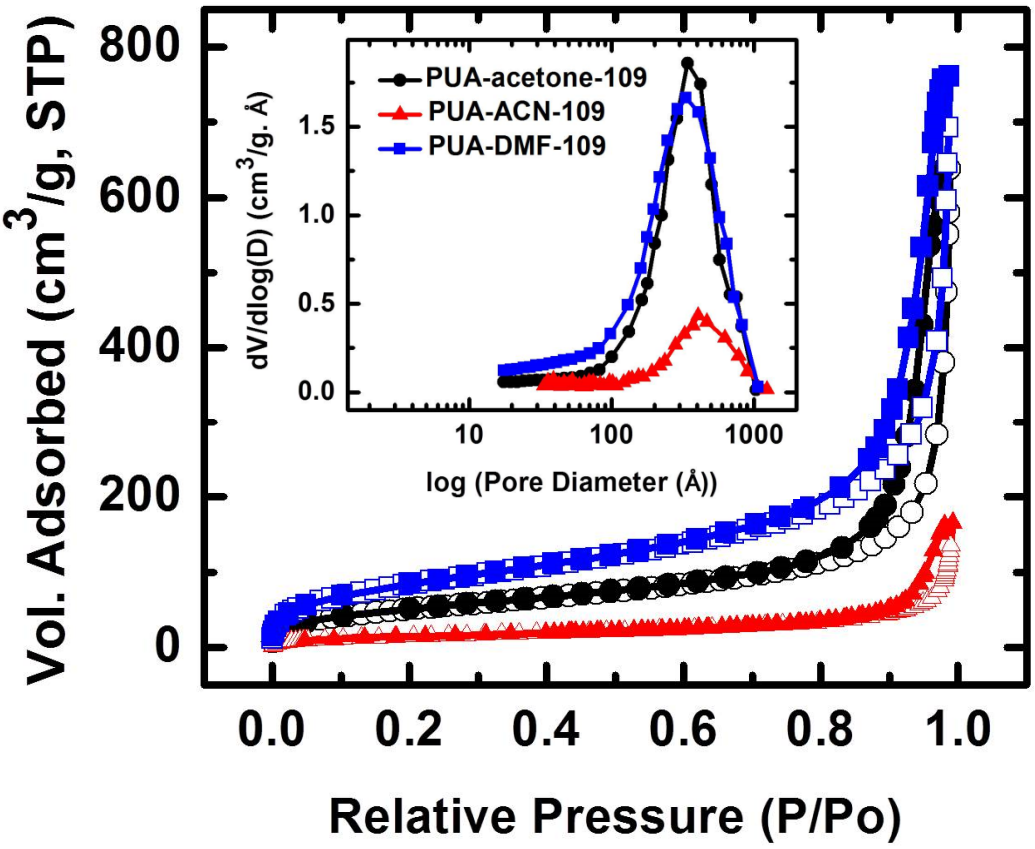

Figure S.4 Representative N_2-sorption isotherms (obtained at 77K) of the three low-density samples (**PUA-solvent-109**) as indicated ([N3300A]=0.109 M). Inset: Pore size distribution via the Barrett-Joyner-Halenda (BJH) plot applied on the desorption branch of the corresponding isotherms. (Open symbols: absorption; Dark symbols: desorption.)

Appendix S.6 X-ray diffraction (XRD) data

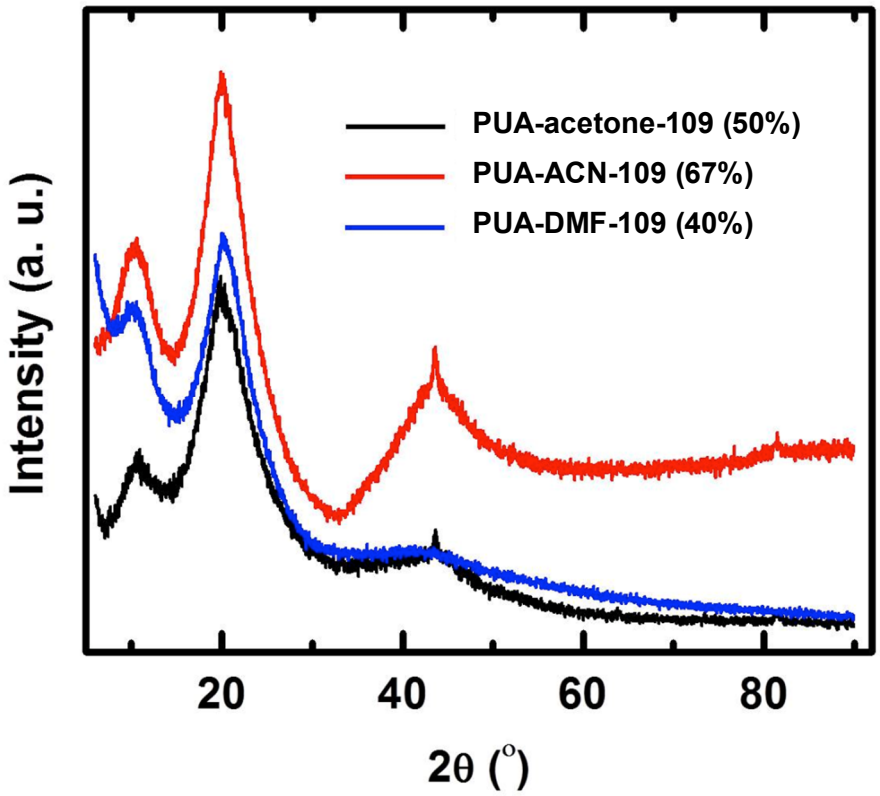

Figure S.5 XRD of low-density samples as shown. Degrees of crystallinity (given in parentheses) were calculated from the areas above the broad background of each sample. (For other sample information refer to Table S.1 above.)

Appendix S.7 Oil absorption data

Table S.5. Oil absorption data for all aerogel samples of this study [a]

Sample	Bulk density ρ_b (g cm^{-3})	Porosity Π (% v/v)	Aerogel sample weight (g)	Free volume in sample (cm^{-3})	Theoretical mass of oil needed to fill the free volume (g)	Mass of oil used (g)	Mass of sample after 12 h in oil-on-water (g)	Mass of sample after 20 min strained on paper (g)	(Mass of oil) : (Mass of aerogel)	w/w fraction of the theoretical oil uptake
PUA-ACN-109	0.073	94	0.0787	1.013	0.9363	0.9475	1.0163	0.9360	10.9	0.91
PUA-ACN-207	0.126	89	0.0717	0.506	0.4679	0.4669	0.5079	0.4812	5.7	0.89
PUA-ACN-296	0.172	86	0.1154	0.577	0.5331	0.5338	0.5597	0.5201	3.5	0.80
PUA-ACN-517	0.347	70	0.1021	0.206	0.1903	0.1900	0.3156	0.2958	1.9	1.01
PUA-DMF-109	0.076	94	0.0841	1.040	0.9611	0.9621	0.7060	0.6785	7.1	0.65
PUA-DMF-207	0.426	66	0.0672	0.104	0.0962	0.0967	0.1850	0.1742	1.6	1.06
PUA-acetone-109	0.075	94	0.0675	0.852	0.7817	0.7977	0.2544	0.2180	2.2	0.25
PUA-acetone-207	0.126	90	0.0715	0.510	0.4719	0.4725	0.3076	0.2466	2.4	0.45
PUA-acetone-296	0.172	86	0.1036	0.518	0.4786	0.4894	0.5272	0.4909	3.7	0.83
PUA-acetone-517	0.465	61	0.0960	0.116	0.1259	0.1260	0.2558	0.2161	1.6	0.97

[a] For experimental details see Appendix S.1 above. Bulk densities and porosities from Table S.1. Density of oil = 0.924 g cm^{-3}.

III. Multifunctional Porous Aramids (Aerogels) by Efficient Reaction of Carboxylic Acids and Isocyanates

Nicholas Leventis[*,1], Chakkaravarthy Chidambareswarapattar[1], Dhairyashil P. Mohite[1], Zachary J. Larimore[2], Hongbing Lu[*,3] and Chariklia Sotiriou-Leventis[*,1]

1. Department of Chemistry, Missouri University of Science and Technology, Rolla, MO 65409, USA, e-mail: leventis@mst.edu, cslevent@mst.edu

2. Department of Mechanical Engineering, Missouri University of Science and Technology, Rolla, MO 65409, USA

3. Department of Mechanical Engineering, The University of Texas at Dallas, Richardson, TX 75080, USA, e-mail: hongbing.lu@utdallas.edu

Published as an article in the *Journal of Materials Chemistry*

Abstract: Polymerization of trifunctional polyaromatic carboxylic acids and isocyanates in dilute DMF solutions using the rather underutilized reaction of the carboxylic acid group (-COOH) with isocyanates (-N=C=O) towards amides (-NH(C=O)-) induces early phase separation of surface-active aramid nanoparticles that form a solvent-filled 3D network stabilized against collapse by the chemical energy of the interparticle covalent bridges (crosslinks). Those wet-gels can be dried with liquid CO_2 taken out at the end as a supercritical fluid into lightweight (bulk density ~0.3 g cm^{-3}) highly porous (77% v/v) multifunctional materials classified as aerogels with high specific energy absorption (37 J g^{-1}), open-air speed of sound (338 m s^{-1}) and Styrofoam-like thermal conductivity (0.028 W m^{-1} K^{-1}).

1. Introduction

Polymeric cellular solids (foams) nearly eliminate convective heat transfer and thus combine low density with low thermal conductivity, both properties desirable for

thermal insulation.[1] Further reduction in the rate of heat transfer is realized with pore sizes below the mean free path of the pore-filling gas (68 nm for air at standard temperature-pressure (STP)).[2] Such mesoporous (2-50 nm) materials include aerogels,[3] which are commonly associated with poor mechanical properties. Arguably, systematic efforts to improve the mechanical properties of polymeric aerogels started about 10 years ago with crosslinking fibrous cellulose wet-gels with isocyanates.[4] However, post-gelation crosslinking is inherently time-consuming and thus inefficient. Alternatively, it is reasonable to seek one-step polymeric aerogels among materials known for their mechanical strength. Linear thermoplastic aromatic polyamides (aramids), either drawn into fibers (e.g., Kevlar®, from 1,4-phenylenediamine and 1,4-dicarboxylic acid), or built into honeycombs (e.g., Nomex®, from the corresponding 1,3-isomers) are well-known strong materials.[5] It is hence sensible to combine the high mechanical strength of aramids with the pore structure of aerogels.

The design of such materials imposes several interrelated chemical and structural issues. According to cellular solid theory, the mechanical strength of porous solids (e.g., honeycombs) increases with density and pore wall thickness.[6] In aerogels, that design rule is complicated by well-defined weak points on the pore walls, the interparticle necks. Bridging covalently (crosslinking) inorganic skeletal nanoparticles (e.g., silica, vanadia, rare earth oxides) with polymers renders the structure extremely robust, without adding substantially to the pore wall thickness; normalized for density, the mechanical properties of those porous materials (referred to as polymer-crosslinked aerogels) compete with those of bulk materials and in some aspects, e.g., the specific energy absorption under compression, far surpass the latter.[7] Since the role of the inorganic backbone in those

systems is basically that of a simple template, purely organic aerogels with the nanostructure and interparticle connectivity of inorganic/polymer core-shell aerogels should display similar mechanical properties. To accomplish this with Kevlar®- or Nomex®-type aramids is not trivial: with limited chances for crosslinking, long polymeric strands pack densely in order to maximize their non-covalent interactions (e.g., hydrogen-bonding).[8] Thus, under the conditions described below difunctional, single aromatic core monomers formed flocs, not characterized further. On the other hand, crosslinking at the monomer level would decrease solubility, promoting phase separation of small particles with high surface-to-volume ratio, hence more surface functional groups for enhanced interparticle connectivity and rigidity. Hyperbranched structures of that sort, based on trifunctional single aromatic core monomers, still exhibit significant solubility and liquid crystalline properties; in certain solvents, however, e.g., DMF they form large aggregates (molecular weights in the 700K-1M range), which at high concentrations behave as shear thinning gels.[9] Using this information as our point of departure, and in order to decrease the solubility of those systems, our strategy was to increase the aromatic content of the monomer per functional group reacting. For this, we have resorted to a rather underutilized synthetic method for amides from carboxylic acids and isocyanates.[10] The process is implemented with benzene-1,3,5-tricarboxylic acid (trimesic acid, TMA) and tris(4-isocyanatophenyl)methane (TIPM) according to eq 1.

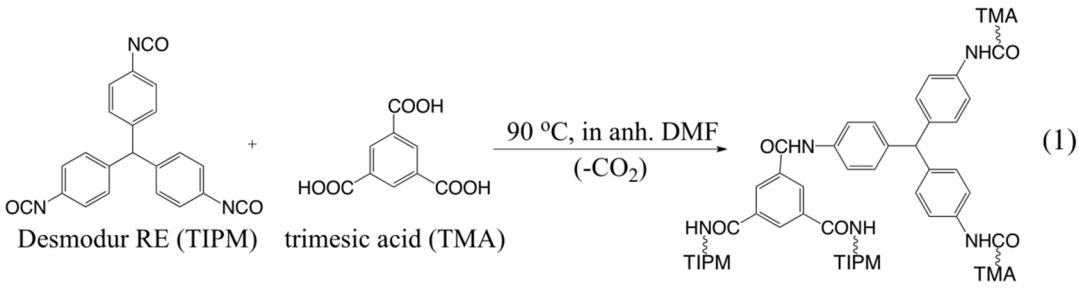

(1)

2. Results and Discussion

2.1 Synthesis of polyamide aerogels. This is essentially a one-pot, one-step process carried out according to eq 1. Monolithic aerogels of variable density were obtained by varying the monomer concentration in the sol (abbreviated herewith as [monomers]). By IR (Figure 1) we clearly observe the NH stretch at 3027 cm^{-1}, the amide cabonyl stretch at 1671 cm^{-1} and the NH bending vibration coupled to the C-N stretch at 1509 cm^{-1}. The reaction of –COOH with –N=C=O is basically a room temperature process involving a mixed carbamic-carboxylic anhydride intermediate (eq 2) that yields amide either by losing the isocyanate sp carbon (eq 3a), or bimolecularly through urea and anhydride intermediates (eq 3b). However, once urea and anhydride have been fixed on the network by reaction of their other functional groups via eq. 3a, they can no longer diffuse and react further to amide via eq 3b. Indeed, the presence of TIPM-derived polyurea was detected with solids ^{13}C NMR at 157 ppm (Figure 2) by comparison with the spectrum of the pure polymer published recently.[11] The amount of TIPM-derived urea decreases by gelation at elevated temperatures (Figure 2), implying that eq 3a and the first step of eq 3b proceed with comparably fast rates, while the second step of 3b (formation of amide by loss of CO_2) is significantly slower and is accelerated by heating. All data presented below concern gels obtained at 90 ^oC (eq 1).

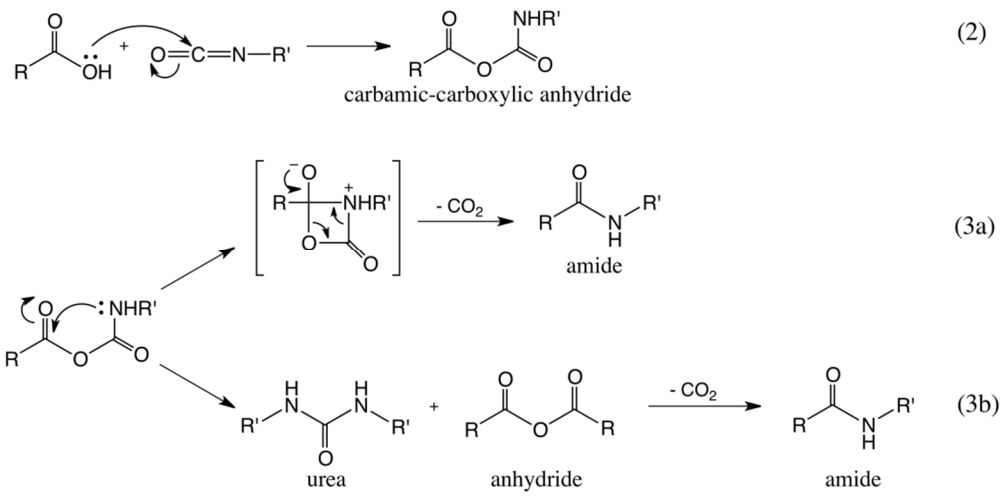

2.2 Materials characterization. Characterization data are summarized in Table 1. Monoliths shrink significantly (from 11% to 41% in linear dimensions relative to their molds, Table 1) in inverse order to [monomers]. Consequently, bulk densities (ρ_b) do not vary proportionally to [monomers], ranging from 0.21 to 0.40 g cm^{-3}, even though [monomers] was varied five-fold, from 5% to 25% w/w solids (lower [monomers] did not gel).

Table 1. Materials characterization data of polyamide aerogels.

Solids [% w/w]	Shrinkage [%] [a,b]	ρ_b [g cm^{-3}] [a]	ρ_s [g cm^{-3}] [c]	Crystallinity (2θ) [% (degrees)]	Porosity [% v/v]	BET surface area (micropore) [m^2 g^{-1}]	Pore diameter [nm] [d] ([e])	Particle diameter [nm] [f]
5	40.9±0.9	0.205± 0.008	1.266±0.014	79 (19,44)	84	380 (37)	23.7 (43.0)	12.5
10	31.1±0.5	0.288 ± 0.005	1.268±0.010	47 (19,44)	77	354 (42)	28.1 (30.3)	13.4
15	22.5±0.3	0.324 ± 0.010	1.282±0.010	51 (19,44)	75	172 (29)	19.8 (53.6)	27.2
20	17.4±0.1	0.361 ± 0.008	1.277±0.008	60 (20,44)	72	65 (10)	22.9 (122.3)	72.3
25	11.2±0.6	0.399 ± 0.005	1.279±0.007	58 (20,44)	69	15 (2)	33.5 (459.8)	313

[a]. Average of 3 samples. [b]. Shrinkage = 100 × [1-(sample diameter/mold diameter)]. [c]. Single sample, average of 50 measurements. [d]. By the $4\times V_{Total}/\sigma$ method. V_{Total} by the single-point adsorption method. [e]. In parentheses, V_{Total} via $V_{Total} = (1/\rho_b)-(1/\rho_s)$. [f]. Particle diameter = $6/\rho_s\sigma$.

Shrinking does not take place during gelation, aging, or solvent exchange; on the contrary, wet-gels swell by ~10% in linear dimensions upon transfer from their molds into fresh DMF. All shrinking takes place during drying with supercritical fluid (SCF) CO_2. Therefore, behaving as semi-permeable membranes, polyamide wet-gels swell till stretching of the framework –which, therefore must be rather flexible– balances the osmotic pressure of the internal "solution."[12] Then, complete collapse upon drying is halted by the covalent bonding of the network. Skeletal densities, ρ_s, fall in the 1.27-1.28 g cm^{-3} range, close to, but lower than the densities of Kevlar® and Nomex® (1.44 g cm^{-3}).[8] The invariance of ρ_s with [monomers] signifies absence of closed pores, and the values reflect the effect of crosslinking on molecular packing. Indeed, X-ray diffraction (see Electronic Supplementary Information, ESI) shows high crystallinity, but peaks are broad (unlike in Kevlar® where they are sharp),[13] precluding large-scale order. Porosities, Π, calculated from ρ_b and ρ_s via $\Pi=100\times[(1/\rho_b)-(1/\rho_s)]/\rho_b$,[7] decrease from 84% to 69% v/v as ρ_b increases. Despite shrinkage, all samples are highly porous.

Microscopically, aramid aerogels show aerogel-like connectivity of smaller particles into larger agglomerates (Figure 3). Particle size increases with [monomers]. All N_2 sorption isotherms rise above $P/P_o=0.9$ and do not reach saturation, consistently with the macroporosity observed in SEM. Nevertheless, narrow hysteresis loops and substantial specific volumes adsorbed at low P/P_o values indicate also the presence of both meso and microporosity. Brunauer-Emmett-Teller (BET) analysis yields high surface areas (σ, 380 m^2 g^{-1}) for the lower-density samples, decreasing dramatically (to 15 m^2 g^{-1}) as [monomers] increases. In all cases, about 10% of σ is attributed to micropores (via *t*-plot analysis, Harkins and Jura Model).[14] Average pore diameters

calculated by the $4V_{Total}/\sigma$ method using V_{Total} either from the highest adsorption point in the isotherm, or via $V_{Total}= (1/\rho_b)-(1/\rho_s)$, diverge as ρ_b increases, consistently with larger particles yielding macropores. Calculated particle diameters ($=6/\rho_s\sigma$, Table 1) increase with [monomers], but remain smaller than those observed in SEM. Therefore, SEM particles are higher aggregates. The lower shrinkage and the increasing particle size with [monomers] parallels the well-studied base-catalyzed gelation of resorcinol-formaldehyde at high resorcinol-to-catalyst ratios (slower reaction), suggesting microphase separation convoluted with kinetically controlled polymerization.[15]

2.3 Application Related Properties. Those include mechanical response under compression and thermal conductivity.

2.3.a Mechanical characterization. Larger particles are expected to have fewer interparticle contacts, therefore lower covalent connectivity and thus lower chemical energy stored in the 3D structure. Hence, not surprisingly, for not very different ρ_b, the mechanical properties under quasi-static compression (Figure 4) decrease precipitously as [monomers] increases (Table 2). Overall, stress-strain curves show a short linear range (<3% strain) followed by plastic deformation and inelastic hardening. At low ρ_b, i.e., with smaller particles, samples fail at high (~80%) strain, but not catastrophically. The ultimate compressive strength per unit density (238 MPa/(g cm^{-3}), calculated from Table 2 for the 0.324 g cm^{-3} samples) is within 10% equal to that of Kevlar® 49 (257 MPa/(g cm^{-3}), calculated from literature values of 370 MPa at 1.44 g cm^{-3}).[16] The Young's modulus, *E*, (slope of the linear range at <3% strain, see Figure 4, inset), is controlled by the amide interparticle bridges and is comparable to that of other isocyanate-derived

organic aerogels of similar ρ_b,[11,17] but is also significantly lower than that of polyurea-crosslinked silica and vanadia (233 and 206 MPa, at 0.55 and 0.44 g cm^{-3} respectively), whose stiffness is controlled by the inorganic framework.[7,11] The low values of the Young's modulus translate into open-air-like speed of sound waves (calculated via eq 4, see Table 2), rendering

$$\text{speed of sound} = (E/\rho_b)^{0.5} \quad (4)$$

those materials suitable for acoustic insulation. At the same time, however, combination of high fail strains and high ultimate compressive strengths yield high integrated areas under the stress-strain curves. Thus, the specific energy absorption under compression (a measure of toughness) reaches 37 J g^{-1}, surpassing Kevlar® 49-epoxy composites (11 J g^{-1}),[18] and renders polyamide aerogels appropriate for similar applications, for example as core for armor plates.[19]

Table 2. Selected mechanical characterization data of polyamide aerogel under uniaxial quasi-static compression at 23 °C.

Solids [% w/w]	ρ_b [g cm^{-3}]	Strain rate [s^{-1}]	Young's modulus [*E*, MPa]	Speed of sound [m s^{-1}] [a]	Ultimate strength [MPa]	Utimate strain [%]	Specific energy [J g^{-1}]
10	0.288	0.008	33±4	338	71±9	80±2	37.03
15	0.324	0.006	46±12	375	77±10	74±2	36.52
20	0.361	0.005	50±0.$_0$	372	23±1	61±3	14.64
25	0.399	0.006	0.9±0.1	47	5.2±1.7	21±7	2.77

[a]. Calculated via eq 4.

2.3.b Thermal conductivity. The thermal conductivity, λ, was calculated via eq 5 from bulk

$$\lambda = \rho_b \times c_P \times R \quad (5)$$

density, ρ_b, thermal diffusivity, R, and heat capacity, c_P, data. R was determined with a flash diffusivity method with disk samples ~1 cm in diameter, ~2.5 mm thick (the thickness of each sample was measured with 0.01 mm resolution and was entered as required by the data analysis software). Samples were coated with gold and carbon on both faces to minimize radiative heat transfer and ensure complete absorption of the heat pulse. Typical data are shown in Figure 5. Dashed reference lines indicate t_{50}, the time for the detector voltage (which is proportional to temperature) to reach half its maximum value. Data have been fitted to the pulse-corrected Cowan model.[20] Heat capacities, c_P, at 23 ^oC of powders of the same samples, were measured using Modulated Differential Scanning Calorimetry (MDSC) against several standrards, as described in the Experimental Section. All relevant data for two polyamide aerogel samples at densities that yield the best mechanical properties in terms of Young's modulus, ultimate strength and energy absorption (Table 2), are summarized in Table 3.

Table 3. Thermal conductivity data for polyamide aerogels samples prepared by using the 10% w/w and the 15% w/w solids formulations at 23 ^oC.

Material	Bulk density, ρ_b [g cm^{-1}]	Heat capacity, c_p [J g^{-1} K^{-1}]	Thermal diffusivity, R [mm^2 s^{-1}]	Thermal conductivity, λ [W m^{-1} K^{-1}]
10% w/w	0.280 ± 0.009	0.913±0.028	0.111 ± 0.005	0.028±0.002
15% w/w	0.310 ± 0.023	1.114±0.034	0.112 ± 0.002	0.039±0.003

Although the lowest thermal conductivity achieved (0.028 W m^{-1} K^{-1}) is above the record-low values reported for aerogels (<0.020 W m^{-1} K^{-1}), nevertheless it is noted that it is between those for Styrofoam (0.030 W m^{-1} K^{-1}) and polyurethane foam (0.026 W m^{-1} K^{-1}).[21] This fact should be put in perspective together with the relatively low density, the exeptional mechanical strength and the acoustic insulation value of these materials.

3. Experimental

3.1. Materials. Anhydrous DMF and TMA were purchased from Sigma-Aldrich. Desmodur RE was courtesy of Bayer Corporation USA.

3.1.a Synthesis of aramid aerogels. Typically, a solution of TIPM as received (Desmodur RE, 13.3 mL (13.6 g), containing 3.67 g of TIPM in anhydrous ethylacetate, 0.01 mol) and TMA (2.10 g, 0.01 mol) in variable amounts of anhydrous DMF (e.g., 24.0 mL (22.6 g) for 15% w/w solids) was stirred at 90 ^{o}C under N_2 for 1 h. The sol was poured into polypropylene molds (Wheaton polypropylene OmniVials, Part No. 225402, 1 cm diameter), which were sealed in a glove box and heated at 90 ^{o}C for 24 h. (The 15% w/w sol gels in 2.5 h from mixing.) Gels were washed with DMF, acetone (4× with each solvent, using 4× the volume of the gel) and dried with CO_2 taken out as a supercritical fluid (SCF). The same procedure was followed at room temterature and at 135 ^{o}C (using glass molds) for the CPMAS ^{13}C NMR studies of Fig. 1.

3.2. Methods. SCF drying in an autoclave (SPI-DRY Jumbo Supercritical Point Dryer, SPI Supplies, Inc. West Chester, PA). Bulk densities from sample weight and dimensions. Skeletal densities with helium pycnometry using a Micromeritics AccuPyc II

1340 instrument. N_2 sorption porosimetry with a Micromeritics ASAP 2020 Surface Area and Porosity Analyzer. IR in KBr pellets with a Nicolet-FTIR Model 750 Spectrometer. Solid-state ^{13}C NMR with a Bruker Avance 300 Spectrometer set at 75.475 MHz for carbon frequency using magic angle spinning (at 7 kHz) with broadband proton suppression and the CPMAS TOSS pulse sequence for spin sideband suppression. SEM with Au-coated samples on a Hitachi S-4700 field emission microscope. X-ray diffraction (XRD) with a PANalytical X-Pert Pro Multi-Purpose Diffractometer (MPD) and a Cu K_α radiation source. Mechanical testing under compression with an Instron 4469 universal testing machine frame, following the testing procedures and specimen length (2.0 cm) to diameter (1.0 cm) ratio specified in ASTM D1621-04a (Standard Test Method for Compressive Properties of Rigid Cellular Plastics). Thermal diffusivity, R, with a Netzsch NanoFlash Model LFA 447 flash diffusivity instrument using disk samples ~1 cm in diameter, 2.0-2.2 mm thick. Heat capacities, c_P, at 23 ^oC of powders of the same samples (4-8 mg), needed for the determination of their thermal conductivity, λ, were measured using a TA Instruments Differential Scanning Calorimeter Model Q2000 calibrated against a sapphire standard and run from -10 ^oC to 40 ^oC at 0.5 ^oC min^{-1} in the modulated T4P mode. The raw c_P data for the polyamide aerogels were multiplied by a factor of 0.920±0.028 based on measuring the heat capacities of rutile, KCl, Al, graphite, and corundum just before our experiments and comparing with the literature values (Table S.1 in ESI).

4. Conclusions

Organic aerogels provide the means for the explicit manipulation of molecular and interparticle crosslinking. With aramids, crosslinking at the molecular level induces early phase separation of small surface-reactive particles, promoting inter-particle crosslinking that improves the mechanical properties of the material inversely with the particle size. Implicitly, those principles seem to underlie all bottom-up synthesis of other recentry reported organic aerogels, as of polyureas,[11,22] polyimides,[17,23] polydicyclopentadiene,[24] polybenzoxazines,[25] and may comprise a base for further developments in the synthesis of mesoporous organic foams. Shrinkage, which might be regarded as an issue, is apparently accommodated by the flexible polymeric backbone, hence it does not cause cracking and is reproducible, thereby can be engineered into specific porous objects. With low density, high toughness, open air-like speed of sound and Styrofoam-like thermal conductivity, aramid aerogels are multifunctional materials suitable for a variety of defence, civil and transportation related applications.

Acknowledgements. We thank ARO (W911NF-10-1-0476) and NSF (CHE 0809562) for financial support, Bayer Corporation USA for the generous supply of Desmodur RE, Dr. Wei Wycoff at UM-Columbia for solids ^{13}C NMR, and the Materials Research Center of MS&T for SEM and XRD.

Electronic Supplementary Information (ESI) available: Solids ^{13}C NMR of polyamide aerogel and peak assignment. Liquid ^{13}C NMR spectra of monomers. XRD spectra of polyamide aerogels at variable density. Heat capacities of standard samples at 23 ^{o}C.

5. References

1. M. F. Ashby, *Phil. Trans. R. Soc. A*, 2006, **364**, 15-30.

2. (a) S. S. Kistler, *J. Phys. Chem.*, 1935, **39**, 79-86. (b) S. G. Jennings, *Aerosol Sci.*, 1988, **19**, 159-166.

3. A. C. Pierre and G. M. Pajonk, *Chem. Rev.*, 2002, **102**, 4243-4265.

4. C. Tan, B. M. Fung, J. K. Newman and C. Vu, *Adv. Mater.*, 2001, **13**, 644-646.

5. G. Odian, *Principles of Polymerization, Fourth Edition*, Wiley Interscience, New York, N.Y., USA 2004, pp 100-101.

6. L. J. Gibson and M. F. Ashby, *Cellular Solids: Structure and Properties 2nd Edition*, Cambridge, University Press, Cambridge, U.K. 1997.

7. N. Leventis, *Acc. Chem. Res.*, 2007, **40**, 874-884.

8. M. G. Northolt, *Eur. Polym. J.*, 1974, **10**, 799-804.

9. Y. H. Kim, *J. Am. Chem. Soc.*, 1992, **114**, 4947-4948.

10. (a) I. S. Blagbrough, N. E. Mackenzie, C. Ortiz and A. I. Scott, *Tetrahedron Lett.*, 1986, **27**, 1251-1254. (b) W. R. Sorensen, *J. Org. Chem.*, 1959, **24**, 978-980.

11. N. Leventis, C. Sotiriou-Leventis, N. Chandrasekaran, S. Mulik, Z. J. Larimore, H. Lu, G. Churu and J. T. Mang, *Chem. Mater.*, 2010, **22**, 6692-6710.

12. (a) D. H. Everett, "*Basic Principles of Colloid Science*," The Royal Society of Chemistry, London, U.K., 1988, p 189. (b) F. Ilmain, T. Tanaka and E. Kokufuta, *Nature*, 1991, **349**, 400-401.

13. R. V. Iyer, K. Sooryanarayana, T. N. Guru Row and K. Vijayan, *J. Mater. Sci.*, 2003, **38**, 133-139.

14. P. A. Webb and C. Orr, *Analytical Methods in Fine Particle Technology*, Micromeritics Instrument Corporation, Norcross, GA USA 1997 pp 67-68.

15. D. W. Schaefer, R. Pekala and G. Beaucage, *J. Non-Cryst. Solids*, 1995, **186**, 159-167.

16. J. W. Downing, Jr. and J. A. Newell, *J. Appl. Polym. Sci.*, 2004, **91**, 417-424.

17. C. Chidambareswarapattar, Z. J. Larimore, C. Sotiriou-Leventis, J. T. Mang and N. Leventis, *J. Mater. Chem.*, 2010, **20**, 9666-9678.

18. S. M. Lee, *Handbook of Composite Reinforcements*, John Wiley and Sons, New York, N.Y., USA 1992, pp 20-22.

19. P. J. Hogg, *Science*, 2006, **314**, 1100-1101.

20. (a) R. Cowan, *J. Appl. Phys.*, 1961, **32**, 1363-1369. (b) R. Cowan, *J. Appl. Phys.*, 1963, **34**, 926-927.

21. Lide, D. R. *CRC Handbook of Chemistry and Physics 84th Edition*; CRC Press: Boca Raton, FL, 2003; pp 12/22612/227.

22. J. K. Lee, G. L. Gould and W. L. Rhine, *J. Sol-gel Sci. Technol.*, 2009, **49**, 209-220.

23. K. Kawagishi, H. Saito, H. Furukawa and K. Horie, *Macromol. Rapid Commun.*, 2007, **28**, 96-100.

24. J. K. Lee and G. L. Gould, *J. Sol-gel Sci. Technol.*, 2007, **44**, 29-40.

25. P. Lorjai, T. Chaisuwan and S. Wongkasemjit, *J. Sol-Gel Sci. Technol.*, 2009, **52**, 56-64.

6. Figures

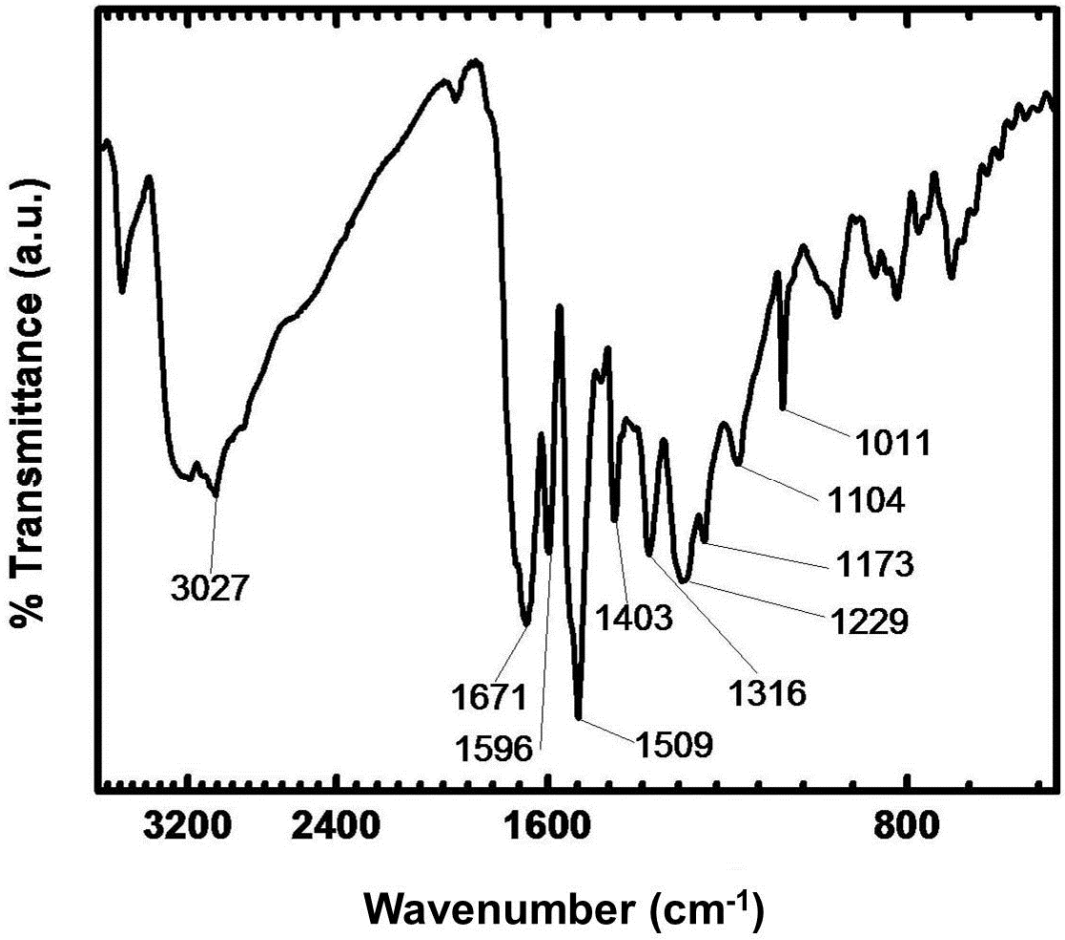

Figure 1. IR spectrum of a polyamide aerogel prepared from trimesic acid and tris(4-isocyanatophenyl)methane using 15% w/w solids in DMF.

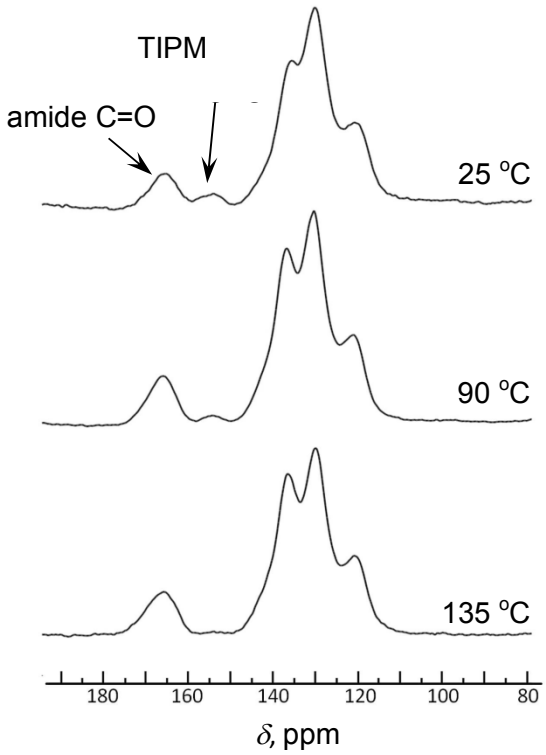

Figure 2. Solid state ^{13}C NMR spectra of polyamide aerogels prepared from trimesic acid and tris(4-isocyanatophenyl)methane using 15% w/w solids in DMF at the three temperatures indicated. (For peak assignments and the spectra of the monomers see ESI.)

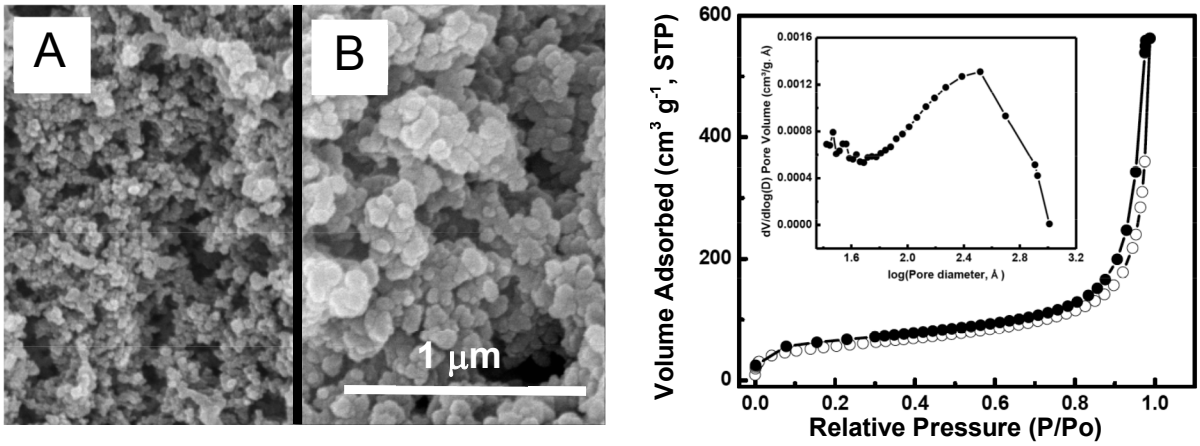

Figure 3. Left: SEM of aramid aerogels at 5% w/w solids (A) and 25% w/w solids (B). Right: N_2-sorption isotherm (obtained at 77K) of a 15% w/w solids sample (open circles: adsorption; dark circles: desorption). Inset: Pore size distribution via the Barrett- Joyner-Halenda (BJH) plot applied on the desorption branch of the isotherm.

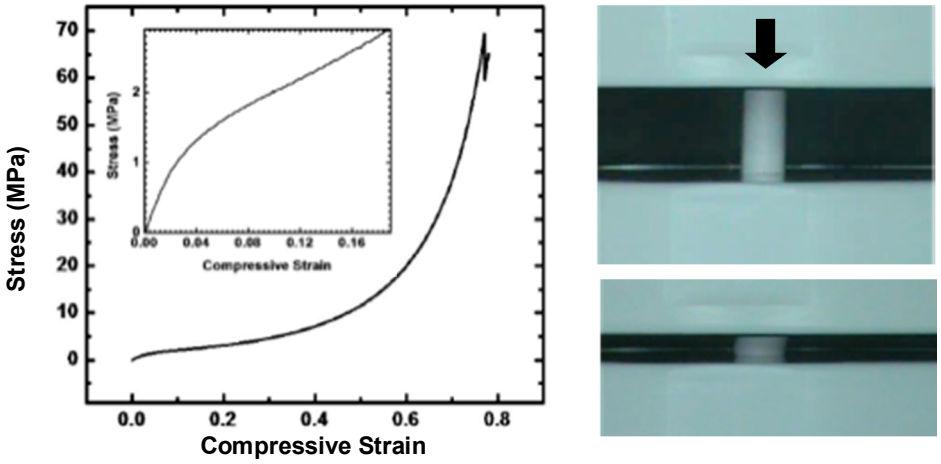

Figure 4. Typical quasi-static compression data of a 15% w/w solids aramid aerogel sample. (Diameter~0.78 cm; Length:Diameter=2:1.) Inset: Low-strain region magnified. indicated.

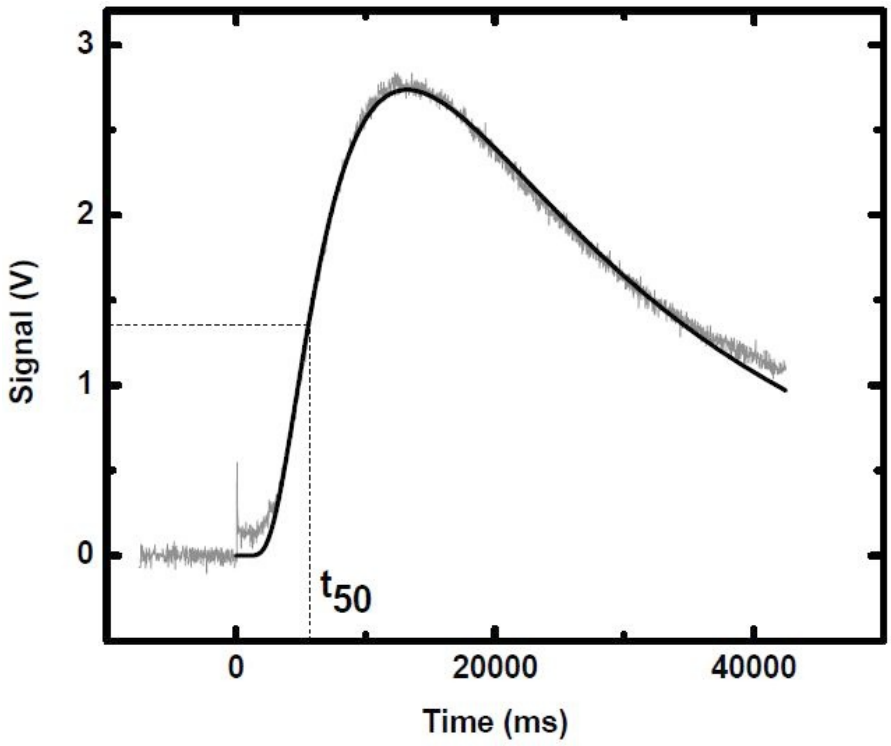

Figure 5. Temperature curve of the back face of a polyamide aerogel disk (~1 cm in diameter, 2.53 mm thick, ρ_b = 0.28 g cm^{-3}) coated with gold and carbon on both faces, following a heat pulse incident to the front face. Dashed reference lines indicate t_{50}, the time for the detector voltage (proportional to temperature) to reach half its maximum value. Data have been fitted to the pulse-corrected Cowan model.[20]

7. Electronic Supplementary Information

Figure S.1 (A) Solid state ^{13}C NMR spectrum of a polyamide aerogel prepared from trimesic acid and tris(4-isocyanatophenyl)methane using 15% w/w solids in DMF. (B) Liquid ^{13}C NMR spectrum of trimesic acid. (C) Liquid ^{13}C NMR spectrum of tris(4-isocyanatophenyl)methane. (Product is supplied as an ethylacetate solution, hence the residual peaks above baseline.)

Figure S.2 X-ray diffraction (XRD) data of polyamide aerogels prepared in DMF from trimesic acid and tris(4-isocyanatophenyl)methane using various solids formulations. Degrees of crystallinity calculated from the integrated peak intensity above the broad background.

Table S.1 Heat capacities of standard samples at 23 ^{o}C run at the heating rates indicated.

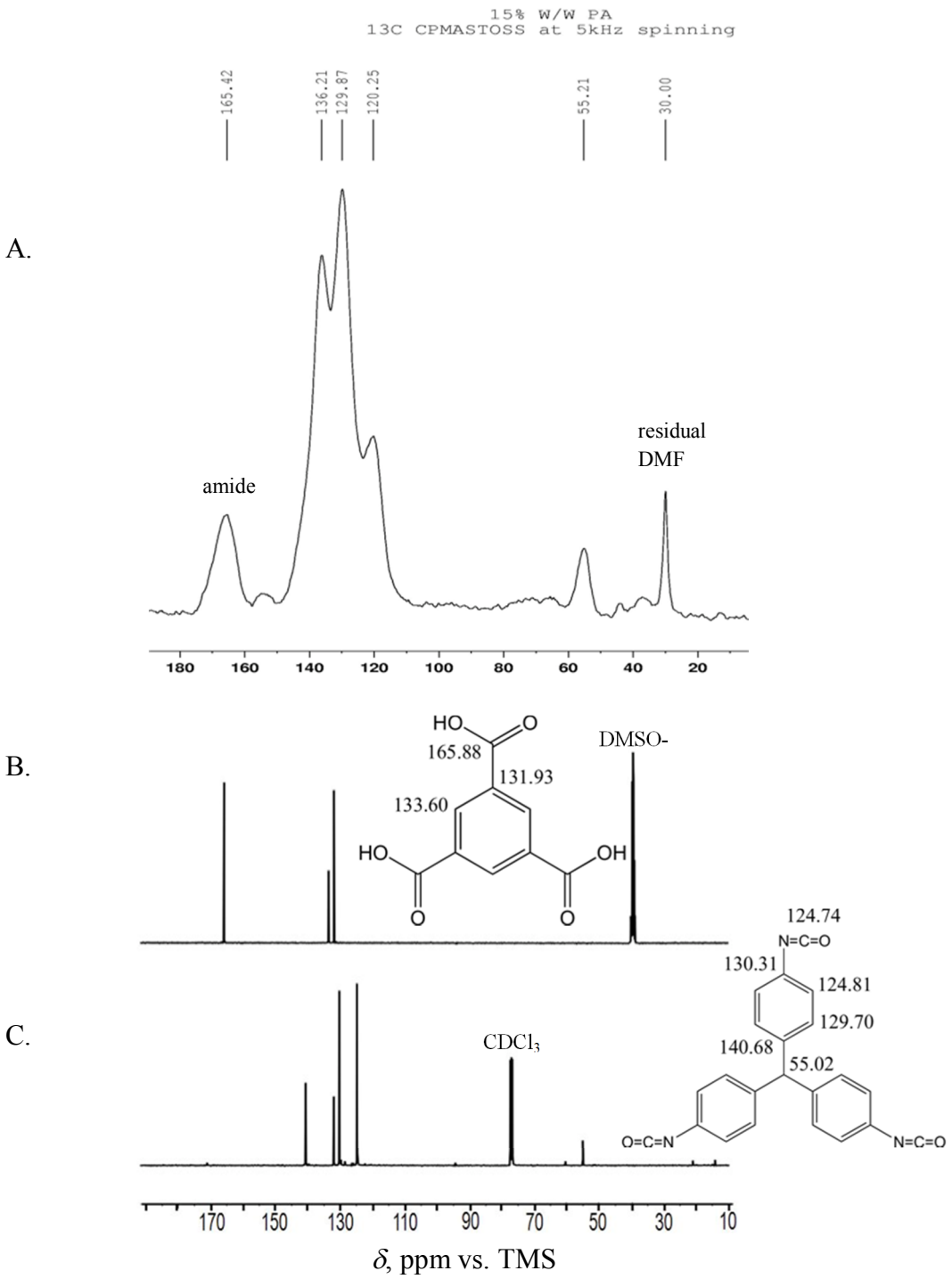

Figure S.1 (A) Solid state ^{13}C NMR spectrum of a polyamide aerogel prepared from trimesic acid and tris(4-isocyanatophenyl)methane using 15% w/w solids in DMF. (B) Liquid ^{13}C NMR spectrum of trimesic acid. (C) Liquid ^{13}C NMR spectrum of tris(4-isocyanatophenyl)methane. (Product is supplied as an ethylacetate solution, hence the residual peaks above baseline.)

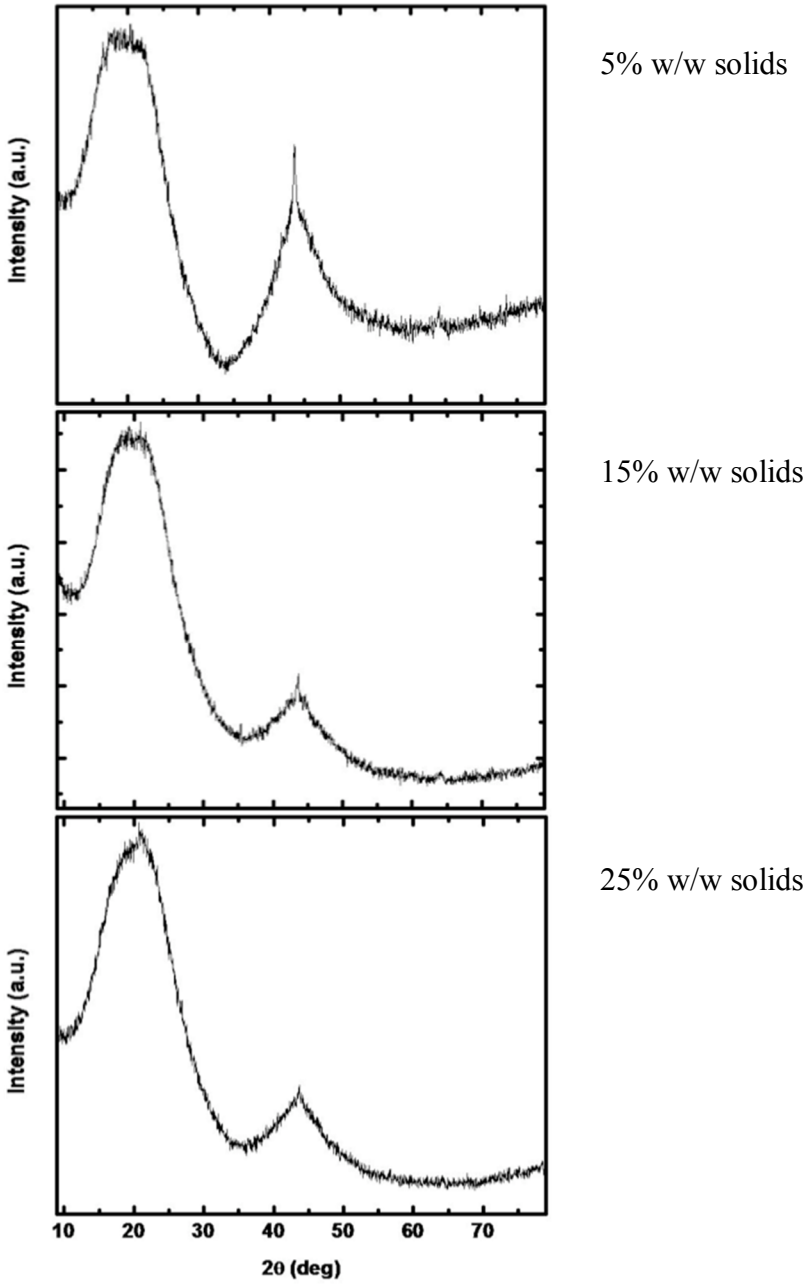

Figure S.2 X-ray diffraction (XRD) data of polyamide aerogels prepared in DMF from trimesic acid and tris(4-isocyanatophenyl)methane using various solids formulations. Degrees of crystallinity calculated from the integrated peak intensity above the broad background.

Table S.1 Heat capacities of standard samples at 23 ^{o}C run at the heating rates indicated.

	Observed [J g^{-1} K^{-1}]	Literature Value [J g^{-1} K^{-1}]	ratio [Lit./Obs.]
Rutile (TiO_2 at 0.5 ^{o}C min^{-1})	0.770	0.711	0.92
Rutile (TiO_2 at 2 ^{o}C min^{-1})	0.770	0.711	0.92
KCl (at 2 ^{o}C min^{-1})	0.746	0.695	0.93
Aluminum (at 0.5 ^{o}C min^{-1})	0.941	0.91	0.97
Graphite (at 2 ^{o}C min^{-1})	0.805	0.72	0.89
Corundum (Al_2O_3 at 2 ^{o}C min^{-1})	0.857	0.775	0.90
		Average:	0.92
		Standard Deviation:	0.02_8

IV. One-Step Room-Temperature Synthesis of Fibrous Polyimide Aerogels from Anhydrides and Isocyanates and Conversion to Isomorphic Carbons

Chakkaravarthy Chidambareswarapattar[a], Zachary Larimore[a], Chariklia Sotiriou-Leventis[*,a], Joseph T. Mang[*,b] and Nicholas Leventis[*,a]

a. Department of Chemistry, Missouri University of Science and Technology (*formerly,* University of Missouri-Rolla), Rolla, MO 65409, U. S. A.

b. Los Alamos National Laboratory, Los Alamos, NM 87545, U.S.A.

Published as an article in the *Journal of Materials Chemistry*

Abstract: Monolithic polyimide aerogels (PI-ISO) have been prepared by drying wet-gels synthesized via a rather underutilized room–temperature reaction of pyromellitic dianhydride (PMDA) with 4,4′-methylene diphenyl diisocyanate (MDI). The reaction is followed by liquids ^{13}C-NMR in DMSO-d_6 and it proceeds through a seven-member ring intermediate that collapses to the imide by expelling CO_2. PI-ISO are characterized comparatively with aerogels referred to as PI-AMN, obtained via the classic reaction of PMDA and 4,4′-methylenedianiline (MDA). The two materials are chemically identical, they show similar degrees of crystallinity (30-45%, by XRD) and they both consist of similarly sized primary particles (6.1-7.5 nm, by SANS). By N_2-sorption porosimetry they contain both meso- and macroporosity and they have similar BET surface areas (300-400 m^2 g^{-1}). Their major difference, however, is that PI-AMN are particulate while PI-ISO are fibrous. The different morphology has been attributed to the rigidity of the seven-member ring intermediate of PI-ISO. PI-AMN shrink significantly during processing (up to 40% in linear dimensions), but mechanically are much stronger materials than PI-ISO of the same density. Upon pyrolysis at 800 ^{o}C both PI-ISO and PI-AMN are converted to porous carbons; PI-AMN loose their nanomorphology and more than 2/3 of their surface area, as opposed to PI-ISO, which retain both. Etching with CO_2

at 1000 ^{o}C increases the surface area of both PI-AMN (to 417 m^2 g^{-1}) and PI-ISO (to 1010 m^2 g^{-1}), and improves the electrical conductivity of the latter by a factor of 70.

1. Introduction

Aerogels are low-density solids with high open porosity and surface area.[1] Importantly, most or all pores are classified as mesopores sized between 2 and 50 nm, namely below the mean free path of the air molecules at room temperature and atmospheric pressure (~60-70 nm). This provides for exceptionally low thermal conductivities, thereby offering a distinct advantage over conventional blown foams for thermal insulation. There are two main types of aerogels, organic and inorganic. They were first reported together in 1931 by Kistler, who used high temperature and pressure to convert the pore-filling solvent of wet-gels into a supercritical fluid (SCF) that was vented off slowly, yielding air-filled solids with the same dimensions as his original wet-gels. Although Kistler himself reported that his most robust materials were of the organic type,[2] nevertheless most subsequent studies focused on inorganic aerogels (mainly silica). Further development of organic aerogels remained dormant for almost 60 years until in 1989 R. Pekala reported the synthesis of phenolic resin type wet-gels and aerogels, via condensation of resorcinol with formaldehyde (RF aerogels).[3] Owing to the record-low thermal conductivity of Pekala's materials (0.012 W m^{-1} K^{-1} at 0.16 g cm^{-3}),[4] as well as their pyrolytic conversion to electrically conducting carbon aerogels,[5] RF aerogels were investigated intensely and today a typical literature search shows that for several years the terms "organic" and "RF aerogels" were practically synonymous. The first post-RF organic aerogels followed the original phenolic resin paradigm (phenol-furfural,[6] cresol-

formaldehyde,[7] melamine-formaldehyde[8]), however, several other systems have been also reported including polyurethane[9] and polyurea aerogels,[10] polystyrene,[11] polyacrylonitrile,[12] polybenzoxazine,[13] poly(bicyclopentadiene) aerogels synthesized via ring opening metathesis polymerization (ROMP) of the monomer,[14] and more recently polyimide aerogels.[15,16]

Among engineering plastics, polyimides demonstrate good chemical resistance, as well as excellent mechanical properties and stability at high temperatures.[17] For example, a special formulation referred to as PMR-15 is emerging as an aerospace industry standard for replacing metal components in jet engines and is rated at 290 ^{o}C for 10,000 h.[18] In that regard, polyimide aerogels could be ideal materials for high-temperature low-k dielectrics for fast electronics (k: dielectric constant),[19] and for high-temperature thermal insulation with an edge over blown closed-cell macroporous polyimide-foams already in used for that purpose.[20] Polyimide aerogels have been synthesized[15,16] by the typical two-step DuPont route from di-anhydrides and di-amines.[21] The two monomers react at room temperature yielding a polyamic acid solution that subsequently is dehydrated to the polyimide with acidic anhydride and a base-catalyst (e.g., pyridine, triethylamine). A post-gelation high-temperature treatment of wet-gels ensures complete imidization and conversion of undesirable isoimides to imides. It is noted though that chemical dehydration of the polyamic acid is energy-intensive and introduces by-products; industrially, dehydration and imidization are carried out by direct heating of the polyamic acid at high temperatures (~200 ^{o}C).[17,22] In an attempt to adopt this method for the synthesis of aerogels, we obtained precipitates rather than gels.

Thus, drawing from our familiarity with the chemistry of isocyanates in the synthesis of mechanically strong aerogels,[23] and in an effort to improve the economics of the polyimide process, we report herewith polyimide aerogels synthesized via a rather under-utilized one-step room-temperature route that involves reaction of anhydrides with isocyanates[24] structurally similar to the amines used in the classic DuPont route.[21] From that perspective, this is a comparative study based on a model system that involves pyromellitic dianhydride (PMDA) reacting with 4,4′-methylene diphenyl diisocyanate (MDI) on one hand, and 4,4′-methylenedianiline (MDA) on the other. The resulting

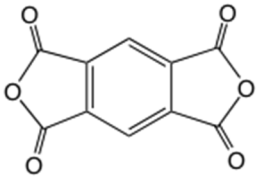

PMDA

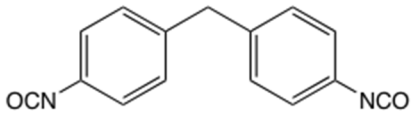

MDI

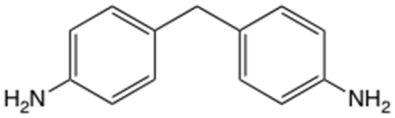

MDA

aerogels from both routes are chemically identical (by IR and solids CPMAS ^{13}C-NMR), and despite similar degrees of crystallinity and primary particle sizes (by XRD and SANS, respectively) their nano-morphology (by SEM) is vastly different: polyimides from the amine route (PI-AMN) are particulate, while those from the isocyanate route (PI-ISO) are fibrous. Those differences are attributed to the rigidity of the chemical intermediates involved in the two processes. Overall, the isocyanate route has several distinct advantages: (a) it is a low-temperature process, yielding polyimides even at room temperature; (b) it does not require sacrificial dehydrating agents (acetic anhydride/pyridine) for gelation; (c) CO_2 is the only byproduct; (d) sturdy, higher-density aerogels are easily accessible, while the polyamic acid route encounters early solubility issues as the concentration of the sol increases limiting the higher densities attainable; and, (e) PI-ISO shrink less than the corresponding PI-AMN, making lower density

materials more easily accessible. Upon pyrolysis, both kinds of polyimide aerogels are converted to carbon aerogels, which, in the case of PI-ISO retain the fibrous morphology of their parent polyimides.

2. Results and Discussion

2.1 Synthesis of PI-ISO versus PI-AMN. Scheme 1 summarizes the synthesis of PI-AMN and PI-ISO aerogels. Typical samples processed under the different conditions discussed below are shown in Figure 1.

PI-AMN were prepared through a polyamic acid (Scheme 2) according to a modification of the ASPEN adaptation[15] of the classic DuPont route.[21] According to the latter, typically, the polyamic acid is not isolated from its preparation solution (in *N*-methyl-2-pyrrolidone, NMP), and is dehydrated either thermally (>190 ^{o}C), or chemically at room temperature with acetic anhydride/base (e.g., pyridine, triethylamine, etc.).[25] At first, to improve the ASPEN protocol that opts for chemical dehydration, we attempted to bypass the latter step by direct heating of NMP solutions of the polyamic acid. However, that resulted in precipitation rather than gelation. Thus, necessarily, we had to use room-temperature (RT) chemical dehydration with acetic anhydride/pyridine staying close to the ASPEN protocol.[15] The bulk density of the final aerogels was varied by successive dilutions of the polyamic acid solution before adding the dehydrating agents. Although addition of the dehydrating agents into the polyamic acid solution induces gelation, in general polyimides obtained by that route still require heating at elevated temperatures in order to complete imidization and to convert any kinetically formed isoimides to thermodynamically more stable imides:[15]

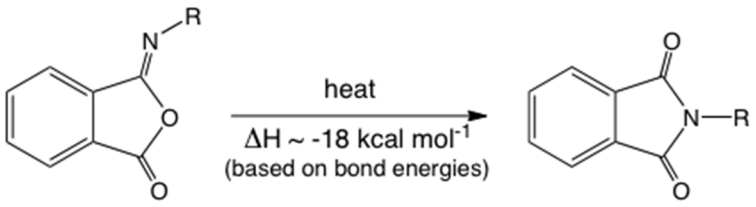
N
R
O
O
heat
ΔH ~ -18 kcal mol-1
(based on bond energies)
O
N—R
O

Scheme 1. Synthesis of polyimide aerogels

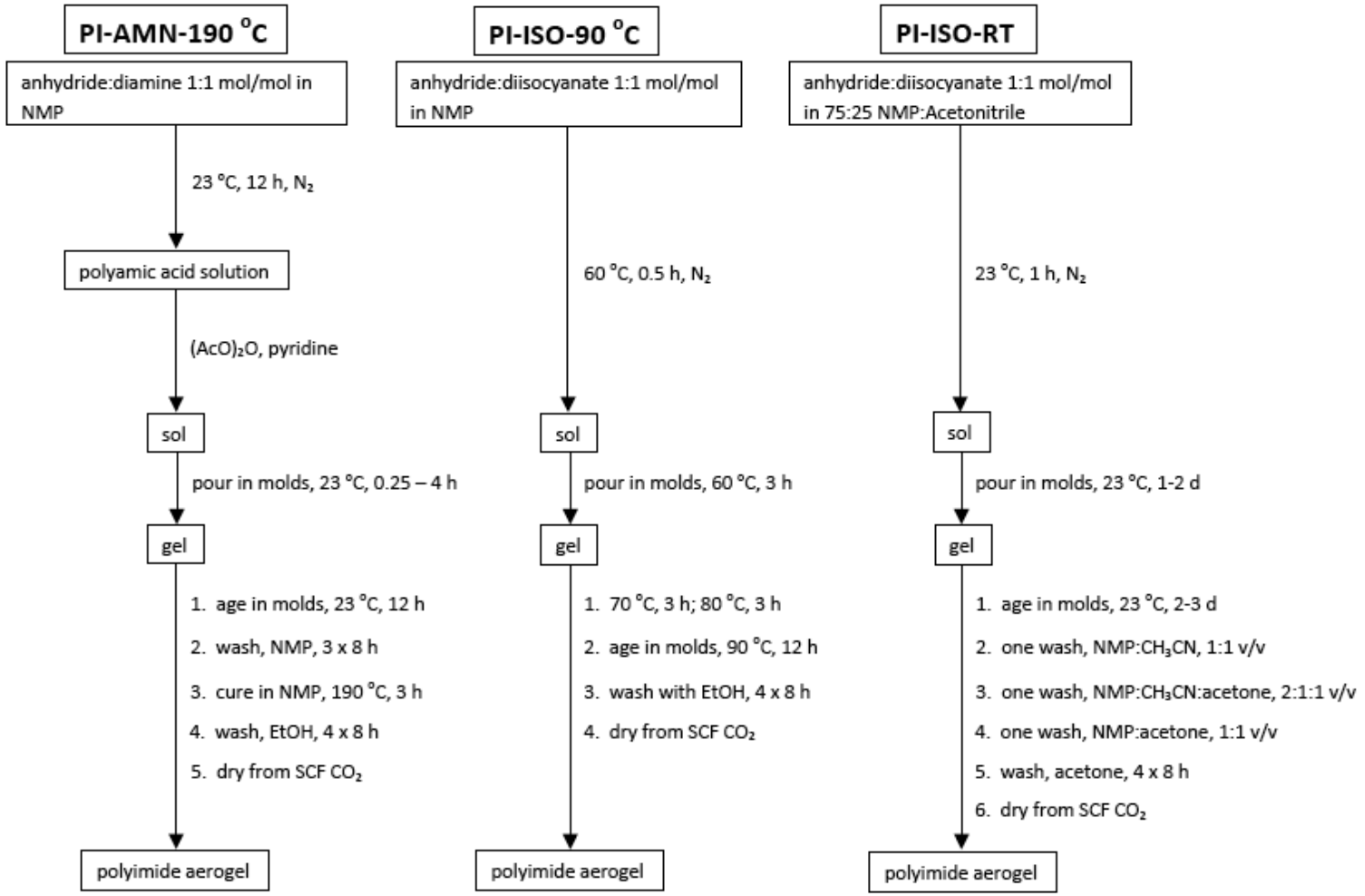

Room-temperature PI-AMN gels can be solvent-exchanged with ethanol and dried to aerogels (abbreviated as PI-AMN-RT, see Figure 1) using liquid CO_2 taken out supercritically. According to IR (Figure 2),[26] PI-AMN-RT aerogels do not contain detectable amounts of isoimide (expected absorption at 1800 cm^{-1}),[27] but the absorption at ~3500 cm^{-1} indicates that they may contain amides, and therefore unreacted polyamic acid. Heating PI-AMN-RT aerogels at 190 ^{o}C caused extensive shrinkage, and resulted into xerogel-like materials with loss of all surface area. Hence, it was decided to heat PI-AMN in the solvent-swollen state, and thus imidization was completed before drying by transferring wet-gels in NMP, followed by heating at 190 ^{o}C. Subsequently, such wet-gels were cooled to RT, NMP was exchanged with ethanol, and ethanol-filled wet-gels were dried with liquid CO_2 into PI-AMN-190. It is important to note that even though the absorption at ~3500 cm^{-1} has been decreased, nonetheless it has not disappeared. Further, even by heating in the solvent-swollen state PI-AMN samples shrink significantly relative to their molds (up to 40% in linear dimensions) irrespective of their bulk density; shrinkage is not caused by the heat treatment at 190 ^{o}C, as aerogel samples either dried directly after gelation (PI-AMN-RT) or after heating at 190 ^{o}C in NMP according to Scheme 1 (PI-AMN-190) are similar in size (see Figure 1). Therefore, the shrinkage of PI-AMN samples is attributed to the innate chemistry of the gel-forming process (see Section 2.3 below).

On the other hand, PMDA/MDI solutions gel directly at room temperature without use of additional reagents. The reaction was followed up to the gelation point with liquid ^{13}C-NMR in DMSO-d_6 (Figure 3), and by comparison with Scheme 2 it can be seen clearly that the reaction proceeds through a seven-member ring intermediate,

which collapses to the imide by expelling CO_2.[24] At the gelation point (~7.5 h, Figure 3) there is significant amount of the seven-member ring intermediate remaining and still reacting. On the other hand, the reaction proceeds much slower in NMP at RT and gelation may take up to 48 h depending on the monomer concentration (see Experimental). Therefore, it could be considered reasonable to carry out gelation at RT in DMSO. In that regard, it should be noted that although all PI aerogels are opaque, their wet-gel precursors are translucent allowing visual inspection of their interior. Thus, we can see easily that PI-ISO aerogels obtained from DMSO sols at RT contain large bubbles (CO_2) entrapped

Scheme 2. The two routes resulting into the same polyimide aerogel composition

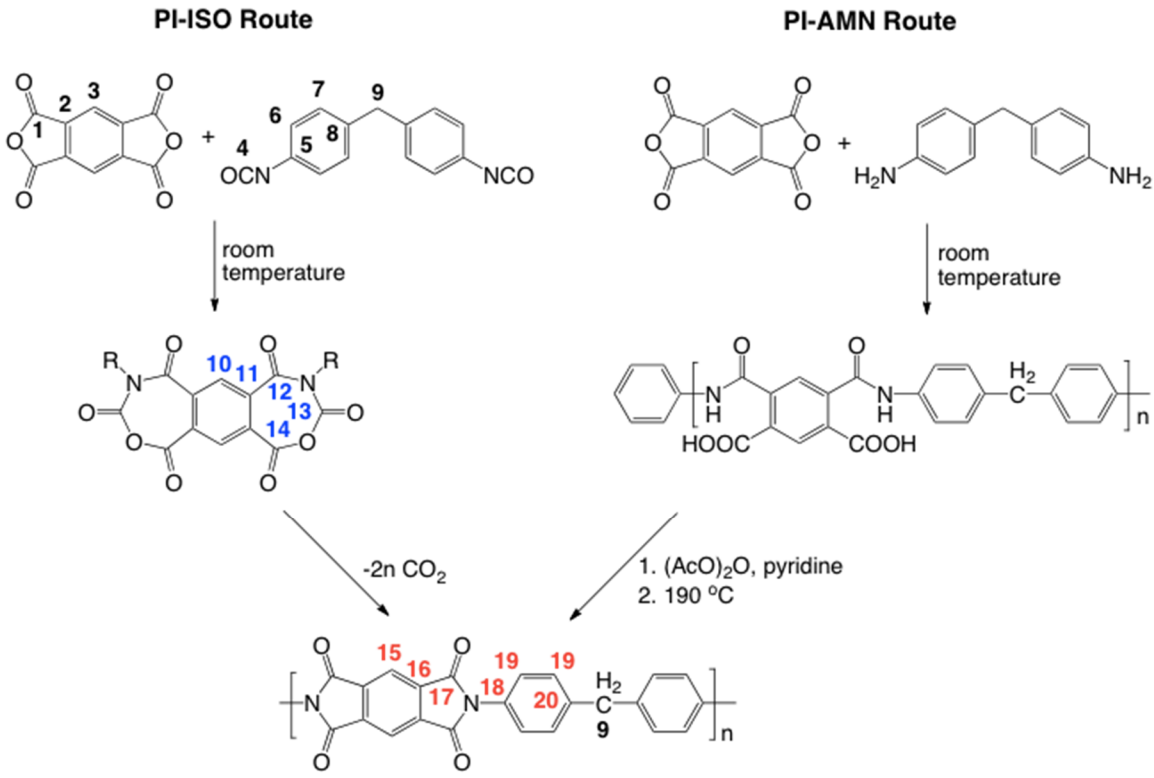

in their bulk. That feature deserves further investigation as the seven-member intermediate can be considered as an *in-situ* foaming agent leading to PI-ISO foams defined by porous walls. However, for the purposes of this study, namely a direct comparison of the materials properties of PI-ISO and PI-AMN monoliths (in terms of bulk densities, porosities, surface areas etc.), it was necessary to obtain bubble-free PI-ISO aerogel monoliths, hence gelation in pure DMSO was not considered further. Void-free PI-ISO aerogel monoliths were obtained by two methods (Scheme 1): either, (a) by RT gelation of PMDA/MDI in mixtures of NMP with DMSO or acetonitrile (samples referred to as PI-ISO-RT); or, (b) by gelation in pure NMR at slightly elevated temperatures by stepwise heating from 60 ^{o}C to 90 ^{o}C (see Scheme 1, samples referred to as PI-ISO-90). The first method combines sufficiently low-viscosity sols with affordable gelation times (30-33 h for the 15% w/w solids formulation) allowing CO_2 to be dissipated and bubble formation to be avoided. The second method has the advantage of comparing PI-ISO and PI-AMN prepared in environments of similar polarity (both in NMP); step-wise heating of the PMDA/MDI sol in NMP ensured defect-free monoliths, while direct heating at 90 ^{o}C led to foams qualitatively similar to those obtained in DMSO at RT (i.e., with bubbles). All gels were aged ~4× their gelation time in their molds, they were solvent-exchanged with ethanol and dried with liquid CO_2.

By IR (Figure 2) PI-ISO-RT look practically identical to PI-AMN-190, but the solids ^{13}C-NMR spectra of the two materials show differences in the relative peak intensities (Figure 4), which in turn are attributed to differences in the polymer length, and therefore to the polarity of the sol (reminder: PI-ISO-RT were prepared in NMP/acetonitrile (or DMSO) mixtures, while PI-AMN-190 in pure NMP). Most

notably, the peak in the ^{13}C-NMR spectrum of PI-AMN-190 at 142 ppm (carbon-16, see Scheme 2) appears only as a shoulder in the spectrum of PI-ISO-RT. According to ^{13}C-NMR spectra simulations of the PMDA/MDI dimer to pentamer, we expect an upfield shift for the resonance of carbon-16 as the polymer becomes longer, suggesting that PI-ISO-RT consists of longer polymer chains than PI-AMN-190. By the same token, we also see in Figure 4 that the ^{13}C-NMR spectrum of PI-ISO-90, (which was also prepared in NMP just like PI-AMN-190), is identical to the spectrum of the latter, signifying the importance of the solvent polarity in the nucleation and growth mechanism by which the two materials are formed.

2.2 Macroscopic characterization of PI-ISO versus PI-AMN. General materials properties of polyimide aerogels synthesized by all methods of Scheme 1 are summarized in Table 1. It is noted that despite that sols were formulated based on weight percent of solids in solvents of different densities, attention was paid so that the molar monomer concentrations in the different sols, ([C], see Table 1), remained about equal, allowing for a direct comparison. PI-AMN aerogels appear mechanically stronger than the corresponding PI-ISO, but as mentioned above they also shrink significantly with respect to their molds (from 42% at the lowest gelation limit of 2.5% w/w solids, to 25% at the maximum solubility limit of 20% w/w solids). On the other hand, PI-ISO samples are also robust but soft, they shrink much less than PI-AMN under any preparation conditions, and in some cases their shrinkage is even less than 1%. All shrinkage data are summarized in Figure 5. Shrinkage is reflected upon the bulk densities (ρ_b) of the final aerogels. At similar solids formulations the density of the PI-ISO samples is always lower than that of the PI-AMN samples (e.g., at 20% w/w solids formulation,

Table 1. Materials characterization data for polyimide aerogels

sample-process temp-% w/w solids [a]	[C], M	linear shrinkage (%) [e]	bulk density, ρ_b (g cm^{-3})	skeletal density, ρ_s (g cm^{-3}) [g]	crystallinity (%) [2θ]	porosity, Π (% void space)	BET surface area, σ (m^2 g^{-1})	average pore diam. (nm) [h]
PI -AMN-190-2.5[d]	5.78×10^{-5}	41.6	0.090	1.547 ± 0.104	45 [21, 29]	94	385	17.0 [108.5]
PI-ISO-RT -2.5 [c,d]	5.14×10^{-5}	35.3	f	1.595 ± 0.102	f	f	297	14.7 [f]
PI–AMN-190-5	1.17×10^{-4}	38.0 ± 0.1 [j]	0.142 ± 0.021 [j]	1.478 ± 0.045	37 [21, 28]	90	412	29.6 [62.0]
PI –ISO-RT-5 [b]	1.18×10^{-4}	5.0	f	1.526± 0.045	42 [19, 25]	f	374	13.8 [f]
PI-ISO-RT-5 [c]	1.04×10^{-4}	18.87 ± 0.02 [j]	0.047 ± 0.002 [j]	1.534 ± 0.080	37 [18]	97	333	23.0 [250.4]
PI-AMN-190-10	2.37×10^{-4}	30.04 ± 0.02 [k]	0.186 ± 0.016 [k]	1.453 ± 0.015	41 [21,29,42]	87	431	29.5 [45.8]
PI-ISO-RT-10 [b,k]	2.33×10^{-4}	2.1±0.9 [k]	0.112 ± 0.003 [k]	1.490 ± 0.023	23 [18]	93	373	28.9 [88.9]
PI-ISO-RT-10 [c,k]	2.11×10^{-4}	10.03 ± 0.03 [k]	0.090 ± 0.006 [k]	1.473± 0.022	59 [43, 49]	94	316	25.6 [131.6]
PI-AMN-190-15	3.61×10^{-4}	28.24 ± 0.01 [k]	0.232 ± 0.008 [k]	1.474 ± 0.024	35 [22, 26]	84	413	26.5 [35.3]
PI-AMN-RT-15	3.61×10^{-4}	35.0± 0.3 [k]	0.376 ± 0.006 [k]	1.432 ± 0.018	37 [35, 48]	74	299	11.2 [26.2]
PI –ISO-90- 15	3.43×10^{-4}	17.48 ± 0.02 [k]	0.223 ± 0.014 [k]	1.551 ± 0.037	33 [22, 27,44]	85	244	14.2 [62.6]
PI-ISO-RT -15 [b]	3.54×10^{-4}	<1.0 [k]	0.167±0.002 [k]	1.447 ± 0.021	17 [17]	88	391	25.5 [54.3]
PI-ISO-RT-15 [c]	3.22×10^{-4}	3.19 ± 0.01 [k]	0.124 ± 0.001 [k]	1.398± 0.009	42 [43,49]	91	315	33.5 [93.2]

PI-AMN-190-20	4.89×10^{-4}	24.89 ± 0.02 [k]	0.291 ± 0.022 [k]	1.437± 0.016	31 [21,29]	80	378	18.2 [29.0]
PI-ISO-90 -20	4.64×10^{-4}	5.87 ± 0.01 [k]	0.266 ± 0.011 [k]	1.454 ± 0.009	33 [18]	80	246	20.0 [50.0]
PI-ISO-RT-20 [b]	4.77×10^{-4}	2.78 ± 0.03 [k]	0.208 ± 0.001 [k]	1.415 ± 0.022	22 [18]	85	366	23.0 [44.7]
PI-ISO-RT-20 [c]	4.36×10^{-4}	1.27 ± 0.01 [k]	0.196 ± 0.001 [k]	1.461 ± 0.014	31 [17, 19]	87	352	22.7 [84.7]
PI-ISO-90 -30	7.17×10^{-4}	$4.71\pm0.00_1$ [l]	0.382±0.003 [l]	1.473 ± 0.031	31 [17]	74	303	13.2 [51.2]
PI-ISO-RT-30 [c]	6.78×10^{-4}	<1.0 [l]	0.285 ± 0.027 [l]	1.445 ± 0.009	33 [17, 20]	80	339	22.4 [33.3]
PI-ISO-90-40	9.84×10^{-4}	$4.90\pm0.00_1$ [l]	0.513±0.011 [l]	1.432 ± 0.009	32 [17, 19]	64	278	10.7 [17.8]
PI-ISO-RT-40 [c]	9.36×10^{-4}	3.8 ± 0.2 [l]	0.417 ± 0.008 [l]	1.443 ± 0.007	42 [27, 43]	71	171	12.0 [39.7]
PI-ISO-90-50	1.27×10^{-3}	$5.50\pm0.00_3$ [l]	0.679 ± 0.002 [l]	1.452 ± 0.014	33 [19, 25]	53	222	6.3 [14.1]

a. PI-AMN: Polyimide samples synthesized through the amine route; PI-ISO: Polyimide samples synthesized through the isocyanate route; PI-AMN-190: samples cured in NMP at 190 °C before drying; PI-AMN-RT: samples dried supercritically without further curing at 190 °C. PI-ISO-90: samples synthesized at 60-90 °C in NMP; PI-ISO-RT: samples synthesized at room temperature. b. PI-ISO-RT samples synthesized in NMP/DMSO. c. PI-ISO-RT samples synthesized in NMP/acetonitrile). d. Single sample. e. Shrinkage = 100 × (mold diameter – sample diameter)/(mold diameter). f. Irregular shape / was not measured. g. Single sample, average of 50 measurements. h. By the $4\times V_{Total}/\sigma$ method. For the first number, V_{Total} was calculated by the single-point adsorption method; for the number in brackets, V_{Total} was calculated via $V_{Total} = (1/\rho_b)-(1/\rho_s)$. i. From the BJH plots: The first numbers are the peak maxima; the numbers in brackets are the width at half maxima of the BJH plots. j. Average of 2 samples. k. Average of 4 samples. l. Average of 3 samples.

which is the highest solubility limit of PI-AMN, the density of the PI-ISO samples is 0.2 g cm^{-3} versus 0.3 g cm^{-3} for the PI-AMN samples). Further, the lowest ρ_b values that have been possible with PI-AMN are ~0.09 g cm^{-3}, while easy-to-handle PI-ISO monoliths with ρ_b as low as 0.05 g cm^{-3} can be prepared readily.

Partly owing to the similar chemical composition of the two materials, partly to their similar degree of crystallinity (30-45% by XRD, see Table 1) and partly to similar packing distances within the crystalline phases (expressed by similar 2θ values, see Table 1), skeletal densities, ρ_s, of all samples are in the 1.4-1.5 g cm^{-3} range, that is comparable with the density of bulk polyimides obtained from PMDA and MDA (1.357 g cm^{-3}).[28] The similar ρ_s values but the different ρ_b's are reflected on the porosities, which are higher for the PI-ISO aerogels relative to the corresponding PI-AMN samples. However, BET surface areas, σ, from N_2-sorption data (Figure 6) show an opposite trend from the porosities: despite much higher shrinkage, higher bulk densities and lower porosities, PI-AMN samples have about equal or higher surface areas than the PI-ISO samples. These data point to significant differences in the nanomorphology of the PI-AMN versus the PI-ISO samples, which is discussed in the next section.

2.3 Structural characterization of PI-ISO versus PI-AMN. The microstructure of polyimide aerogels was evaluated in terms of their pore-size distribution and the nanomorphology of their skeletal frameworks. The pore-size distribution at the meso/macro scale was evaluated semi-quantitatively by analysis of the N_2-sorption data (Figure 6) in combination with SEM (Figure 7), while the elementary building blocks of the skeletal framework were probed with SANS (Figure 8). All data shown concern

samples obtained with the 15% w/w solids formulation. Similar data and trends have been observed with samples prepared with all other solids formulations (Table 1).

For both PI-AMN and PI-ISO samples, N_2-sorption isotherms show a rapid increase of the volume adsorbed at relative pressures above 0.9, which in combination with the narrow desorption loop indicates the presence of both meso and macroporosity. Indeed, pore size analysis via the relationship (pore diameter)=$4\times V_{Total}/\sigma$, where V_{Total} is calculated either from the maximum adsorption point in the isotherm, or the relationship $V_{Total}=(1/\rho_b)-(1/\rho_s)$, gives quite different values (Table 1), which get progressively closer as the bulk density increases, as expected by the fact that more dense materials should have smaller pores. The BJH-desorption method (Figure 6, inset) reflects the mesoporosity and yields pore diameters closer to those obtained by the single point absorption method (Table 1), but more importantly, it shows quite broad pore size distributions (evaluated by the width at half maxima of the BJH plots, see Table 1). Overall, the N_2-sorption method indicates that both PI-AMN and PI-ISO aerogels are meso/macroporous materials. SEM, however, shows that their pore structures are quite different: at all densities PI-AMN are particulate while PI-ISO are fibrous (Figure 7). At high magnifications, we are able to discern a primary/secondary particle structural hierarchy in the case of PI-AMN, while in some cases it can be also claimed that the PI-ISO ribbons consist of particles.

The make-up of the skeletal frameworks in PI-AMN and PI-ISO was probed quantitatively with SANS (Figure 8). To exclude the effect of the solvent, which controls phase-separation, and therefore affects the size of the particles, the specific materials

compared were both prepared in NMP (PI-ISO-90 and PI-AMN-190). The solid lines in Figure 8 are fits to the Unified Model of G. Beaucage,[29] which is used for analyzing data from multi-scale structures such as foams. While scattering from PI-AMN and PI-ISO is distinct, there are similarities. To facilitate analysis, scattering has been broken down into four regions. Each material displays two length-scales (regions I and III) and two power-law regions (linear sections on a log-log plot, regions II and IV). In region IV both materials display power-law scattering with exponents of ~ 5 (PI-ISO: 5.0 ± 0.1; PI-AMN: 5.1 ± 0.1). For smooth (abrupt) interfaces, the exponent in this region is typically 4, while for fractally-rough interfaces it is 3-4.[30] Exponents >4 have been reported before,[31] and they have been attributed to rapidly changing density at the interface. In region III, both materials display a "knee," which is indicative of a fundamental length-scale and may relate to small pores, the cross section of a foam strut, or the primary particle size of aggregates forming the material. The first two possibilities are excluded based on the similar skeletal densities of the two materials (absence of small pores) and the quite different SEM microstructures (different cross-sections of the skeletal frameworks). Thus, the region III knees are attributed to the primary particles forming the materials. Analysis according to the Unified Model provides the radius of gyration (R_g), where for spherical particles $R_g \approx 0.77R$ (R is the average radius of the particles). For PI-AMN, R_g=5.8 nm and for PI-ISO, R_g=4.7 nm. Now, in region II, both materials exhibit power-law scattering again. PI-AMN exhibits a power-law with an exponent of ~2 and PI-ISO exhibits an exponent of ~1. For fractal systems, an exponent of 2 would indicate pore (or mass) fractals, while for simple shapes it is indicative of a sheet- or disk-like morphology; an exponent of 1 is indicative of a cylindrical-like morphology, which

would describe the fibers of PI-ISO. Finally, in region I both materials display "knees," which may again relate to larger pores, the cross section of a foam strut or the size of an aggregate of particles. For PI-AMN, R_g=35 nm and for PI-ISO, R_g=41.6 nm. Based on SEM, in the case of PI-AMN those structural elements are attributed to secondary particles and in the case of PI-ISO to the diameter of the fibers. It is noted that all length-scales identified by SANS agree well with the feature sizes seen at the higher magnification SEM (Figure 7).

Overall, chemically identical (case of PI-AMN-190 and PI-ISO-90) and structurally very similar primary particles (in terms of crystallinity and size) seem to form secondary particles in the case of PI-AMN, and fibers in the case of PI-ISO. It is reasonable to assume that the size of the primary particles is controlled by the common solvent (NMP). Then, the only variable that remains different in the two systems is the actual chemistry of the two processes, which is translated into the surface functionality of the primary particles. It is thus suggested that the flexible amic acid bridges between PI-AMN primary particles allows pivoting, closer packing and a 3D growth resulting into secondary particles; on the other hand, the rigidity of the 7-member ring between PI-ISO primary particles, in combination with steric hindrance from neighboring particles, imposes growth at the exposed ends of the assembly resulting in directional growth and fibers (Scheme 3). The 3D growth in PI-AMN should create numerous crosslinks between secondary particles while in the case of PI-ISO, crosslinking should be taking place only at the contacts between fibers. This model for PI-AMN versus PI-ISO aerogels is supported by the higher shrinkage of PI-AMN (Figure 1), and also explains their high compressive mechanical strength (Figure 9), which in fact compares favorably with that

of structurally analogous polymer crosslinked silica aerogels at the same densities.[32] On the other hand, at similar percent solids formulations, PI-ISO aerogel monoliths are mechanically much weaker materials, undergoing premature catastrophic failure to large pieces with much smaller loads. However, this behavior of PI-ISO aerogels is not justified based on data concerning the compressive behavior of polymer-coated nanofibrous silica or vanadia[33] versus nanoparticulate silica;[32] entangled nanofibrous structures are generally mechanically stronger (the bird-nest effect).[33] The failure mode of PI-ISO aerogels seems to suggest that monoliths fail prematurely because of subtle cracks traceable probably to the CO_2 evolution rather than an innate material weakness, and therefore this issue can be addressed although it is beyond the scope of this work.

Scheme 3. The interfacial chemistry of primary particles in PI-AMN and PI-ISO

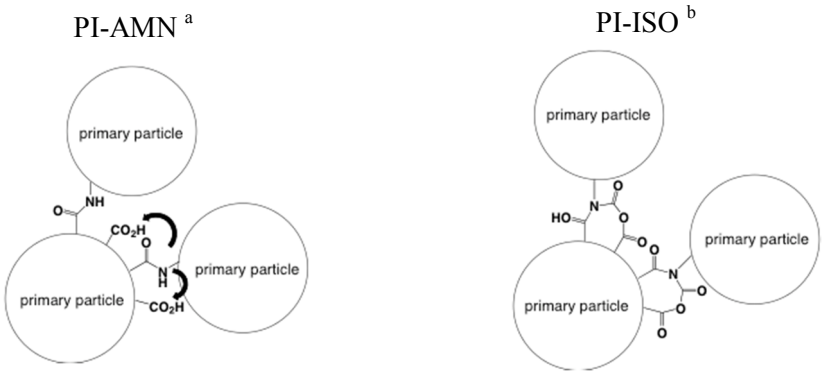

a. Curved arrows show that a surface amic acid has more than one option in forming an imide, bringing particles closer. b. The rigidity of the seven-member ring intermediate "locks" the particles in the position of their initial encounter.

2.4 Pyrolysis of polyimide aerogels and conversion to carbon. Porous carbons are pursued as electrodes for fuel cells and batteries.[34] Polyimides generally have good carbonization yields,[35] and in fact the first PI-AMN aerogels reported were also investigated for their conversion to carbon aerogels (pyrolytically) and metal carbide

aerogels (carbothermally, after doping with selected sol-gel derived metal oxides).[15] Carbonizable polymers are capable of either cyclizing, or undergoing ring fusion and chain coalescence by heating.[36] For this the chain should either contain aromatic moieties or be aromatizable (usually by oxidation). In the former case, there should be just one carbon atom between aromatic rings; otherwise, pyrolytic chain scission will prevail leading to loss of fragments.[36] The PMDA/MDI or MDA polyimides of this study fulfill the last criterion. By thermogravimetric analysis under N_2 (TGA, Figure 10) both PI-AMN and PI-ISO are stable up to about 550 ^oC, subsequently loosing 40-50% of their mass before 650 ^oC (presumably by loss of small molecules like CO and CO_2). The additional gradual mass loss at higher temperatures is attributed to loss of nitrogen-containing fragments.[37] Thus, it was decided to carry out carbonization pyrolysis at 800 ^oC under Ar for 3 h. Pertinent data concerning the resulting carbon aerogels are summarized in Table 2 for various samples prepared with the 15% w/w and the 10% w/w solids formulations (for comparison, refer to Table 1).

Table 2. Properties of PI-AMN and PI-ISO derived carbon aerogels [a]

C-sample from: (see to Table 1) Additional Processing	carbon-yield % (w/w)	shrinkage linear (%) [g]	bulk density, ρ_b (g cm^{-3})	skeletal density, ρ_s (g cm^{-3}) [j]	porosity, Π (% v/v)	BET surface area, σ (m^2 g^{-1})
PI-AMN-190-15	58±2 [e]	48.0±0.5 [63]	1.018±0.153 [h]	1.896±0.070	46	113
PI-ISO-90-15	55±2 [e]	40.8±0.4 [52]	0.665±0.064 [h]	1.998±0.057	67	279
PI-ISO-RT-10 [b]	53±2 [e]	61.6±0.9 [64]	1.012±0.117 [i]	1.863±0.034	46	336
PI-ISO-RT-10 [c]	53.6±0.4 [e]	62±2 [66]	0.967±0.160 [i]	1.729±0.021	44	361
PI-AMN-190-15 3 h-CO_2 [d]	79 [f]	3 [63]	0.701	2.114±0.069	67	417
PI-ISO-RT-10 3h-CO_2 [b,d]	59 [f]	8.7 [65]	0.670	2.310±0.052	71	1010

a. PI-AMN and PI-ISO samples as indicated, processed at 800 ^oC under Ar for 3 h. b. PI-ISO-RT samples synthesized at in NMP/DMSO. c. PI-ISO-RT samples synthesized in NMP/acetonitrile. d. Resulting carbon samples processed for an additional 3h at 1000 ^oC under flowing CO_2. e. Average of four samples. f. Single sample; yield relative to the sample before treatment with CO_2 at 800 ^oC for 3 h. g. Shrinkage = 100 × (sample diameter before pyrolysis – sample diameter after pyrolysis)/(sample diameter before pyrolysis); for the number in the brackets, shrinkage was calculated with respect to the original mold diameter. h. Average of two samples. i. Average of 3 samples. j. Single sample, average of 50 measurements.

All polyimide aerogels remain as quite sturdy monoliths after pyrolysis. All samples are black. PI-AMN derived carbons, however, have a metallic luster, while PI-ISO derived samples are dull. The carbonization yield in all cases is between 51-56 % w/w, that is comparable with carbon aerogels derived from resorcinol-formaldehyde aerogels.[38] All samples shrink further beyond their initial imidization shrinkage (Table 1), but interestingly, PI-ISO-RT samples shrink more (~60%) than the PI-AMN samples (~50%), so that the total shrinkage calculated from the initial molds (Table 2) is approximately the same for both kinds of samples (63-66%). The PI-ISO-90 samples seem to have a small edge over the rest in terms of shrinkage (overall 52% relative to the molds), although it is rather safe to assume that as far as polyimide-derived carbon aerogels are concerned, there seems to be no particular advantage in terms of shrinkage for any of the two kinds of aerogels.

Chemically, pyrolytic samples consist only of carbon (by EDS). XRD shows very broad diffractions. Typical Raman spectra (Figure 11) show both the G (graphitic) and D (disordered) peaks at 1352 cm^{-1} and 1597 cm^{-1}, respectively. The ratios of the integrated peak intensities (I_D/I_G) are 1.12 and 0.98 for carbon aerogels obtained from PI-ISO and PI-AMN, respectively, indicating that all carbons are nanocrystalline/amorphous.[39] Indeed, the skeletal densities of all samples are in the 1.7-2.0 g cm^{-3} range (Table 2), which is what is expected from amorphous carbon (1.8-2.0 g cm^{-3}).[40] Combination of bulk and skeletal densities yields porosities in the range of ~45% v/v of empty space, which are significantly lower than the porosities of the parent polyimide aerogels (compare Tables 1 and 2). An exception is the PI-ISO-90 samples where the porosity is 67% v/v of empty space, and is attributed to their lower pyrolytic shrinkage (Table 2).

Microscopically (by SEM, see Figure 12), PI-AMN-derived carbons are different from their parent polyimide aerogels (refer to Figure 7). The structure is dominated by large macropores surrounded by "solid" walls, although N_2-sorption isotherms show the presence of all three kind of pores: microporores (significant quick rise of the volume adsorbed at low partial pressures), mesopores (presence of a hysteresis loop) and macropores (second quick rise of the volume adsorbed above P/P_o~0.9). The lower BET surface area relative to that of PI-AMN samples before pyrolysis (113 $m^2 g^{-1}$ versus 413 $m^2 g^{-1}$, respectively) is consistent with the changes observed by SEM. On the other hand, PI-ISO-derived carbons retain the fibrous nanomorphology of the parent polyimide aerogels (Figure 12), but the fine structure that could be seen on the fibers of the parent PI-ISO aerogels (compare with Figure 7) has been erased. Again, N_2-sorption isotherms indicate the presence of all three kinds of pores, while the BET surface area of the PI-ISO-derived carbon aerogels has been increased somewhat relative to that of the parent polyimides (compare Tables 1 and 2). This pyrolytic behavior of both PI-AMN and PI-ISO samples is consistent with the model of Scheme 3: at the early stages of pyrolysis bond breaking and reforming at the surfaces of the primary and secondary particles (case of PI-AMN), leads to rearrangement and a more compact structure. Macroscopically, that mechanism is expected to lead to shrinkage, and microscopically into large voids defined by compact walls (case of PI-AMN). On the other hand, in the case of PI-ISO bond breaking and reforming leads to smoother thinner fibers, but the pore structure is retained.

The presence of micropores indicated by the N_2-sorption isotherms suggests that a significant gain in surface area could be achieved by etching. That was carried out under

flowing CO_2 at 1000 ^oC. (Carbon and CO_2 comproportionate to CO.) The results are included in Table 2. Thus CO_2-treated samples loose 20-40% of their mass, shrink only 3-9% and remain monolithic. Consequently, bulk densities decrease, however, skeletal densities increase to the 2.1-2.3 g cm^{-3} range (density of graphite at 2.26 g cm^{-3}).[40] The porosity is dominated by the bulk density decrease, reaching up to ~70% v/v of empty space. Microscopically (Figure 13), PI-ISO samples remain fibrous as expected, while PI-AMN samples show macropores similar in shape to those observed before etching (Figure 12). Nevertheless, the number of those macropores has increased and the surrounding walls seem rougher; considering these data together suggests that before etching many pores are masked by a thin porous crust of carbon. After CO_2-etching, the N_2-sorption isotherms indicate that the majority of the empty space is attributed to micropores, while the BET surface areas of the samples increases dramatically, reaching the levels of the parent polyimide aerogels in the case of PI-AMN-derived carbons (417 m^2 g^{-1}), or far surpassing those levels in the case of PI-ISO-derived samples (1010 m^2 g^{-1}). For reasons not well understood yet, despite the mass loss CO_2-etching increases the electrical conductivity of PI-ISO-derived carbon aerogels by ~70×, from 0.013 mho cm^{-1} (at ρ_b =0.967 g cm^{-3}) to 8.697 mho cm^{-1} (at ρ_b=0.670 g cm^{-3}). (By comparison the electrical conductivity of CO_2-etched PI-AMN-derived carbon aerogels is 4.491 mho cm^{-1} at ρ_b=0.701 g cm^{-3}.) Those values are comparable with the literature conductivity values (0.6-20 mho cm^{-1} for densities ranging from 0.06 to 0.65 g cm^{-3})[41] and our previously reported conductivity values (0.147 mho cm^{-1} at ρ_b=0.138 g cm^{-3})[38] for carbon aerogels derived from RF-aerogels, or our conductivity values for carbon aerogels derived from

polyurea-crosslinked RF-aerogels (2.0 mho cm^{-1} at ρ_b=0.254 g cm^{-3}),[38] and render polyimide-derived carbon aerogels particularly attractive as electrochemical electrodes.

3. Experimental Section

3.1. Materials. All reagents and solvents were used as received unless noted otherwise. Pyromellitic dianhydride (PMDA) was purchased from Chriskev Company, Inc. 4,4′-Diisocyanatodiphenylmethane (4,4′-methylene diphenyl diisocyanate, MDI), 4,4′-methylenedianiline (MDA), and acetic anhydride ($(Ac)_2O$), were obtained from Acros Chemicals. Pyridine was purchased from Fisher Scientific. Anhydrous *N*-methyl-2-pyrrolidone (NMP), acetonitrile, dimethylsulfoxide (DMSO) and absolute ethanol were obtained from Aldrich Chemical Co. Deuterated DMSO (DMSO-d_6) was obtained from Cambridge Isotope Laboratories, Inc.

Preparation of polyimide aerogels via the anhydride/diamine route (PI-AMN): Pyromellitic dianhydride (15.696 g, 0.072 mol) and 4,4′-methylenedianiline (14.256 g, 0.072 mol) were added in variable amounts of NMP in a 250 mL round bottom flask under magnetic stirring. For example, for the 15% w/w solids formulation (samples referred to as PI-AMN-15) the amount of NMP was 169.7 g. The solution was stirred at room temperature under nitrogen for 12 h and the color changed from colorless to yellow. At that point, acetic anhydride (in 6.3 mol excess to pyromellitic dianhydride) and pyridine (1:1 mol ratio to acetic anhydride) were added to the resulting polyamic acid solution, and the new solution (sol) was poured into molds and was allowed to gel at room temperature. As molds for samples used for general chemical and physical

characterization we used Wheaton 4 mL Polypropylene Omni-Vials 1.04 cm inner diameter, Fisher part No. 225402, and for samples used for mechanical testing we used 30 mL Fisherbrand Class B Amber Glass Treaded Vials, 2.1 cm inner diameter, Fisher part No. 03-339-23E. The gelation time depends on the formulation: for 2.5%, 5%, 10% and 20% w/w solids (PMDA+MDA) in the original NMP solution the gelation time was ~4 h, ~1.5 h, 15 min and <15 min, respectively. The gels were aged in the molds for 12 h, subsequently they were washed with NMP (3×, 8 h each time, using 4× the volume of the gel each time), cured at 190 ^{o}C for 3 h in the last NMP wash solution, cooled to room temperature, washed with ethanol (4×, 8 h each time, using 4× the volume of the gel for each wash) and dried into polyimide aerogels in an autoclave with liquid CO_2, taken out at the end supercritically.

Preparation of polyimide aerogels via the isocyanate route (PI-ISO). A. At room temperature: MDI (2.50 gm 0.01 mol) was added under stirring to a mixture of NMP and acetonitrile (3:1 w/w), or NMP and DMSO (1:1 w/w) in a three-neck round bottom flask under N_2 at room temperature. Once the isocyanate was dissolved, pyromellitic dianhydride (2.18 g, 0.01 mol) was added. For example, for a 15% w/w solids formulation the amount of NMP and acetonitrile were 19.88 g (19.34 mL) and 6.62 g (8.43 mL), respectively. Similarly for a 10% w/w solids formulation the amounts of NMP and DMSO were 21.06 g and 21.06 g respectively. The reaction mixture was stirred under nitrogen for 1 h. The resulting sol was poured in molds (see above), which were allowed to stand at room temperature. Gelation takes usually 6 h – 48 h depending on the formulation. For example, in NMP:CH_3CN (3:1 w/w), the 10%, 15%, 20% and 30% w/w solids formulations take 2 days, 36 h, 18 h and 12 h, respectively. (By comparison, a 15%

w/w solids formulation in NMP takes 48 h for gelation at RT.) Gels were aged in the molds for 24 h – 8 days depending on the gelation time, typically 4 times the gelation time. Subsequently, gels were removed from the molds and were initially washed (solvent-exchanged) with NMP:acetonitrile (3:1 v/v), then with NMP:acetonitrile:acetone (2:1:1 v/v/v), NMP:acetone (1:1 v/v), and finally with pure acetone. Similarly, gels synthesized in NMP/DMSO were placed in pure NMP, the second wash was carried out with NMP:acetone (3:1 v/v) the third with NMP:acetone (1:1 v/v), and finally gels were placed in pure acetone. After 4 acetone washes (8 h each time, using 4× the volume of the gel for each wash) wet gels were dried into polyimide aerogels in an autoclave with liquid CO_2, taken out at the end supercritically.

B. At 90 ^{o}C: A more time-wise efficient synthesis of PI-ISO was carried out at slightly (by polyimide standards) elevated temperatures as follows: pyromellitic dianydride (2.18 g, 0.01 mol) and MDI (2.50 g, 0.01 mol) were added in variable amounts of NMP in a three-neck round bottom flask under nitrogen at room temperature. For example, for a 15% w/w solids formulation the amount of NMP was 26.52 g. The flask was placed in a 60 ^{o}C bath and the solution was stirred under N_2 for 0.5 h. The resulting sol was poured into molds (see above), which were heated in an oven successively at 60 ^{o}C, 70 ^{o}C and 80 ^{o}C for 3 h at each temperature. Although gelation of the PMDA/MDI/NMP mixture may occur even at room temperature over longer periods of time as described above, according to this protocol, gelation usually occurs at the early stages of the 60 ^{o}C heating. Gels were first aged at 90 ^{o}C for 12 h in their molds, and subsequently they were removed from the molds and they were placed directly in fresh ethanol. After four ethanol washes (8 h each time, using 4× the volume of the gel for each

wash) wet gels were dried into polyimide aerogels in an autoclave with liquid CO_2, taken out at the end supercritically.

Conversion of polyimide aerogels into carbon aerogels: PI-AMN and PI-ISO aerogels were pyrolyzed at 800 ^oC for 3 h in a tube furnace under a flowing stream of Ar. Before heating, the tube was purged with Ar for 10 min, and the heating rate was set at 5 $^oC\ min^{-1}$. At the end of the heating period, the power to the furnace was disconnected and the tube was allowed to cool slowly back to room temperature under flowing Ar.

Etching of carbon aerogels: Carbon aerogels were placed in a tube furnace under flowing argon and were heated at 1000 ^oC. The flowing gas was switched to CO_2 and the temperature was maintained at that level for 3 h. Subsequently the flowing gas was switched back to Ar and the power to the furnace was disconnected, allowing for slow cooling back to room temperature.

3.2. Methods. Drying with supercritical fluid CO_2 was conducted in an autoclave (SPI-DRY Jumbo Supercritical Point Dryer, SPI Supplies, Inc. West Chester, PA). Aerogel bulk densities (ρ_b) were calculated from the weight and physical dimension of the samples. Skeletal densities (ρ_s) were determined with helium pycnometry using a Micromeritics AccuPyc II 1340 instrument. Porosities, Π, were determined from ρ_b and ρ_s according to: $P=100\times[(1/\rho_b)-(1/\rho_s)]/(1/\rho_b)$. BET surface areas ($\sigma$) and pore size distributions were measured with nitrogen adsorption/desorption porosimetry using a Micromeritics ASAP 2020 Surface Area and Porosity Analyzer. Samples for surface area and skeletal density determination were outgassed for 24 h at 80 ^oC under vacuum before analysis. Average pore diameters were determined by the $4\times V_{Total}/\sigma$ method,

where V_{Total} is the total pore volume per gram of sample. V_{Total} is calculated either from the single highest volume of N_2 adsorbed along the adsorption isotherm or from the relationship $V_{Total}=(1/\rho_b)-(1/\rho_s)$. The single point N_2 adsorption method tends to underestimate V_{Total} significantly when macropores are involved,[42] and thus numerical proximity of the values determined by the two methods is used as a semi-quantitative criterion for evaluating macroporosity. Scanning electron microscopy (SEM) was conducted using a Hitachi S-4700 Field Emission instrument. Chemical characterization of all polyimide aerogels was based on IR and solid state ^{13}C NMR. Infrared spectra were obtained in KBr pellets using a Nicolet-FTIR model 750 Spectrometer. Solid-state ^{13}C NMR spectra were obtained with samples ground in fine powders on a Bruker Avance 300 spectrometer (75.475 MHz carbon frequency), using magic angle spinning (5 kHz) with broadband proton suppression and the CPMAS TOSS pulse sequence for spin sideband suppression. ^{13}C NMR spectra were externally referenced to the carbonyl of glycine (176.03 ppm relative to tetramethylsilane). ^{13}C-NMR peak assignment was aided by NMR spectra simulations using ChemDraw Ultra 7.0. Thermogravimetric analysis (TGA) was conducted under nitrogen with a TA Instrument, model Hi-Res-TGA 2950 using ~10 mg samples and a heating rate of 10 °C min^{-1}. The reaction between PMDA and MDI was monitored in DMSO-d_6 at room temperature up to the gelation point by liquid ^{13}C NMR using a 400 MHz Varian Unity Inova NMR instrument. The crystallinity of the polyimide samples was determined by x-ray diffraction (XRD) using a Scintag 2000 diffractometer with Cu Kα radiation and a proportional counter detector equipped with a flat graphite monochromator. The identity of the fundamental building blocks of the two materials was probed with small angle neutron scattering (SANS) using ~2 mm

thick discs cut with a diamond saw from cylinders like those shown in Figure 1, on a time of flight, low-Q diffractometer, LQD, at the Manuel Lujan Jr. Scattering Center of the Los Alamos National Laboratory.[43] The scattering data are reported in the absolute units of differential cross section per unit volume (cm^{-1}) as a function of Q, the momentum transferred during a scattering event. Quasi-static mechanical testing under compression was conducted on an Instron 4469 universal testing machine frame, following the testing procedures and specimen length/diameter ratio (equal to one) in ASTM D1621-04a (Standard Test Method for Compressive Properties of Rigid Cellular Plastics). The recorded force as a function of displacement (machine-compliance corrected) was converted into stress as a function of strain. Four-point-probe conductivity measurements were conducted on flat surface of rectangular block of carbon aerogel samples (made with a fine sand paper) using an Alesis contact probe station model CPS-06 with a Cascade Microtech electrode model C4S-44/5S. The reliability of the probe was confirmed with silicon wafers and indium-tin-oxide coated glass slides of known sheet resistance.

4. Conclusions

Polyimide aerogels are high value-added materials with a potential niche in high temperature thermal insulation. However, polyimide aerogels synthesized via the typical polyimide formation route from dianhydrides and diamines compound two expensive processes: supercritical drying and high temperature imidization. Recent reports on imide formation in water with microwave heating[44] may certainly have a positive impact on polyimide aerogels. Alternatively, however, here we have described polyimide aerogels

synthesized via a low temperature process through the rather underutilized reaction of dianhydrides with diisocyanates. Although the model system has been based on MDI, other monomers like 4,4´-oxybis(phenylisocyanate) behave similarly and the resulting polyimides have the chemical composition of Kapton®.[21c,45] Polyimide aerogels from PMDA/MDI are fibrous and can be converted pyrolytically to isomorphic carbon aerogels, which, owing to their large surface area, are currently investigated for their reactivity with nanoparticulate oxidizing agents in analogy to recently published work on resorcinol-formaldehyde/copper oxide interpenetrating networks.[46]

Acknowledgements. We thank the National Science Foundation for financial support (CHE-0809562 and CMMI-0653919). We also acknowledge the Materials Research Center of Missouri S&T for support in sample characterization (SEM, XRD, EDS). Solids NMR work was conducted at the University of Missouri Columbia by Dr. Wei Wycoff. Finally, this work benefited from the use of the SANS instrument, LQD at the Manuel Lujan, Jr. Neutron Scattering Center of the Los Alamos National Laboratory, supported by the DOE office of Basic Energy Sciences and utilized facilities supported in part by the National Science Foundation under Agreement No. DMR-0454672.

5. References and Notes

1. Pierre, A. C.; Pajonk, G. M. *Chem. Rev.* **2002**, 102, 4243-4265.

2. Kistler, S. S. *J. Phys. Chem.* **1932**, 36, 52-63.

3. Pekala, R. K. "Low Density, Resorcinol-Formaldehyde Aerogels," U.S. Patent No. 4,873,218.

4. Lu, X.; Arduini-Schuster, M. C.; Kuhn, J.; Nilsson, O.; Fricke, J.; Pekala, R. W. *Science* **1992**, *255*, 971-972.

5. Mayer, S. T.; Pekala, R. W.; Kaschmitter, J. L. *J. Electrochem. Soc.* **1993**, *140*, 446-451.

6. Pekala, R. W.; Alviso, C. T.; Lu, X.; Gross, J.; Fricke, J. *J. Non-Cryst. Solids* **1995**, *188*, 34-40.

7. Li, W.-C.; Lu, A.-H.; Guo, S.-C. *J. Coll. Interface Science* **2002**, *254*, 153-157.

8. Pekala, R. W. "Melamine-formaldehyde aerogels," US Patent No. 5,086,085.

9. Biesmans, G.; Mertens, A.; Duffours, L.; Woignier, T.; Phalippou, J. *J. Non-Cryst. Solids* **1998**, 225, 64-68.

10. Lee, J. K.; Gould, G. L.; Rhine, W. L. *J. Sol-Gel Sci. Technol.* **2009**, 49, 209-220.

11. Daniel, C.; Giudice, S.; Guerra, G. *Chem. Mater.* **2009**, 21, 1028-1034.

12. Gouerec, P.; Talbi, H.; Miousse, D.; Tran-Van, F.; Dao, L. H.; Lee, K. H. *J. Electrochem. Soc.* **2001**, 148, A94-A101.

13. Lorjai, P.; Chaisuwan, T.; Wongkasemjit, S. *J. Sol-Gel Sci. Technol.* **2009**, 52, 56-64.

14. Lee, J. K.; Gould, G. L. *J. Sol-Gel Sci. Technol.* **2007**, 44, 29-40.

15. Rhine, W.; Wang, J.; Begag, R. "Polyimide aerogels, carbon aerogels, and metal carbide aerogels and methods of making same," U.S. Patent No. 7,074,880 (2006).

16. (a) Kawagishi, K.; Saito, H.; Furukawa, H.; Horie, K. *Macromol. Rapid Commun.* **2007**, *28*, 96-100. (b) Meador, M. A. B.; Malow, E. J.; He, Z. J.; McCorkle, L.; Guo, H.; Nguyen, B. N. *Polymer Preprints* **2010**, *51*, 265-266.

17. Sroog, C. E.; Endrey, A. L.; Abramo, S. V; Berr, C. E.; Edward, W. M.; Oliver, K. L. *J. Polym. Sci. Part A* **1965**, *3*, 1373-1390.

18. (a) Iroh, J. O.; Kevin, J. *J. Appl. Polym. Sci.* **1997**, *66*, 2529-2538. (b) Baugher, A. H.; Espe, M. P.; Goetz, J. M.; Schaefer, J.; Pater, R. H. *Macromolecules* **1997**, *30*, 6295-6301. (c) Meador, M. A. *Annu. Rev. Mater. Sci.* **1998**, *28*, 599-630.

19. Maier, G. *Prog. Polym. Sci.* **2001**, 26, 3-65.

20. (a) Williams, M. K.; Weiser, E. S.; Fesmire, J. E.; Grimsley, B. W.; Smith, T. M.; Brenner, J. R.; Nelson, G. L. *Polym. Adv. Technol.* **2005**, *16*, 167-174. (b) Weiser, E. S.; Johnson, T. F.; St Clair, T. L.; Echigo, Y. Kaneshiro, H. Grimsley, B. W. *High Performance Polymers* **2000**, *12*, 1-12. (c) Williams, M. K.; Holland, D. B.; Melendez, O.; Weiser, E. S.; Brenner, J. R.; Nelson, G. L. *Polymer Degradation and Stability* **2005**, *88*, 20-27.

21. (a) Edwards, W. M.; Robinson, I. M. "Polyimides of Pyromellitic Acid," U.S. Patent 2,710,853 (1955). (b) Edwards, W. M.; Robinson, I. M. "Preparation of Pyromellitimides," U.S. Patent 2,867,609 (1959). (c) Sroog, C. E. *Prog. Polym. Sci.* **1991**, *16*, 561-694.

22. (a) Kreuz, J. A. "Preparation of Aromatic Polyiminolactones," U.S. Patent 3,271,366 (1966). (b) Angelo, R. J. "Treatment of Aromatic Polyamide-acids with Carbodiimides," U.S. Patent 3,282,898 (1966).

23. Leventis, N. *Acc. Chem. Res.* **2007**, *40*, 874-884.

24. (a) Meyers, R. A. *J. Polym. Sci.: Part A-1* **1969**, *7*, 2757-2762. (b) Barikani, M.; Mehdipour-Ataei, S. *J. Polym. Sci.: Part A: Polym. Chem.* **1999**, *37*, 2245-2250. (c) Yeganeh, H.; Mehdipour-Ataei, S. *J. Polym. Sci.: Part A: Polym. Chem.* **2000**, *38*, 1528-1532.

25. Sroog, C. E. *J. Polym. Sci.: Macromolecular Reviews*, **1976**, *11*, 161-208.

26. (a) Schneider, B.; Schmidt, P.; Marek Jr, M.; Straka, J.; Bednar, B.; Kralicek, *Eur. Polym, J.* **1990**, *26*, 941-945. (b) Pryde, C. A. *J. Polym. Sci: Part A: Polym. Chem.* **1989**, *27*, 711-724.

27. Zhai, Y.; Yang, Q.; Zhu, R.; Gu, Y. *J. Mater. Sci.* **2008**, 43, 338-344.

28. Xu, Y.; Chen, C.; Li, J. *Chemical Engineering Science* **2007**, 62, 2466-2473.

29. Beaucage, G. *J. Appl. Cryst*. **1995**, *28*, 717-728.

30. Bale, H. D.; Schmidt, P. W. *PRL* **1984**, *53*, 596-599.

31. Schmidt, P. W.; Avnir, D.; Levy, D.; Hohr, A.; Steiner, M.; Roll, A. *J. Chem. Phys.* **1991**, *94*, 1474-1479.

32. Katti, A.; Shimpi, N.; Roy, S.; Lu, H.; Fabrizio, E. F.; Dass, A.; Capadona, L. A.; Leventis, N. *Chem. Mater.* **2006**, *18*, 285-296.

33. (a) Leventis, N.; Sotiriou-Leventis, C.; Mulik, S.; Dass, A.; Schnobrich, J.; Hobbs, A.; Fabrizio, E. F.; Luo, H.; Churu, G.; Zhang, Y.; Lu, H. *J. Mater. Chem.* **2008**, *18*, 2475-2482. (b) Leventis, N.; Mulik, S.; Wang, X.; Dass, A.; Patil, V. U.; Sotiriou-Leventis, C.; Lu, H.; Churu, G.; Capecelatro, A. *J. Non-Cryst. Solids* **2008**, *354*, 632-644.

34. (a) Smirnova, A.; Ding, X.; Hara, H.; Vasiliev, A.; Sammes, N. *International Journal of Hydrogen Energy* **2005**, *30*, 149-158. (b) Kwon, O. J. ; Jung, Y. S.; Kim, J. H.; Oh, S. M. *J. Power Sources* **2004**, *125*, 221-227. (c) Fialkov, A. S. *Russ. J. Electrochem.* **2000**, *36*, 345-366.

35. For example, at 1000 ^{o}C PMDA/4,4'-oxydianiline (ODA) polyimide (Kapton®) gives 60% carbon, PMDA/phenelene diamine polyimide gives 48% carbon and 3,3',4,4'-benzophenone tetracarboxylic dianhydride (BTDA)/ODA polyimide gives 63%; see: (a) Buerger, A.; Fitzer, E.; Heim, M; Terwiesch, B. *Carbon*, **1975**, *13* 149-157. (b) Hishiyama, Y.; Yasuda, S.; Yoshida, A.; Inagaki, M. *J. Mater. Sci.* **1988**, *23*, 3272-3277.

36. Jenkins, G. M.; Kawamura, K. "Polymeric Carbons, Carbon Fibre, Glass and Char," Cambridge University Press: New York, N.Y., 1976.

37. Inagake, M.; Ibuki, T.; Takeichi, T. *J. Appl. Polym. Sci.* **1992**, *44*, 521-525.

38. Leventis, N; Mulik, S.; Sotiriou-Leventis, C. *Chem. Mater.* **2008**, *20*, 6985-6997.

39. (a) Tuinstra, F.; Koenig, J. L. *J. Chem. Phys.* **1970,** *53*, 1126-1130; (b) Ferrari, A. C.; Robertson, J. *Phil. Trans. R. Soc. Lond. A* **2004**, *362*, 2477-2512. (c) Cheng, G.; Long, D.-H.; Liu, X.-J.; Ling, L.-C. *New Carbon Mater.* **2009**, *24*, 243-250.

40. McKenzie, D. R.; Muller, D.; Pailthorpe, B. A. *Phys. Rev. Lett.* **1991**, *67*, 773-776.

41. (a) Lu, X.; Nilsson, O.; Fricke, J.; Pekala, R. W. *J. Appl. Phys.* **1993**, *73*, 581-584. (b) Wang, J.; Zhang, S. Q.; Shen, J.; Guo, Y. Z.; Attia, S. M.; Zhou, B.; Lai, Z. Q.; Zheng, G. Z.; Gui, Y. S. *J. Porous Mater.* **2001**, *8*, 167-170.

42. Fricke, J.; Reichenauer, G. *J. Non-Cryst. Solids* **1987**, *95&96*, 1135-1142.

43. Seeger, P. A.; Hjelm, R. P. Jr. *J. Appl. Cryst.* **1991**, *24*, 467-478.

44. (a) Brunel, R.; Marestin, C.; Martin, V.; Mercier, R. *High Perform. Polym.* **2009**, *22*, 82-94. (b) Dao, B.; Groth, A. M.; Hodgkin, J. H. *High Perform. Polym.* **2008**, *20*, 38-52. (c) Chiefari, J.; Dao, B.; Groth, A. M.; Hodgkin, J. H. *High Perform. Polym.* **2006**, *18*, 31-44. (d) Chiefari, J.; Dao, B.; Groth, A. M.; Hodgkin, J. H. *High Perform. Polym.* **2006**, *18*, 437-451. (e) Chiefari, J.; Dao, B.; Groth, A. M.; Hodgkin, J. H. *High Perform. Polym.* **2003**, *15*, 269-279.

45. http://www2.dupont.com/Kapton/en_US/

46. Leventis, N.; Chandrasekaran, N.; Sadekar, A. G.; Sotiriou-Leventis, C.; Lu, H. *J. Am. Chem. Soc.* **2009**, *131*, 4576-4577.

6. Figures

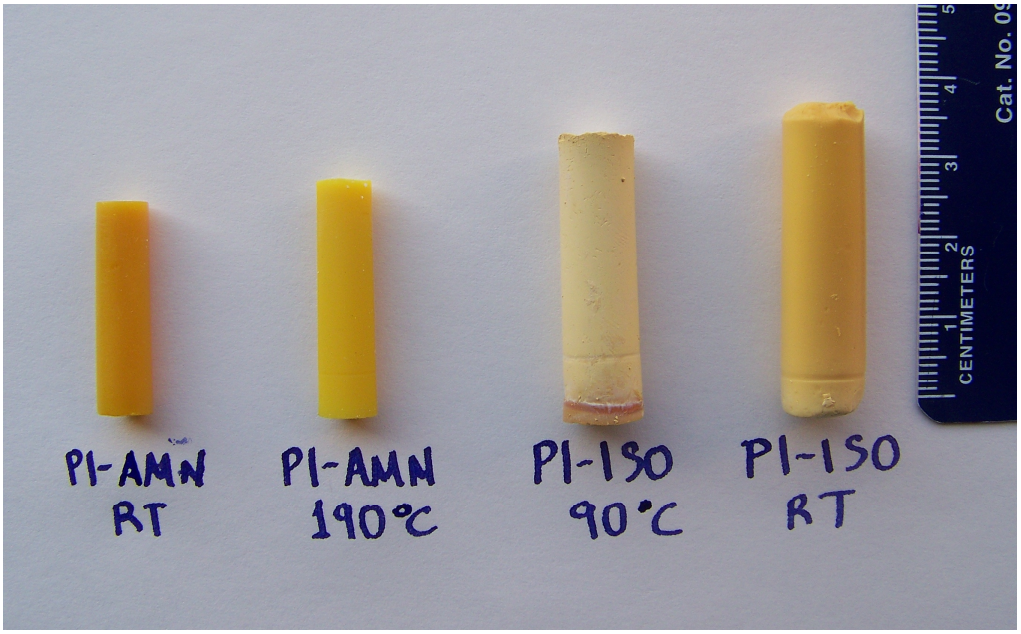

Figure 1. Photographs of polyimide aerogels synthesized with 15% solids under various conditions (see Table 1).

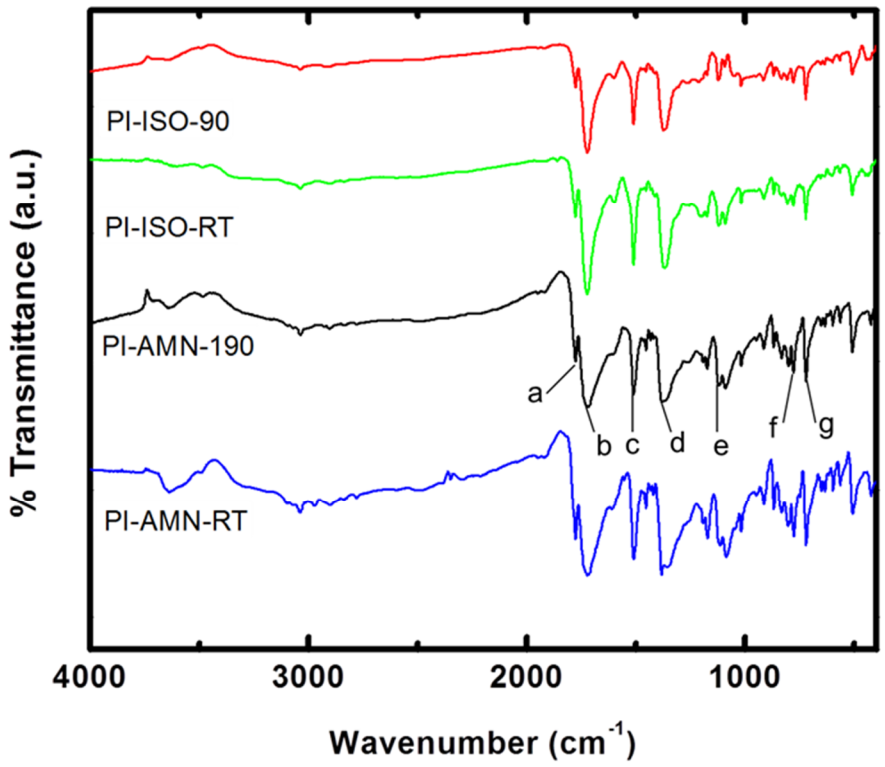

Figure 2. Infrared (IR) spectra of the samples shown in Figure 1. Peak assignment: a,b (1777 cm^{-1} and 1723 cm^{-1}) asymmetric and symmetric stretching vibrations of C=O; c (1511 cm^{-1}) aromatic ring breathing modes; d (1366 cm^{-1}) C-N-C imide ring stretching ; e,f (1123 cm^{-1} and 780 cm^{-1}) imide ring vibrations; g (723 cm^{-1}) imide ring bending.

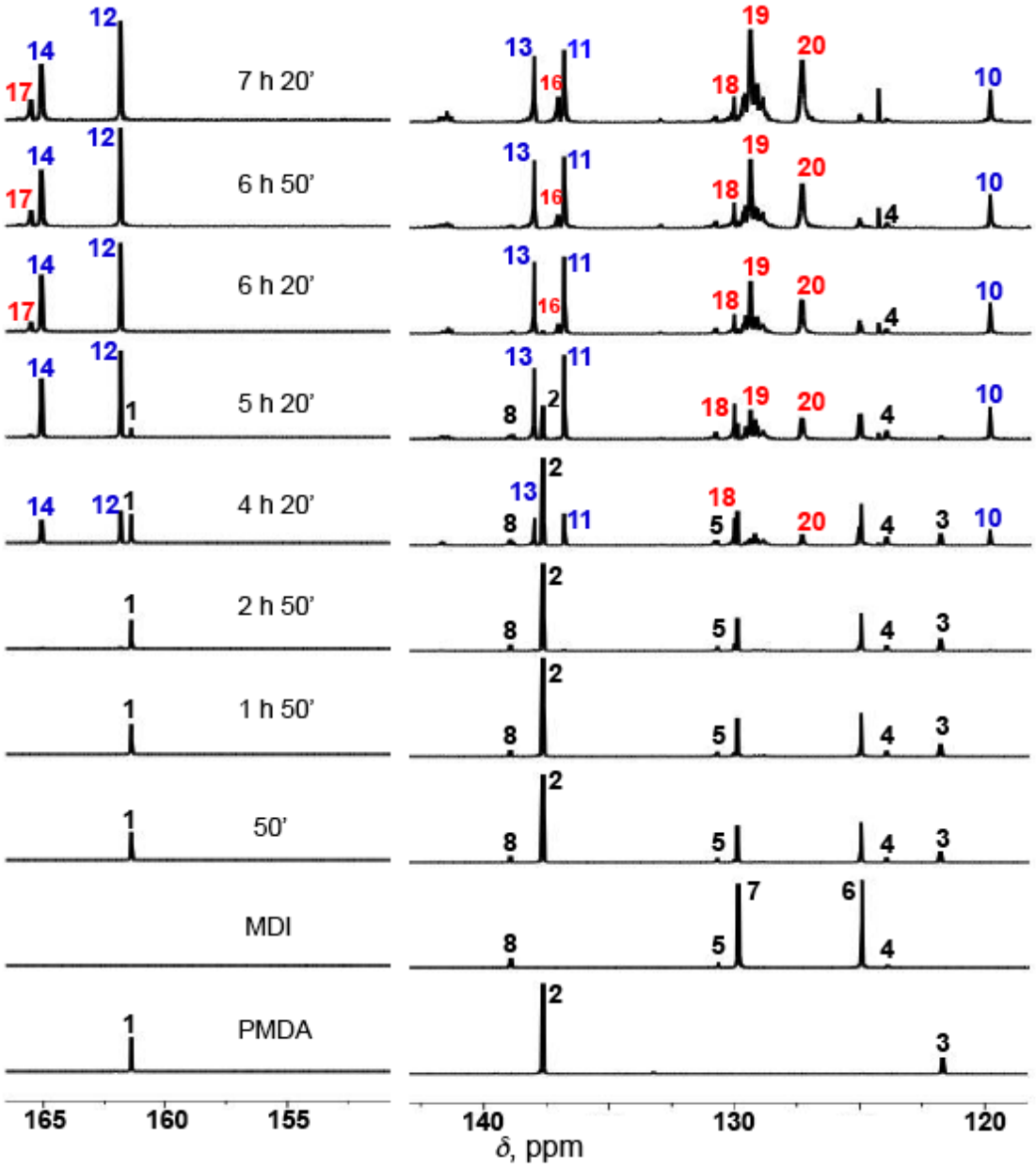

Figure 3. Room temperature liquid ^{13}C-NMR in DMSO-d_6 of a PMDA/MDI mixture (1:1 mol:mol, 12% w/w solids formulation). Bottom two spectra are of the monomers. Times reported refer to time lapsed after mixing. The last spectrum at the top corresponds to the point just before gelation. For peak assignment (by spectra simulation) refer to Scheme 2.

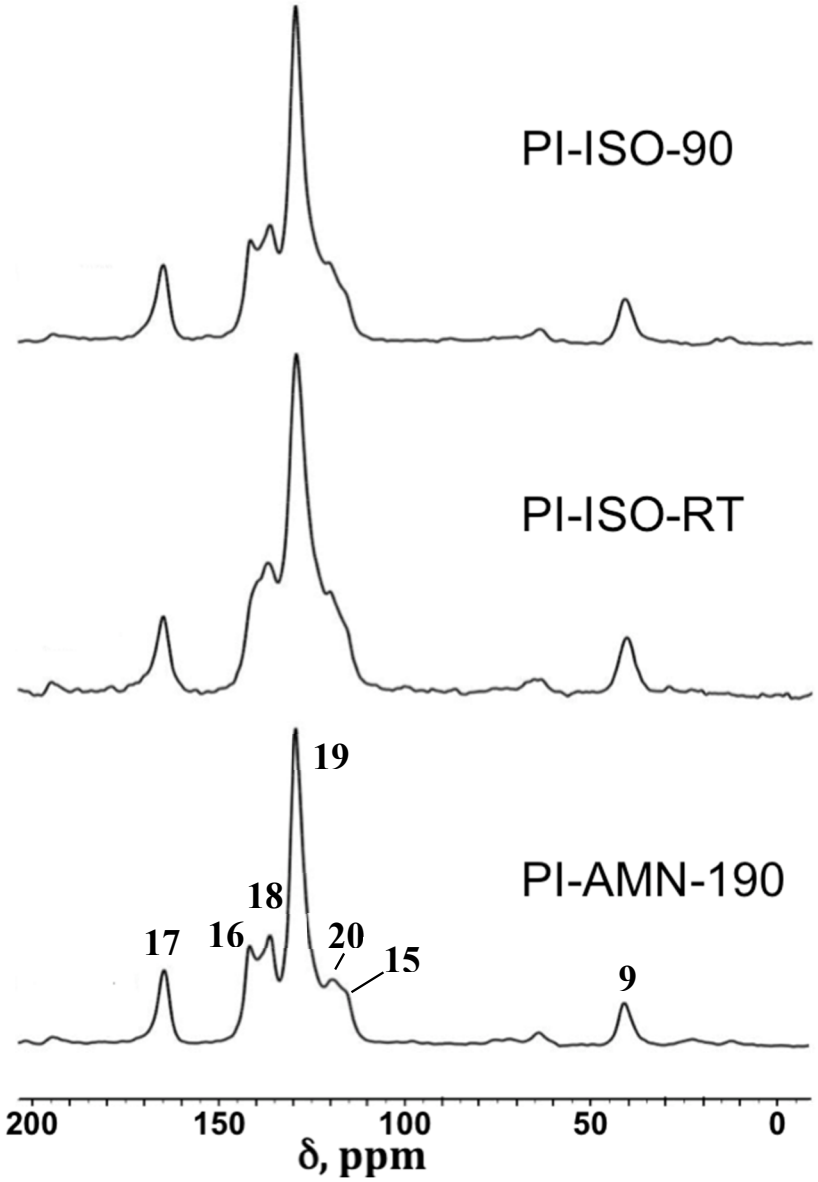

Figure 4. Solids CPMAS ^{13}C-NMR of samples as indicated. All samples prepared using the 15% solids formulation (Table 1). PI-AMN and PI-ISO-90 prepared in NMP; PI-ISO-RT prepared in NMP/CH_3CN (3:1 w/w). For peak assignment (by simulation) refer to Scheme 2.

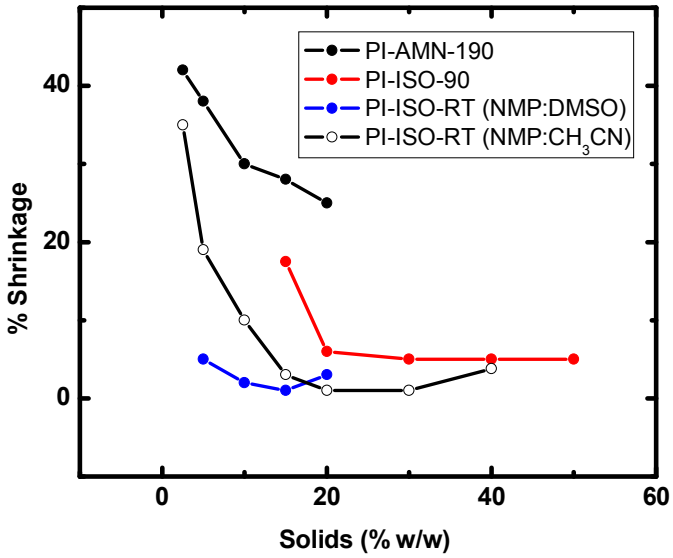

Figure 5. Summary data for shrinkage in a linear dimension (e.g., the cylinder diameter) of the samples of Table 1. PI-AMN samples shrink much more than PI-ISO prepared using similar monomer concentrations (see Figure 1 and Table 1).

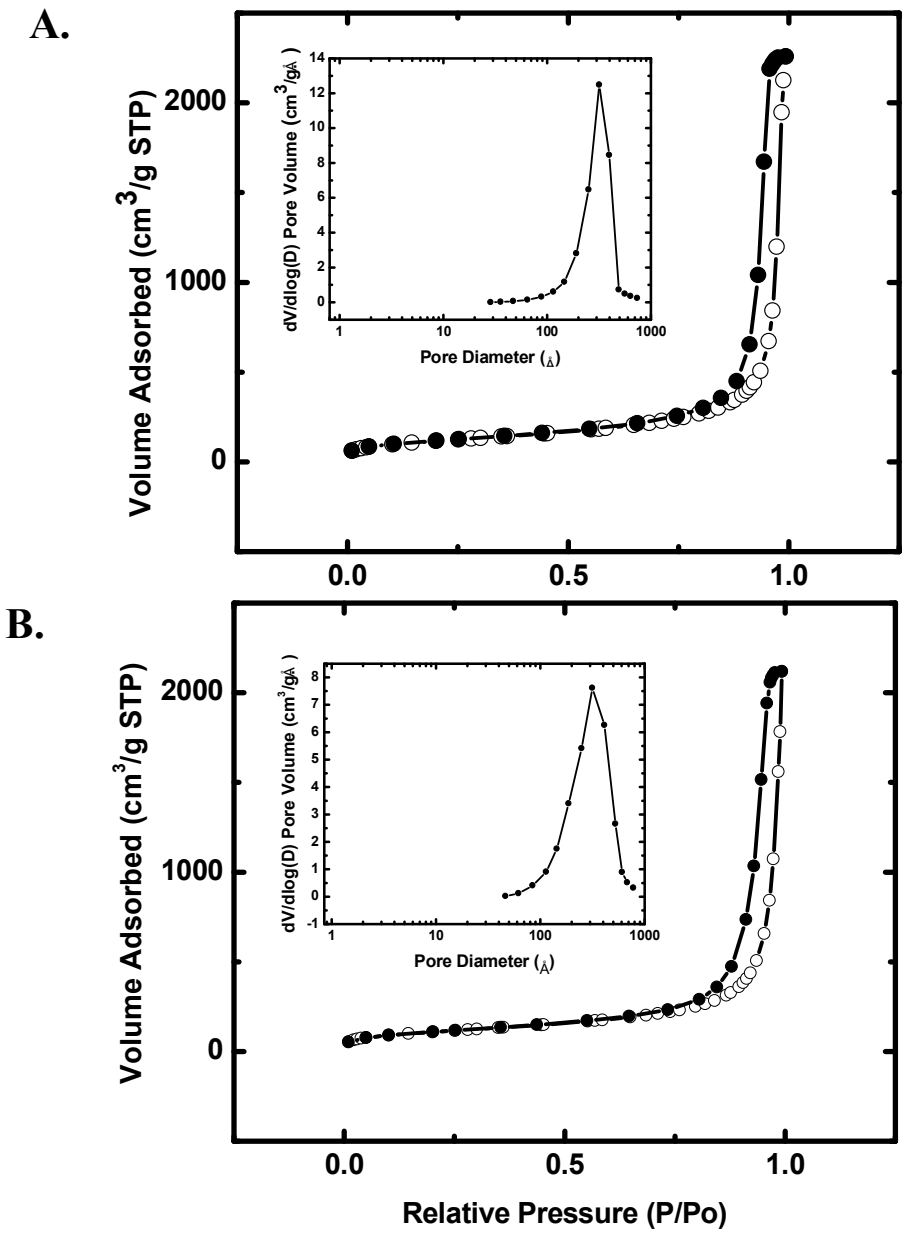

Figure 6. Representative N_2-soprtion data of polyimide aerogels prepared using the 15% w/w solids formulations (Table 1). A: PI-AMN-190 (ρ_b= 0.23 g cm^{-3}); B: PI-ISO-RT prepared in NMP/DMSO 1:1 w/w (ρ_b=0.17 g cm^{-3}). Insets: BJH plots. For other pertinent data see Table 1.

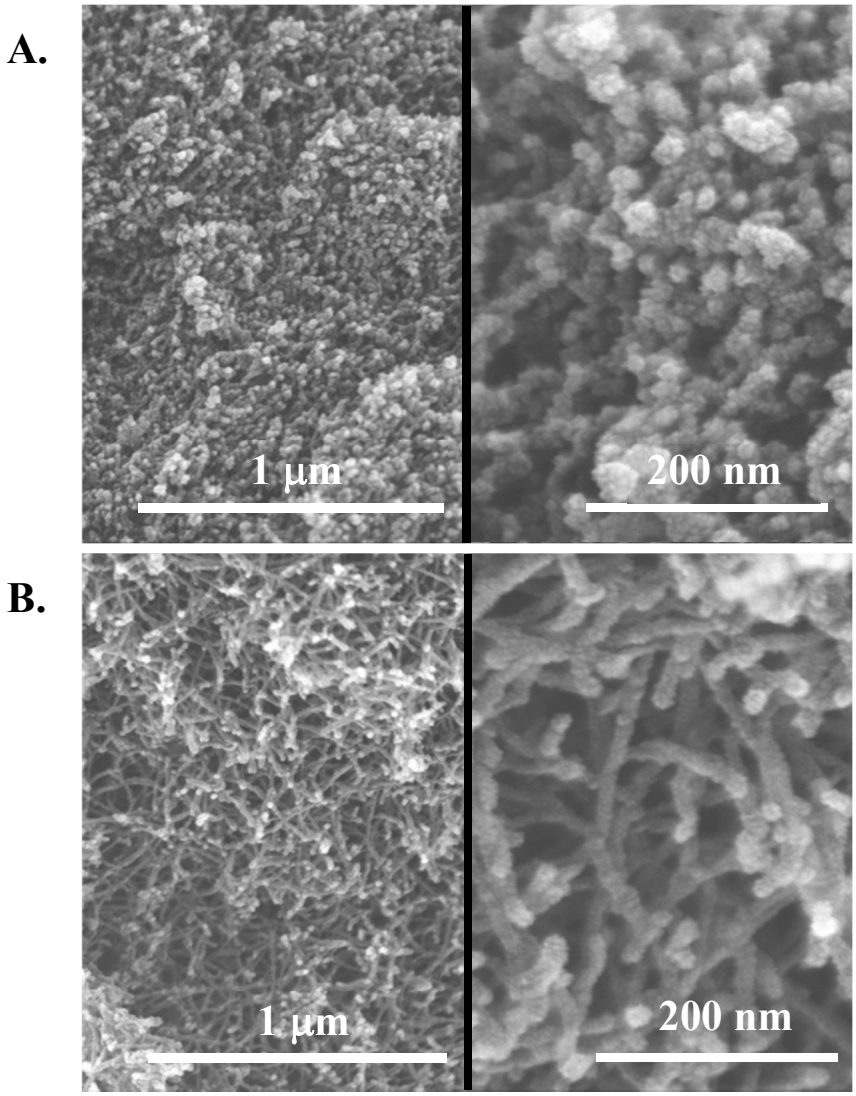

Figure 7. Representative SEM data at two different magnifications of polyimide aerogels prepared using the 15% w/w solids formulations (Table 1). A: PI-AMN-190 (ρ_b= 0.23 g cm^{-3}); B: PI-ISO-RT prepared in NMP/CH_3CN 3:1 w/w (ρ_b=0.12 g cm^{-3})

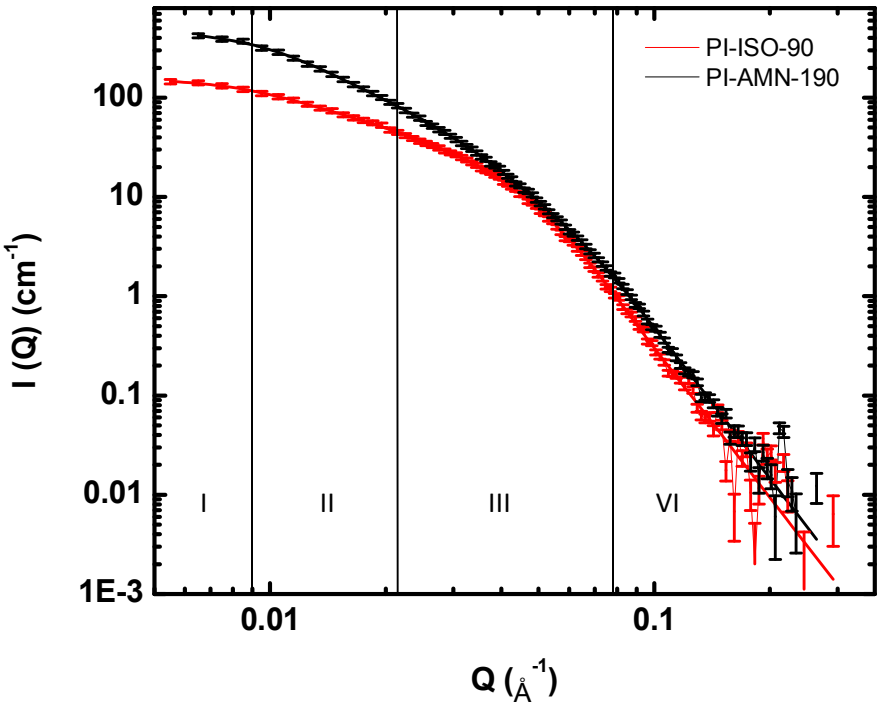

Figure 8. Small angle neutron scattering (SANS) data of PI-AMN-190 (black line, ρ_b= 0.23 g cm^{-3}) and of PI-ISO-90 (red line, ρ_b= 0.22 g cm^{-3}) both prepared in NMP using the 15% w/w solids formulation. Vertical lines separate the power-law regions (II and IV) from the "knee" regions (I and III).

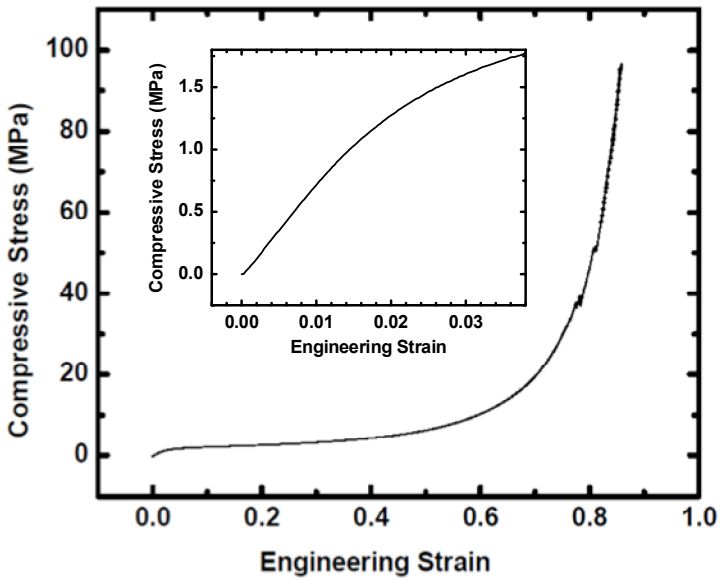

Figure 9. Behavior under compression (ASTM D1621-04a) of a PI-AMN-190 sample prepared using the 20% w/w solids formulation (Table 1): a short linear elastic range (at <(1.175 ± 0.075)% strain, magnified and shown as an inset) is followed by plastic deformation (up to 50% strain) and inelastic hardening thereafter. The samples never failed under compression. Other data pertinent to mechanical characterization (averages of two samples): bulk density ρ_b=0.291±0.006 g cm^{-3}; maximum strength (at 86% engineering strain): 99.27±3.64 MPa; specific energy at maximum load (at 86% engineering strain): 48.04±2.48 J g^{-1}; Young's modulus (from the slope of the linear elastic range in the inset): 27.25±0.84 MPa; yield strength (stress at 0.2% offset strain): 1.525±0.388 MPa (calculated by drawing a parallel line to the slope of the linear elastic range in the inset, starting from engineering strain=0.002); yield stain (i.e., strain at yield strength): 3.10±0.45; linear elastic to total deformation at the yield point: 0.38.

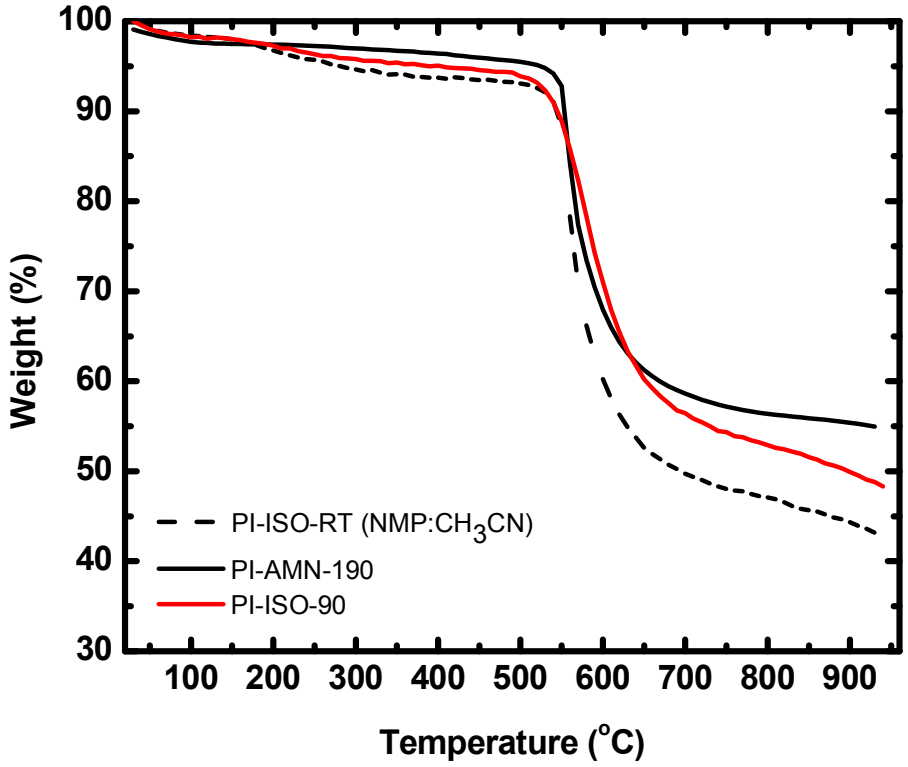

Figure 10. Comparative thermogravimetric analysis (TGA) data for the samples indicated prepared using the 15% w/w solids formulations (see Table 1).

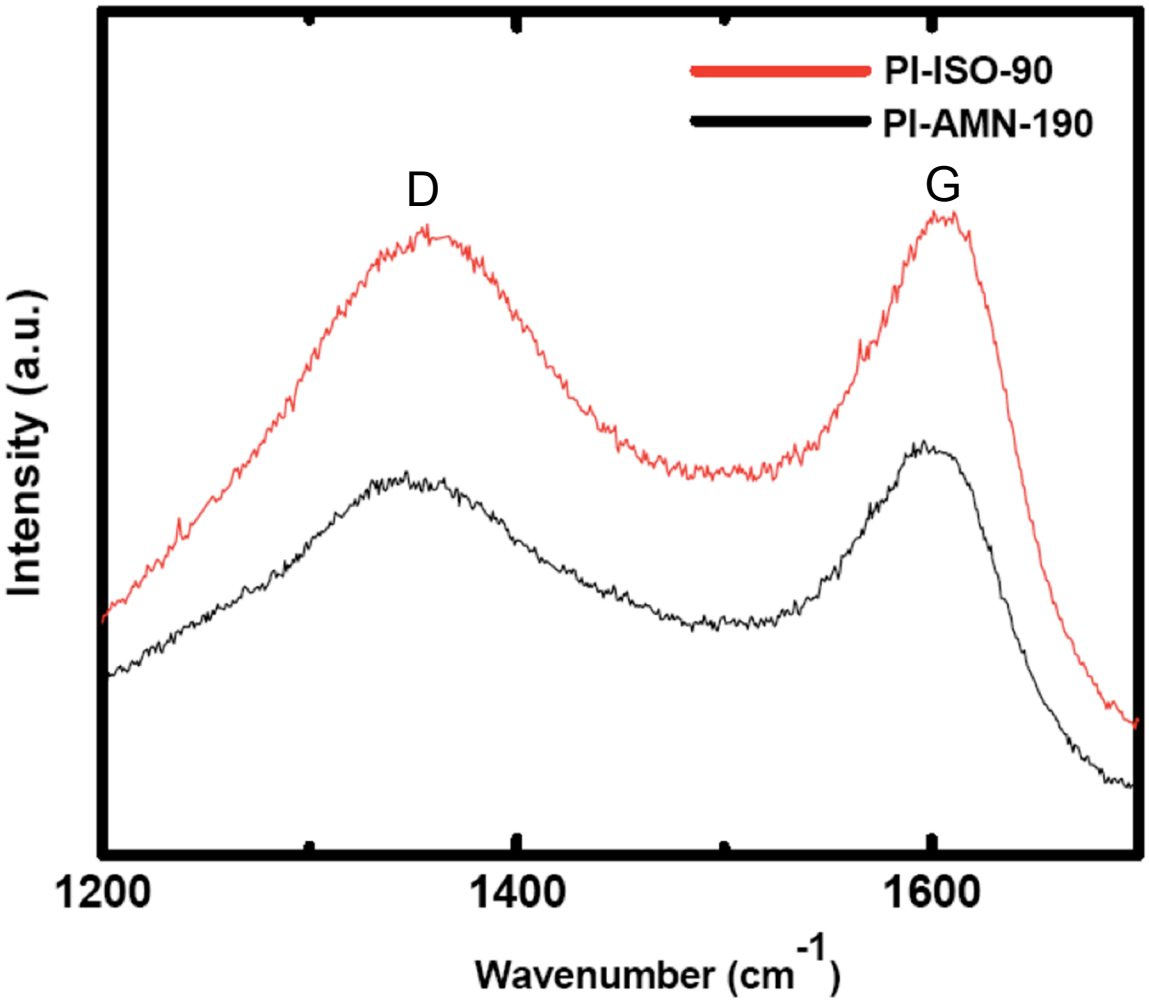

Figure 11. Raman spectra of polyimide aerogels prepared by the two routes. The ratios of the D- over the G-band integrated peak intensities are 0.98 and 1.12 for PI-AMN and PI-ISO, respectively.

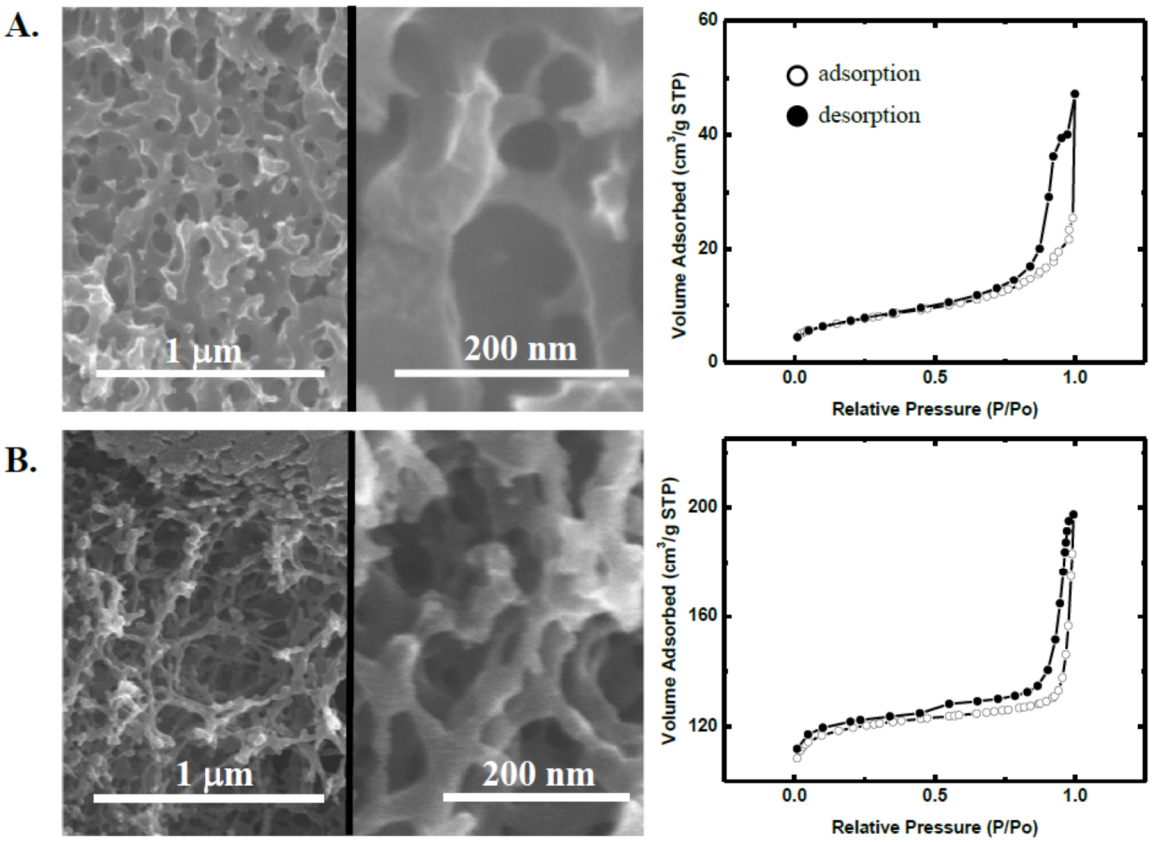

Figure 12. SEM at two different magnifications and N_2-sorption data for carbon aerogels produced by pyrolysis at 800 ^oC under nitrogen of, A: PI-AMN-190 prepared by the 15% w/w solids formulation in NMP; B: PI-ISO-RT prepared by the 10% w/w solids formulation in NMP/CH_3CN 3:1 w/w.

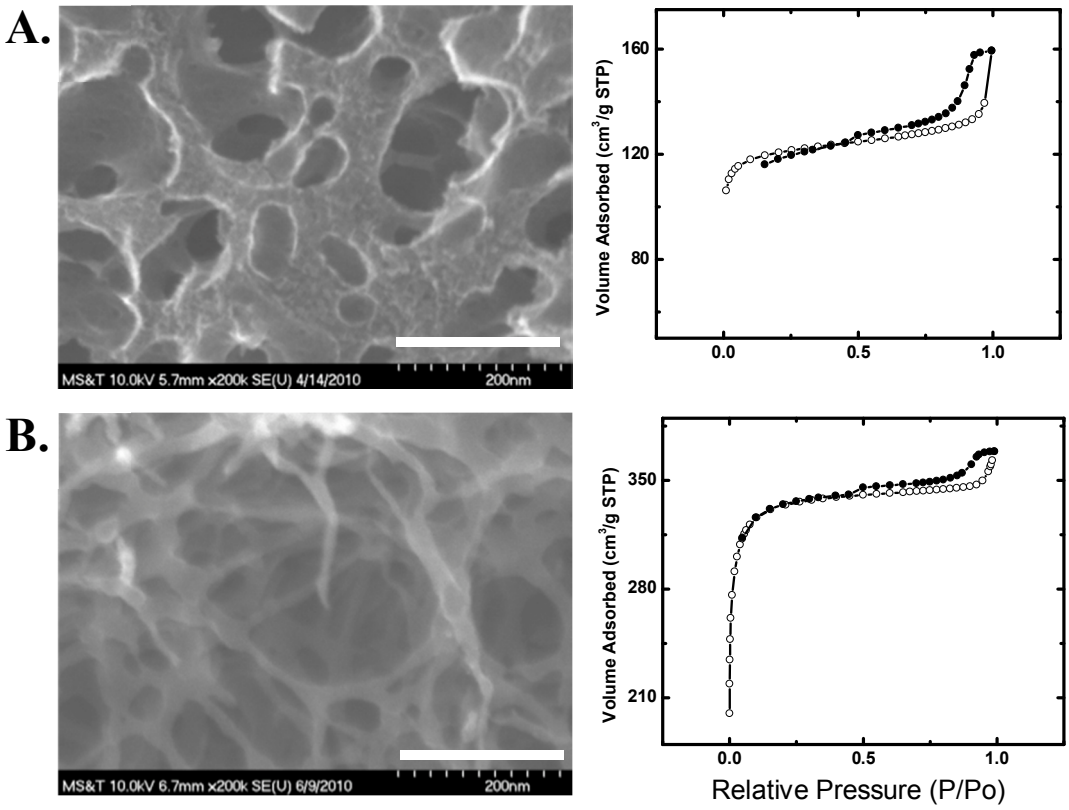

Figure 13. SEM (scale bars at 200 nm) and N_2-sorption data for carbon aerogels after etching at 1000 ^oC under flowing CO_2 for 3 h. A: carbon aerogel from PI- AMN-190 prepared by the 15% w/w solids formulation in NMP; B: carbon aerogel from PI-ISO-RT prepared by the 10% w/w solids formulation in NMP/DMSO 1:1 w/w. Note the rapid rise of the volume adsorbed at low relative pressures, indicating microporosity (pore sizes <2 nm).

V. Nano-engineering multiscale micro-to-macro porosity in robust monolithic polyimides and conformal conversion to carbons

By Chakkaravarthy Chidambareswarapattar, Lai Xu, Chariklia Sotiriou-Leventis, and N. Leventis**

Dr. C. Chidambareswarapattar, Dr. L. Xu, Prof. C. Sotiriou-Leventis, Prof. N. Leventis
Department of Chemistry
Missouri University of Science and Technology
Rolla, MO 65409, U.S.A.
E-mail: cslevent@mst.edu; leventis@mst.edu

Keywords: (multiscale, nanoporous, microporous, aerogels, polyimides, isocyanate, anhydride)

Submitted for Publication as a Communication to the *Advanced Materials*

Microporous materials (pore size < 2 nm) are pursued for applications in catalysis,[1] gas (e.g., hydrogen) storage,[2-4] and gas separations (e.g., CO_2 sequestration from mixtures with CH_4).[5,6] They range from inorganic zeolites[7] to metal oxide frameworks (MOFs),[8,9] and more recently to crystalline covalent organic frameworks (COFs),[10,11] amorphous hypercrosslinked polymers (HCPs),[12,13] conjugated microporous polymers (CMPs),[14,15] polymers with intrinsic microporosity (PIMs),[16-18] and desymmetrized organic cages by dynamic covalent scrambling.[19] Typically, microporous polymers are obtained as precipitates (powders), or at best as membranes. Yet, it has been suggested that for commercial implementation they need to be "fabricated into useful forms,"[16,17] and as such dispersion in other macroporous supports (e.g., cellulose filter paper) has been proposed.[19] However, since for the applications above the micropore-guest interaction is based on adsorption rather than size exclusion, it is recognized herewith that it will be beneficial if microporous materials are self-supporting and extend along the mass transfer path of the guest. This is essentially a chromatographic requirement that has been addressed successfully with multiscale

monolithic columns, whereas macroporosity provides quick (convective) mass transport of the analyte to the vicinity of the active sites, which are located on high-surface-area mesoporous space.[20]

Adopting that rationale, we report monolithic multiscale nanoporous polyimides which, owing to their molecular rigidity, are under current investigation as polymeric materials with intrinsic microporosity.[18,21-23] In turn, drawing from the synthesis of sturdy monolithic nanoporous polyureas,[24] aramids[25] and crosslinked polyacrylonitrile,[28] mesoporosity and monolithicity are addressed together with trifunctional monomers yielding hyperbranched polymers that aggregate and phase-separate into small primary nanoparticles. Monomer multifunctionality is expressed into multiple reactive sites on the surface of the primary particles, which bond covalently to one another forming secondary particles, which again aggregate into higher-order self-supporting robust covalent 3D nanoparticle networks filling the reaction vessel (gels). Macroporosity is primarily controlled by the overall amount of material filling space, therefore the monomer concentration; as a result, lower density monoliths are generally macroporous. Polyimide wet-gels obtained by that route were solvent-exchanged in an autoclave with liquid CO_2, which was taken above its critical point and vented off as a gas. That process eliminates surface tension forces of an evaporating liquid through the skeletal framework and preserves the structure of the wet-gel into the final dry objects, which, therefore, are classified as aerogels.[27]

With an eye to introducing an *in situ* porogen (CO_2), and because of the commercial availability of inexpensive trifunctional isocyanates in bulk quantities, the polyimide network was synthesized conveniently with the rather underutilized reaction of

anhydrides with isocyanates, which proceeds through a 7-member intermediate followed by loss of CO_2 (Eq. 1).[28] For this, pyromellitic dianhydride (PMDA) and benzophenone

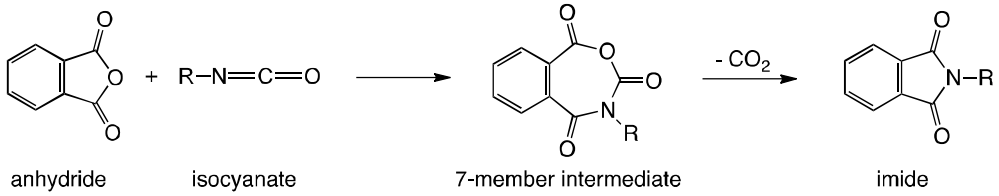

tetracarboxylic dianhydride (BTDA) reacted in a 1.5:1 mol ratio with a rigid aromatic (TIPM), or a flexible aliphatic triisocyanate (N3300A), both courtesy of Bayer Corp. USA under trade names Desmodur RE and Desmodur N3300A,[24] respectively (Scheme 1). Resulting polyimides are referred to as **aR-(**or **aL-)DANH-xx** whereas **aR-** or **aL-** denote aRomatic TIPM or aLiphatic N3300A, **DANH** stands for the abbreviation of the dianhydride, and extension **–xx** provides the weight percent concentration of the two monomers in the sol. In **aR-DANH-xx**, **-xx** was varied at three levels: -6, -12.5 and -20. For **aL-** materials, **-xx** was set at -20.

Scheme 1. Monomers used for the synthesis of nanoporous polyimides

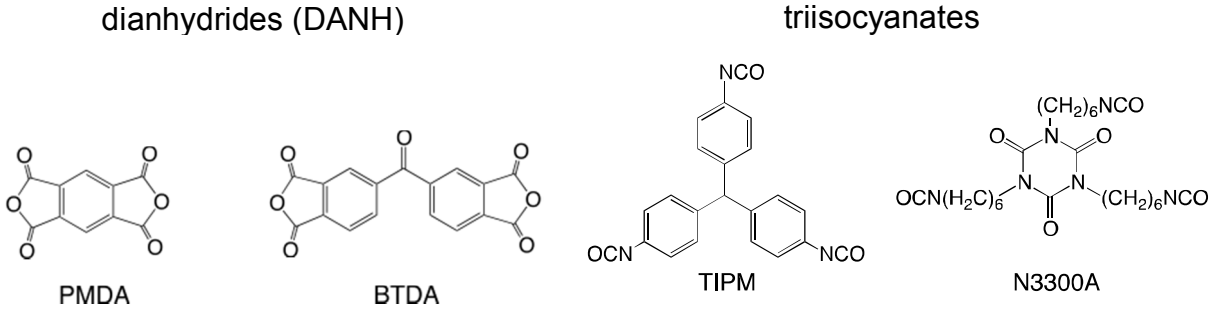

CHN analysis (Table S.1) agrees well with the DANH:isocyanate mol ratio in the sol. Solid state CPMAS ^{13}C NMR spectra (Appendix S.1, Fig.s S.1-S.4) include all structural features from both reagents, but cannot assert complete imidization as the broad resonance peaks (maxima in the 165-168 ppm range) are only 4-5 ppm downfield

from the resonance carbonyl peaks of the parent anhydrides. However, no IR stretches due to unreacted isocyanate (at ~2270 cm^{-1}) are detectable in any of the samples (Fig. S.5), and the coupled asymmetric/symmetric anhydride carbonyl stretches (e.g., for BTDA at 1852 cm^{-1} and 1773 cm^{-1}) have been replaced by new ones at 1782 cm^{-1} and 1723 cm^{-1}, which are assigned to the imide. Similarly, solid state CPMAS ^{15}N NMR (Fig. S.6) shows imide resonance peaks at 172 ppm and 165 ppm for **aR-DANH-xx** and **aL-DANH-20**, respectively.[29] The only other N resonance is of the isocyanurate ring in the **aL**-materials at 135 ppm. Incorporation and imidization of both monomers in the prescribed ratio is consistent with hyperbranched growth as shown in Scheme 2. XRD (Fig. S.7) shows two broad diffractions at 20° and 44°. Those have been also observed in other polymers as well (e.g., polyurethanes) and have been attributed to molecular chains spaced 0.4-0.5 nm apart.[30] Integration of those broad diffractions over the broad structureless background yields the degree of crystallinity at 33-34%. The above point to a short-range organization, whereas branches of entangled hyperbranched molecules are aligned in order to maximize their electrostatic (e.g., van der Waals) interactions. The relatively high degree of crystallinity suggests that this pattern is repeated extensively, yet randomly throughout the materials.

Scheme 2. Isocyanate-centered generational growth of hyperbranched polyimides. (Circles denote generations.)

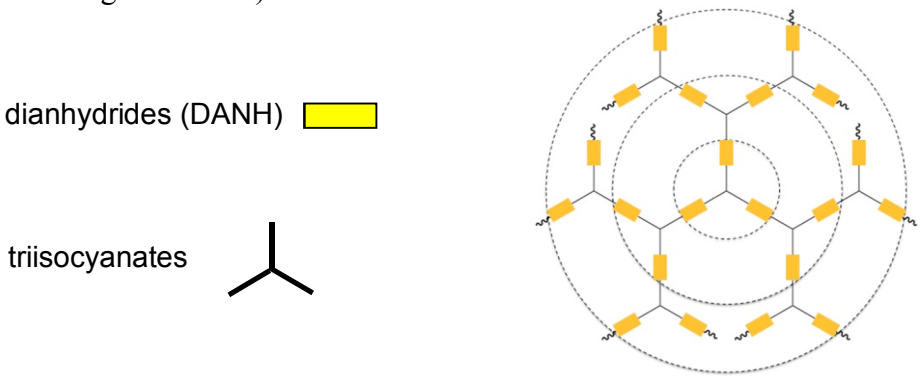

Microscopically (by SEM, Fig. 1), the polymer organizes into small particles with significant void space in between. **aR-PMDA-xx** particles seem to decrease in size as the sol concentration increases from **xx=6** to **20**, and get more evenly distributed in space. As a result, the macroporosity observed in **aR-PMDA-6** is absent from **aR-PMDA-20**, which appear mesoporous. On the contrary, at first glance the particle size of **aR-BTDA-xx** appears about invariant with **xx**, all samples are macroporous, and particles seem to assemble differently as **–xx** increases: into strings of beads at **xx=6** and into larger assemblies of globular clusters at **xx=20**. On the other hand, both **aL-DANH-20** materials are macroporous and consist of particles fused together in interconnected strings reminiscent of those in **aR-BTDA-6**, with a glazing on top. The porous structure is related to the hierarchical make-up of the skeletal framework, hence a quantitative evaluation of the latter was obtained with small angle x-ray scattering (SAXS).

SAXS data (see Appendix S.2) are markedly different among different kinds of polyimide samples. At higher values of the scattering vector Q, **aR-PMDA-xx** show a power-law region with slopes equal to 4.0 (Porod's law), indicating primary particles with sharp interfaces. **aR-BTDA-xx** and both **aL-** materials show high-Q slopes>4.0, indicating primary particles with fuzzy (i.e., density-gradient) interfaces. Primary particle radii, R_1, calculated from the first Guinier "knee" (just below the high-Q power-law region), decrease in both **aR-PMDA-xx** (from 17 nm to 7.4 nm) and **aR-BTDA-xx** (from 35 nm to 5.8 nm) as **-xx** increases from **-6** to **-20**. The R_1 values in both **aL-** materials are larger (48 and 43 nm, for PMDA and BTDA, respectively). Below the first Guinier knee, the scattering profile of **aR-PMDA-xx**, **aR-BTDA-6** and of both **aL-** materials levels off, as higher assemblies observed in SEM are beyond our accessible Q-range. However, in

the cases of **aR-BTDA-12.5** and **-20**, both a second power-law region and a second Guinier knee are within range indicating that the primary particles of **aR-BTDA-12.5** (R_1=13.5 nm) assemble into mass-fractal secondary particles (D_M=2.9; R_2=68 nm), while primary particles of **aR-BTDA-20** (R_1=5.8 nm) assemble into densely-packed surface-fractal secondary particles (D_S=2.1; R_2=43 nm). In all materials, including those with the glazing effect mentioned above, the smallest particles discernible by SEM are closer, size-wise, to the primary particles identified by SAXS. Putting all of the above together, hyperbranched polymers aggregate into molecular assemblies with some short-range internal order. Those assemblies phase-separate and become primary particles, which form mass- or surface-fractal secondary particles, which in turn form the gel network.

General material properties are summarized in Table 1. Wet-gels undergo syneresis during aging, and they shrink further during processing. The overall shrinkage is significant, 25-50% in linear dimensions relative to the molds, but all materials remain defect-free and monolithic. Shrinkage depends on the monomer concentration and molecular structure. Reflecting the higher covalent interconnectivity among more numerous elementary building blocks, materials from higher concentration sols shrink less: **aR-PMDA-6** and **-20** shrink 51% and 35%, respectively, while **aR-BTDA-6** and **-20** shrink 47% and 25%, respectively. At similar sol concentrations, **aL-** materials shrink more (~40%) than their **aR-** counterparts, reflecting the ability of the aliphatic chains in N3300A to coil-up and fold in order to maximize non-covalent interactions. On the contrary, the fact that more rigid **aR-PMDA-xx** shrink more (35-51%) compared to **aR-BTDA-xx** (25-47%) is attributed to the ability of terminal benzyl groups on the surface of particles to pivot in order to accommodate interparticle covalent bonding, thus decreasing

the demand for particle rearrangement. It is speculated that this subtle feature is a main structure-directing property linking the different SEM nanomorphologies of **aR-PMDA-xx** and **aR-BTDA-xx** with their macroscopic shrinkages and bulk densities, ρ_b. The latter does increase from **xx=6** to **xx=20** as designed, however, because of different shrinkages, the ρ_b-range of **aR-PMDA-xx** does *not* overlap with that of **aR-BTDA-xx**, even though both materials were prepared with same amounts of solids. Interestingly, however, the elastic (Young's) moduli (E) of *all* nanoporous polyimides of this study (including **aL-**), tested under quasi-static compression, scale similarly with ρ_b (Fig. 2). That reflects the monomer structural/functional similarity, which, therefore, should be expressed similarly (via the aggregates of the hyperbranched network of Scheme 2) on the surface of the primary particles and result in similar interparticle connectivity, irrespective of their size or specific chemical composition. Yet, upon closer examination, the elastic moduli of **aR-BTDA-xx** scale with ρ_b slightly differently from **aR-PMDA-xx** (note the power-law exponents in Fig. 2: 2.21 vs. 2.98 for **aR-BTDA-xx** and **aR-PMDA-xx**, respectively). Tentatively, that difference is attributed to the somewhat different assembly of the **aR-PMDA-xx** nanoparticles vs. those of **aR-BTDA-xx**, supporting the almost intuitive assumption whereas the mesoporous globular nanostructure of the former promotes interconnectivity more efficiently than the macroporous strings-of-beads of the latter. Further support for this hypothesis is found in the higher ultimate compressive strength and the specific energy absorption of **aR-PMDA-xx** vs. the **aR-BTDA-xx** materials. (Complete characterization data under quasi-static compression are provided in Appendix S.3.)

The skeletal densities, ρ_s, of all **aR-** materials are in the 1.33-1.37 g cm^{-3} range, and do not vary systematically with the sol concentration, signifying absence of closed pores. As expected, the total percent porosity, Π, of both **aR-** materials (via $\Pi=100\times[(1/\rho_b)-(1/\rho_s)]/\rho_b$), decreases as ρ_b increases (Table 1). Overall, porosities of **aR-PMDA-xx** are lower (67-47%) than those of **aR-BTDA-xx** (80-68%), reflecting the higher shrinkage and bulk densities of the former. For similar reasons, the porosities of the **aL-** samples (46% and 51%) are lower than those of the corresponding **aR-** materials at comparable densities.

N_2 sorption isotherms (Appendix S.4) closely match the qualitative description derived from SEM. The isotherms of all **aR-BTDA-xx** and both **aL-** materials rise only at $P/P_o>0.9$, do not reach saturation and their hysteresis loops are narrow (e.g., Fig. 3A), consistent with the macroporous voids in SEM. **aR-PMDA-6** shares several common features with **aR-BTDA-xx**, but its isotherm does reach a narrow plateau. The isotherms of **aR-PMDA-12.5** and **-20** are Type IV with H2-type hysteresis loops (Fig. 3A), characterizing mesoporous materials with ink-bottle pores. Also, irrespective of the shape isotherms take as $P/P_o\rightarrow1$, all **aR-** materials show a quick and substantial rise at $P/P_o<0.1$ (region enclosed by a dashed oval in Fig. 3A) indicating a significant amount of open microporosity. Indeed, analysis of the isotherms by the Brunauer-Emmett-Teller (BET) method yields relatively high specific surface areas for the **aR-** materials (σ), with a significant portion (12-16%) assigned (via t-plot analysis) to micropores (Table 1). Overall, the σ values of more rigid **aR-PMDA-xx** are higher than those of **aR-BTDA-xx**. The surface areas of both **aL-DANH-20** are much lower than those of the **aR-** materials, with no portion assignable to micropores.

The total pore volume, V_{Total}, was calculated via $V_{Total}=(1/\rho_b)-(1/\rho_s)$. The cumulative volume of pores with diameters in the 1.7-300 nm range, $V_{1.7\text{-}300\_nm}$, was obtained from the desorption branch of the isotherms. $V_{1.7\text{-}300\_nm}$ includes all mesopores (2-50 nm) and some of the macropores (50-300 nm). Notably, V_{Total} and $V_{1.7\text{-}300\_nm}$ converge, as expected, for **aR-PMDA-xx** whose isotherms reach saturation, while $V_{Total} >> V_{1.7\text{-}300\_nm}$ in all other cases.

Macroporosity was further probed with Hg-intrusion (Appendix S.5). Although pore sizes (Table 1) agree with the conclusions from SEM and N_2-sorption, that information should be considered cautiously, as most samples -particularly at low densities- collapse at the high pressures applied during the experiment. Mesopore size distributions (e.g., Fig. 3A-inset) were calculated with the Barrett-Joyner-Halenda (BJH) equation applied to the desorption branches of the isotherms. BJH plots are narrow for mainly mesoporous **aR-PMDA-xx** and relatively broad for meso/macroporous **aR-BTDA-xx** and **aL-**materials. (Distribution maxima and widths at half maxima are included in Table 1.)

Micropore volumes and size distributions were calculated by applying the Horvath-Kawazoe (HK) method on N_2-sorption data obtained under low-pressure dosing in separate experiments. In agreement with the discussion above, it is noted (Table 1) that $V_{1.7\text{-}300\_nm}+V_{Micropore}\approx V_{Total}$ for **aR-PMDA-xx**, and $V_{Total} >> V_{1.7\text{-}300\_nm}+V_{Micropore}$ in all other cases. Micropore-size distributions (Fig. 4) are broad and span the 0.5-1.0 nm range. Better fits are obtained by assuming cylindrical rather than slit-pore geometry.

Microporosity in polymers may be intrinsic or free-volume.[31] The latter can be substantial, but typically collapses upon drying, while useful intrinsic microporosity is an

innate property due to molecular rigidity and survives.[5] Extending this line of reasoning, intrinsic microporosity should be inherited to relevant pyrolytic carbons, while free-volume porosity should be erased long before carbonization.

Thus, **aR-**materials were subjected to repetitive cycles of drying-rewetting (acetone),[5] and the amount of solvent uptake (by thermogravimetric analysis – TGA) remains constant (Appendix S.6, Fig. S.13). In fact, that amount (5.7% w/w of **aR-BTDA-12.5**) agrees remarkably well with the amount of acetone needed to fill the microporous space (0.078 g per g of **aR-BTDA-12.5** (or 7.2% w/w of re-wetted sample), calculated from $V_{\text{Micropore}} \times \rho_{\text{acetone}}$, whereas $V_{\text{Micropore}}$ was taken from Table 1 and ρ_{acetone} = 0.791 g cm^{-3} at standard conditions).

TIPM includes aromatic rings separated by a single carbon atom, which is one of the key features of carbonizable materials.[32] Based on TGA under N_2 (Appendix S.6), **aR-** polyimides are stable up to 500 ^{o}C. Bulk carbonization was conducted by pyrolysis at 800 ^{o}C for 5 h under high purity Ar. The carbonization yield was 52-59% w/w, comparable to that of resorcinol-formaldehyde aerogels used for the synthesis of porous carbons.[33] Characterization data are shown in Appendix S.7 and results are summarized in Table 2. Carbon samples shrink linearly by an additional 22-26%, however they remain monolithic and sturdy. Their skeletal densities (1.6-1.8 g cm^{-3}) are near the range for amorphous carbon (1.8-2.0 g cm^{-3}). CHN analysis shows that they loose a large fraction of their H and O but retain N. Microscopically (by SEM, Fig. 1) both **C-aR-PMDA-xx** and **C-aR-BTDA-xx** retain the morphological features of the parent polyimides (globular appearance throughout in the former, strings of beads in the latter) albeit they appear more compact, consistent with the additional shrinkage. N_2-sorption

isotherms retain the relative features of the parent polyimides (Fig. 3B) suggesting that samples have shrunk conformally, retaining the structural ratios among different length-scales. The BET surface areas of **C-aR-PMDA-xx** are reduced relative to those of the parent polyimides, but retain a 5-7% portion assignable to micropores. Remarkably, the BET surface areas of **C-aR-BTDA-6** and **-12.5** are much higher (533 and 478 $m^2\ g^{-1}$) than those of the original samples (146 and 295 $m^2\ g^{-1}$, respectively), and are assigned (via t-plot analysis) mainly to micropores (65% and 58%, respectively). That surface area increase is accompanied by an increase in the micropore volume (e.g., from 0.048 $cm^3\ g^{-1}$ in **aR-BTDA-6** to 0.109 $cm^3\ g^{-1}$ in **C-aR-BTDA-6**). The micropore size distribution remains in the 0.5-1.0 nm range, fits well only to a cylindrical pore geometry, and three distinct maxima are discernible (Fig. 4). Based on similar CHN analysis results and the invariance of the carbonization yield between PMDA- and BTDA-based materials, a self-etching mechanism similar to that proposed in certain poly(acrylonitrile)-co-poly(diacrylate)s[24] is rather improbable. It is speculated that additional microporosity in lower density BTDA- materials reflects the somewhat more flexible BTDA-based polymer, and is created by pyrolysis gasses pushing the framework outwards. By the same token, the decrease of the overall surface area (but not porosity) in higher-density **C-aR-BTDA-20** mirrors a similar decrease in the parent polyimides (Table 1), and may be related to the transition of secondary particles from mass-fractals in **aR-BTDA-12.5** to densely-packed surface-fractals in **aR-BTDA-20**.

With sufficiently small closely-packed primary particles, the interstitial voids may fall in the range of micropores. That might have been relevant to **aR-BTDA-20**, yet, despite close packing (by SAXS), primary particles are not sufficiently small (11.6 nm in

diameter) for creating micropores. Hence, microporosity should be traced to the packing of hyperbranched structures inside primary particles. That was investigated with molecular simulations[21,23b] using the Accelrys Materials Studio 6.1 software package with interactions described by the Universal Force Field (UFF)[34] and a fully atomistic model. As inferred experimentally, a variable number (e.g., 4, 8, 16) of various generations of force-field optimized hyperbranced polyimides were packed into a periodic box to target densities equal to the experimental skeletal densities (Table 1).[35] After packing, the individual hyperbranched polymers were allowed to interact electrostatically (e.g., via van der Waals forces) using molecular dynamics relaxation at 298 K for 200 ps. The process was repeated with several structures till the x-ray diffraction pattern calculated based on scattering theory[36] with the Forcite module of Materials Studio, matched the experimental data. Several such converging attempts are shown in Appendix S.8. The best matches for **aR-PMDA-xx** and **aR-BTDA-xx** were with their 2nd generation structures, and the pack-4 and pack-8 assemblies, respectively. Results are included in Fig. 5 along with the corresponding assemblies and magnifications showing representative voids that match well with the micropore sizes identified with low-pressure N_2 dosing porosimetry (Fig. 4 and Table 1).

In conclusion, it has been demonstrated that borrowing methods akin to the synthesis of macro/mesoporous aerogels, polyimides with intrinsic microporosity can be cast in robust monolithic form, and importantly, this nano-engineering approach can be extended to the design of pyrolytically-derived multiscale nanoporous carbons. The choice of unconventional isocyanate chemistry for the synthesis of polyimides was based on the low-cost of monomers, and the fact that the only by-product is CO_2, which,

conceivably, can be utilized as a porogen. The monomer selection was made with the intention to probe the effect of molecular features in the properties of the resulting materials. Most notably, the small flexibility associated with the rotational freedom in BTDA seems to have important implications at all structural levels, including the pyrolytic behavior during carbonization. The properties of the multiscale nanoporous polyimides described herewith have not been optimized. Based on recent reports on microporous polyimides synthesized via the conventional amine/anhydride reaction,[5,6,18,21-23] much higher micropore volumes and surface areas are expected by adopting our approach to tetrafunctional isocyanates and/or trifunctional anhydrides.

Experimental

Materials: All chemicals were used as received unless noted otherwise. Tris(4-isocyanatophenylmethane) (TIPM) and N3300A were donated from Bayer Corp. U.S.A. PMDA and BTDA dianhydrides (abbreviated DANH) were purchased from Chriskev Company, Inc. (Leawood, KS); acetone, as well as anhydrous and reagent grade DMF and acetonitrile (ACN) from Aldrich Chemical Co.; deuterated chloroform ($CDCl_3$), and dimethyl sulfoxide (DMSO-d_6) from Cambridge Isotope Laboratories, Inc. PMDA was purified by sublimation at 170 ^oC under vacuum. BTDA was recrystallized from acetic anhydride followed by drying under vacuum at 125 ^oC.

Synthesis of ***aR-DANH-xx***: A mixture of a TIPM solution as received (Desmodur RE, 13.3 mL (13.6 g), containing 3.67 g of TIPM (0.01 mol) in anhydrous ethyl acetate) and a BTDA (4.83 g, 0.015 mol) or a PMDA (3.27 g, 0.015 mol) solution in variable amounts of anhydrous DMF was stirred at room temperature under N_2 for 20 min. The

solids concentration (w/w, extension **-xx**) was adjusted by varying the volume of DMF. The resulting sols were poured into molds (Wheaton 4 mL Polypropylene Omni-Vials 1.04 cm in inner diameter, Fisher part No. 225402), which were sealed and heated at 90 ^{o}C for 3 h. Gels were aged for 24 h at 23 ^{o}C in their molds, then were removed, washed with DMF (3×), acetone (4×) and were dried with CO_2 taken out as a supercritical fluid (SCF). Each solvent wash was conducted using 4× the volume of the gel. The same procedure was followed for **aL-DANH-20** materials with aliphatic isocyanate N3300A in DMF/ACN mixtures (75:25 w/w).

Carbonization: **aR-PMDA-xx** and **aR-BTDA-xx** materials were pyrolyzed at 800 ^{o}C for 5 h in a tube furnace under a flowing stream of high purity Ar (250 mL min^{-1}). Before heating, the tube was purged with Ar for 10 min, and the heating rate was set at 5 ^{o}C min^{-1}. At the end of the heating period, the power to the furnace was disconnected and the tube was cooled down to room temperature under flowing Ar.

SCF drying: Supercritical fluid (SCF) CO_2 drying was carried out in an autoclave (Spe-ed SFE system, Applied Separations, Allentown, PA).

Physical Characterization: Bulk densities, ρ_b, were calculated from the sample weight and dimensions. Skeletal densities, ρ_s, were determined with He pycnometry using a Micromeritics AccuPyc II 1340 instrument.

Chemical Characterization: CHN elemental analysis was conducted using Perkin Elmer Elemental Analyzer 2400 CHN calibrated by running first 5 blanks and acetanilide thrice as standard. IR spectra were obtained in KBr pellets with a Nicolet-FTIR Model 750 Spectrometer. Liquid ^{1}H and ^{13}C NMR of monomers were recorded with a 400 MHz Varian Unity Inova NMR instrument (100 MHz carbon frequency). Solid-state ^{13}C NMR

spectra were obtained with samples ground into fine powders on a Brucker Avance 300 Spectrometer with a 75.475 MHz carbon frequency using magic angle spinning (at 7 kHz) with broadband proton suppression and the CPMAS TOSS pulse sequence for spin sideband suppression. Solid-state ^{15}N NMR spectra were obtained on a Bruker Avance 400 Spectrometer with a 40.557 MHz nitrogen frequency using magic angle spinning (at 5 kHz).

Structural Characterization: N_2-sorption porosimetry was conducted with a Micromeritics ASAP 2020 surface area and porosity analyzer, equipped with a low-pressure transducer for micropore analysis. **aR-DANH-xx** and **aL-DANH-20** samples were outgassed under vacuum for 24 h at 90 ^oC and 40 ^oC, respectively. For micropore analysis, samples were degassed further in the analysis port at 80 ^oC for 4 h. Hg-intrusion porosimetry was conducted with a Micromeritics AutoPore IV 9500 instrument; scanning electron microscopy (SEM) using Au-coated samples on a Hitachi S-4700 field emission microscope; powder X-ray diffraction (XRD) with a PANalytical X'Pert Pro Multi-Purpose Diffractometer (MPD) with a Cu Kα radiation source (□= 1.54 Å). Small-angle X-ray scattering (SAXS) was conducted on the same instrument configured for SAXS with a 1/32^o SAXS slit and a 1/16^o anti-scatter slit on the incident beam side, and a 0.1 mm anti-scatter slit and a Ni 0.125 mm automatic beam attenuator on the diffracted beam side. Scattering data are reported in arbitrary units as a function of Q ($=4\pi\sin\theta/\lambda$), the momentum transferred during a scattering event. Data analysis was conducted with the *Irena SAS* tool for modeling and analysis of small angle scattering, within the commercial *Igor Pro* application (WaveMetrics, Portland, OR).

Mechanical Characterization: Quasi-static compression testing was performed according to the ASTM D1621-04a (Standard Test Method for Compressive Properties of Rigid Cellular Plastics) on cylindrical specimens using an Instron 4469 universal testing machine frame, following the testing procedures and specimen length (2.0 cm) to diameter (1.0 cm) ratio specified in the ASTM standard.

Thermal Characterization: Thermogravimetric analysis (TGA) was conducted with a TA Instrument, model Q50, under air and N_2 at a heating rate of 10 $^{o}C\ min^{-1}$.

Supporting Information

Supporting Information (Appendices S.1-S-8) is available from the Wiley Online Library or from the author.

Acknowledgements. We thank the Army Research Office for financial support (Award No. W911NF-10-1-0476). We also thank the Bayer Corporation U.S.A for the generous supply of Desmodur RE and Desmodur N3300A, the Materials Research Center of MS&T for support with materials characterization, Mr. Joseph A. Counsil for his assistance with micropore analysis and Dr. Wei Wycoff for her assistance with solid state NMR.

References

[1] J. Lee, O. K. Farha, J. Robers, K. A. Scheidt, S. T. Nguyen, J. T. Hupp, *Chem. Soc. Rev.* **2009**, *38*, 1450-1459.

[2] L. J. Murray, M. Dinca, J. R. Long, *Chem. Soc. Rev.* **2009**, *38*, 1294-1314.

[3] R. Banerjee, A. Phan, B. Wang, C. Knobler, H. Furukawa, M. O'Keefe, O. M. Yaghi *Science* **2008**, *319*, 939-943.

[4] J. Weber, M. Antonietti, A. Thomas, *Macromolecules* **2008**, *41*, 2880-2885.

[5] O. K. Farha, A. M. Spokoyny, B. G. Hausen, Y.-S. Bae, S. E. Brown, R. Q. Snurr, C. A. Mirkin, J. T. Hupp, *Chem. Mater.* **2009**, *21*, 3033-3035.

[6] O. K. Farha, Y.-S. Bae, B. G. Hauser, A. M. Spokoyny, R. Q. Snurr, C. A. Mirkin, J. T. Hupp, *Chem. Commun.* **2010**, *46*, 1056-1058.

[7] D. R. Rolison, *Chem. Rev.* **1990**, *90*, 867-878.

[8] O. M. Yaghi, M. O'Keefe, N. W. Ockwig, H. K. Chae, M. Eddaoudi, J. Kim, *Nature* **2003**, *423*, 705-714.

[9] A. P. Côté, A. I. Benin, N. W. Ockwig, M. O'Keefe, A. J. Matzger, O. M. Yaghi, *Science* **2005**, *310*, 1166-1170.

[10] A. I. Cooper, *Adv. Mater.* **2009**, *21*, 1291-1295.

[11] A. Thomas, *Angew. Chem. Int. Ed.* **2010**, *49*, 8328-8344.

[12] V. A. Davankov, M. P. Tsyurupa, *React. Polym.* **1990**, *13*, 27-42.

[13] M. P. Tsyurupa, V. A. Davankov, *React. Funct. Polym.* **2002**, *53*, 193-203.

[14] J. Weber, A. Thomas, *J. Am. Chem. Soc.* **2008**, *130*, 6334-6335.

[15] A. P. Katsoulidis, M. G. Kanatzidis, *Chem. Mater.* **2011**, *23*, 1818-1824.

[16] N. B. McKeown, P. M. Budd, *Chem. Soc. Rev.* **2006**, *35*, 675-683.

[17] N. B. McKeown, P. M. Budd, K. J. Msayib, B. S. Ghanem, H. J. Kingston, C. E. Tattershall, S. Makhseed, K. J. Reynolds, D. Fritsch, *Chem. Eur. J.* **2005**, *11*, 2610-2620.

[18] N. B. McKeown, P. M. Budd, *Macromolecules* **2010**, *43*, 5163-5176.

[19] S. Jiang, J. T. A. Jones, T. Hasell, C. E. Blythe, D. J. Adams, A. Trewin, A. I. Cooper, *Nature Commun.* **2011**, *2*, 207-214.

[20] F. Svec, C. G. Huber, *Anal. Chem.* **2006**, *78*, 2100-2107.

[21] A. Trewin, A. I. Cooper, *CrystEngComm* **2009**, *11*, 1819-1822.

[22] K. V. Rao, R. Haldar, C. Kulkarni, T. K. Maji, S. J. George, *Chem. Mater.* **2012**, *24*, 969-971.

[23] (a) Z. Wang, B. Zhang, H. Yu, L. Sun, C. Jiao, W. Liu, *Chem. Commun.* **2010**, *46*, 7730-7732. (b) G. Li, Z. Wang, *Macromolecules* **2013**, *46*, 3058-3066.

[24] N. Leventis, C. Sotiriou-Leventis, N. Chandrasekaran, S. Mulik, Z. J. Larimore, H. Lu, G. Churu, J. T. Mang, *Chem. Mater.* **2010**, *22*, 6692-6710.

[25] N. Leventis, C. Chidambareswarapattar, D. P. Mohite, Z. J. Larimore, H. Lu, C. Sotiriou-Leventis, *J. Mater. Chem.* **2011**, *21*, 11981-11986.

[26] A. G. Sadekar, S. S. Mahadik, A. N. Bang, Z. J. Larimore, C. A. Wisner, M. F. Bertino, A. K. Kalkan, J. T. Mang, C. Sotiriou-Leventis, N. Leventis, *Chem. Mater.* **2012**, *24*, 26-47.

[27] A. C. Pierre, G. M. Pajonk, *Chem. Rev.* **2002**, *102*, 4243-4265.

[28] (a) R. A. Meyers, *J. Polym. Sci., Part A1* **1969**, *7*, 2757-2762.
(b) H. Yeganeh, S. Mehdipour-Ataei, *J. Polym. Sci., Part A: Polym. Chem.* **2000**, *38*, 1528-1532.
(c) C. Chidambareswarapattar, Z. Larimore, C. Sotiriou-Leventis, J. T. Mang, N. Leventis, *J. Mater. Chem.* **2010**, *20*, 9666-9678.

[29] P. D. Murphy, R. A. Di Pietri, C. J. Lund, W. D. Weber, *Macromolecules* **1994**, *27*, 279-286.

[30] (a) Y. Zhang, J. Shang, F. Lv, P. Chu, *J. Appl. Polym. Sci.* **2012**, *125*, 1486–1492.
(b) J. Xu, W. Shi, W. Pang, *Polymer* **2006**, *47*, 457–465.

[31] See for example: (a) P. M. Budd, B. S. Ghanem, S. Makhseed, N. B. McKeown, K. J. Msayib, C. E. Tattershall, *Chem. Commun.* **2004**, 230-231. (b) Y. Tsujita, *Prog. Polym. Sci.* **2003**, *28*, 1377-1401.

[32] G. M. Jenkins, K. Kawamura, *Polymeric Carbons, Carbon Fibre, Glass and Char*, Cambridge University Press, New York, NY, 1976.

[33] N. Leventis, S. Mulik, C. Sotiriou-Leventis, *Chem. Mater.* **2008**, *20*, 6985-6997.

[34] A. L. Rappe, C. J. Casewit, K. S. Colwell, W. A. Goddard, W. M. Skiff, *J. Am. Chem. Soc.* **1992**, *114*, 10024-10035.

[35] (a) D. N. Theodorou, U. W. Suter, *Macromolecules* **1985**, *18*, 1467-1478.
(b) D. N. Theodorou, U. W. Suter, *Macromolecules* **1986**, *19*, 139-154.

[36] D. S. Sivia, *Elementary Scattering Theory: For X-ray and Neutron Users*, Oxford University Press, New York, N.Y., 2011.

Table 1. Materials characterization data for nanoporous polyimides

Sample	Shrinkage [%] [a] [b]	Bulk density ρ_b [g cm^{-3}] [a]	Skeletal density ρ_s [g cm^{-3}] [c]	Porosity Π[% v/v]	BET surface area, σ (micropore) [m^2 g^{-1}] [d]	Pore volume (cm^3 g^{-1})			Macropore diameter [nm] [h]	Mesopore diameter [nm] [i]	Micropore width cylindrical/slit pores [Å] [j]
						V_{Total} [e]	$V_{1.7\text{-}300\_nm}$ [f]	$V_{micropore}$ [g]			
aR-PMDA-6	51.4 ± 0.6	0.437 ± 0.010	1.333 ± 0.007	67	427 (52)	1.54	1.49	0.11	231	29.6 (6.6)	10.11 (7.9) / 5.89 (5.6)
aR-PMDA-12.5	45.7 ± 0.3	0.684 ± 0.010	1.367 ± 0.004	50	435 (68)	0.73	0.68	0.09	30.2	8.8 (3.0)	9.53 (4.8) / 5.59 (5.4)
aR-PMDA-20	35.4 ± 0.4	0.715 ± 0.006	1.360 ± 0.007	47	328 (38)	0.66	0.63	0.11	74.7	10.7 (4.3)	9.56 (1.1) / 5.60 (0.6)
aL-PMDA-20	40.1 ± 0.1	0.692 ± 0.017	1.277 ± 0.002	46	16 ([l])	0.66	0.080	[l]	[k]	64.0 (59.9)	[l]
aR-BTDA-6	46.8 ± 0.7	0.259 ± 0.017	1.323 ± 0.015	80	146 (17)	3.11	0.41	0.048	{621}	60.0 (65.0)	9.79 (-) / 5.72 (-)
aR-BTDA-12.5	34.3 ± 0.2	0.372 ± 0.008	1.349 ± 0.007	72	295 (36)	1.95	1.28	0.099	{210}	41.7 (27.4)	10.09 (11.3) / 5.88 (5.1)
aR-BTDA-20	24.7 ± 0.2	0.426 ± 0.007	1.335 ± 0.008	68	209 (33)	1.60	0.70	0.055	162	51.1 (69.8)	9.70 (9.3) / 5.68 (4.3)
aL-BTDA-20	41.1 ± 0.2	0.624 ± 0.027	1.281 ± 0.006	51	53 ([l])	0.82	0.45	[l]	[k]	43.6 (56.4)	[l]

[a] Average of 5 samples. [b] Shrinkage = 100 × [1-(sample diameter/mold diameter)]. [c] Single sample, average of 50 measurements. [d] In (parentheses): micropore surface area via t-plot analysis using the Harkins and Jura equation for the adsorbed layer thickness. [e] Total pore volume: $V_{Total} = (1/\rho_b)-(1/\rho_s)$. [f] BJH-desorption cumulative pore volume. [g] Cumulative volume of N_2 adsorbed at $P/P_o \leq 0.1$ using a low-pressure N_2 dosing routine. [h] Maxima of pore-size distributions via Hg-intrusion porosimetry. Samples in { } collapsed under pressure. [i] Maxima of BJH-desorption plots (e.g., Fig 3A, Inset); values in (parentheses): widths at half maxima (nm). [j] By applying the Horvath-Kawazoe method on N_2-sorption data under low-pressure dosing ($P/P_o \leq 0.1$). First values, assuming cylindrical pores; second values, assuming slit pores (Fig. 4); in (parentheses), widths at half maxima (nm). [k] Not measured. [l] No microporosity was detected.

Table 2. Properties of nanoporous carbons derived from **aR-PMDA-xx** and **aR-BTDA-xx** polyimides

Sample	Carbonization yield [% w/w] [a]	Shrinkage [%] [a] [b]	Bulk density ρ_b [g cm^{-3}] [a]	Skeletal density ρ_s [g cm^{-3}] [c]	Π [% v/v]	BET Surface area, σ (micropore) [m^2 g^{-1}]	Pore volume (cm^3 g^{-1})			Mesopore diameter [nm] [g]
							V_{Total} [d]	$V_{1.7\text{-}300\_nm}$ [e]	$V_{micropore}$ [f]	
C-aR-PMDA-6	52 ± 1	23.4 ± 0.2 (64)	0.599 ± 0.010	1.623 ± 0.033	63	253 (18)	1.05	1.02	[h]	21.9 (6.3)
C-aR-PMDA-12.5	55 ±1	26.4 ± 0.1 (62)	1.052 ± 0.063	1.817 ± 0.019	42	153 (13)	0.40	0.27	[h]	6.2 (2.5)
C-aR-PMDA-20	59 ± 1	21.6 ± 0.1 (54)	1.133 ± 0.042	1.666 ± 0.017	32	147 (7)	0.28	0.33	[h]	9.0 (2.6)
C-aR-BTDA-6	56 ±1	21.6 ± 0.4 (59)	0.359 ± 0.018	1.750 ± 0.040	79	533 (346)	2.21	0.78	0.11	46.4 (63.3)
C-aR-BtDA-12.5	57 ± 1	25.2 ± 0.2 (52)	0.534 ± 0.030	1.732 ± 0.019	69	478 (276)	1.30	1.19	0.15	33.4 (16.2)
C-aR-BTDA-20	59 ±1	21.0 ± 0.1 (42)	0.534 ± 0.011	1.820 ± 0.010	70	113 (8)	1.32	0.73	[h]	49.5 (33.8)

[a] Average of 3 samples. [b] Shrinkage relative to parent polyimides = 100 × [1-(C sample diameter/polyimide diameter)]. Values in (parentheses): total shrinkage relative to the original molds. [c] Single sample, average of 50 measurements. [d] Via $V_{Total} = (1/\rho_b)-(1/\rho_s)$]. [e] BJH-desorption cumulative pore volume. [f] Cumulative volume of N_2 adsorbed at $P/P_o \leq 0.1$ using a low-pressure N_2 dosing routine. [g] Maxima of BJH-desorption plots (e.g., Fig 3B, Inset). Values in (parentheses): widths at half maxima (nm). [h] Not measured

Figures

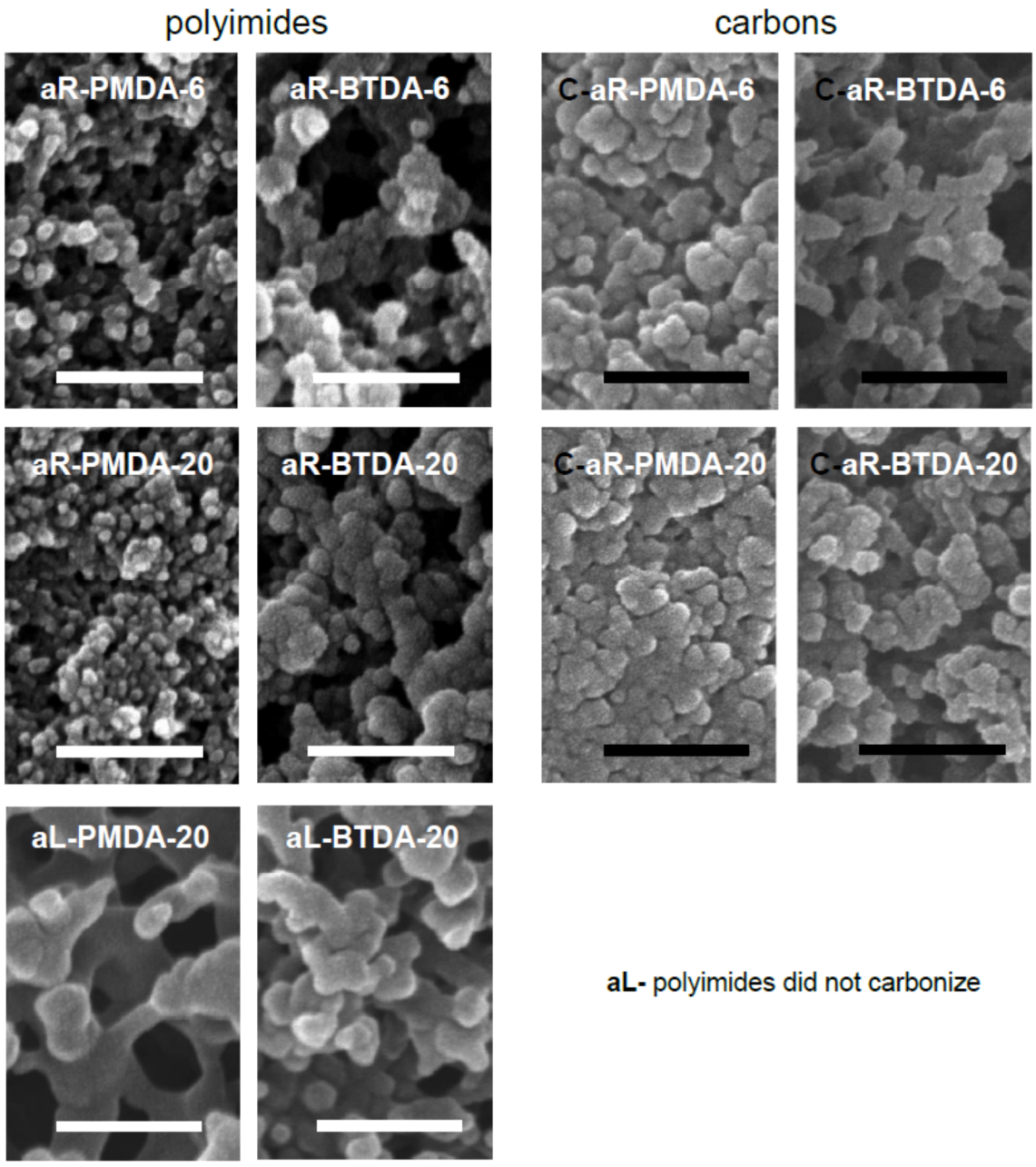

Figure 1. SEM of nanoporous polyimides and the derived carbons as indicated. Scale bars at 200 nm. For other materials information see Tables 1 and 2.

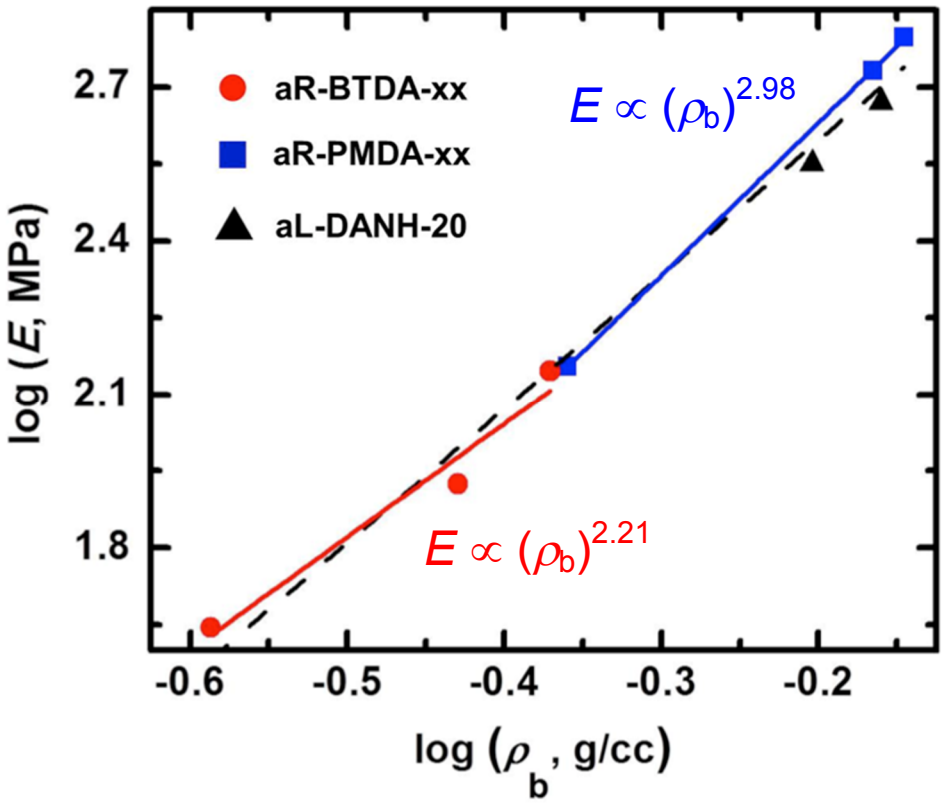

Figure 2. Log-Log plots of the Young's modulus, E, versus bulk density, ρ_b, of materials as indicated. Data obtained under quasi-static compression (Appendix S.3). Dashed black line: linear fit of all data. Exponential expressions: from the slopes of the separate linear fits for **aR-BTDA-xx** and **aR-PMDA-xx**.

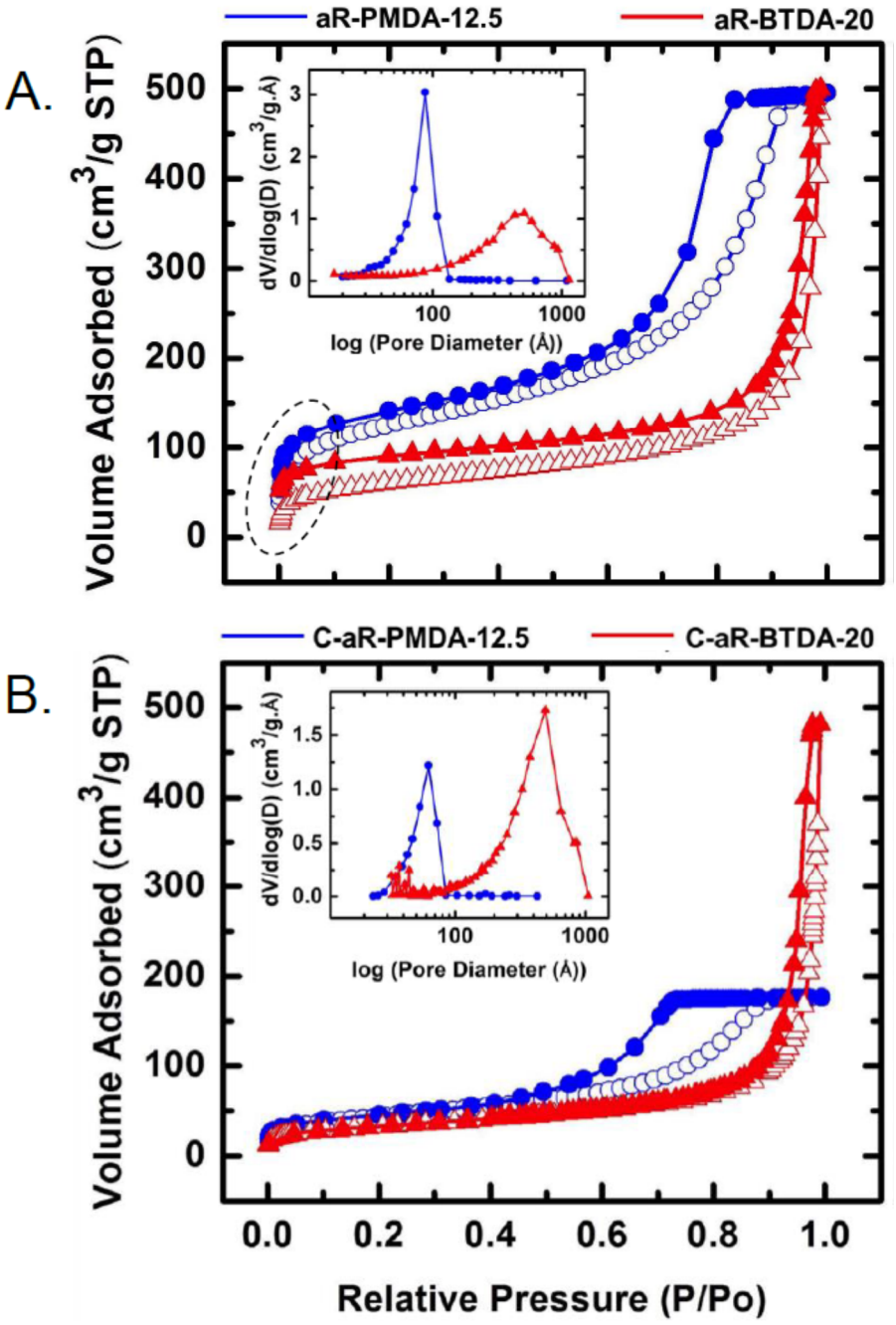

Figure 3. Representative N_2-sorption isotherms (open symbols: adsorption; full symbols: desorption). A. Polyimide samples as shown. B. Corresponding carbons. Dashed oval: rapid rise of N_2 adsorbed at low P/P_o indicating microporosity. Insets: pore size distributions by the Barrett-Joyner-Halenda (BJH) method applied on the desorption branches of the isotherms. (Complete data set in Appendix S.4.)

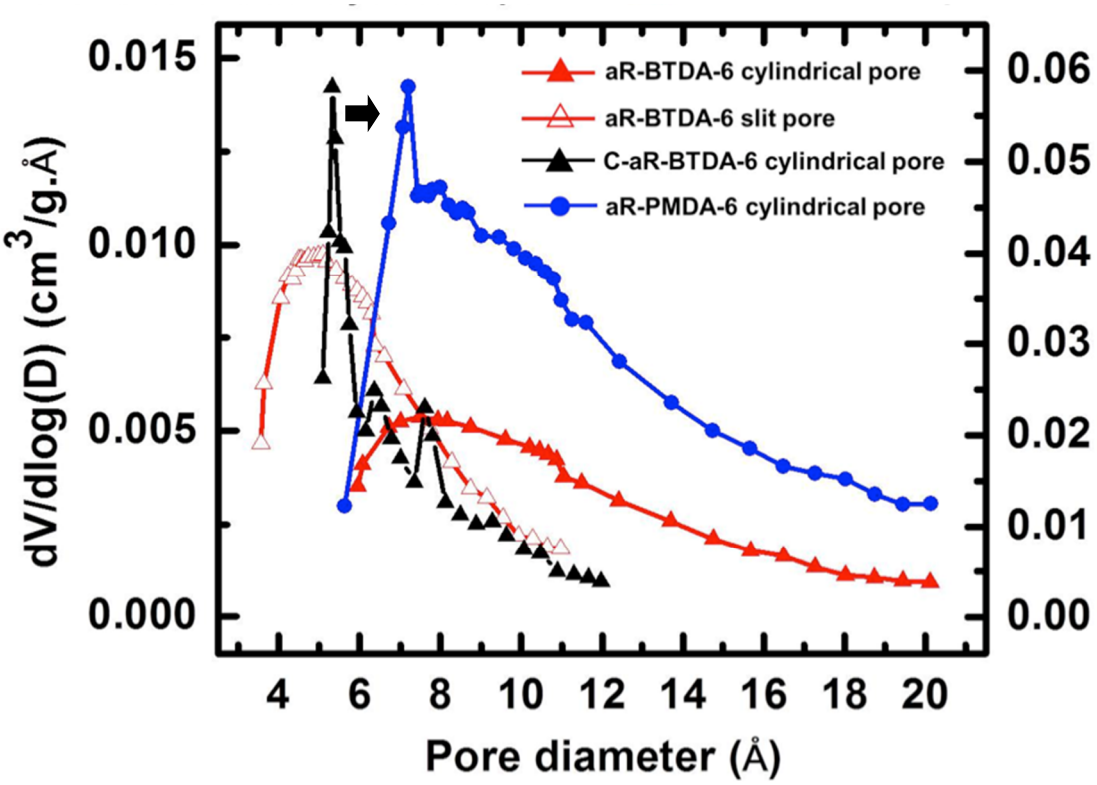

Figure 4. Representative micropore size distributions by the Horvath-Kawazoe (HK) method on N_2-sorption data obtained under low-pressure dosing and assuming pore geometries as indicated.

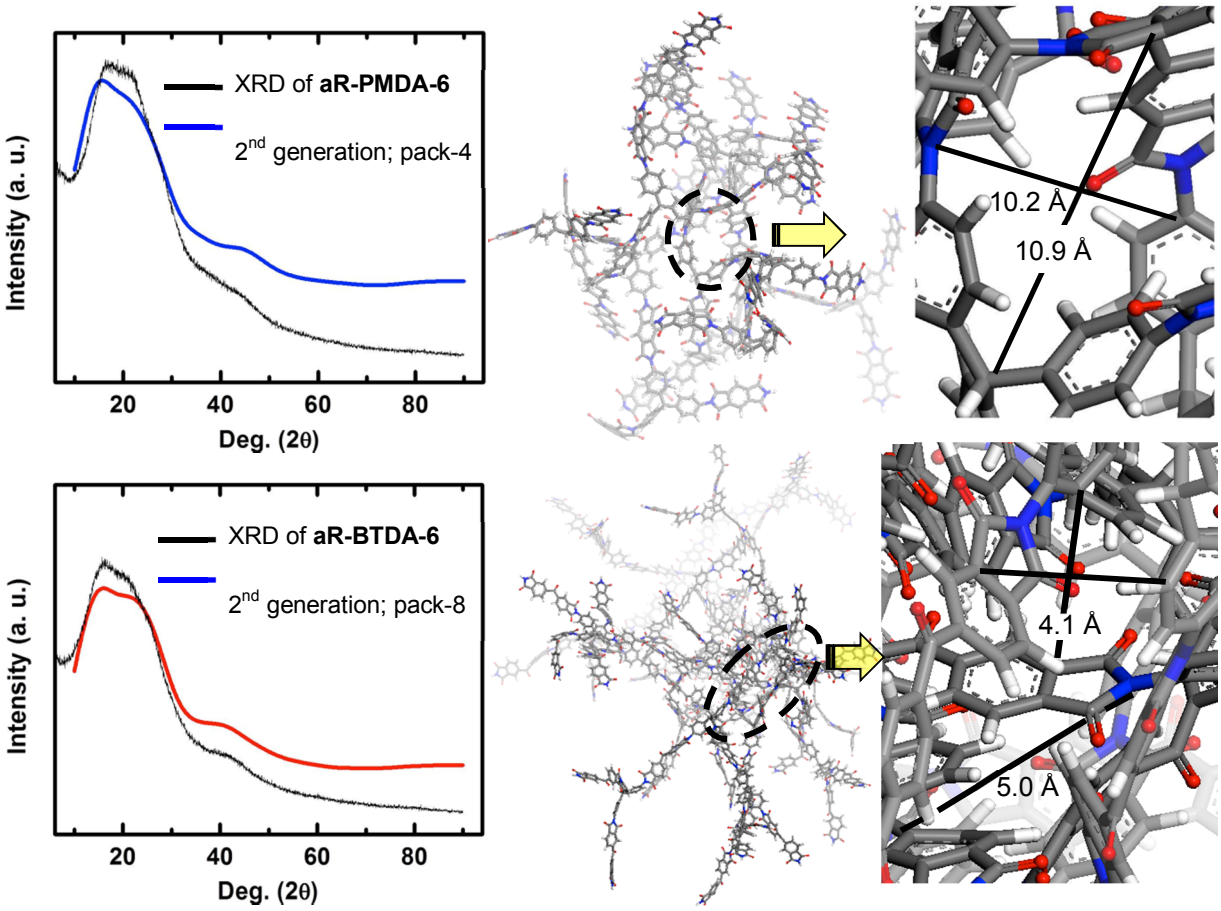

Figure 5. Left: Best-match of simulated XRD patterns with the experimental data as indicated. ("Pack-x" refers to the number of hyperbranched structures (Scheme 2) introduced in the molecular dynamics simulations. Results from several attempts are shown in Appendix S.8.) Middle: Structures corresponding to the best-match simulated XRDs on the Left. Right: magnification of the voids enclosed by dashed ovals in Middle.

Supporting Information

Appendix S.1 Chemical characterization data (NMR, FTIR, CHN, XRD)

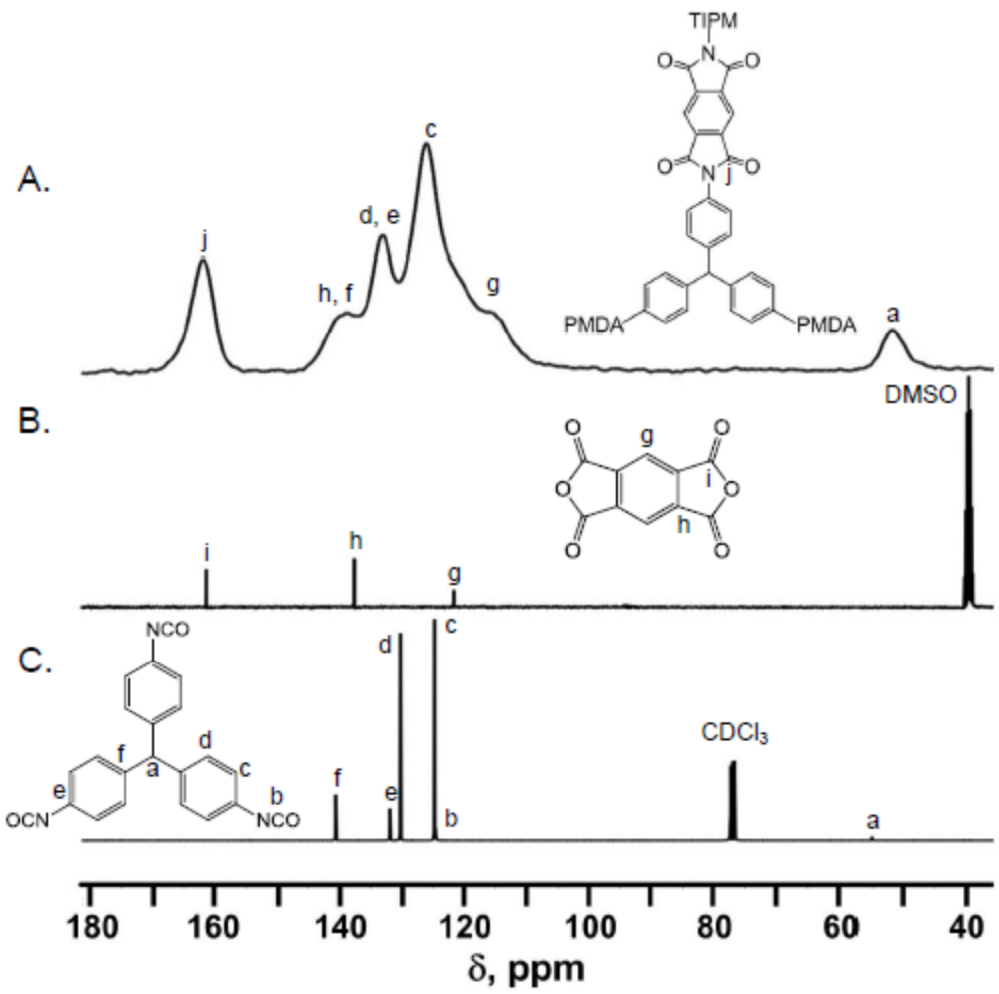

Figure S.1 (A) Solid state CPMAS ^{13}C NMR spectrum of **aR-PMDA-12.5**. (B) Liquid ^{13}C NMR spectrum of PMDA in DMSO-d_6. (C) Liquid ^{13}C NMR spectrum of TIPM in $CDCl_3$.

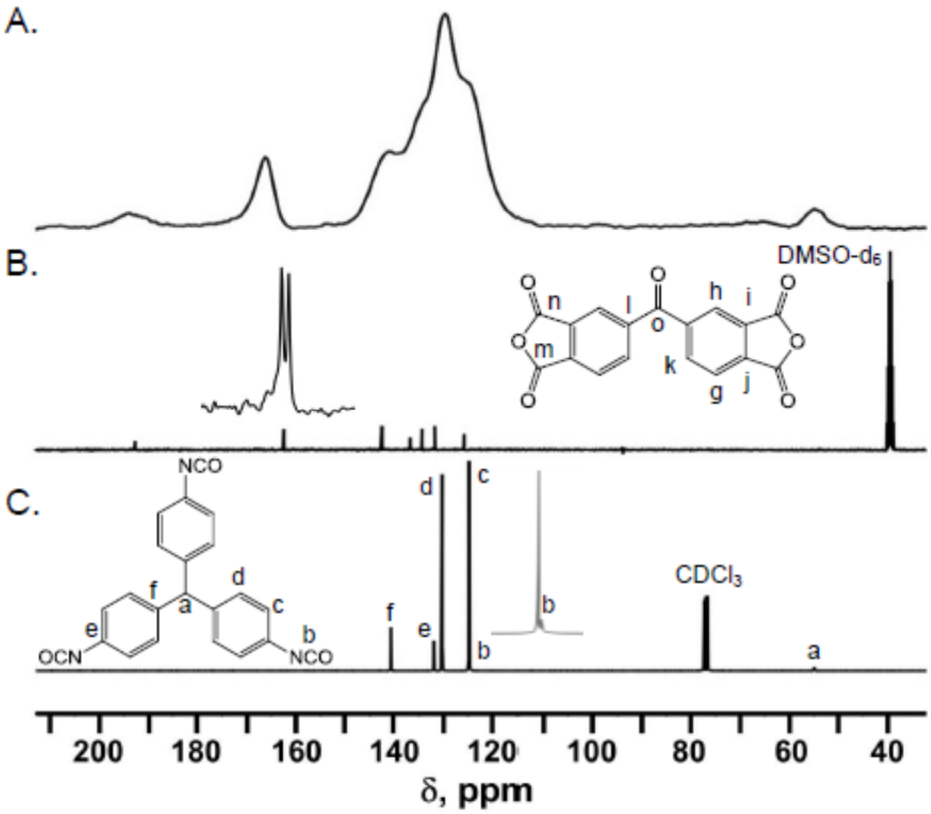

Figure S.2 (A) Solid state CPMAS ^{13}C NMR spectrum of **aR-BTDA-12.5**. (B) Liquid ^{13}C NMR spectrum of BTDA in DMSO-d_6. (C) Liquid ^{13}C NMR spectrum of TIPM in $CDCl_3$.

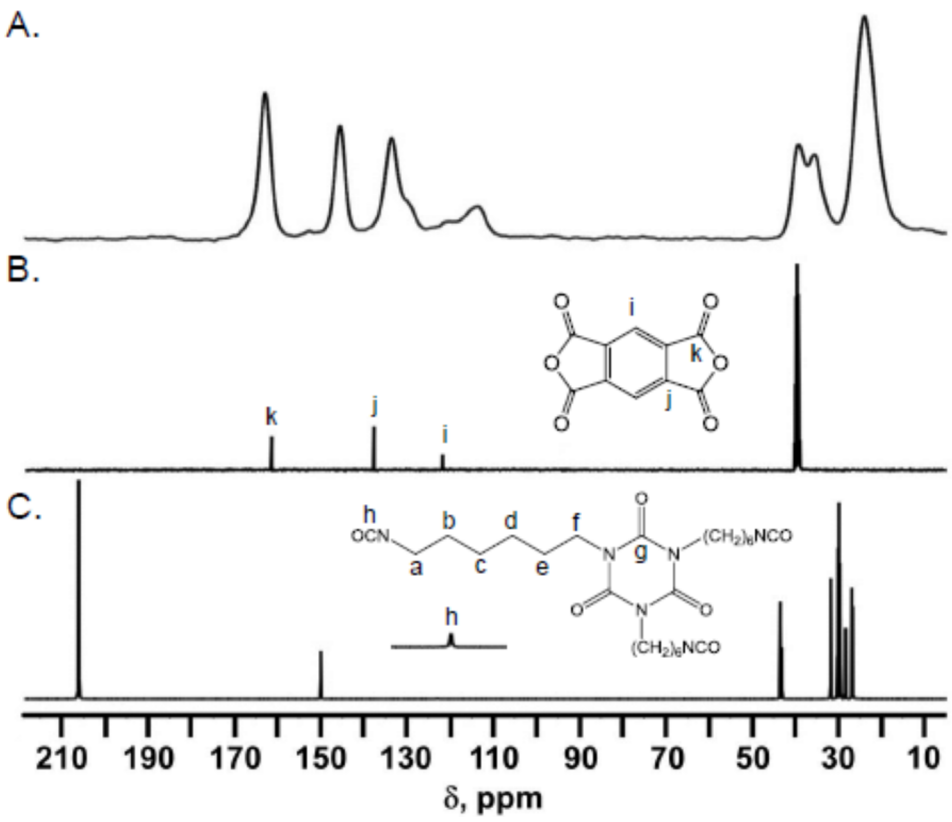

Figure S.3 (A) Solid state CPMAS ^{13}C NMR spectrum of **aL-PMDA-20**. (B) Liquid ^{13}C NMR spectrum of PMDA in DMSO-d_6. (C) Liquid ^{13}C NMR spectrum of N3300A in acetone-d_6.

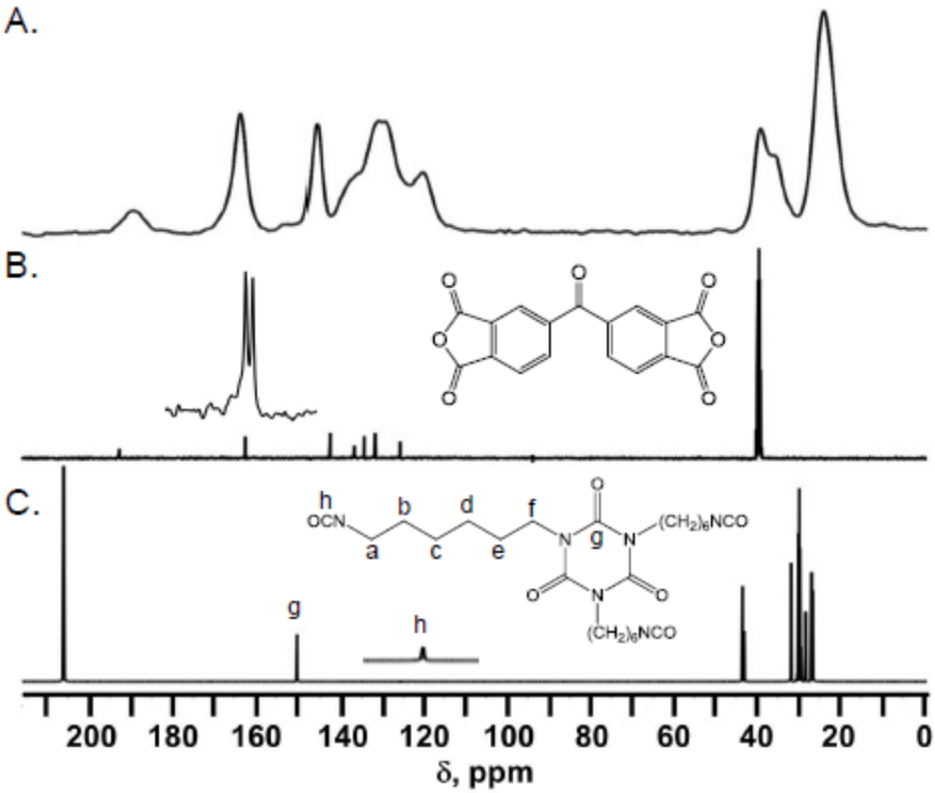

Figure S.4 (A) Solid state CPMAS ^{13}C NMR spectrum of **aL-BTDA-20**. (B) Liquid ^{13}C NMR spectrum of BTDA in DMSO-d_6. (C) Liquid ^{13}C NMR spectrum of N3300A in acetone-d_6.

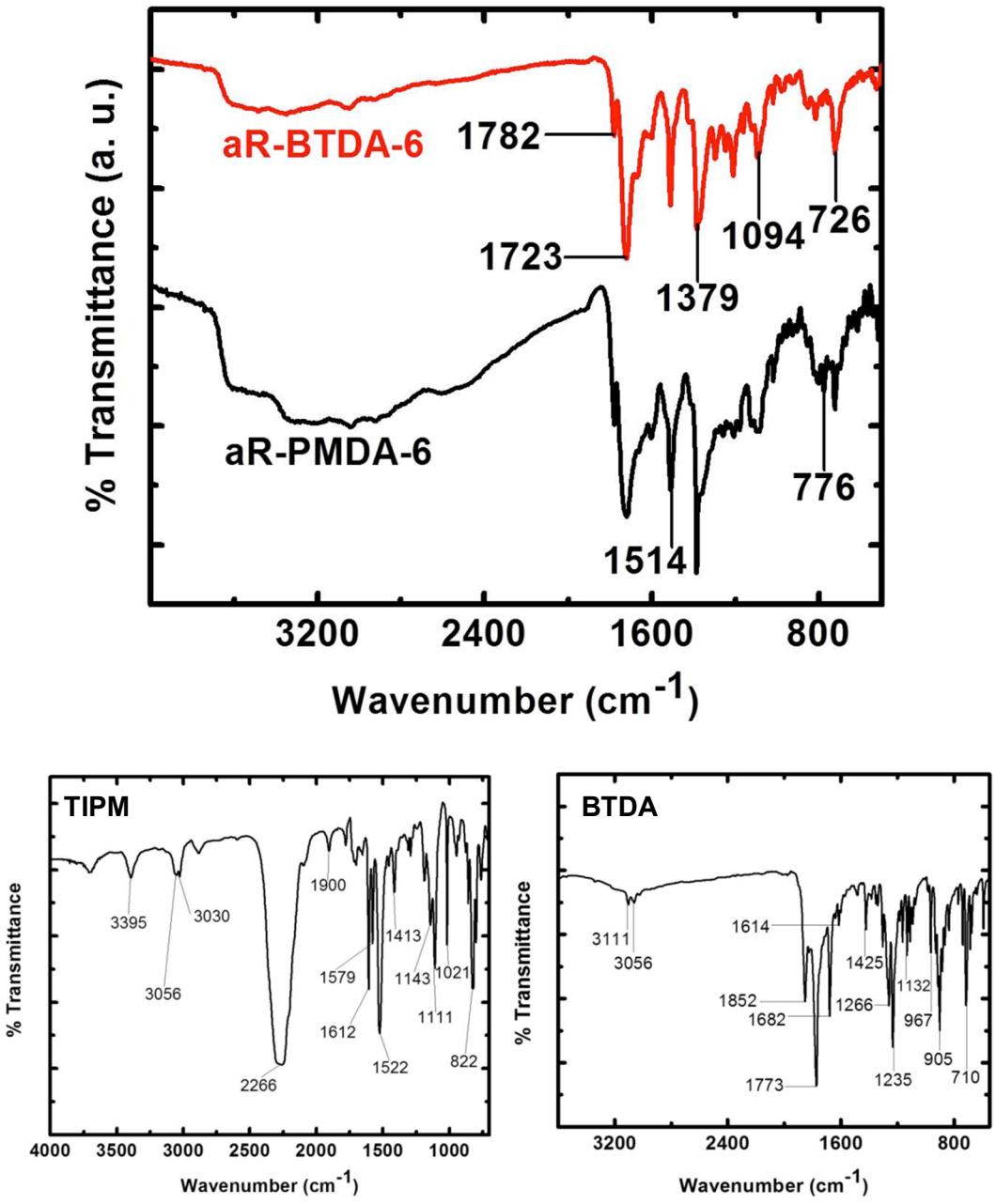

Figure S.5 FTIR spectra of nanoporous polyimides from aromatic TIPM. For comparison the spectra of TIPM and BTDA are shown below. The isocyanate stretch at 2266 cm^{-1} is not present in the spectra of the polyimides. The anhydride bands of BTDA at 1852 cm^{-1} and 1773 cm^{-1} have been replaced by bands at 1782 cm^{-1} and 1723 cm^{-1}, which are assigned to the asymmetric and symmetric stretching vibrations of the imide carbonyls, respectively. The band at ~1379 cm^{-1} is assigned to the C-N-C imide ring stretching. Bands at 1094 cm^{-1} and 776 cm^{-1} are assigned to imide ring bending.

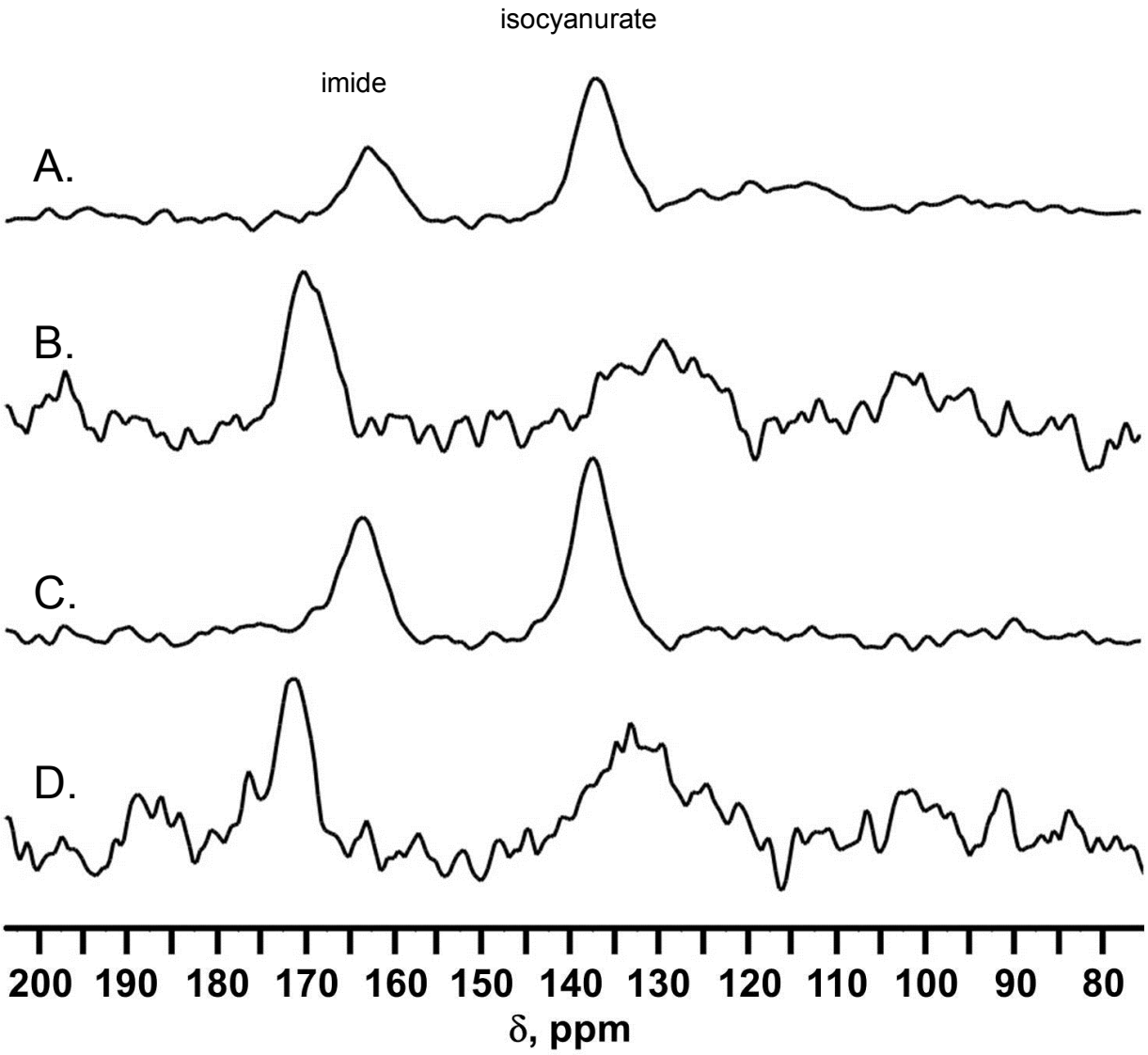

Figure S.6 Solid state CPMAS ^{15}N NMR spectra of nanoporous polyimides, as follows: (A) **aL-BTDA-20**. (B) **aR-BTDA-12.5**. (C) **aL-PMDA-20**. (D) **aR-PMDA-12.5**. Spectra referenced to glycine. For the liquid ^{15}N NMR spectra of the monomers (referenced to CD_3NO_2) see Supporting Information of: N. Leventis, C. Sotiriou-Leventis, N. Chandrasekaran, S. Mulik, Z. J. Larimore, H. Lu, G. Churu, J. T. Mang, *Chem. Mater.* **2010**, *22*, 6692-6710.

Table S.1. CHN Elemental analysis data for **aR-PMDA-xx** and **aR-BTDA-xx** polyimides

material	% C w/w	% H w/w	% N w/w	% residual w/w [a]
aR-PMDA-6	62.80 ± 0.01	3.78 ± 0.01	6.67 ± 0.01	26.75
aR-PMDA-12.5	63.61 ± 0.03	4.01 ± 0.04	6.86 ± 0.01	25.52
aR-PMDA-20	64.11 ± 0.05	4.17 ± 0.02	6.91 ± 0.08	24.81
theoretical for **aR-PMDA-xx** [b]	76.98	3.02	7.92	18.11
aR-BTDA-6	67.70 ± 0.08	3.51 ± 0.04	5.59 ± 0.01	23.20
aR-BTDA-12.5	69.60 ± 0.04	3.41 ± 0.01	5.05 ± 0.04	21.94
aR-BTDA-20	70.15 ± 0.06	3.29 ± 0.06	4.96 ± 0.02	21.6
theoretical for **aR-BTDA-xx** [b]	74.37	3.06	5.84	16.71
2^{nd} generation OH-terminated [c]	69.59	2.99	4.26	
2.66 generation OH-terminated [c]	72.55	3.10	4.61	

[a] By difference, presumably oxygen. [b] Based on the 1.5:1 mol/mol formulation for DANH:TIPM. [c] Assuming hypothetical DANH-terminated hyperbranched structures as in Scheme 2 in the article. Terminal anhydrides are presumed converted to OHs.

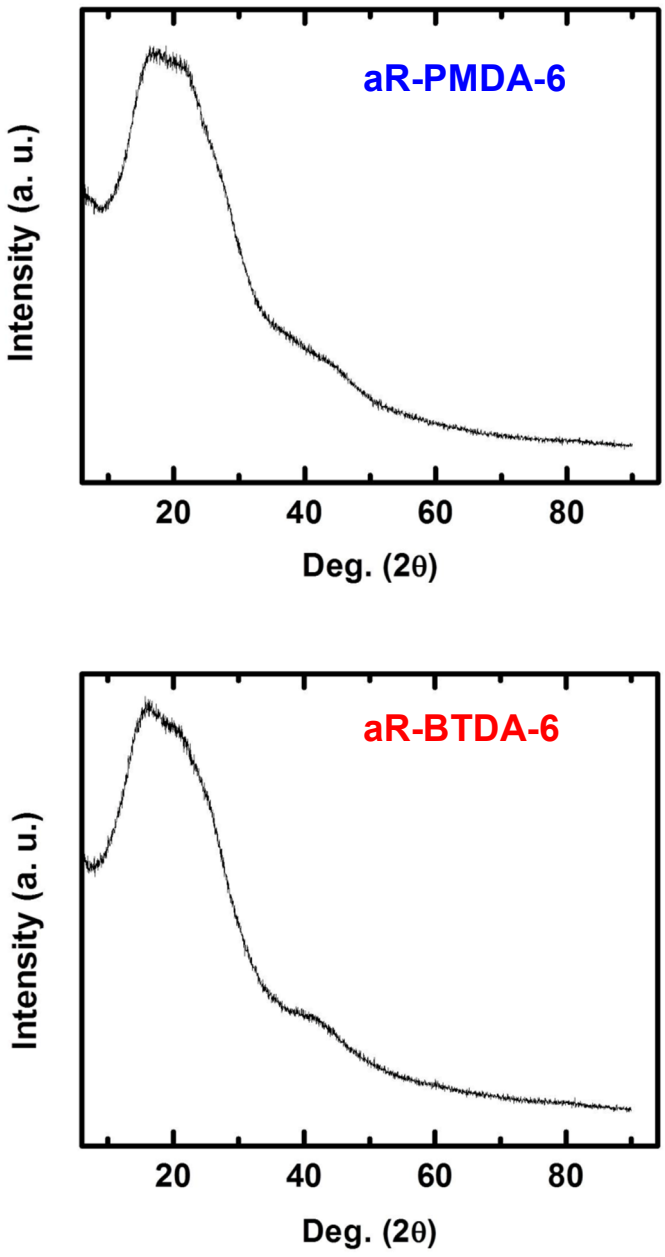

Figure S.7 Representative XRD of nanoporous polyimides derived from aromatic TIPM triisocyanate.

Appendix S.2 Small angle X-ray scattering data

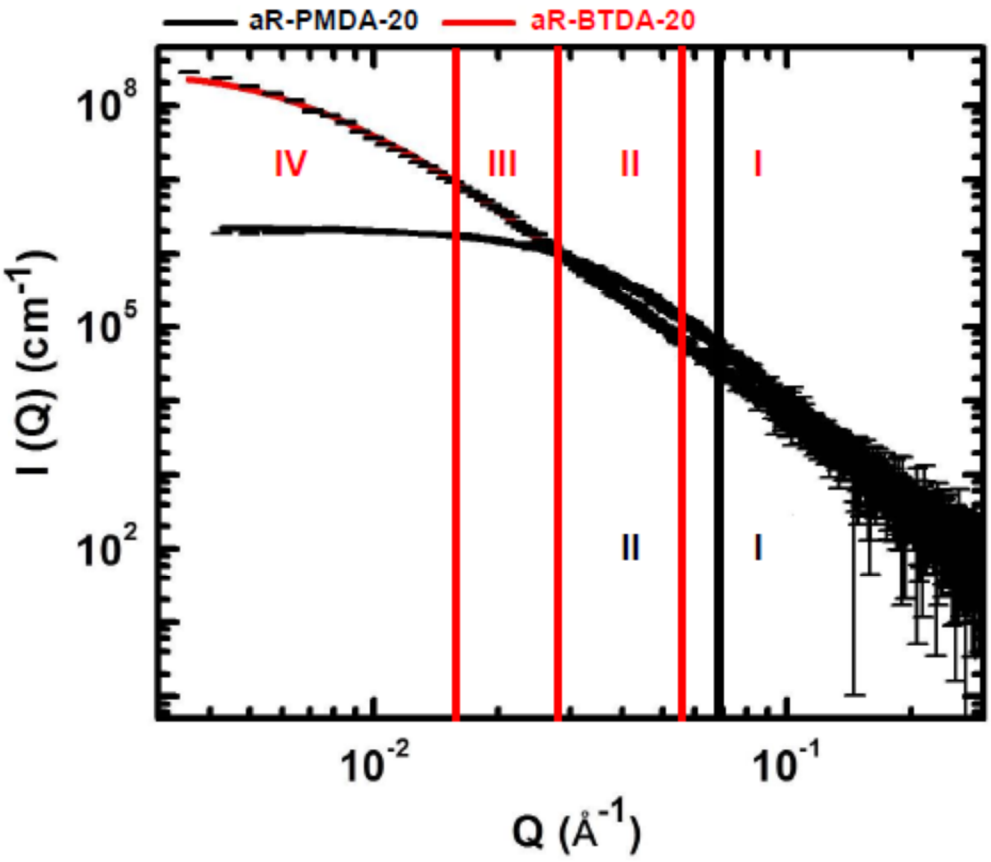

Figure S.8 Typical small angle X-ray scattering (SAXS) data exemplified with **aR-PMDA-20** (information in black) and **aR-BTDA-20** (information in red). Data were fitted to the Beaucage Unified Model. Primary particle radii of gyration (R_G) from first Guinier knee (Region II). Fractal dimension of secondary particles from the slope of power-law Region III. Secondary particle radii of gyration from second Guinier knee (Region IV). Results are summarized in Table S.2.

Table S.2. SAXS characterization data of nanoporous polyimides as indicated

	Primary Particles			Secondary Particles		
bulk density (ρ_b, g cm^{-3})	high-Q slope [a]	$R_G(1)$ [nm] [b]	R_1 [nm] [c]	low-Q slope [d]	$R_G(2)$ [nm] [e]	R_2 [nm] [c]
aR-PMDA-xx **(-xx: -6; -12.5; -20)**						
0.437 ± 0.010	4.00 ± 0.01	13.4 ± 0.1	17.4 ± 0.1	[f]	[f]	[f]
0.684 ± 0.010	4.00 ± 0.01	6.4 ± 0.1	8.3 ± 0.1	[f]	[f]	[f]
0.715 ± 0.006	4.00 ± 0.01	5.7 ± 0.1	7.4 ± 0.1	[f]	[f]	[f]
aL-PMDA-20						
0.692 ± 0.017	4.65 ± 0.01	36.8 ± 0.4	47.8 ± 0.5	[f]	[f]	[f]
aR-BTDA-xx **(-xx: -6; -12.5; -20)**						
0.259 ± 0.017	4.04 ± 0.01	26.6 ± 4.25	34.5 ± 5.5	[f]	[f]	[f]
0.372 ± 0.008	4.31 ± 0.01	10.4 ± 0.7	13.5 ± 0.9	2.88 ± 0.48	52.1 ± 7.2	67.7 ± 9.4
0.426 ± 0.007	4.03 ± 0.16	4.45 ± 0.53	5.8 ± 0.7	3.87 ± 0.02	32.8 ± 0.6	42.6 ± 0.8
aL-BTDA-20						
0.624 ± 0.027	4.56 ± 0.01	32.9 ± 0.7	42.7 ± 0.9	[f]	[f]	[f]

Referring to Fig. S.8: [a] From power-law Region I. [b] Radii of gyration, $R_G(1)$, from Guinier Region II. [c] Particle radius $R = R_G/0.77$. [d] From power-law Region III. [e] Radii of gyration, $R_G(2)$, from Guinier Region IV. [f] Beyond the accessible Q-range.

Appendix S.3 Mechanical characterization under quasi-static compression

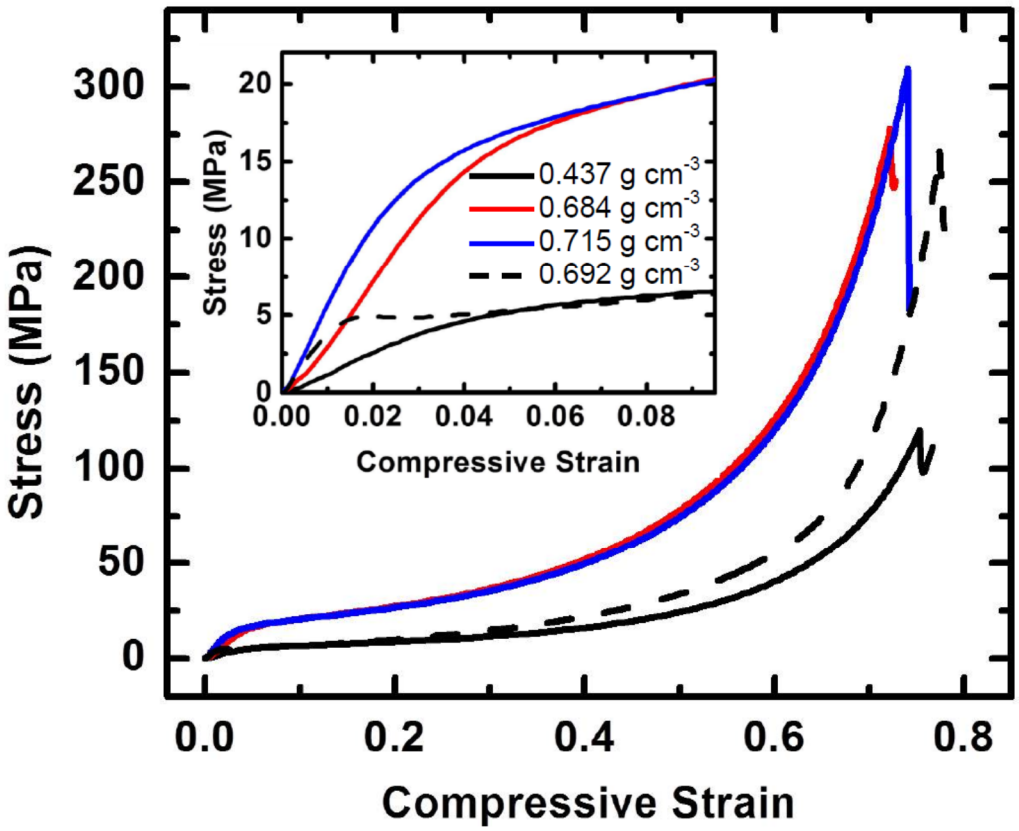

Figure S.9 Typical quasi-static compression data at 23 °C of nanoporous polyimides as follows: Solid lines: **aR-PMDA-xx** at three different densities as color-coded; Dashed black line: **aL-PMDA-20**. Inset: Magnified low-strain region. Elastic (Young's) modulus, *E*, from the slope of the linear part of the low-strain region (<0.02). Ultimate compressive strength from the maximum stress. Specific energy absorption (a measure of toughness) from the area under the stress-strain curve. Data are summarized in Table S.3.

Table S.3. Mechanical characterization data of PI aerogel under uniaxial quasi-static compression at 23 ^{o}C

bulk density [ρ_b, g cm^{-3}]	strain rate [s^{-1}]	Young's modulus [*E*, MPa]	speed of sound [m s^{-1}]	yield stress at 2% offset strain [MPa]	ultimate strength [*UCS*, MPa]	ultimate strain [%]	specific energy abs. [*T*, J g^{-1}]
aR-PMDA-xx **(-xx: -6; -12.5; -20)**							
0.437 ± 0.010	0.006	143 ± 6	572	4.00 ± 0.00	119 ± 2	76 ± 1	50 ± 2
0.684 ± 0.010	0.006	538 ± 53	887	13.63 ± 0.18	273 ± 6	72 ± 0	82 ± 4
0.715 ± 0.006	0.006	625 ± 35	935	13.16 ± 0.28	298 ± 15	74 ± 1	81 ± 2
aL-PMDA-20							
0.692 ± 0.017	0.008	466 ± 12	820	4.90 ± 0.42	255 ± 18	75 ± 2	47 ± 2
aR-BTDA-xx **(-xx: -6; -12.5; -20)**							
0.259 ± 0.017	0.005	44 ± 10	412	0.40 ± 0.08	1.82 ± 0.15	17 ± 2	2.3 ± 0.2
0.372 ± 0.008	0.006	84 ± 1	475	2.75 ± 0.02	112 ± 7	80 ± 1	47 ± 1
0.426 ± 0.007	0.006	140 ± 7	573	3.48 ± 0.38	218 ± 9	82 ± 1	72 ± 2
aL-BTDA-20							
0.624 ± 0.027	0.008	358 ± 38	757	3.95 ± 0.35	297 ± 13	80 ± 0	65 ± 5

Appendix S.4 N_2-sorption porosimetry of all aR- and both aL- materials

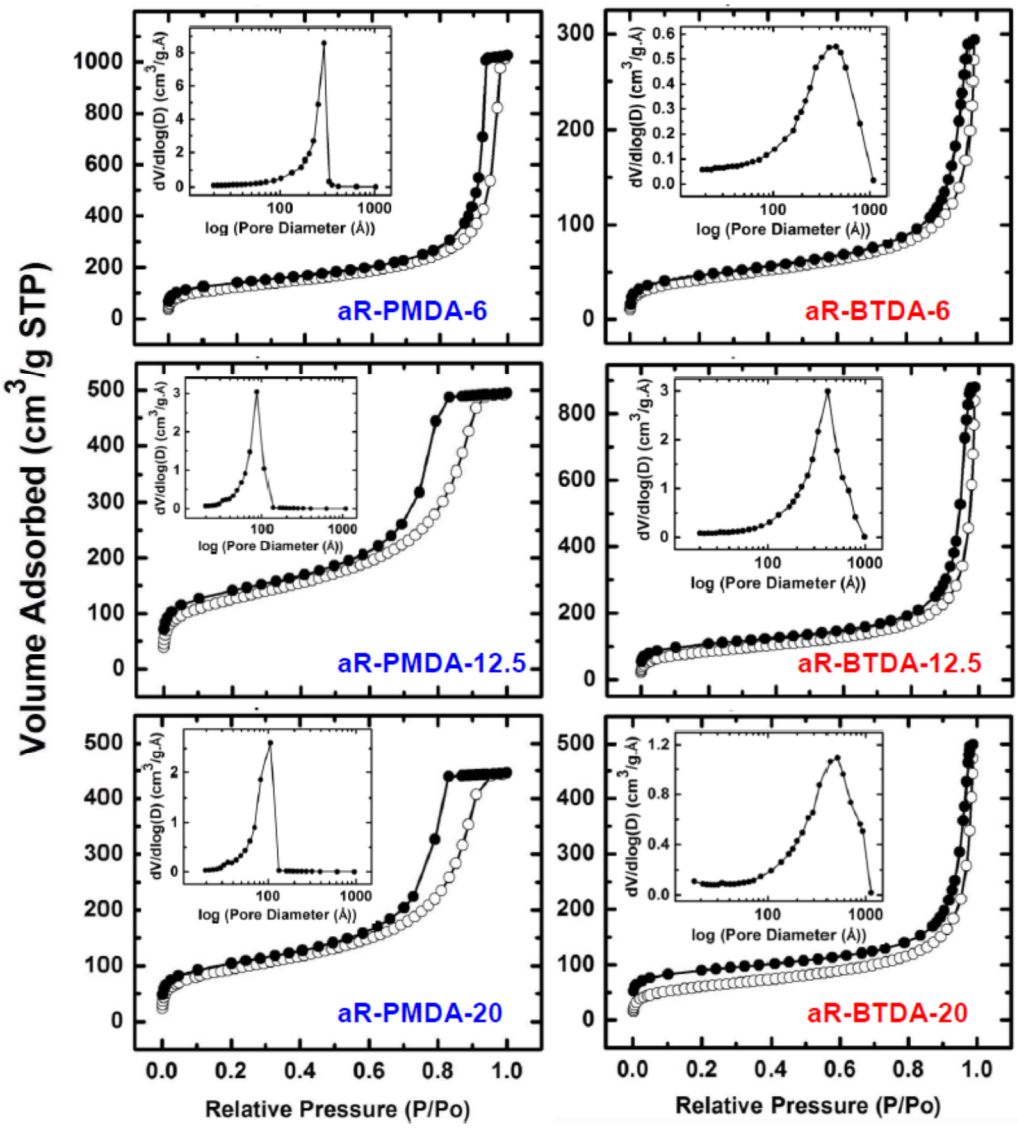

Figure S.10 N_2-sorption isotherms and pore size distributions (Insets) by the BJH method of porous polyimides derived from aromatic TIPM triisocyanate as shown. (Open circles: adsorption; Dark circles: desorption. For results from data analysis see Table 1, main article.)

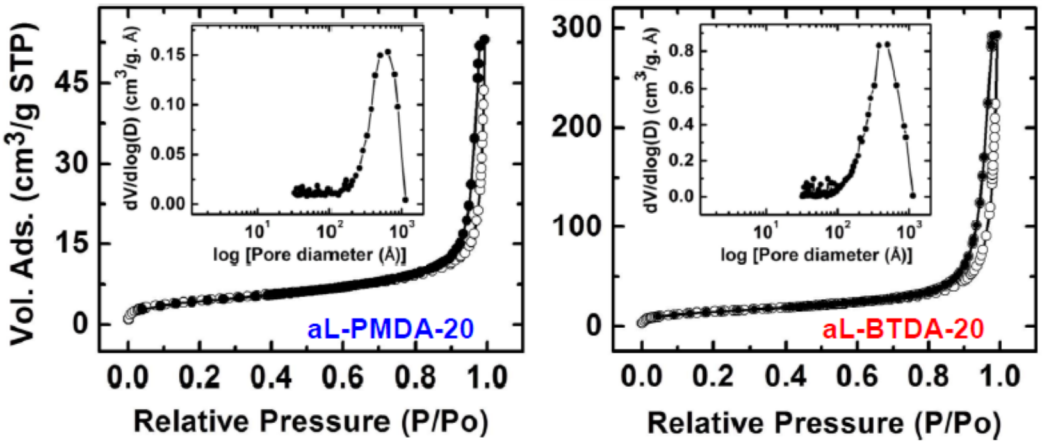

Figure S.11 N_2-sorption isotherms and pore size distributions (Insets) by the BJH method of porous polyimides derived from aliphatic N3300A triisocyanate as shown. (Open circles: adsorption; dark circles: desorption. For results from data analysis see Table 1, main article.

‘

Appendix S.5 Hg-intrusion porosimetry of all aR- materials

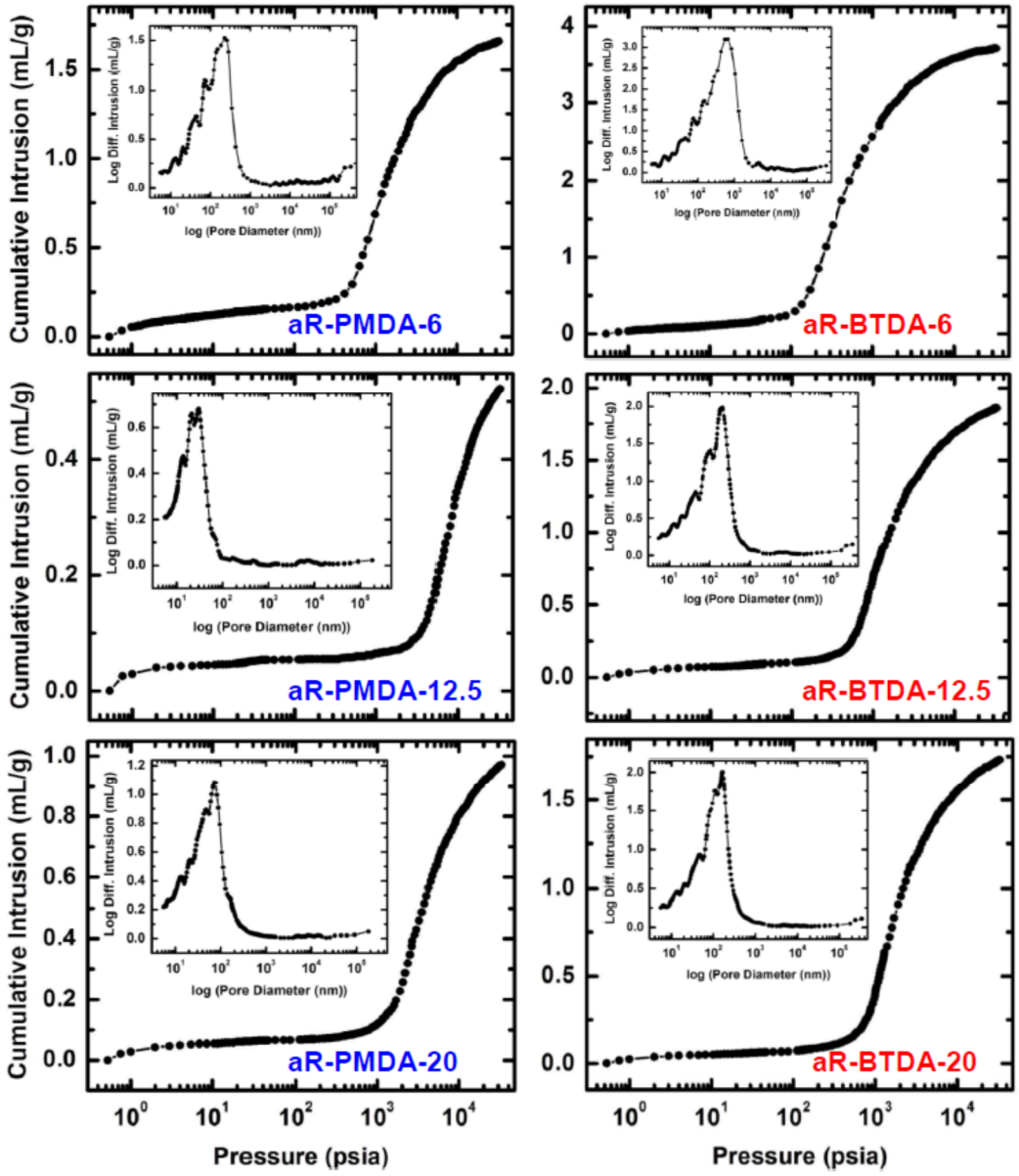

Figure S.12 Hg-intrusion porosimetry of porous polyimides derived from aromatic TIPM triisocyanate as shown. Insets: Pore size distributions. Results in Table 1, main article.

Appendix S.6 Thermogravimetric analysis (TGA) and solvent uptake

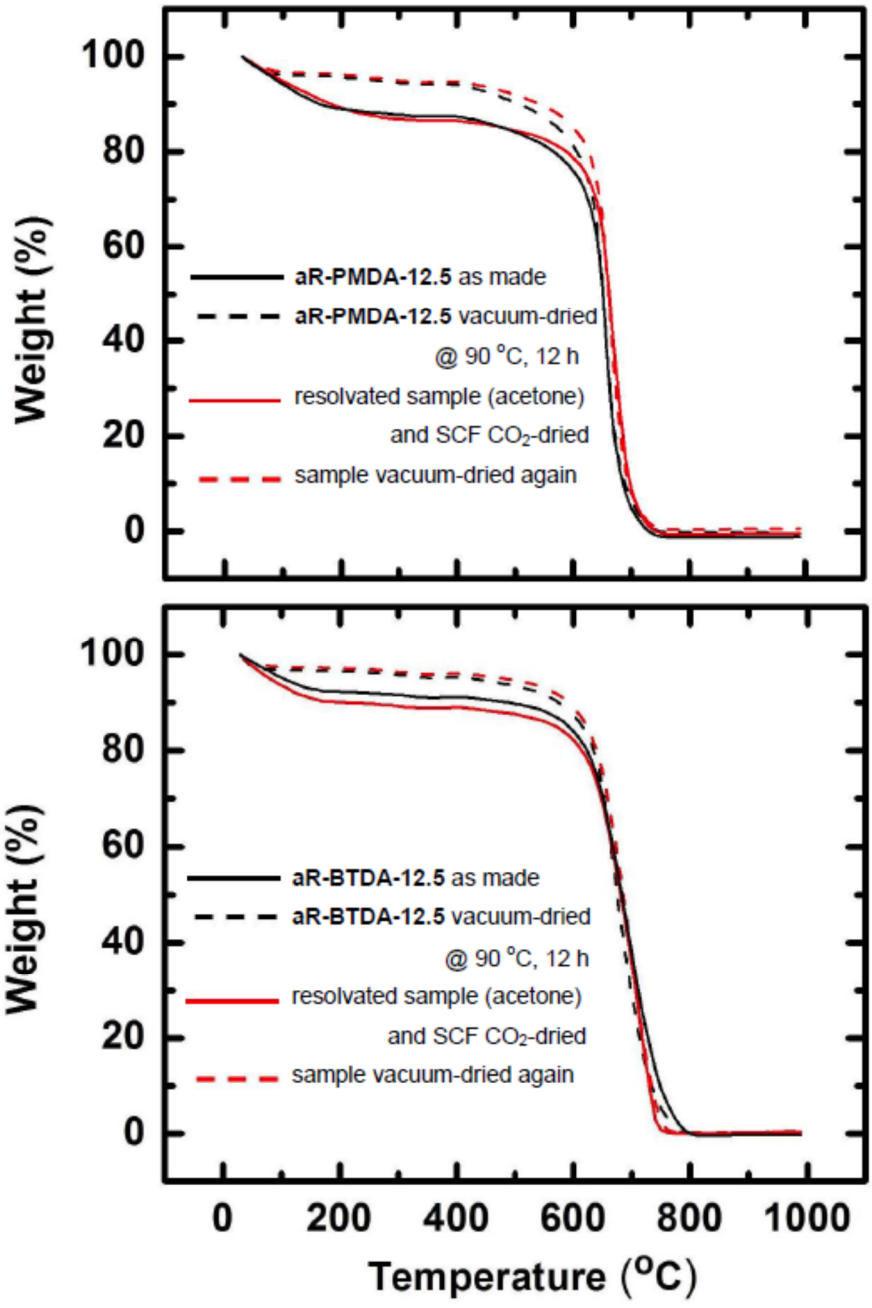

Figure S.13 Thermogravimetric analysis (TGA) in air of the two **aR-DANH-12.5** samples as indicated. (Heating rate: 10 ^{o}C min^{-1}.) The uptake and retention of acetone is not affected by drying via solvent evaporation, hence the pores that retain acetone are not collapsible by surface tension forces suggesting strongly that they are not part of the free volume of the polymer, but rather part of its structure.

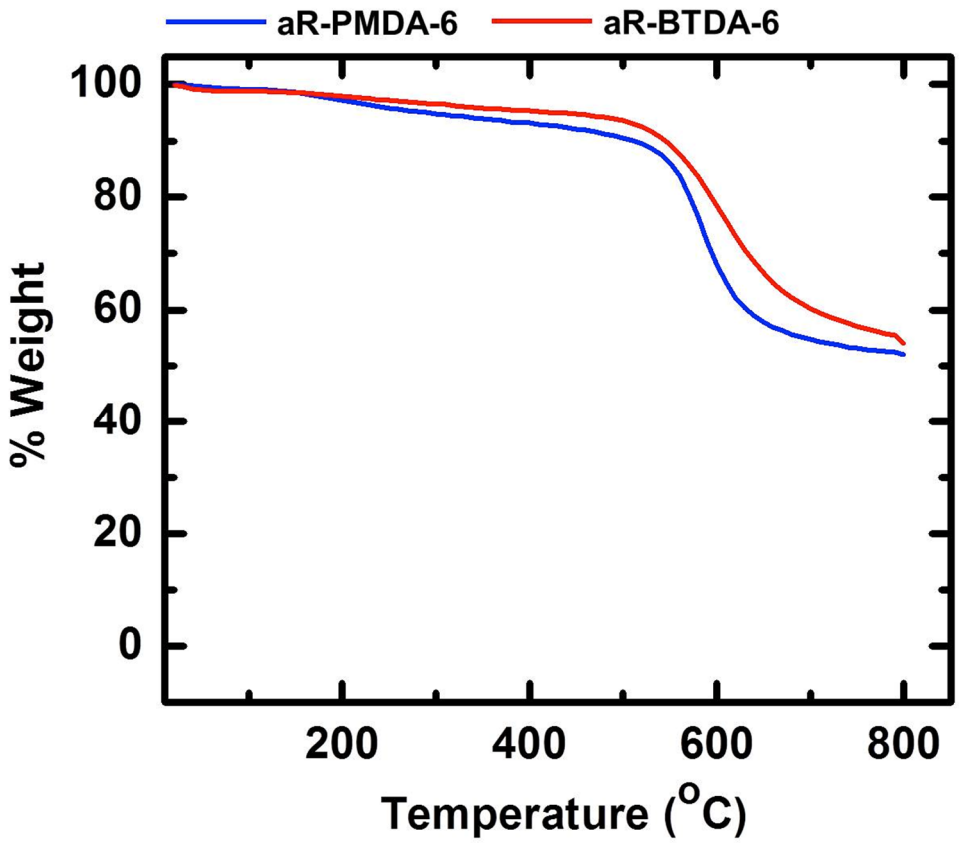

Figure S.14 Thermogravimetric analysis (TGA) under N_2 of the two **aR-DANH-6** samples as indicated. (Heating rate: 10 ^{o}C min^{-1}.)

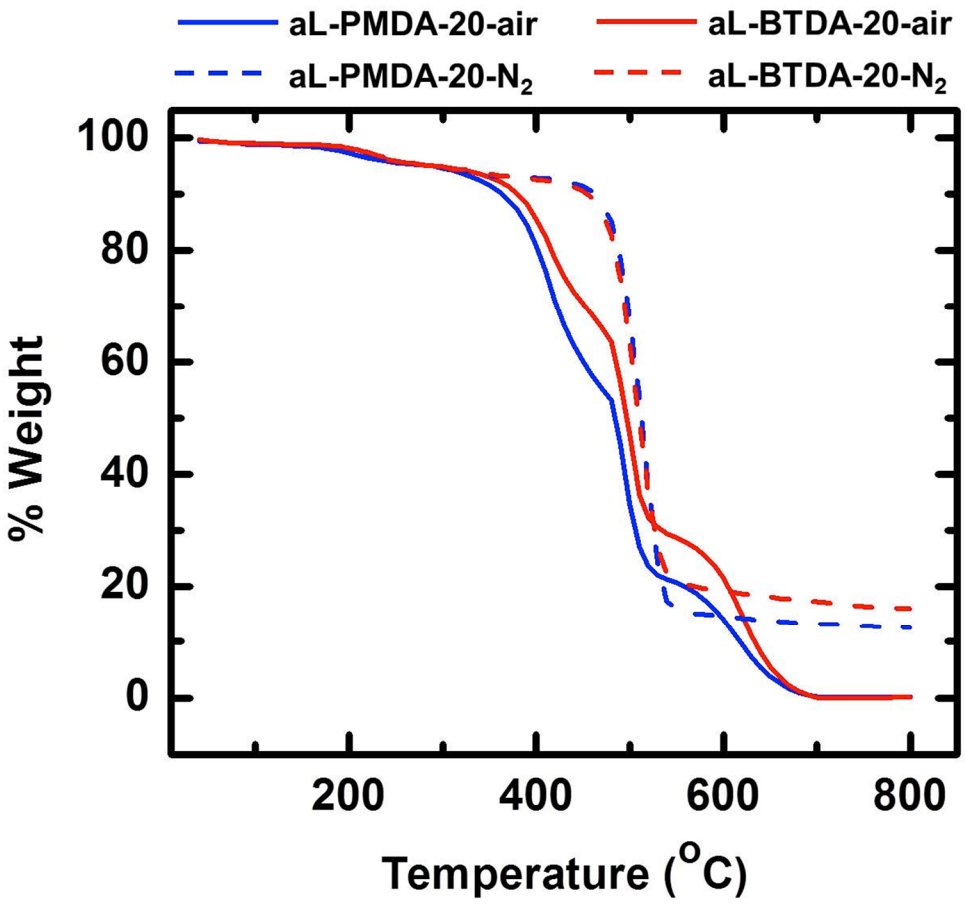

Figure S.15 Thermogravimetric analysis (TGA) under air or N_2 of the two aliphatic triisocyante samples of this study (**aL-DANH-20**) as indicated. (Heating rate: 10 ^{o}C min^{-1}.)

Appendix S.7 Characterization data for polyimide derived carbons

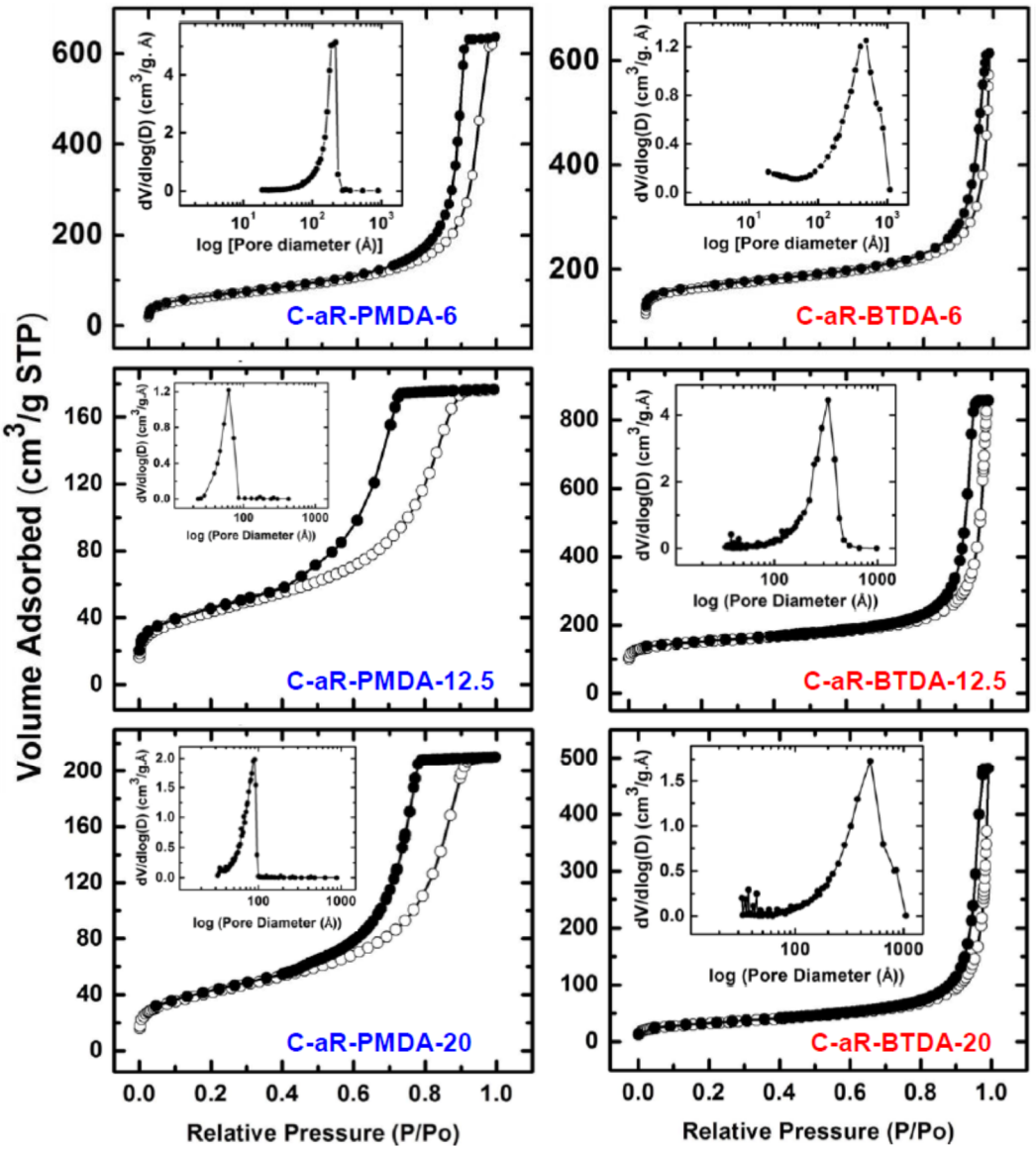

Figure S.16 N_2-Soprtion data of polyimide-derived nanoporous carbons as indicated. Results in Table 2 of main article.

Table S.4. CHN Elemental analysis data for **C-aR-PMDA-xx** and **C-aR-BTDA-xx** carbons

nanoporous carbons	% C w/w	% H w/w	% N w/w	% residual w/w [a]
C-aR-PMDA-6	87.6 ± 0.8	0.41 ± 0.01	7.61 ± 0.2	4.38
C-aR-PMDA-12.5	83.3 ± 0.2	0.38 ± 0.01	10.8 ± 0.6	5.6
C-aR-PMDA-20	81.6 ± 0.08	0.61 ± 0.03	14.8 ± 0.8	2.9
C-aR-BTDA-6	81.8 ± 0.30	0.83 ± 0.01	4.26 ± 0.04	13.11
C-aR-BTDA-12.5	85.4 ± 0.7	0.77 ± 0.03	4.60 ± 0.03	9.23
C-aR-BTDA-20	85.4 ± 0.5	0.5 ± 0.02	5.23 ± 0.18	8.87

[a] By difference, presumably oxygen.

Appendix S.8 Simulated XRD patterns from various optimized structures

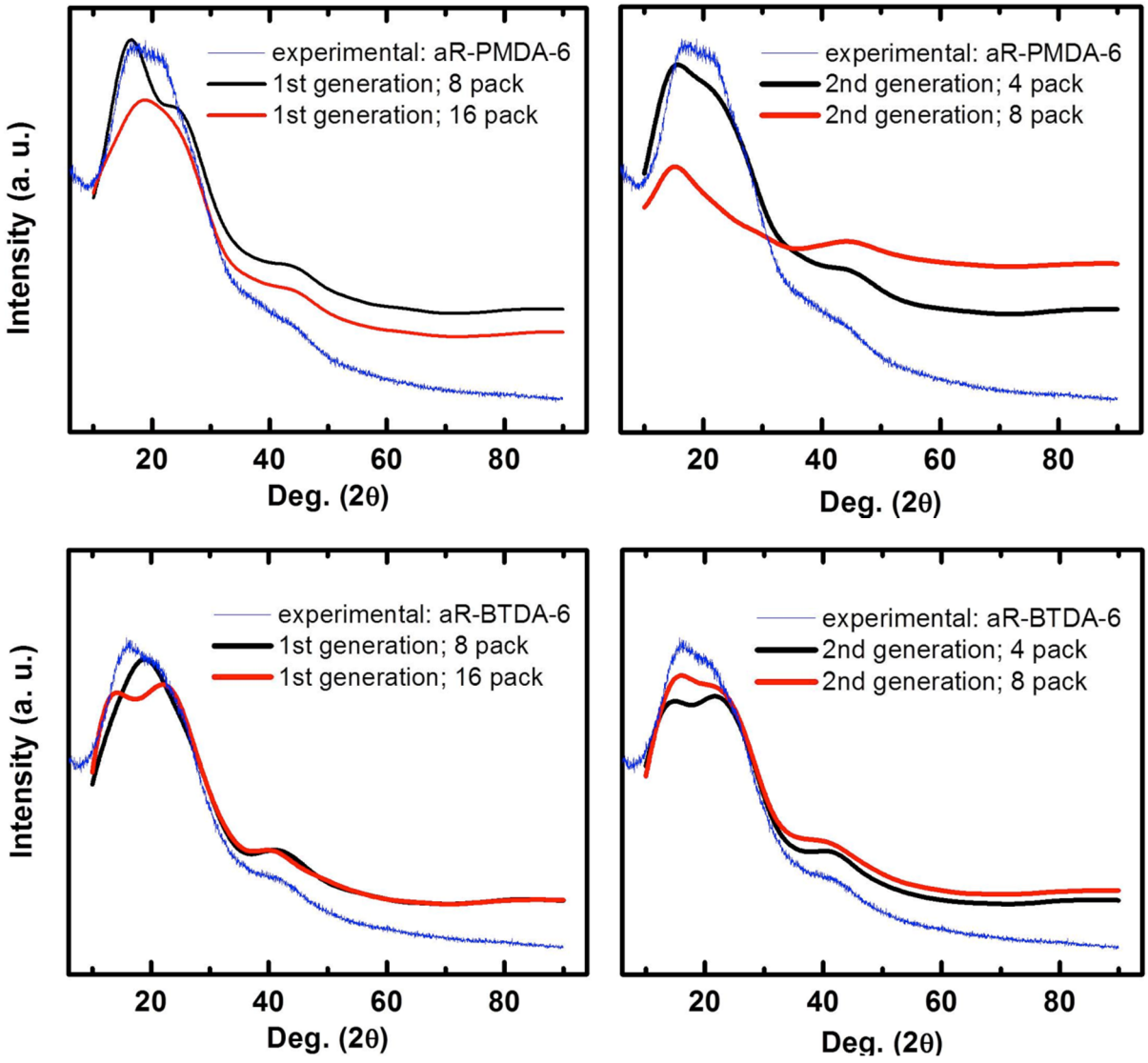

Figure S.17 Simulated versus experimental XRD patterns for **aR-PMDA-xx** and **aR-BTDA-xx** polyimides. "Generation" refers to the hyperbranched growth as shown in Scheme 2 of the main article, and "pack" refers to the number of hyperbrached structures packed in the periodic box and optimized via molecular dynamics relaxation at 298 K for 200 ps.

SECTION

2. CONCLUSIONS

Purely organic aerogels with the same nanostructure and interparticle connectivity as that of crosslinked silica aerogels were synthesized using well-known as well as under-utilized isocyanate chemistry. Materials were synthesized using wide range of polymer chemistry such as polyurethanes, polyureas, polyamides and polyimides and they were studied and explored from an aerogels perspective.

In paper 1, polyurethane aerogels based on two monomeric triisocyanates, one flexible aliphatic and one rigid aromatic, in combination with two aromatic triols and four diols have been prepared and their structure-property relationships have been examined. Macroscopically, samples range from flexible to extremely rigid. Reasoning that bulk behavior cannot be rationalized through a static description of the framework in which individual nanoparticles have no knowledge of one another, we used a top-down characterization approach, whereas we correlated solid thermal conduction with the elastic modulus. It was concluded that the controlling parameter of interparticle connectivity is the functional group density of the monomer. That parameter is expressed as functional group density at the surface of primary particles and controls the efficiency of interparticle bonding.

In Paper 2, polyurea (PUA) aerogels were synthesized using isocyanates and water in three different solvents. The nanomorphology of those aerogels was varied from fibrous in acetone to cocoon-like structures embedded in a fiber web in acetonitirile, to particles in DMF for similar monomer (isocyanate) concentrations. Interestingly, PUA

aerogels synthesized from acetonitirile are highly flexible and superamphiphobic with a contact angle (117 – 150^{o}) compared to aerogels synthesized from acetone. High contact angles are attributed to their surface-fractal microstructure. As demonstrated, PUA aerogels synthesized from acetonitrile can also be used for absorbing oil spills.

In Paper 3, polyamide (aramids) aerogels are demonstrated for the first time, using the reaction of multifunctional aromatic isocyanates with aromatic carboxylic acids. Specifically, it is demonstrated that polyamide aerogels can be prepared in one-step as mesoporous to macroporous materials over a wide density range with high porosities, high surface areas, high elastic modulus, high ultimate strength and high specific energy absorption (toughness). Combining high mechanical strength with relatively-low thermal conductivities and low speed of sound wave propagation, those materials are reasonable candidates for thermal and acoustic insulation at elevated temperatures.

In Paper 4, we describe polyimide aerogels synthesized via a low temperature process through the rather underutilized reaction of dianhydrides with diisocyanates (PI-ISO). These materials are characterized comparatively with aerogels obtained via classic reaction of dianhydrides and diamines (PI-AMN). Their major difference is that PI-AMNs are particulate while PI-ISOs are fibrous. The different morphology has been attributed to the rigidity of the seven-member ring intermediate of PI-ISOs. Upon pyrolysis, PI-ISOs can be converted to isomorphic carbon aerogels having very large surface areas.

In Paper 5, we have demonstrated that the mechanical strength of polyimide aerogels synthesized from isocyanates and anhydrides can be improved by increasing the functionality of particles. The monomer selection was made with the intention to probe

the effect of molecular features in the properties of the resulting materials. Hence robust, monolithic multiscale nanoporous polyimides are obtained and the origin of microporsity was traced to the hyperbranched packing of the primary particles. These materials can also be classified as polymeric materials with intrinsic microporosity.

BIBLIOGRAPHY

1. Tillotson, T. M.; Hrubesh, L. W. *J. Non-Cryst. Solids* **1992**, *145*, 44-50.

2. (a) Rolison, D. R.; Dunn, B. J. *Mater. Chem.* **2001**, *11*, 963–980. (b) Pierre, A. C.; Pajonk, G. M. *Chem. Rev.* **2002**, *102*, 4243–4265. (c) Al-Muhtaseb, S. A.; Ritter, J. A. *Adv. Mater.* **2003**, *15*, 101–114.

3. (a) Kistler, S. S. *Nature* **1931**, *127*, 741. (b) Kistler, S. S. *J. Phys. Chem.* **1935**, *39*, 79-86.

4. (a) Kistler, S. S. *J. Phys. Chem*. **1932**, *36*, 52-64. (b) Kistler, S. S.; Sherlock, S.; Appel, E. G. *Ind. Eng. Chem.* **1934**, *26*, 388-391.

5. Peri, J. B. *J. Phys. Chem.* **1966**, *70*, 2937-2945.

6. Pierre, A. C. History of Aerogels. In *Aerogels Handbook*; Agerter, M. A., Leventis, N., Koebel, M. M., Eds.; Springer: New York, 2011, pp 3-18.

7. http://www.materialslibrary.org.uk/materialslibrary/about.htm

8. Livage, J.; Sanchez, C. *J. Non-Cryst. Solids* **1992**, *145*, 11-19.

9. Kanamori, K; Nakanishi, K. *Chem. Soc. Rev.* **2011**, *40*, 754-770.

10. (a) Zarzycki, J.; Prassas, M.; Phalippou, J. *J. Mat. Sci.* **1982**, *17*, 3371-3379. (b) Tewari, P. H.; Hunt, A. J.; Lofftus, K. D. *Mater. Lett.* **1985**, *3*, 363-367.

11. (a) Wittwer, V. *J. Non-Cryst. Solids* **1992**, *145*, 233–236. 16. (b) Gerlach, R.; Kraus, O.; Fricke, J.; Eccardt, P. C.; Kroemer, N.; Magori, V. *J. Non-Cryst. Solids* **1992**, *145*, 227–232.

12. Jo, M. H.; Park, H. H. *Appl. Phys. Lett.* **1998**, *72*, 1391.

13. Pajonk, G. M. *Appl. Catal.* **1991**, *72*, 217–266.

14. Morris, C. A.; Anderson, M. L.; Stroud, R. M.; Merzbacher, C. I.; Rolison, D. R. *Science* **1999**, *284*, 622-624.

15. (a) daCunha, J. P.; Neves, P.; Lopes, M. *Nucl. Instrum. Methods Phys. Res., Sect. A* **2000**, *452*, 401–421. (b) http://ammtiac.alionscience.com/ammt/iacdocs.do?AM034027.

16. Woignier, T.; Phalippou, J. *J. Rev. Phys. Appl.* **1989**, *24*, 179-184.

17. (a) Katti, A.; Shimpi, N.; Roy, S.; Lu, H.; Fabrizio, E. F.; Dass, A.; Capadona, L. A.; Leventis, N. *Chem. Mater.* **2006**, *18*, 285–296. (b) Meador, M. A.; Capadona, L. A.; McCorkle, L.; Papadopoulos, D. S.; Leventis, N. *Chem. Mater.* **2007**, *19*, 2247–2260. (c) Ilhan, U. F.; Fabrizio, E. F.; McCorkle, L.; Scheiman, D. A.; Dass, A.; Palczer, A.; Meador, M. A. B.; Johnston, J. C.; Leventis, N. *J. Mater. Chem.* **2006**, *16*, 3046–3054. (d) Mulik, S.; Sotiriou-Leventis, C.; Churu, G.; Lu, H.; Leventis, N. *Chem. Mater.* **2008**, *20*, 5035–5046.

18. (a) Leventis, N. *Acc. Chem. Res.* **2007**, *40*, 874-884. (b) Leventis, N.; Mulik, S.; Wang, X.; Dass, A.; Sotiriou-Leventis, C.; Lu, H. *J. Am. Chem. Soc.* **2007**, *129*, 10660-10661. (c) Leventis, N.; Sotiriou-Leventis, C.; Zhang, G.; Rawashdeh, A.-M. M. "Nano Engineering Strong Silica Aerogels," *NanoLetters* **2002**, *2,* 957-960.

19. (a) Bayer, O. *Angew. Chem.* **1947**, *A59*, 257-272. (b) Noshay, A.; McGrath, J. E. In *Block Copolymers: Overview and Critical Survey;* Academic Press: New York, 1977, p 515.

20. Lee, S. T.; Ramesh, N. S. In *Polymeric Foams: Mechanism and Materials*; CRC Press: Florida, 2004, pp 150-267.

21. Saunders, J. H.; Frisch, K. C. In *Polyurethane Chemistry and Technology I. Chemistry*, Interscience publishers, pp 63-118.

22. (a) Stevens, M. P. In *Polymer Chemistry. An Introduction.* Oxford University Press, New York, **1990**. (b) Nicholson, J. W. In The Chemistry of Polymers. London, **1997**.

23. Hepburn, C. In *Polyurethane Elastomers;* Elsevier Science Publishing Co., Inc.: New York, 1982, p 402.

24. (a) Davis, T. L.; Ebersole, F. *J. Am. Chem. Soc.* **1934**, 56, 885-886.

25. Neumann, W.; Fischer, P. *Angew. Chem.* **1962**, *74*, 801-806.

26. (a) Wicks, Z. W., Jr.; Jones, F. N.; Pappas, S. P. In *Organic Coatings, Science & Technology;* Wiley-Interscience: New York, 1999, p 180. (b) Odian, G. In *Principle of Polymerization;* Wiley-Interscience: New York, 2004.

27. (a) Baker, J. W.; Bailey, D. N. *J. Chem. Soc.* **1957**, 4652-4662. (b) Baker, J. W.; Davies, M. M.; Gaunt, J. *J. Chem. Soc.* **1949**, 24-27. (c) Baker, J. W.; Holdsworth, B. *J. Chem. Soc.* **1947**, 713-726.

28. (a) Farkas, A.; Flynn, K. G. *J. Am. Chem. Soc.* **1960**, *82*, 642-645. (b) Farkas, A.; Mills, G. A.; Erner, W. E.; Maerker, J. B. *Ind. Eng. Chem.* **1959**, *51*, 1299-1300.

29. Schwetlick, K.; Noack, R.; Stebner, F. *J. Chem. Soc. Perkin Trans.* **1994**, *2*, 599-608.

30. Borkent, G.; Van Aartsen, J. J. In Polymerization Kinetics and Technology; 1973, pp 274-280.

31. Britain, J. W.; Gemeinhardt, P. G. *J. Appl. Polym. Sci.* **1960**, *4*, 207-211.

32. Smith, H. A. *J. Appl. Polymer Sci.* **1963**, *7*, 85-95.

33. Houghton, R. P.; Mulvaney, A. W. *Journal of Organometallic Chemistry* **1996**, *518*, 21-27.

34. (a) Furukawa, I.; Hashiyama, M.; Hashimoto, S. *J. Macromo. Sci. –Chem.* **1985**, *A26*, 761-771. (b) Onder, K.; Chen, A. T. *Polym. Eng. Sci.* **1985**, *25*, 942-946. (c) Simionescu, C.; Comanita, E.; Vata, M. *Angew. Makromol. Chem.* **1975**, *46*, 135.

35. (a) Onder, K.; Smith, C. P. U. S. Patent No. 4,156,065 (1979). (b) Toyoda, T.; Kawamata, M.; Osawa, M.; Itoh, M.; Mizutani, K. U. S. Patent No. 4,395,531 (1983).

36. Wei, Y.; Jia, X.; Jin, D.; Davis, F. A. *Macromol. Rapid Commun.* **1996**, *17*, 897-903.

37. Xiao, H.; Xiao, H. X.; Frisch, K. C.; Malwitz, N. *High Perform. Polym.* **1994**, *6*, 235-239.

38. Sorenson, W. R. *J. Org. Chem.* **1959**, *24*, 978-980.

39. Agre, C. L.; Dinga, G.; Pflaum, R. *J. Org. Chem.* **1955**, *20*, 695-699.

40. Wurtz, A. *Ann. Chem. Phys.* **1854**, *42*, 54.

41. (a) Hurd, C. D.; Prapas, A. G. *J. Org. Chem.* **1959**, *24*, 388-392. (b) Marton, J.; Meisel-Agoston, *J. Acta. Chem. Acad. Sci. Hung.* **1960**, *24*, 327.

42. Meyers, R. A. *J. Polym. Sci. Part A1*, **1969**, *7*, 2757-2762.

43. (a) Hofmann, A. W. *Ber. Dtsch. Chem. Ges.* **1885**, *18*, 764-766. (b) Raiford, L. C.; Freyermuth, H. B. *J. Org. Chem.* **1943**, *8*, 230-238. (c) Delebecq, E.; Pascault, J. –P.; Boutevin, B.; Ganachaud, F. *Chem. Rev.* **2013**, *113*, 80-118.

44. (a) Campbell, T. W.; Smeltz, K. C. *J. Org. Chem.* **1963**, *28*, 2069-2075. (b) Dyer, E.; Read, R. E. *J. Org. Chem.* **1961**, *26*, 4677-78. (c) Khorana, H. G. *Chem. Rev.* **1953**, *53*, 145-166.

45. Shimizu, K.; Phanopoulos, C.; Loenders, R.; Abel, M. –L.; Watts, J. F. *Surf. Interface Anal.* **2010**, *42*, 1432-1444.

46. (a) Leventis, N.; Sotiriou-Leventis, C.; Chandrasekaran, N.; Mulik, S.; Larimore, Z. J.; Lu, H.; Churu, G.; Mang, J. T. *Chem. Mater.* **2010**, *22*, 6692-6710. (b) American Society for Metals, ASM Engineering Materials Handbook, Composites, Volume 1: ASM International: Materials Park, OH, p 178, Table 2, 1998. (c) Luo, H.; Chen, W. *Intern. J. Appl. Ceram. Techn.* **2004**, *1*, 254-260. (d) Luo, H.; Chen, W.; Rajendran, A. M. *J. Am. Ceram. Soc.* **2006**, *89*, 266-273.

47. Malshe, V. C.; Sikchi, M. In *Basics of Paint Technology: Part I*; Sevak Printers: Mumbai, 2002, pp 236-237.

48. Hench, L. L.; West, J. K. *Chem. Rev.* **1990**, *90*, 33-72.

49. Flory, P. J. In *Principles of Polymer Chemistry*; Cornell University Press: Ithaca, NY, 1953, Chapter IX.

50. Zallen, R. In *The Physcis of Amorphous Solids*; Wiley: New York, 1983, Chapter IV.

51. Stauffer, D.; Coniglio, A.; Adam, M. *Adv. Polym. Sci.* **1982**, *44*, 103-158.

52. Benoit, B.; Mandelbrot, W. H. In *The Fractal Geometry of Nature*; Freeman and Company: New York, 1982.

53. (a) Zarzycki, J. In Science of Ceramic Chemical Processing; Hench, L. L., Ulrich, D. R., Eds.; Wiley: New York, 1986; p 21. (b) Keefer, K. D. In Science of Ceramic Chemical Processing; Hench, L. L., Ulrich, D. R., Eds.; Wiley: New York, 1986, p 131. (c) Craievich, A.; Aegerter, M. A.; dos Santos, D. I.; Woignier, T.; Zarzycki, J. *J. Non-Cryst. Solids* **1986**, *86*, 394-406.

54. Pope, E. J. A; Mackenzie, J. D. *J. Non-Cryst. Solids* **1988**, *101*, 198-212.

55. (a) Flory, P. J. *J. Am. Chem. Soc.* **1941**, *63*, 3083-3090. (b) Flory, P. J. *Chem. Rev.* **1946**, *39*, 137-197.

56. Carothers, W. *Trans. Faraday Soc.* **1936**, *32*, 39-49.

57. Everett, D. H. Basic Principles of Colloid Science Royal Society of Chemistry: London, U.K. 1988.

58. Pekala, R.W. *Low Density Resorsinol-Formaldehyde Aerogels*, U.S. Patent No. 4,873,218, 1989.

59. Jarfelt, U.; Ramnas, O. In *10th International Symposium on District Heating and Cooling* 2006, pp. 1-11

60. (a) Biesmans, G.; Randall, D.; Francais, E.; Perrut, M. *J. Non-Cryst. Solids* **1998**, *225*, 36-40. (b) Biesmans, G.; Mertens, A.; Duffours, L.; Woignier, T.; Phalippou, J. *J. Non-Cryst. Solids* **1998**, *225*, 64-68.

61. Tan, C.; Fung, B. M.; Newman, J. K.; Vu, C. *Adv. Mater.* **2001**, *13*, 644-646.

62. Yim, T. J.; Kim, S. Y.; Yoo, K. P. *Korean J. Chem. Eng.* **2002**, *19*, 159-166

63. Rigacci, A.; Marechal, J. C.; Repoux, M.; Moreno, M.; Achard, P. *J. Non-Cryst. Solids* **2004**, *350*, 372-378.

64. Lee, J. K.; Gould, G. L.; Rhine, W. *J. Sol-Gel Sci Technol.* **2009**, *49*, 209-220.

65. Raghavan, S. R.; Chen, L. A.; McDowell, C.; Khan, S. A., Hwang, R.; White, S. *Polymer* **1996**, *37*, 5869-5875.

66. Muthukumar, M. *Macromolecules* **1989**, *22*, 4656-4658.

67. Kolb, M.; Botet, R.; Jullien, R. *Phys. Rev. Lett.* **1983**, *51*, 1123-1126.

68. (a) Lu, X.; Caps, R.; Fricke, J.; Alviso, C. T.; Pekala, R. W. *J. Non-Cryst. Solids*, **1995**, *188*, 226-234. (b) Lu, X.; Nilsson, O.; Fricke, J.; Pekala, R. W. *J. Appl. Phys.* **1993**, *73*, 581-584.

69. (a) Meador, M. A. B.; Malow, E. J.; Silva, R.; Wright, S.; Quade, D.; Vivod, S. L.; Guo, H.; Guo, J.; Cakmak, M. *ACS Appl. Mater. Interfaces* **2012**, *4*, 536-544. (b) Meador, M. A. B. "Improving Elastic Properties of Polymer-Reinforced Aerogels." In *Aerogels Handbook*; Aegerter, M. A.; Leventis, N.; Koebel, M. M. Eds.; Springer: New York, N.Y., 2011, Chapter 15, pp 191-214. (c) Jin, C. "Aerogels Super Thermal Insulation Material by Nano Hi-tech." In *Aerogels Handbook*; Aegerter, M. A.; Leventis, N.; Koebel, M. M. Eds.; Springer: New York, N.Y., 2011, Chapter 40, pp 865-877. (d) Jones, S. M.; Sakamoto, J. "Applications of Aerogels in Space Exploration." In *Aerogels Handbook*; Aegerter, M. A.; Leventis, N.; Koebel, M. M. Eds.; Springer: New York, N.Y., 2011, Chapter 32, pp 721-746.

70. Jones, S. M. *J. Sol-Gel Sci. Technol.* **2007**, *44*, 255-258.

71. Leventis, N.; Sotiriou-Leventis, C.; Chandrasekaran, N.; Mulik, S.; Chidambareswarapattar, C.; Sadekar, A.; Mohite, D.; Mahadik, S.; Larimore, Z. J.; Lu, H.; Churu, G.; Mang, J. T. *MRS Proceedings* **2011**, *1306*, mrsf10-1306-bb03-01 doi:10.1557/opl.**2011**.90

72. Weigold, L.; Mohite, D. P.; Mahadik-Khanolkar, S.; Leventis, N.; Reichenauer, G. *J. Non-Cryst. Solids* **2013**, *368*, 105-111.

73. (a) Sun, M.; Luo, C.; Xu, L.; Ji, H.; Ouyang, Q.; Yu, D.; Chen, Y. *Langmuir* **2005**, *21*, 8978-8981. (b) Dawood, M. K.; Zheng, H.; Liew, T. H.; Leong, K. C.; Foo, Y. L.; Rajagopalan, R.; Khan, S. A.; Choi, W. K. *Langmuir* **2011**, *27*, 4126-4133. (c) Ebert, D.; Bhushan, B. *J. Colloid Interface Sci.* **2012**, *384*, 182-188.

74. Rao, A. V.; Bhagat, S. D.; Hirashima, H.; Pajonk, G. M. *J. Colloid Interface Sci.* **2006**, *300*, 279-285.

75. (a) Bourbigot, S.; Flambard. X. *Fire Mater.* **2002**, *26*, 155-168. (b) Chatzi, E. G.; Koenig, J. L. *Polymer-Plastics Technology and Engineering* **1987**, *26*, 229-270.

76. Carothers, W. H. *J. Am. Chem. Soc.* **1929**, *51*, 2548-2559.

77. Ahmad, Z.; Sarwar, M. I.; Mark, J. E. *J. Mater Chem.* **1997**, *7*, 259-263.

78. (a) Leventis, N.; Chidambareswarapattar, C.; Mohite, D. P.; Larimore, Z. J.; Lu, H.; Sotiriou-Leventis, C. *J. Mater. Chem.* **2011**, *21*, 11981-11986. (b) Chidambareswarapattar, C.; Mohite, D. P.; Larimore, Z. J.; Lu, H.; Sotiriou-Leventis, C.; Leventis N. *MRS Proceedings* **2012**, *1403*, 29-34.

79. C. E. Sroog, A. L. Endrey, S. V. Abrmo, C. E. Berr, W. M. Edward, K. L. Oliver, *J. Polym. Sci. Part A* **1965**, *3*, 1373-1390.

80. (a) Meador, M. A. *Annu. Rev. Mater. Sci.* **1998**, *28*, 599-630. (b) Meador, M. A. B.; Johnston, J. C.; Cavano, P. J. *Macromolecules* **1997**, *30*, 515-519.

81. (a) Williams, M. K.; Weiser, E. S.; Fesmire, J. E.; Grimsley, B. W.; Smith, T. M.; Brenner, J. R.; Nelson, G. L. *Polym. Adv. Technol.* **2005**, *16*, 167-174. (b) Weiser, E. S.; Johnson, T. F.; St Clair, T. L.; Echigo, Y. Kaneshiro, H. Grimsley, B. W. *High Performance Polymers* **2000**, *12*, 1-12. (c) Williams, M. K.; Holland, D. B.; Melendez, O.; Weiser, E. S.; Brenner, J. R.; Nelson, G. L. *Polymer Degradation \and Stability* **2005**, *88*, 20-27.

82. http://www.koo-associates.com/homepage.html

83. Rhine, W.; Wang, J.; Begag, R. U. S. Patent No. 7,074,880 (2006)

84. Meador, M. A. B.; Malow, E. J.; He, Z. J.; McCorkle, L.; Guo, H.; Nguyen, B. N. *Polymer Preprints*, **2010**, *51*, 265-266.

85. (a) Kawagishi, K.; Saito, H.; Furukawa, H.; Horie, K. *Macromol. Rapid Commun.* **2007**, *28*, 96-100; (b) Guo, H.; Meador, M. A. B.; McCorkle, L.; Quade, D. J.; Guo, J.; Hamilton, B.; Cakmak, M.; Sprowl, G. *ACS Appl. Mater. Interfaces* **2011**, *3*, 546-552; (c) Meador, M. A. B.; Malow, E. J.; Silva, R.; Wright, S.; Quade, D.; Vivod, S. L.; Guo, H.; Guo, J.; Cakmak, M. *ACS Appl. Mater. Interfaces* **2012**, 4, 536-544; (d) Guo, H.; Meador, M. A. B.; McCorkle, L.; Quade, D. J.; Guo, J.; Hamilton, B.; Cakmak, M. *ACS Appl. Mater. Interfaces* **2012**, 4, 5422-5429.

86. Leventis, N.; Sotiriou-Leventis, C.; Mohite, D. P.; Larimore, Z. J.; Mang, J. T.; Churu, G.; Lu, H. *Chem. Mater.* **2011**, *23*, 2250-2261.

87. Chidambareswarapattar, C.; Larimore, Z.; Sotiriou-Leventis, C.; Mang, J. T.; Leventis, N. *J. Mater. Chem.* **2010**, *20*, 9666-9678.

88. Chidambareswarapattar, C.; Larimore, Z.; Sotiriou-Leventis, C.; Leventis, N. *Polymeric Materials: Science & Engineering* **2012**, *106*, 193-195.

89. (a) Smirnova, A.; Ding, X.; Hara, H.; Vasiliev, A; Sammes, N. Int. *Journal of Hydrogen Energy*, **2005**, *30*, 149-158. (b) Kwon, O. J.; Jung, Y. S.; Kim, J. H.; Oh, S. M. *Journal of Power Sources*, **2004**, *125*, 221-227. (c) Fialkov, A. S. *J. Electrochem* **2000**, *36*, 345-366.

90. Buerger, A.; Fitzer, E.; Heim, M.; Terwiesch, B. *Carbon* **1975**, *13*, 149-157.

91. Jenkins, G. M.; Kawamura, K. In *Polymeric Carbons, Carbon Fibre, Glass and Char;* Cambridge University Press: New York, **1976**.

92. (a) Lide, D. R. CRC Handbook of Chemistry and Physics, CRC Press, Boca Raton, FL, 84th edn. 2003, pp. 12/22612/227. (b) http://www.engineeringtoolbox.com/thermal-conductivity-d_429.html.

93. Riffat, S. B.; Qiu, G. *International Journal of Low-Carbon Technologies* **2012**, 1-6.

VITA

Chakkaravarthy Chidambareswarapattar was born in 1985 in Tenkasi, Tirunelveli, Tamil Nadu, India. He received his Bachelors degree in Paints Technology from the University Institute of Chemical Technology (UICT) at Mumbai, India in 2006. He worked as a Technical Officer for two years with the Research and Development Division of ICI Paints India Ltd. (now AkzoNobel India Ltd.) before coming to the United States for his graduate studies. In 2008, he joined Missouri University of Science and Technology to pursue a Ph.D. degree in chemistry. In January 2009, he joined Prof. Leventis group and his research work focused on developing multifunctional organic aerogels. During the course of his Ph.D. work, he has published two (2) journal articles, submitted three (3) articles, and presented his research in various National ACS and MRS meetings. He also interned with the Xerox Innovation Group, Xerox Corporation, in the summer of 2012 under the guidance of Dr. Mandakini Kanungo. He was nominated in 2013 for the President's student entrepreneurship award. He is also a co-inventor in four (4) U.S. patent applications. He graduated from Missouri University of Science and Technology with a PhD in chemistry in August 2013.